

## IMPACTS OF TEMPERATURE DEPENDENT THERMAL CONDUCTIVITY AND VISCOSITY ON SLIPPED FLOW OF MAXWELL NANOFUID

 **Debozani Borgohain**

*Department of Mathematics, Dibrugarh University, Dibrugarh, 786004, Assam, India*

*Corresponding Author e-mail: [debozaniborgohain@dibru.ac.in](mailto:debozaniborgohain@dibru.ac.in)*

*Received August 28, 2023; revised October 19, 2023; accepted November 1, 2023*

The mathematical model to inspect the effects of changeable thermo-physical properties such as thermal conduction, slip effects and viscosity on Maxwellian nanofluid is proposed. The thermal conductivity increases rapidly due to presence of nanoparticles such as metals, carbides, oxides etc. in base fluid. The flow occurs from the stagnated point pass a stretched sheet with slipped conditions. The characteristics of the Brownian motion as well as the thermophoresis processes are also taken into consideration. By means of similarity transformations, the ODEs are reduced from the equations influencing the fluid flow. A built-in solver of MATLAB namely bvp4c which is a collocation formula implementing the Lobatto IIIa finite difference numerical method is applied to solve these transformed equations numerically. The graphs of the numerical outcomes representing impacts of variations in different parameters on the fluid movement, transfer of heat along with mass are analyzed. This investigation leads to an important aspect that as the thermal conductivity in the flow is intensified, the temperature of the fluid reduces with high aggregation of the nanoparticles near the sheet's surface. Also, the rates of heat and mass transferral depletes due to the relaxation of Maxwellian fluid. Furthermore, the effectiveness of the present numerical computations is determined by carrying out comparisons of heat and mass transferred rates against the previous analytical results for several values of thermophoresis and Prandtl parameters. The effectiveness of its outcomes can be applied in nanoscience technology and polymeric industries for their developments.

**Keywords:** *Heat transfer; Variable fluid viscosity; Slip Effects; Variable thermal conductivity; Maxwell fluid*

**PACS:** 47.50.-d, 47.15.Cb, 47.11.-j, 44.20.+b, 65.80.-g, 82.60.Qr, 47.57.Ng, 82.35.Np, 83.50, 65.20.-w, 83.60.Bc, 83.60.Df

### Nomenclature

$T_W$	Temperature on the sheet	$T$	Fluid temperature
$C_W$	Nanoparticle fraction on the wall	$\tau$	Ratio of heat capacity of a nanoparticle to heat capacity of an ordinary liquid/gas
$T_\infty$	Free stream temperature	$c$	Rate at which the sheet is stretched
$C_\infty$	Free stream Nanoparticles concentration	$v = \alpha(T_W - T_\infty)$	Dimensionless reference temperature corresponding to viscosity
$u$	velocity along xaxis	$\beta = k_0 c$	Maxwell parameter known as Deborah number
$v$	velocity along yaxis	$\epsilon = b(T_W - T_\infty)$	Dimensionless reference temperature corresponding to thermal conductivity
$\rho_\infty$	density of the base fluid	$A = \frac{k}{c}$	Ratio of rates of velocities
$\nu(T) = \frac{\mu(T)}{\rho_\infty}$	fluid kinematic viscosity	$Pr = \frac{\rho_\infty \nu_\infty C_P}{K_\infty} = \frac{\nu_\infty}{\alpha}$	Prandtl number
$C_P$	specific heat at constant pressure	$Nt = \frac{\tau D_T}{\nu_\infty T_\infty} (T_W - T_\infty)$	Thermophoresis parameter
$D_B$	Brownian diffusion coefficient	$Nb = \frac{\tau D_B}{\nu_\infty} (C_W - C_\infty)$	Brownian motion parameter
$D_T$	Thermophoresis diffusion coefficient	$Le = \frac{\alpha}{\frac{D_B}{\rho_\infty C_P}} = \frac{K_\infty}{\rho_\infty C_P D_B}$	Lewis number
$\kappa_0$	relaxation time of the upper-convected Maxwell fluid	$S = \frac{V_W}{\sqrt{c \nu_\infty}}$	suction parameter
$K(T)$	variable thermal conductivity	$\lambda = F \sqrt{\frac{c}{\nu_\infty}}$	Velocity slip parameter
$C$	Nanoparticles volume fraction	$\delta = G \sqrt{\frac{c}{\nu_\infty}}$	Thermal slip parameter
$P$	Pressure	$\gamma = H \sqrt{\frac{c}{\nu_\infty}}$	Solutal slip parameter
$\psi$	Stream function	$\eta$	Similarity variable

### INTRODUCTION

Over the past few decades, inspection of nonnewtonian fluids flow passing a stretched sheet is a topic of immense curiosity amongst researchers, engineers and scientists because of its vast utilizations in biomechanics and engineering fields such as in extrusion process, annealing, extraction of metals, etc. Changes in shear stress and some properties of fluid lead to further classification of non-Newtonian fluids into Bingham plastic, Pseudoplastic, Viscoelastic. Poisson [1] and Maxwell [2] gave rigorous arguments and stated that all fluids must have some degree of elasticity. In fact,

constitutive theories such as Maxwell and Boltzmann [3] were based on the thoughts that there will be momentary elastic responses in fluids. This concept includes the idea that fluids such as water and glycerin have viscous response while others (like less strong solutions) are somewhat elastic and some viscous. Viscoelastic fluid has both the property of viscosity and elasticity. On sudden removal of stress of viscoelastic fluid, the fluid strain doesn't disappear at once but relaxes quite slowly. The simplest model of viscoelastic fluids is the Maxwell model which has very small dimensionless relaxation time. In order to investigate the role of the parameters such as electrical conductivity in heterogeneous solid particles, J. C. Maxwell proposed a model in 1867. Wide range of applications of Maxwell fluid in technical, engineering and industrial areas has fascinated many researchers.

In 1989, Barnes et al. [4] in their research had conferred that in rheology even a solid-like material would start flowing after a given large amount of time. Keeping this in mind, a nondimensional number is required which is associated with both viscosity and elasticity of material. Thus, a non-dimensional number named as Deborah number was introduced which was well described by Poole [5]. Sadeghy et al. [6] in their work have investigated numerically the stagnated point flow of Maxwellian fluid. Wang and Tan [7] analysed the Maxwellian flow in a porous media. The wide utilizations of stagnated point flow in industrial and engineering applications such as electrochemical engineering, storage devices, waste water management, paper production, aero-engineering, etc. have embarked the interests of numerous investigators. Hiemenz [8] was the first researcher to model the stagnated point flow problem. He used similarity variables to obtain its solution in a precise manner. Chiam [9], [10] followed his work and continued the study under the consideration of the geometry as the stretchable sheet. Later on, Ahmad et al. [11] utilized Buongiorno model of nanofluid to carry on his investigation on stagnated flow of Maxwell nanofluid past a disk. Recently, various researchers such as Sunder Ram et al. [12], Reddy et al. [13], Dessie [14], Reddy and Mangamma [15] and so on, investigated the porosity effects on stagnated point flow of convective magnetized flow of microfluids, Casson fluids and Newtonian fluids. They used several numerical methods such as Shooting method, Runge kutta fourth order method and Keller box method to obtain the numerical solutions.

Recently, a current topic of heat transfer medium has emerged named as Nanofluid coined by Choi [16] which contains nanoparticles of size 01 – 100 nm. These nanoparticles, generally a metal or metal oxide, are stably and uniformly distributed over base fluid which tremendously intensifies the nanofluid thermal conduction, enhances coefficients of conduction and convection thereby favouring more heat transfer. Compared with millimeters and micrometers, Nanoparticles have great potential for enlarging thermal transport facilities. Nanofluids have an extensive applicability for engineering in heat transfer systems, automotive applications, electronic systems and biomedical applications etc. Buongiorno [17] examined various theories explaining the advanced features of heat transfer of nanofluids. He proposed an analytical solution of convection in nanofluids that looked at thermophoresis and Brownian propagation. Kuznetsov and Nield [18] extended the study of Boungiorno and researched on the nanofluid flow passed a vertical surface. Khan & Pop [19] followed them to explore thoroughly the nanofluid flow across an expanded surface with a surface temperature. Makinde and Aziz [20] investigated the condition of the transmission limit to assess the nanofluid flow over the expandable surface. An investigation on the flow over an extended sheet of Oldroyd-B fluid was accomplished by Sajid et al. [21] taking magnetic effects into consideration. Assuming geometry as a sheet with tendency to stretch, the flow of the nanofluid from a stagnated point is investigated numerically by Yasin Abdela et al. [22]. Ramesh et al. [23] inquired on flow of Maxwell fluid from a stagnated point in the existence of nanoparticles. Under various physical conditions, researchers such as Mishra [24] and El-Aziz and Afify [25] investigated the effects of slipped conditions on MHD flow in various non-Newtonian models such as Casson fluid and Jeffrey fluid. Ibrahim and Negera [26] have investigated the stagnation point flows and slip effects of MHD Maxwell nanofluid past a stretched sheet.

Factors of variation in viscosity and thermal conductivity in liquid flow have the use of geothermal energy, the underground storage system and many other areas. Changes in viscosity in liquid or gas flows help predict flow patterns and heat transfer rates, while in heat transfer problems, changes in thermal conductivity help communicate the accuracy of the energy transfer. Makinde et al. [27, 28] and Ali et al. [29] investigated the impacts of variation in viscosity on the stable and unstable flow of nanofluid by assuming different conditions and different geometries. For MHD flow of fluid containing dust particles, the change in fluid viscosity and thermal conduction was inspected by Manjunatha and Gireesha [30]. In their work they inferred that a reduction in the fluid velocities and dust phase occur due to the increased viscousness parameter of the fluid. Borgohain [31] in her work investigated on the radiative Maxwell Nanofluid and numerically forecast the flow rate, temperature and concentration features of the flow. Iranian et al. [32] inspected on impacts of suction/ injection and slip conditions on flow of Maxwell fluid number and concluded that heat transferral rate is boosted by thermal and momentum slip conditions.

In earlier problems of upper-convected Maxwell fluid flow from the stagnation point, the effects of changeable thermal conduction and viscosity were not discussed in the presence of nanoparticles under the slip effects. Owing to the importance of variation in thermal conduction and viscosity in the thermal engineering works of insulation, energy production, devices enhancing thermal power, computer storage devices, cooling systems and polymeric industries, study on this topic has become relevant. The originality of this study is therefore, the modelling of the UCM flow problem under the constraint of changing thermal conduction and viscousness of the fluid along with the slip conditions and presence of nanoparticles in the fluid from a stagnated point.

The central objective of the current article is to investigate the effects of variation in viscousness, slip effects and thermal conduction on the flow of Maxwell fluid past a stretchable surface along with nanoparticles present in the fluid

via programming in MATLAB. Present study can be helpful in the processes that involve engineering, polymeric, insulations and nanofluid operations involving the works of storage systems, extrusion processes, cooling systems, paper production, thermal power generation, etc.

**FORMULATION OF THE PROBLEM**

The problem is considered as a slip flow problem of an upperconvected Maxwell (UCM) fluid in positive y-axis region. At x-axis, a stretching surface is placed with stagnation point fixed at  $x = 0$ . Towards its perpendicular direction, the y-axis is assumed. This flow model of the assumed problem is physically illustrated in Figure 01. The fluid containing nanoparticles passes over this stretched surface. From the stagnation point, the free stream velocity  $U(x)$  and fluid velocity on stretched/ shrunk velocity  $U_w(x)$  are considered to vary linearly i.e. the free stream velocity is taken as  $U(x) = kx$  and fluid velocity on the stretched/ shrunk sheet is taken as  $U_w(x) = cx$  where  $c > 0$  is the stretching sheet velocity,  $c < 0$  is the shrinking sheet velocity and  $k > 0$  are constants. The two-dimensional laminar fluid flow is considered to be incompressible and steady. The thermal conduction and viscousness of the fluid, being dependent on temperature, are taken into account as variables. All the other thermophysical properties of the fluid are considered to be constant.

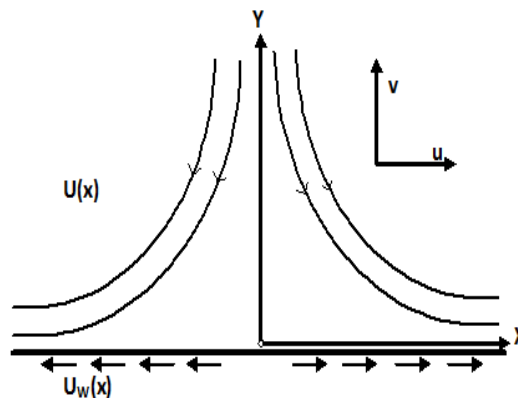


Figure 1. Physical illustration

Taking all these factors into account the Maxwell nanofluid flow governing boundary layer equations [27] over stretched sheet with changeable fluid viscousness and thermal conduction takes the following forms:

$$\frac{\partial v}{\partial y} + \frac{\partial u}{\partial x} = 0, \tag{1}$$

$$u \frac{\partial u}{\partial x} + v \frac{\partial u}{\partial y} = \frac{\partial}{\partial y} \left( \nu(T) \frac{\partial u}{\partial y} \right) + U \frac{dU}{dx} - \kappa_0 \left( u^2 \frac{\partial^2 u}{\partial x^2} + v^2 \frac{\partial^2 u}{\partial y^2} + 2uv \frac{\partial^2 u}{\partial x \partial y} \right), \tag{2}$$

$$u \frac{\partial T}{\partial x} + v \frac{\partial T}{\partial y} = \frac{1}{\rho_\infty c_p} \frac{\partial}{\partial y} \left( K(T) \frac{\partial T}{\partial y} \right) + \frac{\tau D_T}{T_\infty} \left( \frac{\partial T}{\partial y} \right)^2 + \tau D_B \frac{\partial C}{\partial y} \cdot \frac{\partial T}{\partial y}, \tag{3}$$

$$u \frac{\partial C}{\partial x} + v \frac{\partial C}{\partial y} = D_B \left( \frac{\partial^2 C}{\partial x^2} + \frac{\partial^2 C}{\partial y^2} \right) + \frac{D_T}{T_\infty} \left( \frac{\partial^2 T}{\partial x^2} + \frac{\partial^2 T}{\partial y^2} \right). \tag{4}$$

The boundary conditions (bcs) suggested by Ibrahim et al. [26] are

$$\left. \begin{aligned} u &= cx + F \frac{\partial u}{\partial y}, v = V_w(x), T = T_w + G \frac{\partial T}{\partial y}, C = C_w + H \frac{\partial C}{\partial y} \text{ at } y = 0, \\ u &\rightarrow kx, T \rightarrow T_\infty, C \rightarrow C_\infty \text{ as } y \rightarrow \infty, \end{aligned} \right\} \tag{5}$$

where  $c > 0$  for the stretched sheet and  $c < 0$  for the shrinking sheet.

Introduce the similarity transformations as follows:

$$\eta = \sqrt{\frac{c}{\nu_\infty}} y, \psi = \sqrt{c \nu_\infty} x f, \theta = \frac{T - T_\infty}{T_w - T_\infty}, \phi = \frac{C - C_\infty}{C_w - C_\infty}. \tag{6}$$

The dynamic viscosity of Maxwell nanofluid is taken as an exponential decreasing function of temperature [28] defined as

$$\mu(T) = \mu_\infty e^{-a(T - T_\infty)}, \tag{7}$$

where  $\mu_\infty$  signifies fluid viscosity at free stream and  $a$  signifies viscosity variation exponent.

Similarly, the Maxwell nanofluid thermal conductivity [31] is taken as

$$K(T) = K_{\infty}e^{-b(T-T_{\infty})}, \tag{8}$$

where  $K_{\infty}$  signifies ambient fluid conductivity and  $b$  signifies thermal dependence conductivity constant.

Using equations (6) - (8), equations (2) - (4) reduce to

$$(1 - \beta e^{v\theta} f^2) f''' - v\theta' f'' + e^{v\theta} (f f'' - f'^2 + 2\beta f f' f'' + A^2) = 0, \tag{9}$$

$$\theta'' - \epsilon\theta' + Pr e^{\epsilon\theta} (Nb\theta' \phi' + Nt\theta'^2 + f\theta') = 0, \tag{10}$$

$$Nb\phi'' + Nt\theta'' = -LePrNb f\phi'. \tag{11}$$

The corresponding non-dimensional bcs are

$$\left. \begin{aligned} \eta = 0: f = S, f'' = \frac{1}{\lambda}(f' - 1), \theta = 1 + \delta\theta', \phi' = \frac{1}{\gamma}(\phi - 1), \\ \eta \rightarrow \infty: f' \rightarrow A, \theta \rightarrow 0, \phi \rightarrow 0. \end{aligned} \right\} \tag{12}$$

The other important physical quantities are the Sherwood ( $Sh$ ) and Nusselt ( $Nu$ ) numbers which are given as

$$Sh = \frac{-x C_y|_{y=0}}{(C_w - C_{\infty})}, \quad Nu = \frac{-x T_y|_{y=0}}{(T_w - T_{\infty})}.$$

These are dimensionless numbers representing the effectiveness of heat and mass convection at the surface, respectively. Sherwood number represents the ratio of convective mass transfer rate to the mass diffusivity whereas Nusselt number represents the ratio of convective heat transfer to conductive heat transfer coefficient across the boundary layer. Thus, reduced Sherwood number signifies the mass transferral rate and reduced Nusselt number signifies the heat transferral rate for the convective flows at the surface.

These physical quantities under the similarity transformations can be written as:

$$Nu = -\sqrt{Re_x}\theta'(0), Sh = -\sqrt{Re_x}\phi'(0),$$

where  $Re_x = \frac{xU_w}{\nu_{\infty}}$  is localised Reynolds number.

Thus, the reduced Sherwood and Nusselt numbers are given by

$$Sh_x = Re_x^{-1/2} Sh = -\phi'(0), \quad Nu_x = Re_x^{-1/2} Nu = -\theta'(0). \tag{13}$$

### METHODOLOGY

BVP4C of MATLAB is used as the numerical technique to get the outcomes of the present model. Bvp4c is a built-in solver of MATLAB which is a collocation formula used to solve a global system of algebraic equations imposing collocation conditions on the subintervals over the boundary. This formula implements the three stage Lobatto IIIa finite difference numerical method [33]. The equations (9) - (11) under the bcs (12) are first reduced to first order equations as shown below.

Take

$$y1 = f, y2 = f', y3 = f'', y4 = \theta, y5 = \theta', y6 = \phi, y7 = \phi'$$

Then the first order differential matrix is obtained as

$$\frac{dy}{dx} = \begin{bmatrix} y2, \\ y3 \\ \frac{vy5y3 - e^{vy4}(y1y3 - y2^2 + 2\beta y1y2y3 + A^2)}{1 - \beta e^{vy4}y1^2} \\ y5 \\ \epsilon y5 - Pr e^{\epsilon y4} (Nby5y7 + Nty4^2 + y1y5) \\ y7 \\ Pr y7 (-Ley1 + Nte^{\epsilon y4} y5 + \frac{Nt}{Nb} \{-\epsilon y5 + Pr e^{\epsilon y4} (y1y5 + Nty4^2)\}) \end{bmatrix}$$

### RESULTS AND DISCUSSIONS

Reduced system of governing ODEs (9) – (11) so obtained are highly coupled and nonlinear, and cannot be solved analytically. Hence the equations under the bcs (12) are first reduced to first order equations as shown in section methodology and are solved by coding to create appropriate programming in MATLAB by making use of the solver bvp4c and implementing the Lobatto IIIa finite difference numerical method. Finally, the numerical computations for nanoparticles concentration, fluid temperature and its velocity profiles for distinct values of the influencing variables are carried out and the outcomes are displayed graphically in Figures (2) - (14).

To check the effectiveness of the present numerical computations, comparisons with the prior analytical outcomes of Khan and Pop [19] under the absence of slip effects, conductivity and viscosity parameters are carried out and shown in Table 1 and Table 2. It is evident from the tables that the two results are exact upto 3 decimal places showing the relevancy of the present study.

**Table 1.** Comparison table taking variation in thermophoresis parameter

Nt	$-\phi'(0)$ Previous [19]	$-\phi'(0)$ Present	$-\theta'(0)$ Previous [19]	$-\theta'(0)$ Present
0.2	2.2740	2.2740	0.6932	0.6932
0.3	2.5286	2.5286	0.5201	0.5201
0.4	2.7952	2.7951	0.4026	0.4026
0.5	3.0351	3.0351	0.3211	0.3210

**Table 2.** Comparison table for rates of heat transfer with variation in Prandtl number

Pr	$-\theta'(0)$ Previous [19]	Present results	Pr	$-\theta'(0)$ Previous [19]	Present results
0.07	0.0663	0.0663	0.70	0.4539	0.4539
0.20	0.1691	0.1691	2.00	0.9113	0.9113

The range of controlling parameters in plotting the Figures 02 – 14 are taken as  $0 \leq \beta < 1, 0.1 \leq Nb \leq 1.2, 0.1 \leq Nt \leq 0.5, 0 \leq \epsilon \leq 2, Pr = 4, 0.01 \leq \gamma \leq 2.5, 0 \leq \nu \leq 1.5, 0 \leq A \leq 1.5, 0.1 \leq S \leq 3, Le = 1, 0.01 \leq \lambda \leq 1.5, 0.01 \leq \delta \leq 0.35$ . The Figures 02 – 14 yield that the temperature and velocity of Maxwellian fluid and nanoparticles concentration in the nanofluid decrease monotonically across the boundary. At the surface, the value of the fluid property is maximum with a monotonic fall in the property by the end of boundary.

The effects of the variation of dimensionless viscosity parameter  $\nu$  on the nanoparticles volume fraction, fluid temperature and fluid motion are depicted in Figures 2-4. From the figures, it is evident that the growth in viscosity slows down the fluidic motion. The nanoparticles concentration and the fluid temperature upsurge with the hike in viscosity parameter. Increase in viscosity parameter results in greater temperature contrast between the surface and encompassing fluid which diminishes the hydrodynamic boundary layer thereby conferring the depicted results.

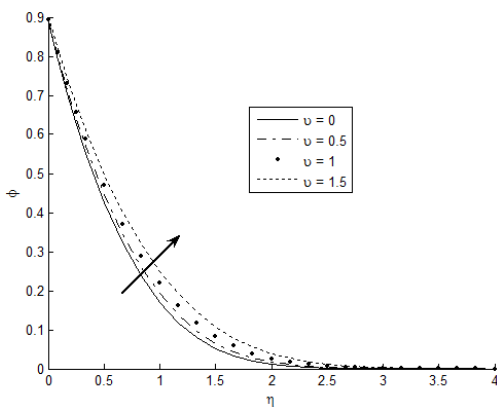


**Figure 2.** Changing viscosity on nanoparticles concentration

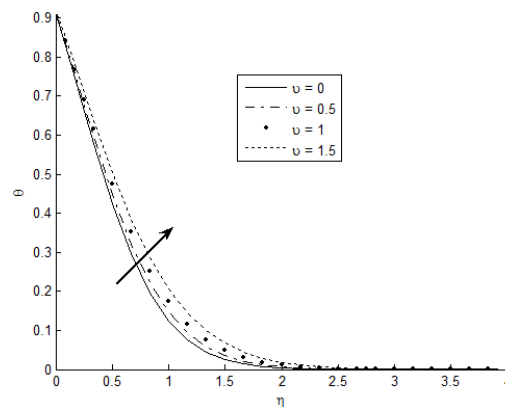


**Figure 3.** Changing viscosity on fluid temperature

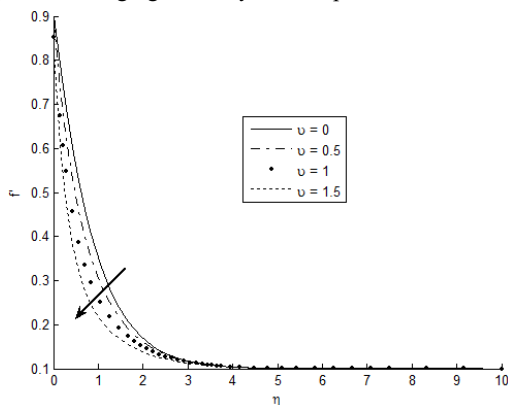


**Figure 4.** Changing viscosity on fluid velocity

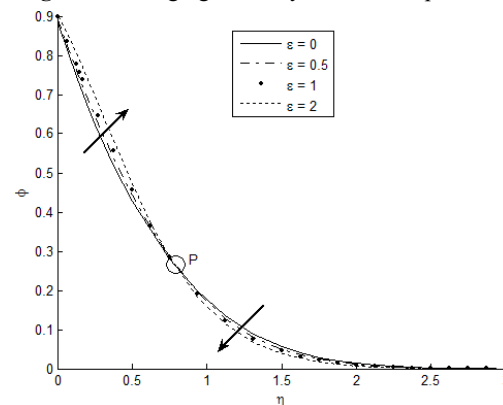


**Figure 5.** Changing thermal conduction on nanoparticles concentration

The effects of various values of thermal conductivity  $\epsilon$  on the concentration and temperature distributions are plotted in Figures 5 and 6. The growth in thermal conductivity cools down the fluid temperature thereby thinning down the

diameter of thermal boundary layer. The nanoparticles volumetric content enhances near the surface but far away from the sheet it gets reversed giving a point of inflexion P where no change in concentration is observed with the rise in thermal conductivity.

In Figures 7 and 8, the distribution of nanoparticles concentration and fluid temperature for variation in nanofluid parameters are shown. The nanofluid parameters  $Nb$  and  $Nt$  have positive effects on the fluid temperature. This is due to the generation of irregular motion known as Brownian motion by the nanoparticles and the thermophoretic force creating fast flow away from the sheet. Also, these lead to the decline in concentration of the nanoparticles by the Brownian motion parameter  $Nb$  but reverse result for thermophoresis parameter  $Nt$ .

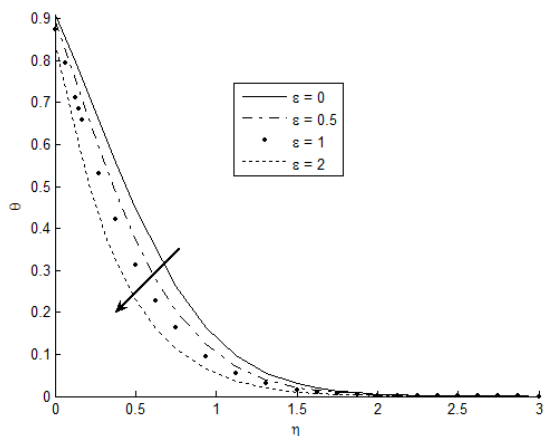


Figure 6. Changing thermal conduction on temperature

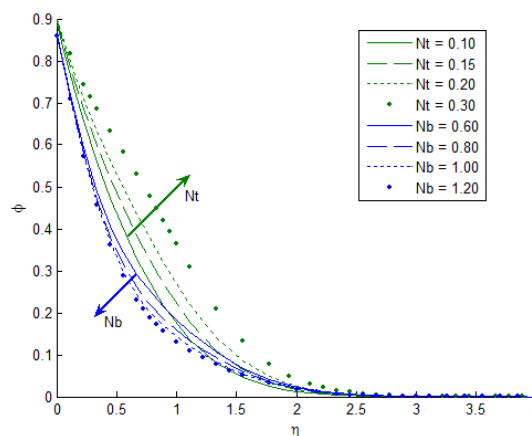


Figure 7. Changing nanofluid parameters on nanoparticles concentration

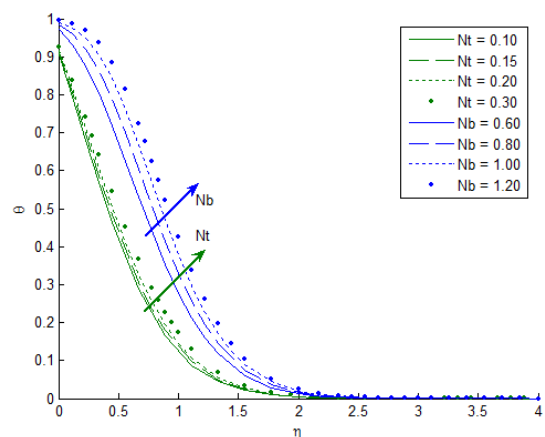


Figure 8. Changing nanofluid parameters on temperature

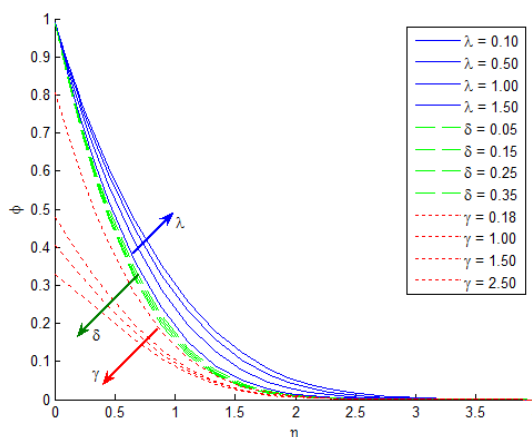


Figure 9. Changing slip parameters on nanoparticles concentration

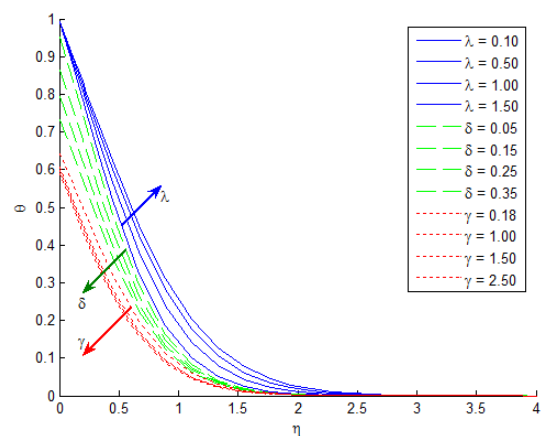


Figure 10. Changing slip parameters on temperature

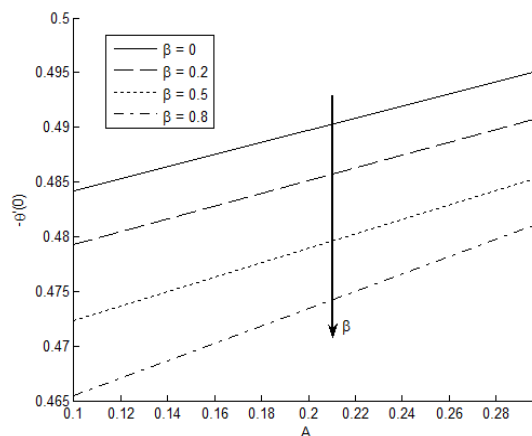


Figure 11. Nusselt number variation with Deborah number and velocity ratio

Figures 9 and 10 present the concentration and temperature distributions for distinct values of slip parameters. It's ascertained that the slip velocity  $\lambda$  enhances the thermal and concentration boundary layer but reverse are the results for

thermal slip  $\delta$  and solutal slip  $\gamma$  parameters. At the occurrence of slip, the velocity of fluid near the plate is not equal to the contraction rate of the plate. So as the slip velocity rises up, the fluid velocity decelerates. These further results in intensification of the fluid temperature and also movement of the nanoparticles, existing in fluid, closer towards each other thereby making the fluid more concentrated.

Finally, the mass transferring and heat transferring rates proportional to  $-\phi'(0)$  and  $-\theta'(0)$ , respectively, are shown in the Figures 11–14 for variation in different parameters. The nanofluid parameters ( $Nt, Nb$ ) boost the frequency of mass transfer but restrict the frequency of heat transfer. The increasing values of  $Nt$  and  $Nb$  result in the rising of the surface temperature thickening the thermal boundary layer and thereby reducing the Nusselt number. The elasticity and viscosity of the Maxwell fluid led to the reduction in the mass and heat transferring rates with the hike in Deborah number  $\beta$  while the ratio of velocities enhances these rates.

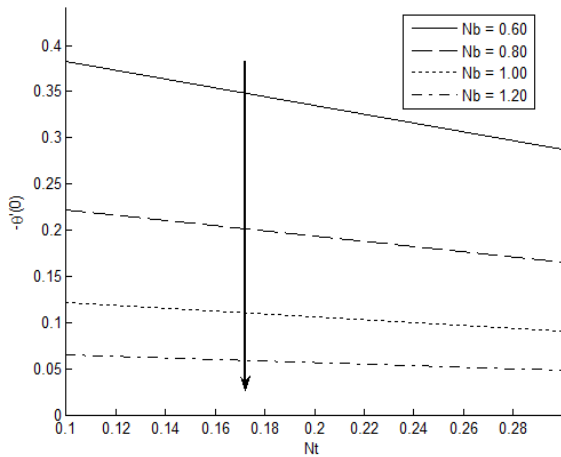


Figure 12. Nusselt number variation with nanofluid parameters

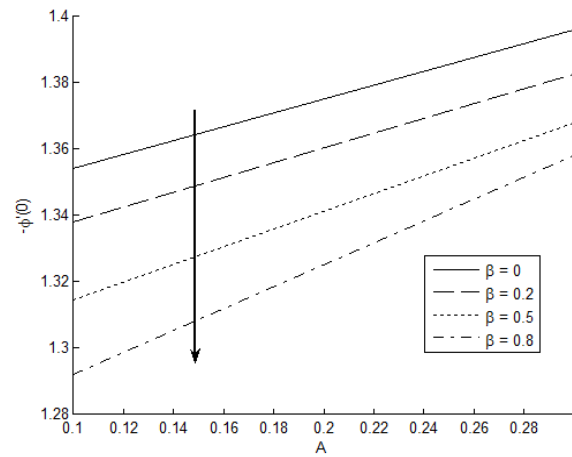


Figure 13. Sherwood number variation with velocity ratio and Deborah number

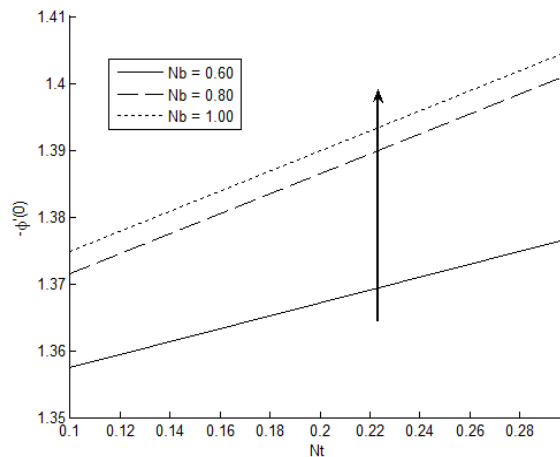


Figure 14. Sherwood number variation with nanofluid parameter

### CONCLUSIONS

The cumulative impacts of changeable thermal conduction, slip effects, viscosity and suction on the movement of Maxwellian fluid past a stretchable surface are investigated from the stagnation point along with nanoparticles present in the fluid. The results are precised as follows:

- The variation in thermal conductivity results in cooling down of the fluid and makes the fluid more concentrated near the surface of the sheet but decreases the nanoparticles volumetric content distant from the sheet.
- The velocity slips, viscosity and thermophoresis parameters favored the fluid temperature and nanoparticle concentration, whereas the thermal and solutal slips reduced the diameter of thermal and concentration boundary layers.
- The presence of nanoparticles in the fluid retards the fluidic motion.
- The upsurge in Brownian motion parameter results in heating up of the fluid and thinning down the concentration boundary layer.
- The rate of heat transfer depletes on upsurge of Deborah number and nanofluid parameters but enhances for higher ratio of velocities.
- The rate of mass transfer is favored by the nanofluid parameters and velocity ratio but is opposed by the rise in Maxwell parameter.

### Acknowledgements

The author is very thankful to the editor and referees for their valuable comments and suggestions, which have definitely improved the quality of the paper considerably.

**Funding.** This research did not receive any specific grant from funding agencies in the public, commercial, or not-for-profit sectors.

**Data Availability Statement.** No data are associated in the manuscript.

**Declarations:**

**Conflict of interest.** The author of the present work declares no competing financial interests.

**Human and animal rights.** In the present study, no human (or animal) tissue was involved.

### ORCID

DebozaniBorgohain, <https://orcid.org/0000-0001-7018-3410>

### REFERENCES

- [1] S.D. Poisson, "Sur les Equations Generale de l'Equilibre et du Mouvement des Corps Solides Elastiques et des Fluides," Journal de l'Ecole Polytechnique, **13**(20), 18 17 (1829).
- [2] J.C. Maxwell, "On double refraction in a viscous fluid in motion," Proc. R. Soc. Long. **22**(148-155),46-47 (1873). <https://doi.org/10.1098/rspl.1873.0011>
- [3] L. Boltzmann, "Zur Theorie der elastischen Nachwirkung sitzungber," Kaiserl-Akad. Wise. (Wien), Math. Naturwisslasse **70**, (II), 1 22, 18 17, 30, 275-306 (1874).
- [4] H.A. Barnes, J.F. Hutton, and K. Walters, *An Introduction to Rheology*, (Elsevier, New York, 1989).
- [5] R.J. Poole, Rheology Bulletin, **53**(2), 32 (2012). [https://pcwww.liv.ac.uk/~robpoole/PAPERS/POOLE\\_45.pdf](https://pcwww.liv.ac.uk/~robpoole/PAPERS/POOLE_45.pdf)
- [6] K. Sadeghy, H. Hajibeygi, and S.M. Taghavi, International Journal of Non-Linear Mechanics, **41**, 1242 (2006). <https://doi.org/10.1016/j.ijnonlinmec.2006.08.005>
- [7] S. Wang, and W. Tan, Int. J. of Heat and Fluid Flow, **32**, 88 (2011). <https://doi.org/10.1016/j.ijheatfluidflow.2010.10.005>
- [8] K. Hiemenz, Dingler's Polytech. J. **326**, 321-324 (1911).
- [9] T.C. Chiam, International Communications in Heat and Mass Transfer, **23**(2), 239-48 (1996). [https://doi.org/10.1016/0735-1933\(96\)00009-7](https://doi.org/10.1016/0735-1933(96)00009-7)
- [10] T.C. Chiam, Acta Mechanica, **129**, 63 (1998). <https://doi.org/10.1007/BF01379650>
- [11] J. Ahmed, M. Khan, and L. Ahmad, Journal of Molecular Liquids, **287**, 110853 (2019). <https://doi.org/10.1016/j.molliq.2019.04.130>
- [12] M. Sunder Ram, K. Spandana, Md. Shamshuddin, and S.O. Salawu, Int. J. of Modelling and Simulation, **43**(5), 670 (2022). <https://doi.org/10.1080/02286203.2022.2112008>
- [13] N.N. Reddy, D.R. Yanala, B.S. Goud, and S.R. Vempati, Heat Transfer, **52**, 3538 (2023). <https://doi.org/10.1002/htj.22839>
- [14] H. Dessie, Heat Transfer. **50**, 6984 (2021). <https://doi.org/10.1002/htj.22213>
- [15] Y.D. Reddy, and I. Mangamma, Numerical Heat Transfer, Part A: Applications, 1-27, (2023). <https://doi.org/10.1080/10407782.2023.2230356>
- [16] S. Choi, "Enhancing thermal conductivity of fluids with nanoparticles," in: *Developments and Applications of Non-Newtonian Flows*, edited by D.A. Siginer, and H.P. Wang, (ASME, New York, 1995), pp. 99-105.
- [17] J. Buongiorno, Journal of Heat Transfer, **128**, 240 (2006). <https://doi.org/10.1115/1.2150834>
- [18] A.V. Kuznetsov, and D.A. Nield, Int. J. Therm. Sci. **49**, 243 (2010). <https://doi.org/10.1016/j.ijthermalsci.2009.07.015>
- [19] W.A. Khan, and I. Pop, Int. J. Heat Mass Transf. **53**, 2477 (2010). <https://doi.org/10.1016/j.ijheatmasstransfer.2010.01.032>
- [20] O.D. Makinde, and A. Aziz, Int. J. of Thermal Sciences, **50**, 1326 (2011). <https://doi.org/10.1016/j.ijthermalsci.2011.02.019>
- [21] M. Sajid, B. Ahmed, and Z. Abbas, J. Egyptian Math. Soc. **23**, 440 (2014). <https://doi.org/10.1016/j.joems.2014.05.013>
- [22] Y. Abdela, B. Shankar, and T. Srinivasulu, Int. J. Comput. Eng. Res. **8**(2), 2250 (2018). <https://api.semanticscholar.org/CorpusID:208625190>
- [23] G.K. Ramesh, B.J. Gireesha, T. Hayat, and A. Alsaedi, Alexandria Engineering Journal, **55**, 857 (2016). <https://doi.org/10.1016/j.aej.2016.02.007>
- [24] R. Mishra, Int. J. Eng. Sci. Res. Technol. **6**(4), 131 (2017). <https://doi.org/10.5281/zenodo.557138>
- [25] M.A. El-Aziz, and A.A. Afify, Math. Probl. Eng. (2018). <https://doi.org/10.1155/2018/9402836>
- [26] W. Ibrahim, and M. Negera, Journal of the Egyptian Mathematical Society, **28**, 7 (2020). <https://doi.org/10.1186/s42787-019-0057-2>
- [27] O.D. Makinde, W.A. Khan, and J.R. Culham, Int. J. Heat Mass Transf. **93**, 595 (2016). <https://doi.org/10.1016/j.ijheatmasstransfer.2015.10.050>
- [28] O.D. Makinde, F. Mabood, W.A. Khan, and M.S. Tshela, Journal of Molecular Liquids, **219**, 624 (2016). <https://doi.org/10.1016/j.molliq.2016.03.078>
- [29] A.O. Ali, and O.D. Makinde, Journal of Appl. Fluid Mech. **8**(4), 793 (2015). <https://doi.org/10.18869/acadpub.jafm.67.223.22967>
- [30] S. Manjunatha, and B.J. Gireesha, Ain Shams Eng. J. **7**, 505 (2016). <https://doi.org/10.1016/j.asej.2015.01.006>
- [31] D. Borgohain, Trends in Sciences, **19**(21), 6306 (2022). <https://doi.org/10.48048/tis.2022.6306>
- [32] D. Iranian, K. Sudarmozhi, I. Khan, and A. Mohamed, International Journal of Thermofluids, **20**, (2023). <https://doi.org/10.1016/j.ijft.2023.100396>
- [33] L.F. Shampine, M.W. Reichelt, and J. Kierzenka, Solving Boundary Value Problems for Ordinary Differential Equations in MATLAB with bvp4c. MATLAB File Exchange, (2004).



## ВПЛИВ ТЕМПЕРАТУРНО-ЗАЛЕЖНИХ ТЕПЛОПРОВІДНОСТІ ТА В'ЯЗКОСТІ НА КОВЗАЮЧИЙ ПОТІК НАНОРІДИНИ МАКСВЕЛЛА



Дебозані Боргохайн

*Факультет математики, Університет Дібругарх, Дібругарх, 786004, Ассам, Індія*

Запропоновано математичну модель для перевірки впливу мінливих теплофізичних властивостей, таких як теплопровідність, ефекти ковзання та в'язкість, на нанорідину Максвелла. Теплопровідність швидко зростає через наявність у базовій рідині наночастинок, таких як метали, карбіди, оксиди тощо. Потік відбувається від застійної точки проходження розтягнутого листа з умовами ковзання. Також враховуються особливості броунівського руху, а також процеси термофорезу. За допомогою перетворень подібності ODE виводяться з рівнянь, що впливають на потік рідини. Вбудований розв'язувач MATLAB, а саме `bvp4c`, який є формулою спільного розташування, що реалізує чисельний метод кінцевих різниць LobattoIIIa, застосовується для чисельного розв'язання цих перетворених рівнянь. Проаналізовано графіки чисельних результатів, що представляють вплив варіацій різних параметрів на рух рідини, передачу тепла разом з масою. Це дослідження призводить до важливого аспекту, що, оскільки теплопровідність у потоці посилюється, температура рідини знижується з високою агрегацією наночастинок біля поверхні листа. Крім того, швидкість тепло- та масообміну зменшується через релаксацію рідини Максвелла. Крім того, ефективність представлених чисельних розрахунків визначається шляхом проведення порівнянь швидкостей тепло- та масопередачі з попередніми аналітичними результатами для кількох значень термофорезу та параметрів Прандтля. Ефективність його результатів може бути застосована в нанонаукових технологіях і полімерних галузях для їх розробок.

**Ключові слова:** теплообмін; змінна в'язкість рідини; ефекти ковзання; змінна теплопровідність; рідина Максвелла

## SYNTHESIS OF PURE AND MANGANESE DOPED ZINC OXIDE NANOPARTICLES BY A SOLUTION GROWTH TECHNIQUE: STRUCTURAL AND OPTICAL INVESTIGATION

 Raymond A. Antwi,  Isaac Nkrumah\*,  Francis K. Ampong,  Mark Paal,  Reuben Y. Tamakloe,  Robert K. Nkum, Francis Boakye

*Department of Physics, Kwame Nkrumah University of Science and Technology, Kumasi, Ghana*

\*Corresponding Author email: [inkrumah.sci@knust.edu.gh](mailto:inkrumah.sci@knust.edu.gh)

Received August 8, 2023; revised September 22, 2023; accepted September 25, 2023

Pure and manganese doped zinc oxide nanoparticles have been successfully synthesized over the composition range,  $Zn_{1-x}Mn_xO$  ( $0 < x < 0.5$ ), by a solution growth process. The effect of Mn doping on the structure, morphology and optical properties were investigated by several techniques. X-Ray diffraction studies confirmed the formation of a single-phase polycrystalline hexagonal wurtzite structure of ZnO within the range,  $0 < x < 0.3$ . No Mn related secondary phases were detected, within this range, which could be attributed to the fact that the dopant atoms had been well incorporated into the ZnO crystal lattice. For  $Zn_{1-x}Mn_xO$  ( $x = 0.5$ ), several low intensity peaks belonging to remnants of Manganese acetate were observed in the diffractogram, establishing a solubility limit for the synthesis technique used. The variation of d-spacing with Mn percent doping showed a very good agreement with Vergard's law within the range ( $0 < x < 0.25$ ). EDAX analysis of the nanoparticles was consistent with the formation of Mn doped ZnO. The optical band gap of the ZnO nanoparticles decreased linearly with increasing Mn percent doping, suggesting the possibility of tuning the band gap of ZnO by doping with Mn.

**Keywords:** *Manganese doped zinc oxide; Solution phase process; Crystal structure; Optical band gap*

**PACS:** 81.15.Fg, 61.05.C, 42.70.Qs

### INTRODUCTION

Metal oxides display a wide range of properties which have useful technological applications, and the possibility of varying these properties by various techniques, has resulted in these compounds being widely studied. Most of the interesting properties displayed by these metal oxides are obtained by doping with transition metals such as; Fe, Co, Ni, Mn and Cu.

Among several metal oxides, ZnO is attracting attention due to its efficiency, low cost, non-toxic nature, and being chemically and mechanically stable [1]. In addition, the relatively large band gap of ZnO (3.37 eV) coupled with its high exciton binding energy (60 meV) at room temperature, renders it a superb host material for doping with Transition metals [2]. Manganese has a peculiar nature, it has several oxidation states, causing diverse chemical and structural forms [3], [4]. These properties make it an important dopant for binary compounds. An additional advantage is the ease of Mn incorporation into the ZnO lattice, due to the relatively small difference in ionic radii between  $Mn^{2+}$  and  $Zn^{2+}$  [5]. An efficient dopant must not cause any structural change when it is incorporated in the host atom [6]. These and many other technological as well as potential applications have been well documented in literature.

With the renewed interest in the properties of these nanomaterials, there is the need to transition towards synthesis techniques which are environmentally friendly, simple, and less costly. Available literature suggests that within the past decade several publications have emerged on the synthesis of pure and Mn-doped ZnO.

Techniques which have generated a lot of interest are the solution growth methods. These techniques usually involve the use of simple, inexpensive equipment, and can be carried out at low temperatures. An additional advantage, the ability to control the size of the ZnO nanostructures [7].

Controlling metastable phases, particle sizes and morphologies are also some of the benefits provided by the low temperature chemical route for synthesizing nanomaterials [8]. In spite of the advantages offered by this technique, incorporation of Mn in ZnO lattice by this route is challenging because of the higher bond energy of Mn-O compared to Zn-O, this means more energy would be needed to substitute  $Zn^{2+}$  with  $Mn^{2+}$  in ZnO lattice. A process which is easily attainable with high temperature techniques [9].

The solubility limit, which is the extent to which the Mn dopant can be incorporated in the ZnO lattice without causing any structural defects, is another important feature worth taking into account. Beyond this doping limit, the structure degrades due to the presence of secondary phases formed by Mn clusters that do not replace  $Zn^{2+}$  in ZnO lattice [10-12].

In our previous work, Armah et al. [13], we reported on the solubility of Mn in ZnO Nanocrystallites grown by wet chemical synthesis. Pure ZnO was obtained at a synthesis temperature of 200 °C. Below this temperature, the diffractogram showed several impurity peaks/secondary phases. For the  $Zn_{1-x}Mn_xO$  nanocrystallites, synthesized at 200 °C the solubility limit was < 20 % and for a synthesis temperature of 180°C, it was < 0.5 %. Beyond these limits, peaks indexed to secondary phases were observed in the diffractogram.

To adopt this technique in producing high-quality pure and Mn doped ZnO nanoparticles, with desirable qualities, for device applications, requires an improvement on the solubility limit. In this current paper, we present a more effective low-temperature route to synthesize  $Zn_{1-x}Mn_xO$  nanoparticles by a solution phase process. The method used is a modification of the solution growth process reported in our previous work. In comparison with other solution phase processes which use synthesis temperatures above 200 °C, this work uses a relatively lower temperature of about 110°C. No sophisticated equipment is used and no toxic gases are released during this process. The resulting changes in the structural, morphology and optical properties of the nanoparticles are examined.

## MATERIALS AND METHODS

The precursors used were zinc acetate dihydrate ( $Zn(CH_3COO)_2 \cdot 2H_2O$ ) and anhydrous manganese acetate ( $Mn(CH_3COO)_2$ ), methanol ( $CH_3OH$ ), absolute ethanol ( $C_2H_5OH$ ) and 2 M ammonium hydroxide ( $NH_4OH$ ), all obtained from Merck limited, India.

### Synthesis of Pure ZnO Nanocrystals

In the synthesis procedure, 50 g of zinc acetate was ground in an agate mortar into a fine powder. The zinc acetate powder was poured into a beaker. 150 ml of methanol was added to the zinc acetate to dissolve it. The beaker and its content were sonicated for 40 minutes until all the solute was dissolved. Dropwise addition of 2 M ammonium hydroxide solution was added to the mixture to obtain a pH of 8. The solution mixture was kept for about 3 hours before it was placed on a hot plate and heated slowly in incremental steps of 10 °C (each temperature held for 15 minutes) until a final temperature of 64 °C was reached for complete dissolution of precursors. At this temperature all the excess water content evaporated and the solution turned into a gel-like material. The temperature was increased further and the resultant gel-like material was maintained at 110 °C until it solidified into pale yellow crystals. These were then allowed to cool down to ambient conditions and ground into fine particles. They were then washed thrice with water, once with ethanol and dried at 100 °C overnight. Afterwards the samples were calcined at 500 °C for 3 hours to produce the ZnO Nanocrystals

The preference for metal acetate precursors, Methanol, etc. have been well explained [13, 14]. The ammonium hydroxide, supplied the oxide oxygen whilst the acetate acts as base. It should be mentioned that, apart from the synthesis temperature which differs, other post synthesis processes such as washing the nanoparticles in water and ethanol, drying overnight at 100 °C, and calcining were not done in our previous work.

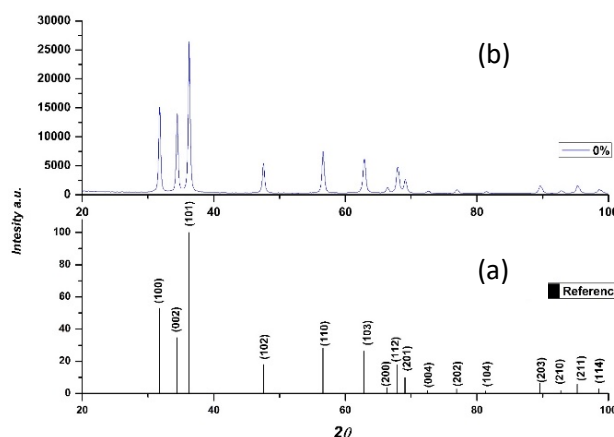
### Synthesis of $Zn_{1-x}Mn_xO$

Specific amounts of the metallic precursors were ground into a fine powder. The same procedure for the synthesis of ZnO described above was used. The solution appeared creamy at low dopant concentrations and became pinkish as the concentration increased. The same procedure was carried out for  $Zn_{1-x}Mn_xO$  ( $0 < x < 0.5$ ).

## RESULTS AND DISCUSSION

### Powder X-Ray Diffraction Analysis

The crystal structure of the nanoparticles was studied by a PANalytical Empyrean Series 2 powder X-ray diffractometer in the  $2\theta$  range 5 to 99 °C with  $CuK\alpha$  (1.5406 Å) radiation.



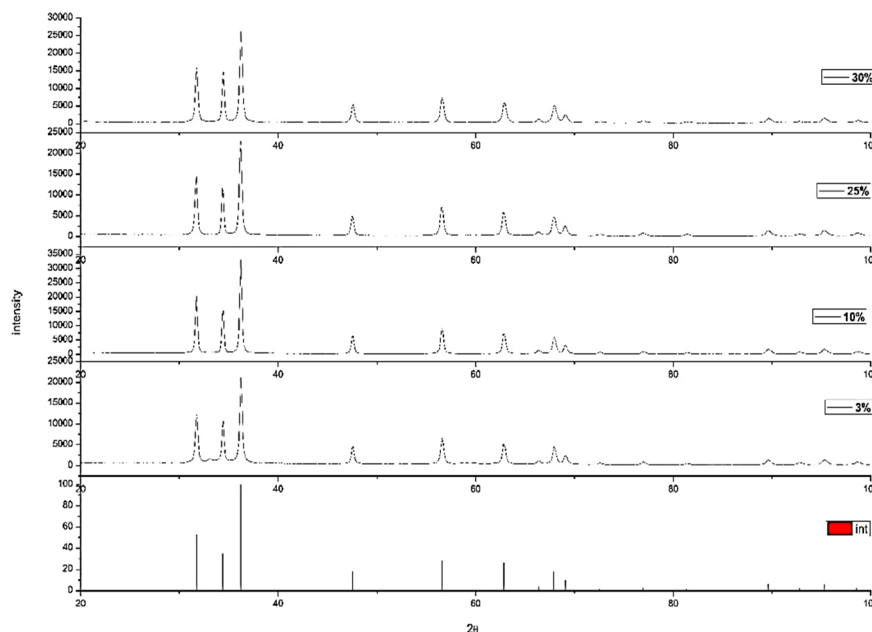
**Figure 1.** (a) Stick pattern for the hexagonal wurtzite structure of ZnO (Ref. Code 01-079-9897) (b) XRD pattern of pure ZnO

Figure 1a and 1b show the stick pattern for the hexagonal wurtzite structure of ZnO (Ref. Code 01-079-9897) and the XRD pattern for pure ZnO nanoparticles respectively. It can be observed that the pattern of prominent peaks in Figure 1(b), are indexed to the hexagonal wurtzite structure of ZnO, the peak corresponding to the (101) plane being the most intense. Authors from other studies have reported similar observations. The lack of any impurity peaks in the diffractogram affirms the purity of the ZnO nanoparticles. Table 1 shows the pattern list which confirms the composition and purity of the synthesized ZnO nanoparticles.

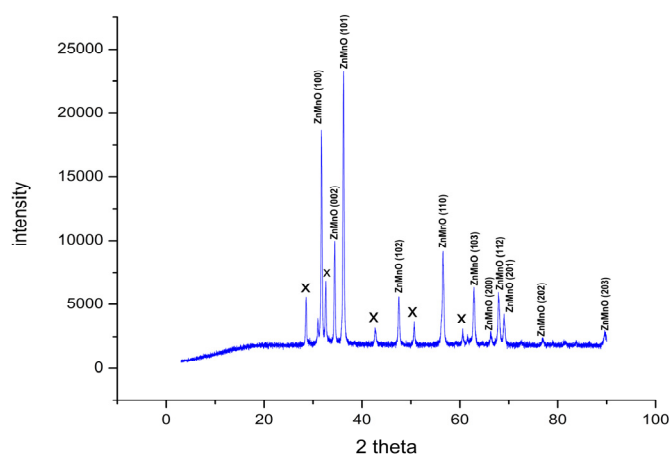
**Table 1.** Pattern List of the synthesized ZnO nanoparticles.

Visible	Ref.Code	Score	Compound Name	Displ.[°2 $\theta$ ]	Scale Fac.	Chem. Formula
*	01-079-9878	99	Zinc Oxide	0.000	1.032	Zn O

It is worth noting that most reports on the production of ZnO by wet chemical synthesis, such as Armah et al. [15] achieved this level of purity only after synthesizing at temperatures above 180 °C.

**Figure 2a.** XRD patterns of  $Zn_{1-x}Mn_xO$  ( $0 < x < 0.5$ ) nanoparticles

The X-Ray diffraction patterns of  $Zn_{1-x}Mn_xO$  ( $0 < x < 0.5$ ) nanoparticles are shown in Figure 2a. The well-defined peaks in all the samples are indexed to pure hexagonal wurtzite structured ZnO with preferred orientation along the (101) plane. Similar observations have been reported by Guermat et al. [16].

**Figure 2b.** XRD pattern for  $Zn_{1-x}Mn_xO$  ( $x = 0.5$ )

The sharpness of the peaks in the diffractogram indicates good crystallinity. We can also see that no secondary phases are observed as compared to our previous work. In the occurrence where there are no discernable peaks indexed to Mn related secondary phases, one may safely conclude that the Mn is replacing  $Zn^{2+}$  in the ZnO lattice. This view is buttressed by Shatnawi et al. [17]. It is also worth noting that whilst some authors; Sebayang et al. [18] have reported a similar behavior with regard to the most intense peak, others such as Singh et al. [19], reported the (002) planes as being the most intense peak. There was a slight shift in 2 theta position with Mn doping percentage.

The XRD pattern of Figure 2b shows that apart from the prominent peaks indexed to the ZnO hexagonal structure, there are several low intensity peaks (labelled as x) which do not belong to any of the phases of  $Zn_{1-x}Mn_xO$ . These impurities are remnants of Manganese acetate in the sample. Thus, based on the synthesis technique used in this work, the doping limit for  $Zn_{1-x}Mn_xO$  can be estimated to be in between  $0.3 < x < 0.5$ . This is an improvement on our previous study using wet chemical synthesis which resulted in the appearance of secondary phases of  $Mn_2O_3$  at  $x = 0.2$  [13]. Table 2 gives a summary of some parameters obtained from the peak analysis.

**Table 2.** Peak shifting of the (101) plane with Mn doping percentage

% of Mn doping	2Theta position of (101) plane	FWHM	d-spacing[Å]
0	36.2637	0.3100	2.47727
3	36.2506	0.3100	2.47813
10	36.2315	0.4133	2.47940
25	36.2080	0.3100	2.48095
30	36.2497	0.4133	2.47819
50	36.2020	0.4133	2.47930

Observations from Table 2 indicate that, with the exception of the sample with 30 % Mn doping, there is a slight shift in 2-Theta position of the (101) plane, towards lower values, with increasing Mn doping percentage and a corresponding increase in the d-spacing. As mentioned in the introductory chapters, Mn can exist in different oxidation states, such as Mn<sup>2+</sup>, Mn<sup>3+</sup> Mn<sup>4+</sup> etc. Thus, when Mn substitutes for Zn<sup>2+</sup> the lattice has to expand or contract depending on which of the oxidation states of Mn is present. The exact distribution of Mn in the lattice cannot be easily ascertained [20] [21]. If Mn<sup>2+</sup> ion which has a much larger ionic radius replaces Zn<sup>2+</sup>, the peaks will shift towards the lower 2-theta angles due to an increase in d-spacing [13]. Thus, the observed shift in d-spacing with Mn doping percentage shown in Table 2, can be associated with the higher ionic radius of Mn<sup>2+</sup>.

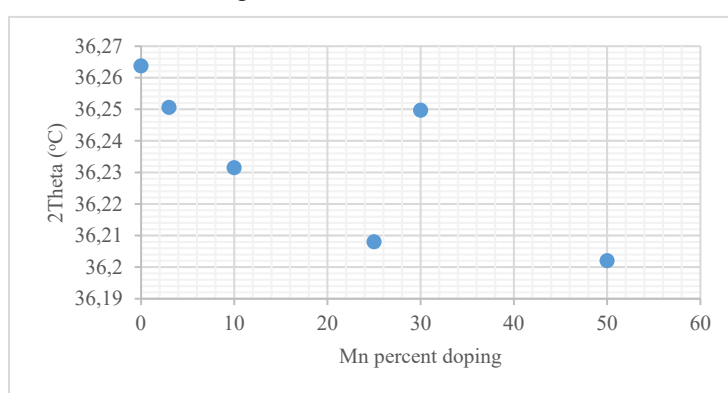


**Figure 3.** Plot of peak shifting of the (101) plane with Mn doping percentage

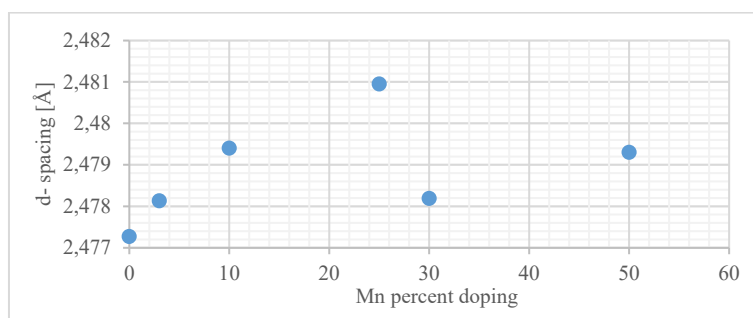


**Figure 4.** Variation of the d-spacing of the (101) plane with Mn doping percentage

Figure 3 shows the shift in 2Theta position of the (101) plane with Mn percent doping, whilst Figure 4 shows the corresponding increase in d-spacing.

There is a linear dependence of the lattice parameters of mixed crystals with composition, and this is true for substituted solid solutions [22]. This linear dependence, referred to as Vegard's law is consistent with the likely behavior of an ideal mixed phase [23]. It is also worth noting that, although there are some publications which hold contrary views to the validity of this law [24], other authors such as Muralikrishna et al. [25] are of the view that Vegard's law is mostly valid in a narrow compositional range. The later view is supported by observations made in Figure 4: variations of the d-spacing with Mn doping percentage is linear up to about 25 % Mn doping. Beyond this range the variation is non-linear.

#### Average grain size

The average grain size was calculated using the formula given by Scherrer [26], [27]:

$$D = \frac{K\lambda}{\beta \cos \theta}$$

Where K is a constant, the X-ray wavelength  $\lambda = 1.541 \text{ \AA}$ ,  $\beta$  is the full width at half maximum of the most intense peak, which is the (101) plane,  $\theta$  is the Bragg angle of the (hkl) planes associated to the structure. The average grain size, D for the entire samples, Zn<sub>1-x</sub>Mn<sub>x</sub>O (0 < x < 0.50), was about 28 nm.

### SEM and EDAX Analysis

SEM and EDX analyses were carried out using a Zeiss SmartEDX Instrument (15 kV nominal electron beam voltage). Figures 5, 6, and 7 show the SEM and EDAX results of pure ZnO and some Mn doped ZnO.

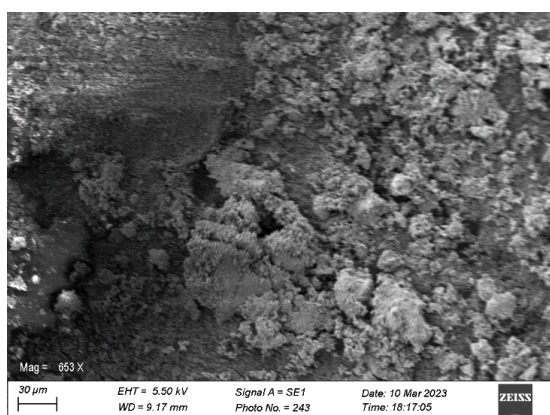


**Figure 5a.** SEM Micrograph of pure ZnO

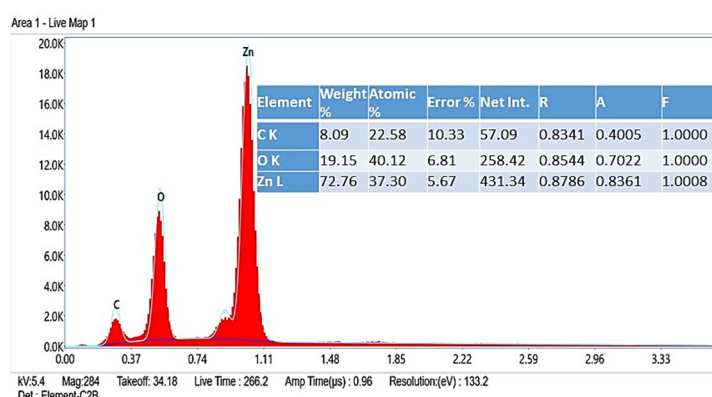


**Figure 5b.** EDAX Spectrum of pure ZnO

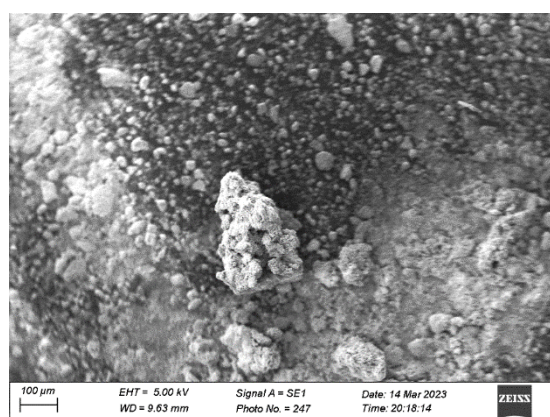


**Figure 6a.** SEM Micrograph of Mn doped ZnO (10 % Mn doping)

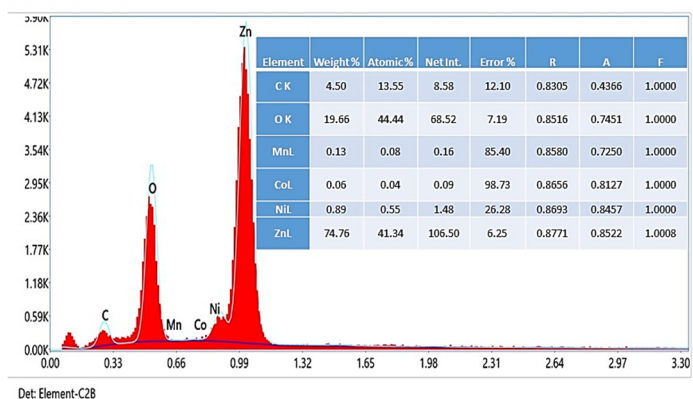


**Figure 6b.** EDAX Spectrum of Mn doped ZnO (10 % Mn doping)

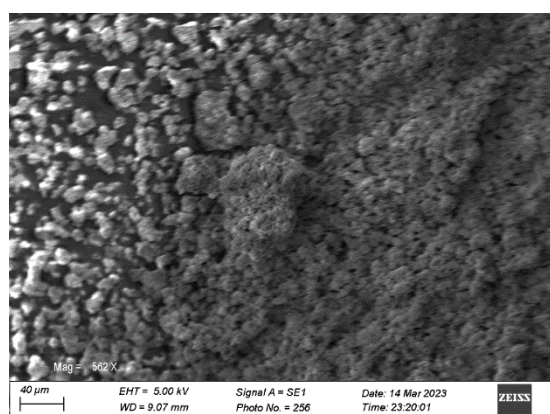


**Figure 7a.** SEM Micrograph of Mn doped ZnO (50 % Mn doping)

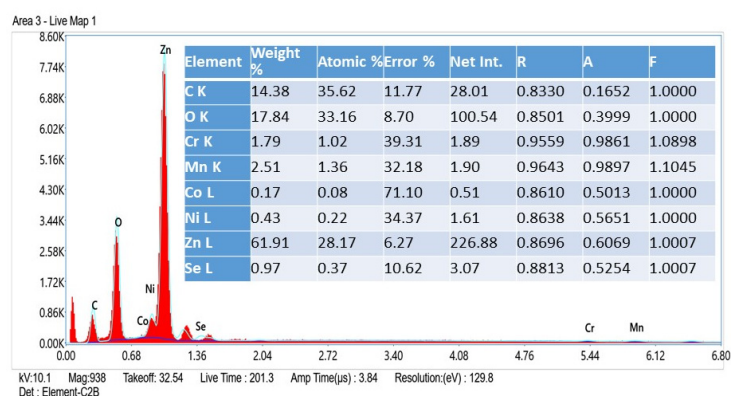


**Figure 7b.** EDAX Spectrum of Mn doped ZnO (50 % Mn doping)

The EDAX spectrum in Figure 5b, indicates that the synthesized nanoparticle is pure ZnO. A close observation of the EDAX spectra of Figures 6b and 7b clearly confirm that the synthesized nanoparticles contain zinc (Zn), oxygen (O), and manganese (Mn). Other elements seen in the tables of Figures 6b and 7b may emanate from the SEM specimen stub used a substrate in the analysis. All the SEM images show the occurrence of clusters.

### Optical Analyses

The absorbance spectra of the  $Zn_{1-x}Mn_xO$  ( $0 < x < 0.5$ ) nanoparticles, dispersed in potassium hydroxide (KOH, 7.5 M), were obtained using a ANALYTIK JENA - SPECORD 200 PLUS- 223E1451 UV-VIS spectrophotometer.

Figure 8 shows the optical absorption spectra for the  $Zn_{1-x}Mn_xO$  ( $0 < x < 0.50$ ) nanoparticles. Generally, there was an increase in absorbance with Mn incorporation. The absorption edge shifted towards the higher wavelengths with increasing Mn doping. This red shift suggests an increase in size of the Mn-doped ZnO. A similar situation was reported by Thakur et al. [28].

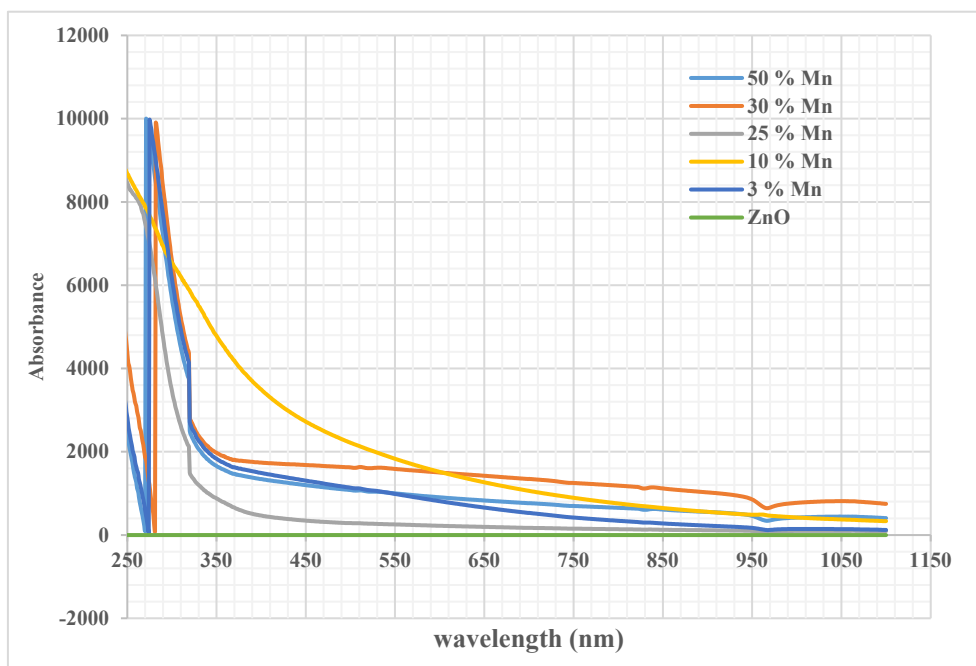


Figure 8. Optical absorption spectra for the  $Zn_{1-x}Mn_xO$  ( $0 < x < 0.50$ ) nanoparticles

#### Determination of the optical band gap

The band gap and type of transition were determined by the Stern equation [29].

$$(Ah\nu) = [K(h\nu - E_g)]^n$$

where  $A$  is the absorbance,  $h\nu$  is the photon energy,  $n$  takes on the value of  $1/2$  or  $2$  depending on whether the optical transitions are indirect or indirect [30], and  $K$  is a constant. The band gap  $E_g$  is determined by first plotting a graph of  $(Ah\nu)^{1/n}$  vs  $h\nu$ . ZnO is a direct band gap material so  $n = 1/2$ , the band gap,  $E_g$  is obtained from the intercept on the  $h\nu$  axis. A plot of  $(Ah\nu)^2$  vs  $h\nu$  for ZnO, 10 and 25 % Mn doped ZnO are shown Figure 9, 10 and 11 respectively.

From Figure 9, the estimated band gap for ZnO is 3.30 eV.

From Table 3, it can be observed that there is a general decrease in the band gap of the nanoparticles with increasing Mn percentage doping. Abdel-Galil et al. [30] have given reasons for the observed decrease in band gap. A plot of the variation in estimated band gaps with Mn percentage doping is shown in Figure 12.

The linear nature of the graph in Figure 12, suggests the possibility of tuning the band gap of ZnO by doping with Mn. The red shift observed in the absorption maxima due to doping with Mn, is ascribed to the decrease in the energy band gap, which makes it favorable for photocatalytic applications [28].

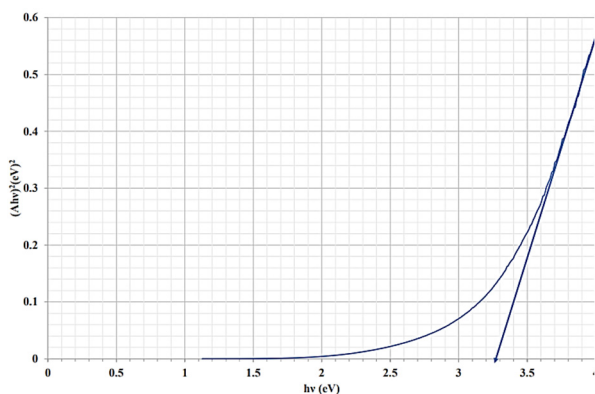


Figure 9. A plot of  $(Ah\nu)^2$  vs  $h\nu$  for ZnO

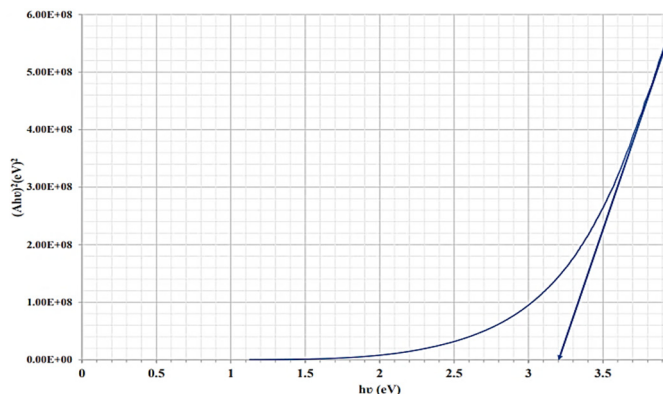


Figure 10. A plot of  $(Ah\nu)^2$  vs  $h\nu$  for 10 % Mn doping

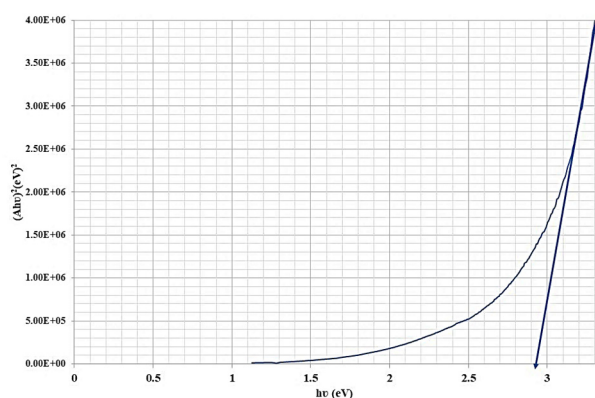


Figure 11. A plot of  $(Ahv)^2$  vs  $hv$  for 25 % Mn doping

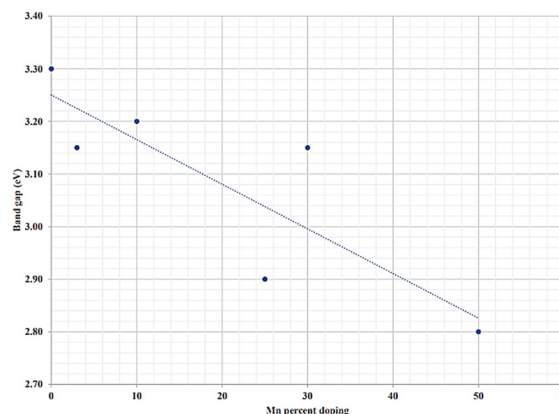


Figure 12. Plot of estimated band gaps against Mn percent doping

Table 3. Summary of the estimated band gaps for  $Zn_{1-x}Mn_xO$  ( $0 < x < 0.50$ ) nanoparticles

Mn percent doping (%)	Estimated band gap (eV)
0	3.30
3	3.15
10	3.20
25	2.90
30	3.15
50	2.80

## CONCLUSIONS

Nanoparticles of  $Zn_{1-x}Mn_xO$  ( $0 < x < 0.5$ ) have been successfully synthesized by a low-temperature solution growth method. All the detectable peaks in the diffractogram were indexed as ZnO with hexagonal wurtzite structure. For the doping range of  $0 < x < 0.3$ , no additional peaks were observed in the diffractogram confirming the formation of pure and single phase of  $Zn_{1-x}Mn_xO$  within this range of Mn doping. For  $Zn_{1-x}Mn_xO$  ( $x = 0.5$ ), several low intensity peaks belonging to remnants of Manganese acetate were observed in the diffractogram. Thus, in this work, the solubility limit for  $Zn_{1-x}Mn_xO$  can be estimated to be in between  $0.3 < x < 0.5$ . This is an improvement on our previous study using wet chemical synthesis which resulted in the appearance of secondary phases of  $Mn_2O_3$  at  $x = 0.2$ . The variation in d-spacing with Mn doping percentage was linear within the range ( $0 < x < 0.25$ ) suggesting the formation of a substitutional solid solution. EDAX confirmed the presence of Mn. The optical band gap of the nanoparticles decreased with increasing Mn percent doping. Overall, it is possible to synthesize good quality manganese doped zinc oxide nanoparticles, especially in the zinc rich end of the composition by adopting the synthesis technique used in this work.

## ORCID

- © Isaac Nkrumah, <https://orcid.org/0000-0003-4030-7931>; © Francis K. Ampong, <https://orcid.org/0000-0003-3562-8183>  
 © Mark Paal, <https://orcid.org/0000-0002-6465-2708>; © Reuben Y. Tamakloe, <https://orcid.org/0000-0002-5563-5930>  
 © Robert K. Nkum, <https://orcid.org/0000-0003-0404-760X>; © Raymond A. Antwi, <https://orcid.org/0000-0002-3488-7143>

## REFERENCES

- [1] P. Chaudhary, F. Fatima, and A. Kumar, *Journal of inorganic and organometallic polymers and materials*, **30**, 5180 (2020). <https://doi.org/10.1007/s10904-020-01674-8>
- [2] R.N. Ali, H. Naz, J. Li, X. Zhu, P. Liu, and B. Xiang, *Journal of Alloys and Compounds*, **744**, 90 (2018). <https://doi.org/10.1016/j.jallcom.2018.02.072>
- [3] F. Giovannelli, A.N. Ndimba, P. Diaz-Chao, M. Motelica-Heino, P.I. Raynal, C. Autret, and F. Delorme, *Powder Technology*, **262**, 203 (2014). <https://doi.org/10.1016/j.powtec.2014.04.065>
- [4] M. Gotić, T. Jurkin, S. Musić, K. Unfried, U. Sydlik, and A. Bauer-Šegvić, *Journal of Molecular Structure*, **1044**, 248 (2013). <https://doi.org/10.1016/j.molstruc.2012.09.083>
- [5] G. Voicu, O. Oprea, B. S. Vasile, and E. Andronescu, *Journal of Nanomaterials and Biostructures*, **8**(2), 667 (2013). [https://chalcogen.ro/667\\_Voicu.pdf](https://chalcogen.ro/667_Voicu.pdf)
- [6] R. Buonsanti, and D.J. Milliron, *Chemistry of Materials*, **25**(8), 1305 (2013). <https://doi.org/10.1021/cm304104m>
- [7] A.K. Singh, G.S. Thool, P.R. Bangal, S.S. Madhavendra, and S.P. Singh, *Industrial & Engineering Chemistry Research*, **53**(22), 9383 (2014). <https://doi.org/10.1021/ie500077v>
- [8] N. Singh, S. Mittal, K.N. Sood, and P.K. Gupta, *Chalcogenide Letters*, **7**(4), 275 (2010). [http://chalcogen.ro/275\\_Singh.pdf](http://chalcogen.ro/275_Singh.pdf)
- [9] D. Wu, Z. Huang, G. Yin, Y. Yao, X. Liao, D. Han, X. Huang, and J. Gu, *Cryst. Eng. Comm.* **12**(1), 192 (2010). <https://doi.org/10.1039/B909780E>
- [10] A.S. Hassan, K. Abdalla, and A.M. Moanes, *IJSRSET*, **3**(8), 94 (2017). <https://ijsrset.com/paper/3167.pdf>
- [11] T.M. Dhruvashi, and P.K. Shishodia, *Adv. Mater. Lett.*, **7**(2), 116 (2016). <https://doi.org/10.5185/amlett.2016.5966>
- [12] A. Boumezoued, K. Guergouri, M. Zaabat, D. Recham, and R. Barille, in: *Proceedings of International Agricultural, Biological & Life Science Conference*, edited by Y. Kaya, and T. Popova, (Edirne, Turkey, 2018), 250-258.



- [13] E.N.A. Armah, F.K. Ampong, M. Egblewogbe, H.A. Koffi, F. Boakye, J.K.A. Amuzu, and R.K. Nkum, *Advanced Nano Research*, **2**(1), 53 (2019). <https://doi.org/10.21467/anr.2.1.53-61>
- [14] T.J. Jacobsson, *Naturvetarprogrammet Kemi*, (Uppsala Universitet, 2009).
- [15] E.N.A.A. Armah, M. Egblewogbe, H.A. Koffi, A.A. Yankson, F.K. Ampong, F. Boakye, J.K.A. Amuzu, and R.K. Nkum, *Adv. Nan. Res.* **3**(1), 28 (2020). <https://doi.org/10.21467/anr.3.1.28-39>
- [16] N. Guermat, W. Daranfedi, I. Bouchama, and N. Bouarissa, *Journal of Molecular Structure*, **1225**, 129134 (2021). <https://doi.org/10.1016/j.molstruc.2020.129134>
- [17] M. Shatnawi, A.M. Alsmadi, I. Bsoul, B. Salameh, M. Mathai, G. Alnawashi, G.M. Alzoubi, et al., *Results in Physics*, **6**, 1064(2016). <https://doi.org/10.1016/j.rinp.2016.11.041>
- [18] P. Sebayang, C. Kurniawan, R.Y. Lubis, I. Priyadi, and D. Aryanto, *Makara Journal of Science*, **24**(2), 5 (2020). <https://doi.org/10.7454/mss.v24i1.11914>
- [19] A.K. Singh, G.S. Thool, P.R. Bangal, S.S. Madhavendra, and S.P. Singh, *Industrial & Engineering Chemistry Research*, **53**(22), 9383 (2014). <https://doi.org/10.1021/ie500077v>
- [20] R. Saravanan, F. Santhanam, and J.L. Berchmans, *Chemical Papers*, **66**(3), 226 (2012). <https://doi.org/10.2478/s11696-011-0129-8>
- [21] D.S. Cook, J.E. Hooper, D.M. Dawson, J.M. Fisher, D. Thompsett, S.E. Ashbrook, and R.I. Walton, *Inorganic Chemistry*, **59**(6), 3805 (2020). <https://doi.org/10.1021/acs.inorgchem.9b03459>
- [22] U. Hotjie, C. Rose, and M. Binnewies, *Solid State Sciences*, **5**(9), 1259 (2003). [https://doi.org/10.1016/S1293-2558\(03\)00177-8](https://doi.org/10.1016/S1293-2558(03)00177-8)
- [23] F.K. Ampong, J.A.M. Awudza, R.K. Nkum, F. Boakye, P.J. Thomas, and P. O'Brien, *Solid State Sciences*, **40**, 50 (2015). <https://doi.org/10.1016/j.solidstatedciences.2014.12.013>
- [24] B. Clavier, A. Zhadan, T. Baptiste, F. Boucher, A. Guet, F. Porcher, V. Brezová, et al., *Dalton Transactions*, **51**(21), 8411 (2022). <https://doi.org/10.1039/D2DT00352J>
- [25] G.M. Muralikrishna, B. Tas, N. Esakkiraja, V.A. Esin, K.H. Kumar, I.S. Golovin, I.V. Belova, et al., *Acta Materialia*, **203**, 116446 (2021). <https://doi.org/10.1016/j.actamat.2020.10.065>
- [26] E.A. Botchway, F.K. Ampong, I. Nkrumah, D.B. Puzer, R.K. Nkum, and F. Boakye, *East European Journal of Physics*, **2**, 249 (2023). <https://doi.org/10.26565/2312-4334-2023-2-28>
- [27] M. Paal, I. Nkrumah, F.K. Ampong, D.U. Ngbiche, R.K. Nkum, and F. Boakye, *Science Journal of University of Zakho*, **8**(3), 97 (2020). <https://doi.org/10.25271/sjuoz.2020.8.3.752>
- [28] D. Thakur, A. Sharma, A. Awasthi, D.S. Rana, D. Singh, S. Pandey, and S. Thakur, *Chemosensors*, **8**(4), 120 (2020). <https://doi.org/10.3390/chemosensors8040120>
- [29] I. Nkrumah, F.K. Ampong, A. Britwum, M. Paal, B. Kwakye-Awuah, R.K. Nkum, and F. Boakye, *Chalcogenide Letters*, **20**(3), 205 (2023). <https://doi.org/10.15251/CL.2023.203.205>
- [30] A. Abdel-Galil, M.R. Balboul, and A. Sharaf, *Physica B*, **477**, 20 (2015). <https://doi.org/10.1016/j.physb.2015.08.001>




#### СИНТЕЗ ЧИСТИХ ТА ЛЕГОВАНИХ МАРГАНЦЕМ НАНОЧАСТИНОК ОКСИДУ ЦИНКУ З РОЗЧИНУ: СТРУКТУРНО-ОПТИЧНЕ ДОСЛІДЖЕННЯ

Реймонд А. Антві, Ісаак Нкрума, Френсіс К. Ампонг, Марк Паал, Рубен Й. Тамакло, Роберт К. Нкум, Френсіс Боак'є  
*Факультет фізики, Університет науки і технологій Кваме Нкрума, Кумасі, Гана*

Чисті та леговані марганцем наночастинки оксиду цинку були успішно синтезовані в діапазоні складу  $Zn_{1-x}Mn_xO$  ( $0 < x < 0,5$ ) за допомогою процесу росту з розчину. Вплив легування Mn на структуру, морфологію та оптичні властивості досліджували кількома методами. Рентгеноструктурні дослідження підтвердили формування однофазної полікристалічної гексагональної структури вюрциту ZnO в діапазоні  $0 < x < 0,3$ . Жодних вторинних фаз, пов'язаних з Mn, у цьому діапазоні не виявлено, що можна пояснити тим фактом, що атоми легуючої домішки були добре включені в кристалічну решітку ZnO. Для  $Zn_{1-x}Mn_xO$  ( $x = 0,5$ ) на дифрактограмі спостерігалось кілька піків низької інтенсивності, що належать до залишків ацетату марганцю, що встановлює межу розчинності для використаної методики синтезу. Зміна d-інтервалу з процентним легуванням Mn показала дуже хорошу узгодженість із законом Вергарда в діапазоні ( $0 < x < 0,25$ ). Аналіз наночастинок EDAX підтвердив утворення ZnO, легovanого Mn. Оптична заборонена зона наночастинок ZnO зменшувалася лінійно зі збільшенням відсотка легування Mn, що свідчить про можливість налаштування ширини забороненої зони ZnO шляхом легування Mn.

**Ключові слова:** оксид цинку легований марганцем; фази процесу розчину; кристалічна структура; оптична заборонена зона

## DESIGN AND SIMULATION OF A TRIPLE ABSORBER LAYER PEROVSKITE SOLAR CELL FOR HIGH CONVERSION EFFICIENCY

 Abderrahim Yousfi<sup>a\*</sup>,  Okba Saidani<sup>a</sup>,  Zitouni Messai<sup>a</sup>, Rafik Zouache<sup>b</sup>  
Mohamed Meddah<sup>a</sup>, Younes Belgoumri<sup>a</sup>

<sup>a</sup> *ETA Laboratory, Department of electronics, Faculty of technology, University Mohamed El Bachir El Ibrahimi of Bordj Bou Arréridj-34030, Algeria*

<sup>b</sup> *Electronic Department, Faculty of Technology, University of Msila, 28000, Algeria*

\*Corresponding Author e-mail: [Abderrahim.yousfi@univ-bba.dz](mailto:Abderrahim.yousfi@univ-bba.dz)

Received August 12, 2023; revised September 17, 2023; accepted September 19, 2023

This paper presents a comprehensive simulation study on the influence of a triple absorber layer configuration in a perovskite-based solar cell using the SCAPS-1D software, under AM1.5 illumination. The simulated structure comprises a Cesium Tin-Germanium Triiodide ( $\text{CsSn}_{0.5}\text{Ge}_{0.5}\text{I}_3$ ) absorber layer sandwiched between Indium gallium zinc oxide (IGZO) and  $\text{Cu}_2\text{O}$  layers. The main objective of this study is to enhance the power conversion efficiency (PCE) by optimizing the thicknesses of each layer. To validate our simulation results, we compare them with experimental data obtained from existing literature, and we observe a satisfactory agreement between the two. Our findings reveal that the maximum PCE of 28% can be achieved by utilizing specific thickness values for each layer. Specifically, the optimal thicknesses are determined to be 20 nm for the IGZO layer, 200 nm for the  $\text{Cu}_2\text{O}$  layer, and 700 nm for the perovskite layer. These optimized thickness values lead to a significant improvement in the PCE of the solar cell, reaching 29%. This achievement highlights the effectiveness of our proposed triple absorber layer configuration and demonstrates its potential to enhance the overall performance of the perovskite-based solar cell. Overall, this study provides valuable insights into the optimization of the absorber layer configuration in perovskite solar cells, leading to improved power conversion efficiency.

**Keywords:** *Perovskite solar cell,  $\text{CsSn}_{0.5}\text{Ge}_{0.5}\text{I}_3$ , Power conversion efficiency, SCAPS-1D*

**PACS:** 84.60.Jt

### 1. INTRODUCTION

Hybrid perovskite materials have gained significant attention in the field of solar cells due to their remarkable properties and their potential as a low-cost solution for photovoltaic applications [1-10]. These materials have experienced a rapid increase in photovoltaic conversion efficiency, rising from approximately 3.9% in 2009 to 25.2% in 2021 [11-14]. Their exceptional characteristics, such as tunable bandgap, long diffusion length, efficient carrier transport, and ease of fabrication, have positioned them as strong competitors to traditional silicon-based solar cells. However, the commercial development of lead halide perovskites is hindered by the issue of lead toxicity. To address this challenge, researchers have been exploring alternative materials with lower toxicity, and among them, tin-based (Sn-based) perovskites have demonstrated promising results, particularly with  $\text{Sn}_2^+$  showing the highest power conversion efficiency. Different studies have investigated Sn-based perovskites, including  $\text{FASnI}_3$ ,  $\text{MASnI}_3$ , and  $\text{CsSnI}_3$ , revealing that organo-based perovskites inherently exhibit low stability. This has led to Cs-based cation perovskite, specifically  $\text{CsSnI}_3$ , emerging as the preferred candidate [15]. In the search for lead-free alternatives, planar heterojunction architecture has been explored as a viable option for Sn-based perovskites. However, Sn-based devices face challenges related to rapid oxidation of  $\text{Sn}_2^+$  to  $\text{Sn}_4^+$  when exposed to air, resulting in device instability and degradation. Furthermore, the self-doping of p-type materials increases the concentration of holes, leading to enhanced carrier recombination rates, which is detrimental to cell performance [16-20]. To overcome these issues, researchers have proposed alloying  $\text{CsSnI}_3$  with  $\text{Ge}_2^+$  to create  $\text{CsSn}_{0.5}\text{Ge}_{0.5}\text{I}_3$  perovskite configuration, which exhibits improved stability and air tolerance [21]. This configuration possesses favorable structural stability factors, including a Goldschmidt tolerance factor of 0.94 and an Octahedral factor of 0.4, contributing to the overall stability of the perovskite solar cell. Additionally, the addition of  $\text{SnF}_2$  to Sn-based perovskites has been shown to effectively reduce the oxidation of  $\text{Sn}_2^+$  to  $\text{Sn}_4^+$ , resulting in enhanced stability [22-24]. Devices fabricated with  $\text{SnF}_2$  have demonstrated performance stability for extended periods, maintaining 98% of their initial power conversion efficiency for over 100 days. Despite advancements in improving the performance of Sn-based perovskite solar cells, their power conversion efficiency still remains relatively low. Therefore, it is crucial to gain a comprehensive understanding of the relationship between material parameters and device architecture to enhance the performance of  $\text{CsSn}_{0.5}\text{Ge}_{0.5}\text{I}_3$ -based devices. In this work, we report on the design and simulation of a novel IGZO /  $\text{CsSn}_{0.5}\text{Ge}_{0.5}\text{I}_3$  /  $\text{CsSnCl}_3$  /  $\text{CsSnCl}_3$  /  $\text{Cu}_2\text{O}$  / Spiro-OMeTAD solar cell configuration using SCAPS-1D software [37]. The objective is to investigate the impact of a triple absorber layer configuration and varying thicknesses on key performance parameters such as short-circuit current density ( $J_{sc}$ ), open circuit voltage ( $V_{oc}$ ), fill factor (FF), and overall power conversion efficiency (PCE). The obtained results offer valuable insights for the design and development of high-performance  $\text{CsSn}_{0.5}\text{Ge}_{0.5}\text{I}_3$  perovskite solar cells.

## 2. DEVICE SETTINGS AND SIMULATION PROCESS

The device structure used in the simulations is based on the numerical design mentioned in reference [25]. It consists of the following layers: IGZO / CsSn0.5Ge0.5I3 / CsSnCl3 / CsSnCl3 / Cu2O / Spiro-OMeTAD, as illustrated in Figure 1. In this structure, IGZO with a thickness of 0.015 μm serves as the electron transport material (ETL). IGZO is chosen for its favorable band alignment, excellent optoelectronic properties, and stability [26,27]. Cu2O [28], with a thickness of 0.4 μm, is used as the hole transport layer (HTL), which is commonly employed in high-efficiency solar cells. The n-type absorber layer consists of a mixed halide perovskite (CsSn0.5Ge0.5I3, CsSnCl3, CsSnCl3) with a thickness of 0.250 μm. In this structure, the HTL and ETL layers are n-type and p-type, respectively. Various parameters were employed for the simulation of each layer, as summarized in Table 1. The input parameters for IGZO, Spiro OMeTAD, and CsSn0.5Ge0.5I3 were adopted from a similar simulation structure documented in the literature [29-31]. The absorption coefficients for the absorber and HTL were obtained from relevant literature sources [35-36]. Additionally, the SCAPS-1D software library, specifically the SOPRA database, provided the required absorption coefficients for the ETL layer. The band gap equation for the mixed halide perovskite CsSn0.5Ge0.5I3, expressed as a function of x, was derived from a numerical reference [22]. Moreover, the simulations were conducted at an operating temperature of 300 K. By utilizing this simulated device structure and incorporating the appropriate parameters and equations, the study aims to gain insights into the performance characteristics of the perovskite solar cell under investigation.

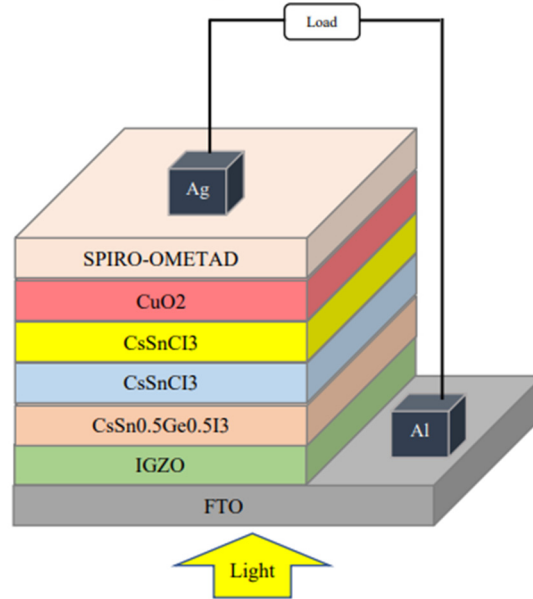


Figure 1. Structure of the suggested solar cell-based perovskite.

SCAPS-1D, also known as Solar Cell Capacitance Simulator One Dimension, is a software application designed for Windows. It was developed at the University of Gent using lab windows/CVI of the national instrument. The primary purpose of this program is to numerically solve fundamental semiconductor equations in a one-dimensional context, specifically under steady-state conditions. By utilizing SCAPS-1D, users are able to define various parameters upon which the program calculates results. These results provide valuable insights into the underlying physics of the model, offering explanations for important aspects such as individual carrier densities, carrier transport mechanisms, electric field distributions, and recombination profiles., which are given below [38]:

$$\left(\frac{\partial^2 \psi}{\partial x^2}\right) = -\frac{\partial E}{\partial x} = -\frac{\rho}{\epsilon_s} = -\frac{q}{\epsilon_s} [p - n + N_d^+ - N_a^- + N_{def}]. \quad (1)$$

Where  $\Psi$  is electrostatic potentiality,  $\epsilon_s$  is static relative permittivity,  $q$  is the charge,  $e$  and  $n$  are the respective electrons and holes,  $N_d^+$  is density of donor,  $N_a^-$  is density of acceptor and  $N_{def}$  is the defect density of both donor and acceptor. The carrier continuity equation in device may be represented as given below:

$$-\frac{\partial j_p}{\partial x} + G - U_p(n, p) = 0, \quad (2)$$

$$-\frac{\partial j_n}{\partial x} + G - U_n(n, p) = 0. \quad (3)$$

Here  $j_p$  and  $j_n$  are the hole and electron current densities,  $G$  is carrier generation rate,  $U_n(n, p)$  and  $U_p(n, P)$  are the recombination rates of electrons and holes respectively. Furthermore, carrier current density may also be obtained from:

$$j_p = qn\mu_p E + qD_p \frac{\partial n}{\partial x}, \quad (4)$$

$$j_n = qn\mu_n E + qD_n \frac{\partial n}{\partial x} \quad (5)$$

Here  $q$  is the charge,  $\mu_p$  and  $\mu_n$  are carrier mobilities, and  $D_p$ ,  $D_n$  are the diffusion coefficients.

By conducting simulations using SCAPS-1D [32-33], it is possible to obtain values for current density ( $J_{sc}$ ), power conversion efficiency (PCE) as a percentage, fill factor (FF) as a percentage, and open circuit voltage ( $V_{oc}$ ) for different thicknesses and temperatures. These simulations are applicable to seven distinct layers of the solar cell and can be performed under both illuminated and dark conditions, considering a range of temperatures [37].

### 3. RESULTS AND DISCUSSION

To enable an efficient extraction of electrons and holes from the perovskite active layer in photovoltaic devices, certain requirements must be met. Specifically, the electron affinity (EA) of the electron transport layer (ETL) should be greater than that of the perovskite, while the hole transport layer (HTL) should have a lower EA than the perovskite [34]. This ensures favorable energy level alignment for the extraction of charge carriers. In our simulated device components, these conditions have been successfully fulfilled, as demonstrated in Table I. Additionally, for proper electron flow from the perovskite to the ETL, the conduction band of the ETL should be situated lower than that of the perovskite. Conversely, to prevent the undesirable backflow of electrons in the opposite direction, the conduction band of the HTL should be higher than that of the perovskite. These considerations ensure unidirectional charge transport. Likewise, to facilitate the flow of holes from the perovskite to the HTL, the valence band of the HTL should be positioned higher than that of the perovskite. Conversely, the valence band of the ETL should be lower than that of the perovskite to prevent the backward movement of holes. By satisfying these band alignment requirements, we ensure the efficient extraction and separation of electrons and holes within the device.

**Table 1.** Properties of the different layers of the proposed structure.

Parameters	IGZO	CsSn0.5Ge0.5I3	CsSnCl3	CsSnCl3	CuO2	Spiro-OMeTAD
Thickness (um)	0.015	0.250	1.000	1.000	0.400	0.100
Band gap (eV)	3.050	1.498	1.220	1.220	3.700	4.005
Electron affinity (eV)	4.160	4.000	3.800	3.700	1.700	1.460
Dielectric Permittivity	10.00	28.000	20.000	20.000	10.000	10.700
CB effective density of states (cm <sup>-3</sup> )	5.000E+21	3.100E+18	5.000E+16	5.000E+16	2.200E+19	2.800E+20
VB effective density of states (cm <sup>-3</sup> )	5.000E+16	3.100E+19	5.000E+16	5.000E+16	1.800E+18	1.000E+20
19 Electron mobility (cm <sup>2</sup> /VS)	1.500E+1	9.740E+2	5.000E+1	7.000E+1	1.000E+2	1.200E+1
Hole mobility (cm <sup>2</sup> /VS)	1.000E-1	2.130E+2	5.000E+1	5.000E+1	2.500E+1	2.800E+0
Shallow uniform donor density N <sub>D</sub> (cm <sup>-3</sup> )	1.000E+18	0.000E+0	0	0	0	0
Shallow uniform acceptor density N <sub>A</sub> (cm <sup>-3</sup> )	1.000E+5	1.100E+18	1.000E+20	1.000E+210	2.000E+21	1.000E+21

The fulfillment of these crucial conditions is illustrated in Figure 2, providing visual evidence of the desired energy level alignment and band structures necessary for effective charge carrier extraction and transport in the perovskite-based photovoltaic device.

To comprehensively assess the behavior and performance of the IGZO / CsSn<sub>0.5</sub>Ge<sub>0.5</sub>I<sub>3</sub> / CsSnCl<sub>3</sub> / CsSnCl<sub>3</sub> / Cu<sub>2</sub>O / Spiro-OMeTAD solar cell, we conducted a series of simulations. Our objective was to investigate the impacts of the Triple Absorber Layer Perovskite and the thicknesses of the electron transport layer (ETL) and the hole transport layer (HTL) on the efficiency of perovskite-based solar cells.

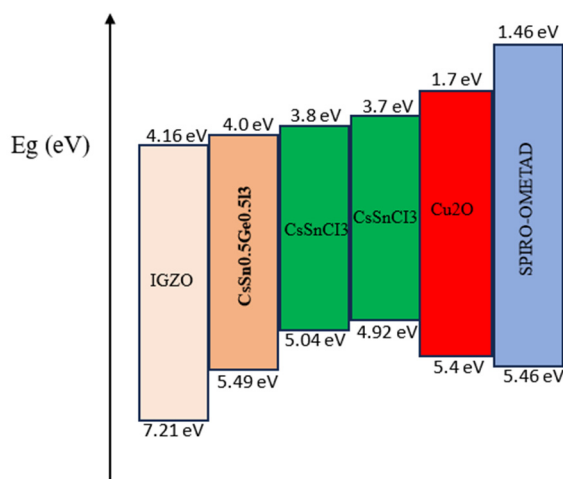


**Figure 2.** Energy band diagram of the materials used in the simulation. The units for the band energies are in electron volt (eV)

### 3.1. Effect of the first perovskite layer (CsSn<sub>0.5</sub>Ge<sub>0.5</sub>I<sub>3</sub>) thickness:

In this section, we aim to investigate the performance of the IGZO / CsSn<sub>0.5</sub>Ge<sub>0.5</sub>I<sub>3</sub> / CsSnCl<sub>3</sub> / CsSnCl<sub>3</sub> / Cu<sub>2</sub>O / Spiro-OMeTAD solar cell using the parameters provided in Table 1. Our focus is on determining the optimal thickness of the CsSn<sub>0.5</sub>Ge<sub>0.5</sub>I<sub>3</sub> absorber layer. Figure 3 presents the evolution patterns of key parameters, including open-circuit voltage (Voc) (Figure 3(b)), short-circuit current density (Jsc) (Figure 3(a)), fill factor (FF) (Figure 3(c)), and overall power conversion efficiency (PCE) (Figure 3(d)), as a function of the n-CsSn<sub>0.5</sub>Ge<sub>0.5</sub>I<sub>3</sub> absorber layer thickness ranging from 0.2 to 0.65 μm. With an increase in the thickness of the CsSn<sub>0.5</sub>Ge<sub>0.5</sub>I<sub>3</sub> layer from 0.25 to 0.65 μm, a significant enhancement in Jsc is observed, rising from 38.4 mA/cm<sup>2</sup> to approximately 38.43 mA/cm<sup>2</sup>. This rise in Jsc can be attributed to the increased path length for photon absorption, resulting in the generation of a higher number of charge carriers. Additionally, the fill factor (FF) displays a remarkable increase from 56.5% to approximately 66.5% as the CsSn<sub>0.5</sub>Ge<sub>0.5</sub>I<sub>3</sub> layer thickness increases. The higher FF indicates improved charge extraction and reduced losses within the solar cell, contributing to enhanced overall performance. Conversely, there is a decrease in the open-circuit voltage (Voc) as the absorber layer thickness increases. Voc decreases from 1.35 V to approximately 1.05 V. At a thickness of 0.25 μm, a higher Voc is observed, indicating reduced recombination. However, as the absorber thickness increases, the generation of more carriers leads to an enhancement in recombination, causing a decline in Voc. The observed variations in Voc, Jsc, and FF have direct implications for the overall power conversion efficiency (PCE) of the solar cell. Optimal thickness selection must strike a balance between maximizing Jsc and FF while minimizing the loss in Voc due to increased carrier generation and recombination. It is worth noting that these findings highlight the influence of the CsSn<sub>0.5</sub>Ge<sub>0.5</sub>I<sub>3</sub> absorber layer thickness on the performance parameters of the solar cell. Careful consideration of these variations is crucial in optimizing the device's PCE.

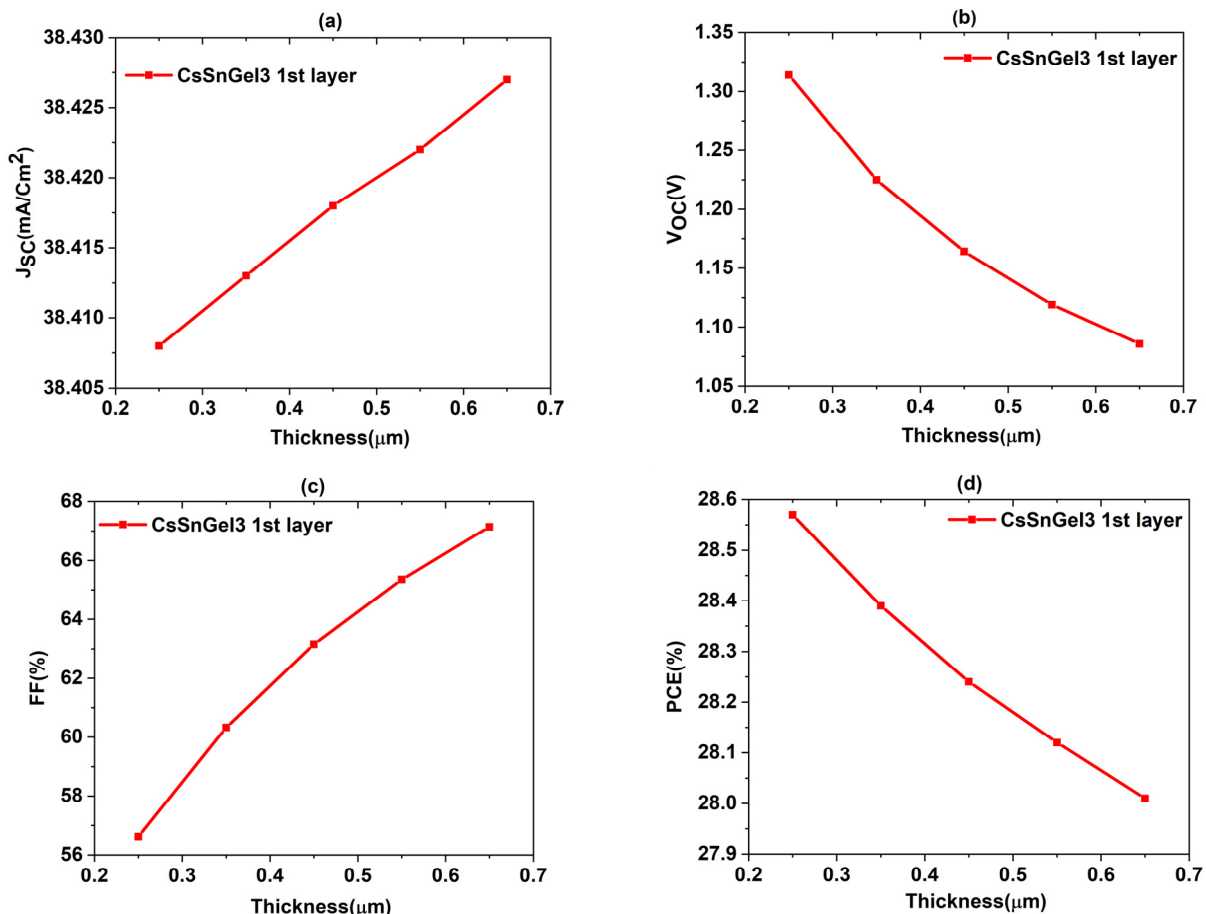


Figure 3. Effect of the first perovskite layer (CsSn<sub>0.5</sub>Ge<sub>0.5</sub>I<sub>3</sub>) thickness

### 3.2. Effect of the second perovskite layer (CsSnCl<sub>3</sub>) thickness:

The effect of the n-CsSnCl<sub>3</sub> absorber layer thickness on the performance of the IGZO / CsSn<sub>0.5</sub>Ge<sub>0.5</sub>I<sub>3</sub> / CsSnCl<sub>3</sub> / CsSnCl<sub>3</sub> / Cu<sub>2</sub>O / Spiro-OMeTAD solar cell is illustrated in Figure 4. The thickness of the CsSn<sub>0.5</sub>Ge<sub>0.5</sub>I<sub>3</sub> layer was varied from 0.6 to 1 μm, and the corresponding evolution patterns of key parameters were analyzed. Firstly, the short-circuit current density (Jsc) (Figure 4(a)) exhibited a notable increase as the CsSn<sub>0.5</sub>Ge<sub>0.5</sub>I<sub>3</sub> layer thickness was increased from 0.6 to 1 μm. Jsc values rose from 38.37 mA/cm<sup>2</sup> to approximately 38.49 mA/cm<sup>2</sup>. This indicates that the thicker CsSn<sub>0.5</sub>Ge<sub>0.5</sub>I<sub>3</sub> layer allowed for more efficient absorption of incident photons, leading to a higher generation of electron-hole pairs within the solar cell. Secondly, the fill factor (FF) (Figure 4(c)) showed a rapid rise as the CsSn<sub>0.5</sub>Ge<sub>0.5</sub>I<sub>3</sub> layer

thickness increased. The FF increased from 57.5% to approximately 58.5%. A higher FF suggests improved charge extraction and reduced losses within the solar cell, contributing to enhanced overall efficiency. On the other hand, the open-circuit voltage ( $V_{oc}$ ) (Figure 4(b)) demonstrated a decrease with increasing  $\text{CsSn}_{0.5}\text{Ge}_{0.5}\text{I}_3$  layer thickness.  $V_{oc}$  decreased from 1.286 V to approximately 1.266 V when the thickness reached 0.6  $\mu\text{m}$ . The decrease in  $V_{oc}$  can be attributed to various factors, including charge recombination losses or changes in energy level alignment at the interfaces. In summary, the inclusion of the  $\text{CsSnCl}_3$  layer in the solar cell configuration (IGZO /  $\text{CsSn}_{0.5}\text{Ge}_{0.5}\text{I}_3$  /  $\text{CsSnCl}_3$  /  $\text{CsSnCl}_3$  /  $\text{Cu}_2\text{O}$  / Spiro-OMeTAD) resulted in increased light absorption, leading to a higher generation of electron-hole pairs. This improvement in the overall efficiency of the solar cell is attributed to the increased capture of photons and their conversion into electrical current.

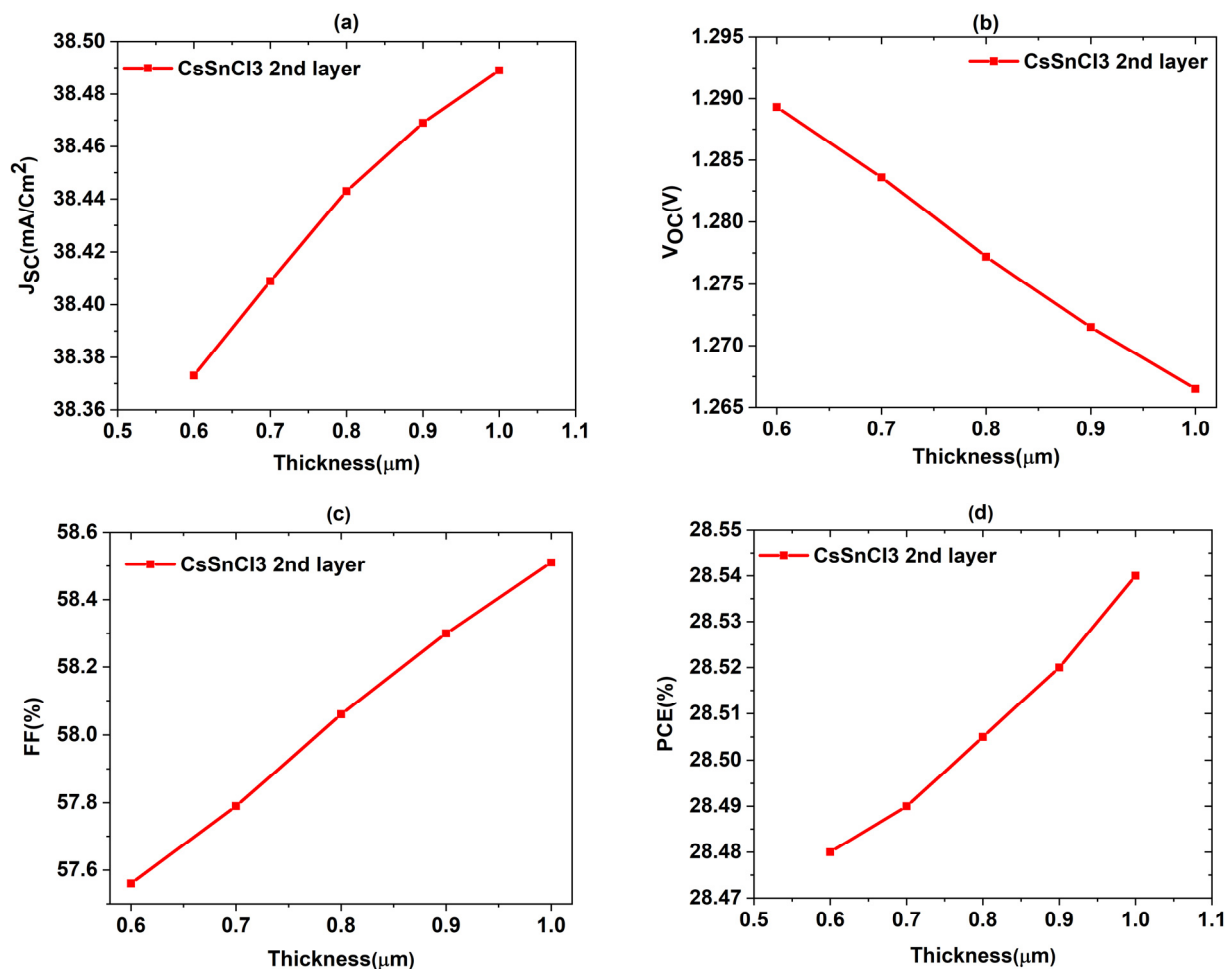


Fig. 4 – Effect of the second perovskite layer ( $\text{CsSnCl}_3$ ) thickness

### 3.3. Effect of the third perovskite layer ( $\text{CsSnCl}_3$ ) thickness:

The impact of the n- $\text{CsSnCl}_3$  third absorber layer thickness on the performance of the IGZO/ $\text{CsSn}_{0.5}\text{Ge}_{0.5}\text{I}_3$ / $\text{CsSnCl}_3$ / $\text{CsSnCl}_3$ / $\text{Cu}_2\text{O}$ /Spiro-OMeTAD solar cell is depicted in Figure 5. The study involved varying the thickness of the  $\text{CsSn}_{0.5}\text{Ge}_{0.5}\text{I}_3$  layer from 1 to 1.5  $\mu\text{m}$ , and the corresponding changes in key parameters were analyzed. Initially, the short-circuit current density ( $J_{sc}$ ) (Figure 5(a)) displayed a noticeable decrease as the thickness of the  $\text{CsSn}_{0.5}\text{Ge}_{0.5}\text{I}_3$  third layer increased from 1 to 1.5  $\mu\text{m}$ . The  $J_{sc}$  values decreased from 38.27  $\text{mA}/\text{cm}^2$  to approximately 38  $\text{mA}/\text{cm}^2$ . This decrease in  $J_{sc}$  suggests that the thicker  $\text{CsSnCl}_3$  layer may have an impact on charge carrier generation. Non-uniform photon absorption throughout the thickness of the  $\text{CsSnCl}_3$  layer could lead to reduced effective generation of electron-hole pairs. This non-uniform absorption might arise from recombination losses or inefficient charge transport within the thicker layer, resulting in a decrease in  $J_{sc}$ . Conversely, the fill factor (FF) (Figure 5(c)) exhibited a rapid increase as the thickness of the  $\text{CsSn}_{0.5}\text{Ge}_{0.5}\text{I}_3$  third layer increased, the FF increased from 54.1% to approximately 55.4%. The increased thickness of the n- $\text{CsSnCl}_3$  layer improved charge carrier collection and reduced charge carrier recombination, resulting in a higher fill factor. This enhancement is attributed to the thicker layer providing more pathways for charge carriers to reach the electrodes, minimizing losses and maximizing the overall power output. However, the open-circuit voltage ( $V_{oc}$ ) (Figure 5(b)) demonstrated a decrease with increasing  $\text{CsSn}_{0.5}\text{Ge}_{0.5}\text{I}_3$  layer thickness,  $V_{oc}$  decreased from 1.382 V to approximately 1.346 V when the thickness reached 1.5  $\mu\text{m}$ . The alteration of band alignment and energy levels, caused by the increased thickness

of the n-CsSnCl<sub>3</sub> layer, contributed to this reduction in Voc. These changes in energy levels resulted in a reduced built-in potential, increased recombination, or modified charge carrier extraction, all of which contributed to the lower Voc observed. Moreover, the power conversion efficiency (PCE) (Figure 5(d)) also experienced a decrease with increasing CsSn<sub>0.5</sub>Ge<sub>0.5</sub>I<sub>3</sub> layer thickness. Voc decreased from 28.64% to approximately 28.5% when the thickness reached 1.5 μm. The thicker n-CsSnCl<sub>3</sub> layer introduced additional losses, such as increased resistive losses or reduced light absorption due to inefficient charge transport or light scattering. These losses further contributed to the overall decrease in the PCE of the solar cell.

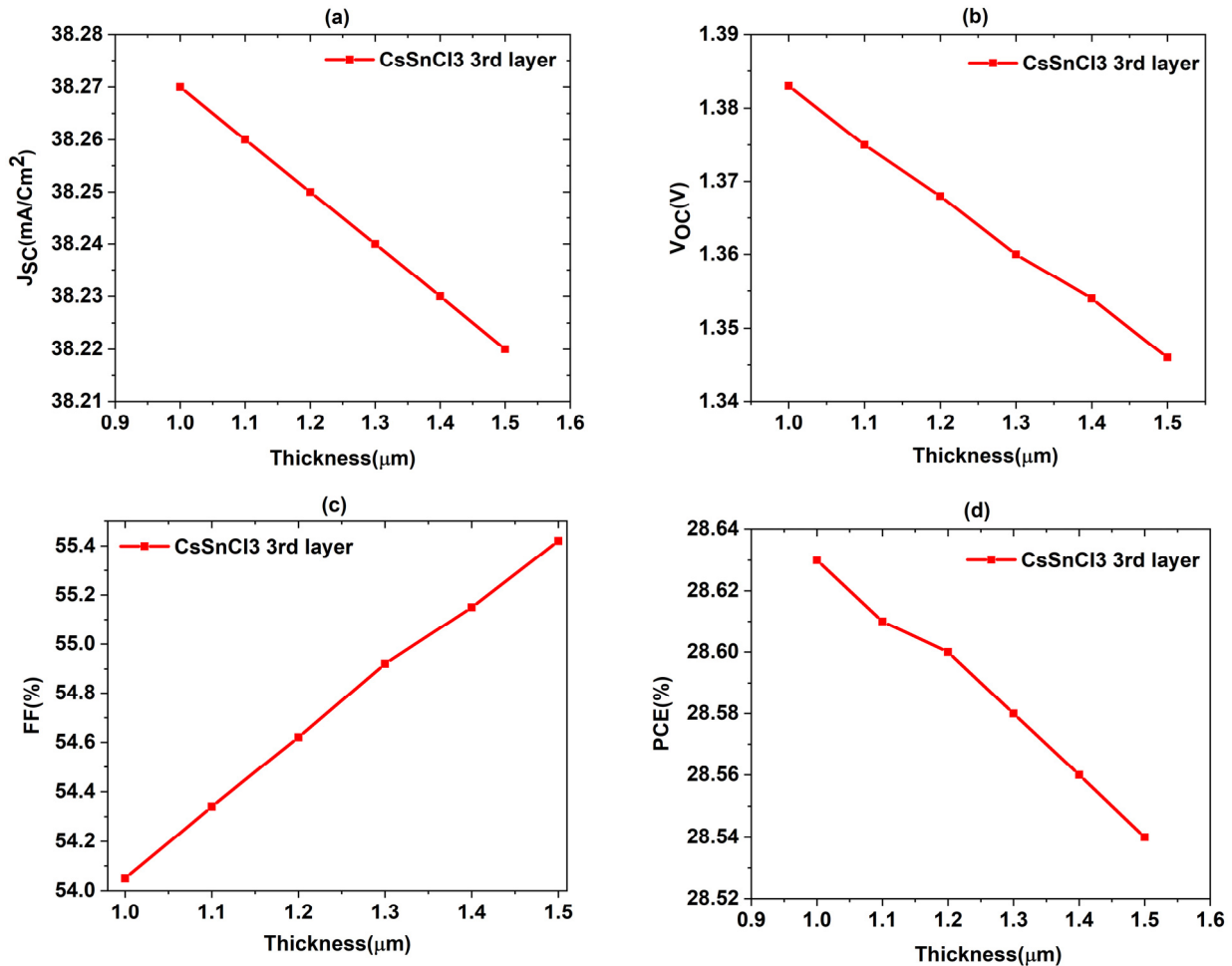


Figure 5. Effect of the third perovskite layer (CsSnCl<sub>3</sub>) thickness

### 3.4. Effect of the layer (ETL) thickness

In a perovskite solar cell, the Electron Transport Layer (ETL) plays a crucial role in enhancing the overall performance of the device by facilitating the movement of electrons from the perovskite layer to the front contact. In this study, we will examine the impact of varying ETL thickness on the output performance of the IGZO/CsSn<sub>0.5</sub>Ge<sub>0.5</sub>I<sub>3</sub>/CsSnCl<sub>3</sub>/CsSnCl<sub>3</sub>/Cu<sub>2</sub>O/Spiro-OMeTAD solar cell, as depicted in Figure 6. By analyzing the evolution of key parameters, we can understand how changes in ETL thickness affect the device's characteristics. Firstly, the short-circuit current density (J<sub>sc</sub>) (Figure 6(a)) experiences a noticeable decrease as the ETL layer thickness increases from 0.02 to 0.17 μm. Specifically, J<sub>sc</sub> values decrease from 38.40 mA/cm<sup>2</sup> to approximately 38.2 mA/cm<sup>2</sup>. This decrease can be attributed to the phenomenon where a thicker ETL layer absorbs a greater amount of incident photons within the ETL itself. Consequently, a portion of the incident light is prevented from reaching the CsSn<sub>0.5</sub>Ge<sub>0.5</sub>I<sub>3</sub> absorber layer, leading to a reduction in the generation of charge carriers through photon absorption. Secondly, the fill factor (FF) (Figure 6(c)) demonstrates a rapid decline with increasing ETL layer thickness. The FF decreases from 60.4% to approximately 59.7%. The introduction of the ETL layer introduces additional resistance within the solar cell. This increased resistance impedes the efficient extraction and transport of charges, resulting in higher losses and a decrease in FF. Furthermore, both the open-circuit voltage (Voc) (Figure 6(b)) and power conversion efficiency (PCE) (Figure 6(d)) exhibit a decrease as the ETL layer thickness increases. This reduction in Voc and PCE can be attributed to multiple factors. For instance, a thicker ETL layer can introduce increased series resistance within the device, hindering the efficient flow of current. Consequently, a voltage drop occurs across the ETL layer, leading to a reduction in Voc. In summary, the thickness of the ETL layer in a perovskite solar cell has a significant influence on its performance. While a thicker ETL layer enhances

photon absorption within itself, it simultaneously hampers the flow of charge carriers, resulting in decreased  $J_{sc}$ , FF,  $V_{oc}$ , and PCE. These findings highlight the importance of carefully optimizing the ETL thickness to achieve optimal performance in perovskite solar cells.

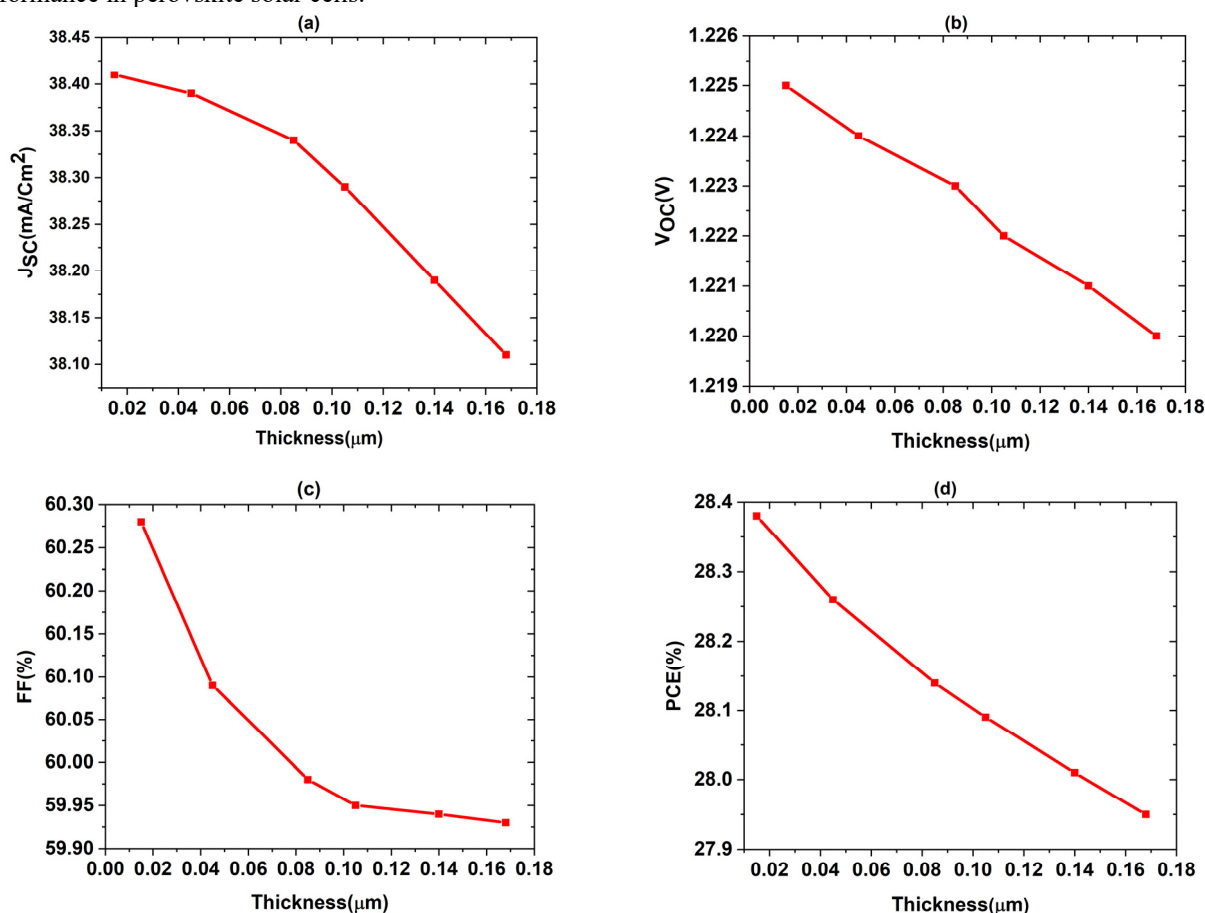


Figure 6. Effect of the layer (ETL) thickness

### 3.5. Effect of the layer (HTL) thickness

The influence of the hole transport layer (HTL) thickness on key performance parameters, including open-circuit voltage ( $V_{oc}$ ), short-circuit current density ( $J_{sc}$ ), fill factor (FF), and overall efficiency, was investigated and depicted in Figure 7. Surprisingly, it was observed that varying the HTL thickness had negligible impact on these parameters. This phenomenon can be attributed to the high absorption of photons by the absorber and electron transport layers (ETL), resulting in the majority of available photons being absorbed before reaching the HTL layer. Consequently, only a small number of charge carriers are generated within the HTL layer, limiting its influence on the device performance. To further elucidate this behavior, the values of  $V_{oc}$  and  $J_{sc}$  were examined, as depicted in Figure 7(a) and (b) respectively. It was found that  $V_{oc}$  remained relatively constant at around 1.47V, while  $J_{sc}$  exhibited a consistent value of approximately 38.51 mA/cm<sup>2</sup>. These observations indicate that the HTL thickness variation has minimal impact on these two parameters. Additionally, the fill factor (FF) and efficiency were evaluated and presented in Figure 7(c) and (d) respectively. Notably, both FF and efficiency demonstrated a stable behavior, hovering around 50% and 29% respectively, regardless of the HTL thickness. These findings suggest that, in this particular solar cell configuration, the HTL thickness does not significantly affect the device performance. The limited carrier generation within the HTL layer, due to the substantial photon absorption in previous layers, mitigates its role in determining  $V_{oc}$ ,  $J_{sc}$ , FF, and efficiency. It is important to note that these conclusions are specific to the investigated solar cell structure, and different device configurations may exhibit diverse responses to HTL thickness variations.

Table 2 presents the design structure that has been achieved through the optimization of layer thicknesses.

Table 2. Comparison between the conventional and the suggested model

Structure	$J_{sc}$ (mA/cm <sup>2</sup> )	$V_{oc}$ (V)	FF (%)	PCE (%)
FTO/ZnO/ CsSn0.5Ge0.5I3/CuI/Au [31]	24.21	1.203	84.07	24.51
FTO/IGZO/CsSn0.5Ge0.5I3/ CsSnCl3/ CsSnCl3/CuO2/Au	38.4	1.486	52.48	28.96

This table provides a comparison between the optimized designs and a non-optimized cell, specifically referred to as the reference cell [37]. The findings in Table 2 clearly demonstrate a significant improvement in performance for the optimized designs when compared to the non-optimized variant. The results obtained from our simulations indicate a



favorable alignment between the performance of the reference cell [37] and our optimized designs. This suggests that our simulation results closely resemble the outcomes reported in the reference study.

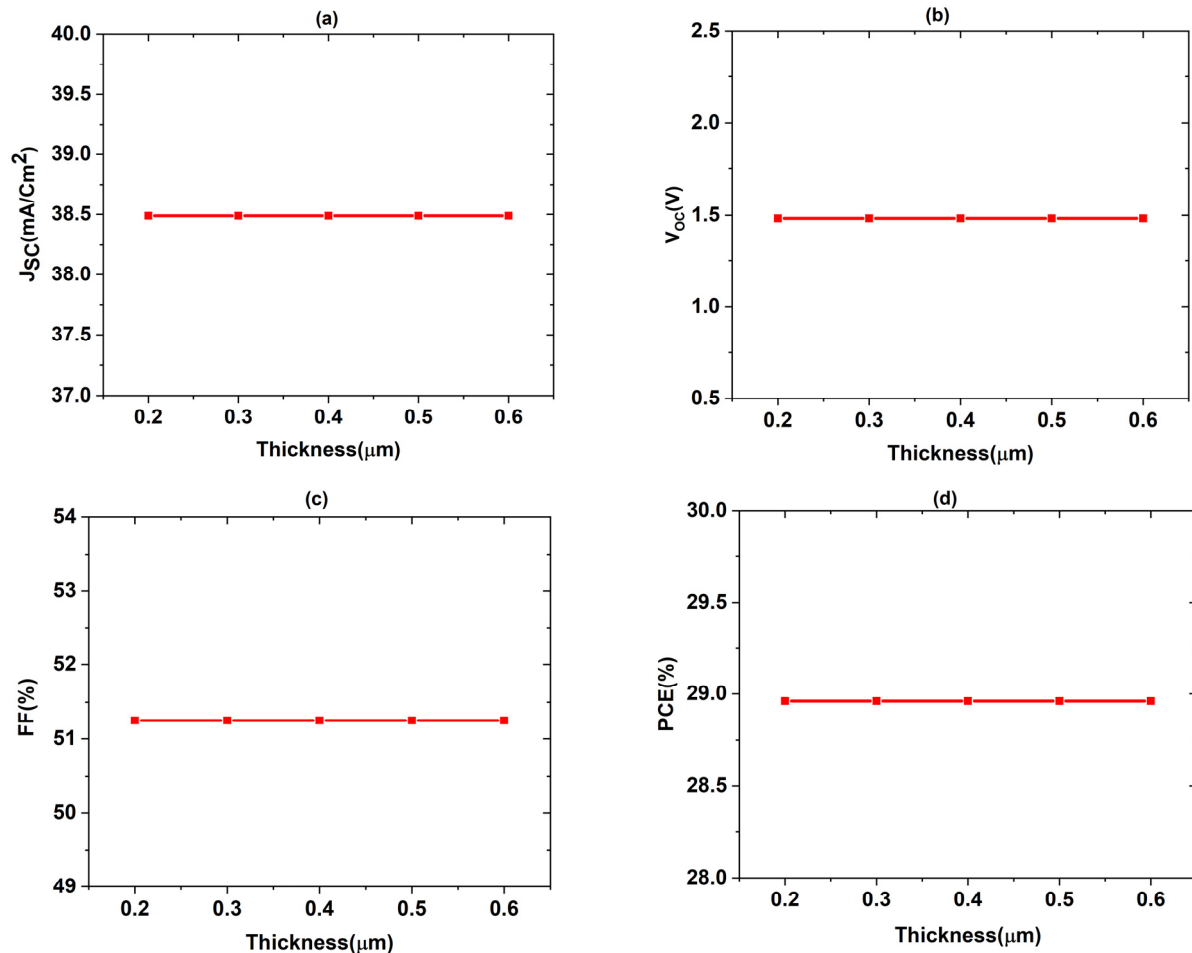


Figure 7. Effect of the layer (HTL) thickness

#### 4. CONCLUSION

In summary, this study investigates the results of a comprehensive simulation study on the influence of a triple absorber layer configuration in a perovskite-based solar cell using the SCAPS-1D software, under AM1.5 illumination. The simulated structure comprises a Cesium Tin-Germanium Tri-iodide ( $\text{CsSn}_{0.5}\text{Ge}_{0.5}\text{I}_3$ ) absorber layer sandwiched between IGZO and  $\text{Cu}_2\text{O}$  layers. The main objective of this study is to enhance the power conversion efficiency (PCE) by optimizing the thicknesses of each layer. To validate our simulation results, we compare them with experimental data obtained from existing literature, and we observe a satisfactory agreement between the two. Our findings reveal that the maximum PCE of 28% can be achieved by utilizing specific thickness values for each layer. Specifically, the optimal thicknesses are determined to be 20 nm for the IGZO layer, 200 nm for the  $\text{Cu}_2\text{O}$  layer, and 700 nm for the perovskite layer. These optimized thickness values lead to a significant improvement in the PCE of the solar cell, reaching 29%. This achievement highlights the effectiveness of our proposed triple absorber layer configuration and demonstrates its potential to enhance the overall performance of the perovskite-based solar cell. Overall, this study provides valuable insights into the optimization of the absorber layer configuration in perovskite solar cells, leading to improved power conversion efficiency.

#### Acknowledgements

This work was supported by the DGRSDT of the ministry of higher education of Algeria.

#### ORCID

Abderrahim Yousfi, <https://orcid.org/0000-0003-2071-728X>; Okba Saidani, <https://orcid.org/0000-0003-0507-5581>  
 Zitouni Messai, <https://orcid.org/0000-0002-2508-3696>

#### REFERENCES

- [1] N.J. Jeon, H. Na, E.H. Jung, T.-Y. Yang, Y.G. Lee, G. Kim, H.-W. Shin, et al., "A fluorene-terminated hole-transporting material for highly efficient and stable perovskite solar cells," *Nature Energy*, **3**(8), 682-689 (2018). <https://doi.org/10.1038/s41560-018-0200-6>

- [2] N. Li, Z. Zhu, J. Li, A.K.-Y. Jen, L. Wang, "Inorganic CsPb<sub>1-x</sub>Sn<sub>x</sub>IBr<sub>2</sub> for efficient wide-bandgap perovskite solar cells," *Advanced energy materials*, **8**(22), 1800525 (2018). <https://doi.org/10.1002/aenm.201800525>
- [3] F. Zhang, B. Yang, Y. Li, W. Deng, and R. He, "Extra-long electron-hole diffusion lengths in CH<sub>3</sub>NH<sub>3</sub>PbI<sub>3-x</sub>Cl<sub>x</sub> perovskite single crystals," *Journal of Materials Chemistry C*, **5**(33), 8431-8435 (2017). <https://doi.org/10.1039/C7TC02802D>
- [4] Q. Ou, X. Bao, Y. Zhang, H. Shao, G. Xing, X. Li, L. Shao, et al., "Band structure engineering in metal halide perovskite nanostructures for optoelectronic applications," *Nano Materials Science*, **1**(4), 268-287 (2019). <https://doi.org/10.1016/j.nanoms.2019.10.004>
- [5] K. Tanaka, T. Takahashi, T. Ban, T. Kondo, K. Uchida, and N. Miura, "Comparative study on the excitons in lead-halide-based perovskite-type crystals CH<sub>3</sub>NH<sub>3</sub>PbBr<sub>3</sub> CH<sub>3</sub>NH<sub>3</sub>PbI<sub>3</sub>," *Solid state communications*, **127**(9-10), 619-623 (2003). [https://doi.org/10.1016/S0038-1098\(03\)00566-0](https://doi.org/10.1016/S0038-1098(03)00566-0)
- [6] K. Yamada, H. Kawaguchi, T. Matsui, T. Okuda, and S. Ichiba, "Structural Phase Transition and Electrical Conductivity of the Perovskite CH<sub>3</sub>NH<sub>3</sub>Sn<sub>1-x</sub>Pb<sub>x</sub>Br<sub>3</sub> and CsSnBr<sub>3</sub>," *Bulletin of the Chemical Society of Japan*, **63**(9), 2521-2525 (1990). <https://doi.org/10.1246/bcsj.63.2521>
- [7] M.S. Chowdhury, S.A. Shahahmadi, P. Chelvanathan, S.K. Tiong, N. Amin, K. Techato, N. Nuthammachot, et al., "Effect of deep-level defect density of the absorber layer and n/i interface in perovskite solar cells by SCAPS-1D," *Results in Physics*, **16**, 102839 (2020). <https://doi.org/10.1016/j.rinp.2019.102839>
- [8] M.A. Green, E.D. Dunlop, J. Hohl-Ebinger, M. Yoshita, N. Kopidakis, and X. Hao, "Solar cell efficiency tables (Version 58)," *Progress in photovoltaics: research and applications*, **29**(7), 657-667 (2021). <https://doi.org/10.1002/pip.3506>
- [9] Y. Jiang, E.J. Juarez-Perez, Q. Ge, S. Wang, M.R. Leyden, L.K. Ono, S.R. Raga, et al., "Post-annealing of MAPbI<sub>3</sub> perovskite films with methylamine for efficient perovskite solar cells," *Materials Horizons*, **3**(6), 548-555 (2016). <https://doi.org/10.1039/C6MH00160B>
- [10] Y.H. Khattak, F. Baig, A. Shuja, S. Beg, and B.M. Soucase, "Numerical analysis guidelines for the design of efficient novel nip structures for perovskite solar cell," *Solar Energy*, **207**, 579-591 (2020). <https://doi.org/10.1016/j.solener.2020.07.012>
- [11] A. Kojima, K. Teshima, Y. Shirai, and T. Miyasaka, "Organometal halide perovskites as visible-light sensitizers for photovoltaic cells," *Journal of the American Chemical Society*, **131**(17), 6050-6051 (2009). <https://doi.org/10.1021/ja809598r>
- [12] J. Wu, Y. Li, Y. Li, W. Xie, J. Shi, D. Li, S. Cheng, and Q. Meng, "Using hysteresis to predict the charge recombination properties of perovskite solar cells," *Journal of Materials Chemistry A*, **9**(10), 6382-6392 (2021). <https://doi.org/10.1039/D0TA12046D>
- [13] J.J. Yoo, G. Seo, M.R. Chua, T.G. Park, Y. Lu, F. Rotermund, Y.-K. Kim, et al., "Efficient perovskite solar cells via improved carrier management," *Nature*, **590**(7847), 587-593 (2021). <https://doi.org/10.1038/s41586-021-03285-w>
- [14] H. Min, D.Y. Lee, J. Kim, G. Kim, K.S. Lee, J. Kim, M.J. Paik, et al., "Perovskite solar cells with atomically coherent interlayers on SnO<sub>2</sub> electrodes," *Nature*, **598**(7881), 444-450 (2021). <https://doi.org/10.1038/s41586-021-03964-8>
- [15] T. Krishnamoorthy, H. Ding, C. Yan, W.L. Leong, T. Baikie, Z. Zhang, M. Sherburne, et al., "Lead-free germanium iodide perovskite materials for photovoltaic applications," *Journal of Materials Chemistry A*, **3**(47), 23829-23832 (2015). <https://doi.org/10.1039/C5TA05741H>
- [16] M.H. Kumar, S. Dharani, W.L. Leong, P.P. Boix, R.R. Prabhakar, T. Baikie, C. Shi, et al., "Lead-free halide perovskite solar cells with high photocurrents realized through vacancy modulation," *Advanced Materials*, **26**(41), 7122-7127 (2014). <https://doi.org/10.1002/adma.201401991>
- [17] B. Wu, Y. Zhou, G. Xing, Q. Xu, H.F. Garces, A. Solanki, T.W. Goh, et al., "Long minority-carrier diffusion length and low surface-recombination velocity in inorganic lead-free CsSnI<sub>3</sub> perovskite crystal for solar cells," *Advanced Functional Materials*, **27**(7), 1604818 (2017). <https://doi.org/10.1002%2Fadfm.201604818>
- [18] H. Wei, P. Qiu, Y. Li, Y. He, M. Peng, X. Zheng, and X. Liu, "Challenges and strategies of all-inorganic lead-free halide perovskite solar cells," *Ceramics International*, **48**(5), 5876-5891 (2022). <https://doi.org/10.1016/j.ceramint.2021.11.184>
- [19] M.-G. Ju, M. Chen, Y. Zhou, J. Dai, L. Ma, N.P. Padture, and X.C. Zeng, "Toward eco-friendly and stable perovskite materials for photovoltaics," *Joule*, **2**(7), 1231-1241 (2018). <https://doi.org/10.1016/j.joule.2018.04.026>
- [20] T. Leijtens, G.E. Eperon, N.K. Noel, S.N. Habisreutinger, A. Petrozza, and H.J. Snaith, "Stability of metal halide perovskite solar cells," *Adv. Energy Mater.*, **5**, 1500963 (2015). <https://doi.org/10.1002/aenm.201500963>
- [21] M. Chen, M.-G. Ju, H.F. Garces, A.D. Carl, L.K. Ono, Z. Hawash, Y. Zhang, et al., "Highly stable and efficient all-inorganic lead-free perovskite solar cells with native-oxide passivation," *Nature communications*, **10**(1), 16 (2019). <https://doi.org/10.1038/s41467-018-07951-y>
- [22] G.G. Chan, C.M. Koch, and L.H. Connors, "Blood proteomic profiling in inherited (ATTRm) and acquired (ATTRwt) forms of transthyretin-associated cardiac amyloidosis," *Journal of Proteome Research*, **16**(4), 1659-1668 (2017). <https://doi.org/10.1021/acs.jproteome.6b00998>
- [23] E.L. Unger, L. Kegelmann, K. Suchan, D. Sörell, L. Kortec, and S. Albrecht, "Roadmap and roadblocks for the band gap tunability of metal halide perovskites," *Journal of Materials Chemistry A*, **5**(23), 11401-11409 (2017). <https://doi.org/10.1039/C7TA00404D>
- [24] M. Saliba, T. Matsui, J.-Y. Seo, K. Domanski, J.-P. Correa-Baena, M.K. Nazeeruddin, S.M. Zakeeruddin, et al., "Cesium-containing triple cation perovskite solar cells: improved stability, reproducibility and high efficiency," *Energy & environmental science*, **9**(6), 1989-1997 (2016). <https://doi.org/10.1039/C5EE03874J>
- [25] P. Roy, and A. Khare, "Analysis of an efficient and eco-friendly CsGeSnI<sub>3</sub> based perovskite solar cell: A theoretical study," *Materials Today: Proceedings*, **44**, 2997-3000 (2021). <https://doi.org/10.1016/j.matpr.2021.02.253>
- [26] T. Kamiya, K. Nomura, and H. Hosono, "Present status of amorphous In-Ga-Zn-O thin-film transistors," *Science and Technology of Advanced Materials*, (2010). <https://doi.org/10.1088/1468-6996/11/4/044305>
- [27] H. Hosono, J. Kim, Y. Toda, and S. Watanabe, "Transparent amorphous oxide semiconductors for organic electronics: Application to inverted OLEDs," *Proceedings of the National Academy of Sciences*, **114**(2), 233-238 (2017). <https://doi.org/10.1073/pnas.1617186114>
- [28] T. Minami, Y. Nishi, T. Miyata, and J.-I. Nomoto, "High-efficiency oxide solar cells with ZnO/Cu<sub>2</sub>O heterojunction fabricated on thermally oxidized Cu<sub>2</sub>O sheets," *Applied physics express*, **4**(6), 062301 (2011). <https://doi.org/10.1143/APEX.4.062301>

- [29] N.K. Singh, and A. Agarwal, "Performance assessment of sustainable highly efficient CsSn<sub>0.5</sub>Ge<sub>0.5</sub>I<sub>3</sub>/FASnI<sub>3</sub> based Perovskite Solar Cell: A numerical modelling approach," *Optical Materials*, **139**, 113822 (2023). <https://doi.org/10.1016/j.optmat.2023.113822>
- [30] S. Bhatt, R. Shukla, C. Pathak, and S. K. Pandey, "Evaluation of performance constraints and structural optimization of a core-shell ZnO nanorod based eco-friendly perovskite solar cell," *Solar Energy*, **215**, 473-481 (2021). <https://doi.org/10.1016/j.solener.2020.12.069>
- [31] Raghvendra, R.R. Kumar, and S.K. Pandey, "Performance evaluation and material parameter perspective of eco-friendly highly efficient CsSnGeI<sub>3</sub> perovskite solar cell," *Superlattices and Microstructures*, **135**, 106273 (2019). <https://doi.org/10.1016/j.spmi.2019.106273>
- [32] M. Burgelman, P. Nollet, and S. Degraeve, "Modelling polycrystalline semiconductor solar cells," *Thin Solid Films*, **361-362**, 527-532 (2000). [https://doi.org/10.1016/S0040-6090\(99\)00825-1](https://doi.org/10.1016/S0040-6090(99)00825-1)
- [33] N.K. Singh, A. Agarwal, T. Kanumuri, and T. Varshney, "A Study of an Inorganic-Organic HTM on the Implementation of Lead based PSC Device," in: *2020 IEEE Students Conference on Engineering & Systems (SCES)*, (IEEE, 2020). pp. 1-6. <https://doi.org/10.1109/SCES50439.2020.9236734>
- [34] N. Nikfar, and N. Memarian, "Theoretical study on the effect of electron transport layer parameters on the functionality of double-cation perovskite solar cells," *Optik*, **258**, 168932 (2022). <https://doi.org/10.1016/j.ijleo.2022.168932>
- [35] Y.T. Li, C.F. Han, and J.F. Lin, "Characterization of the electrical and optical properties for a-IGZO/Ag/a-IGZO triple-layer thin films with different thickness depositions on a curved glass substrate," *Optical Materials Express*, **9**(8), 3414-3431 (2019). <https://doi.org/10.1364/OME.9.003414>
- [36] V.K. Jayaraman, A.M. Álvarez, and M. de la luz O. Amador, "Effect of substrate temperature on structural, morphological, optical and electrical properties of IGZO thin films," *Physica E: Low-dimensional Systems and Nanostructures*, **86**, 164-167 (2017). <https://doi.org/10.1016/j.physe.2016.10.029>
- [37] S. Bouazizi, W. Tlili, A. Bouich, B.M. Soucase, and A. Omri, "Design and efficiency enhancement of FTO/PC60BM/CsSn<sub>0.5</sub>Ge<sub>0.5</sub>I<sub>3</sub>/Spiro-OMeTAD/Au perovskite solar cell utilizing SCAPS-1D Simulator," *Materials Research Express*, **9**(9), 096402 (2022). <https://doi.org/10.1088/2053-1591/ac8d52>
- [38] F. Azri, A. Meftah, N. Sengouga, and A. Meftah, "Electron and hole transport layers optimization by numerical simulation of a perovskite solar cell," *Solar energy*, **181**, 372-378 (2019). <https://doi.org/10.1016/j.solener.2019.02.017>
- [39] M. Jamil, A. Ali, K. Mahmood, M.I. Arshad, S. Tahir, M.A. Nabi, S. Ikram, N. Amin, and S. Hussain, "Numerical simulation of perovskite/Cu<sub>2</sub>Zn (Sn<sub>1-x</sub>Ge<sub>x</sub>)S<sub>4</sub> interface to enhance the efficiency by valence band offset engineering," *Journal of Alloys and Compounds*, **821**, 153221 (2020). <https://doi.org/10.1016/j.jallcom.2019.153221>

#### ПРОЕКТУВАННЯ ТА МОДЕЛЮВАННЯ ПЕРОВСКІТНОГО СОНЯЧНОГО ЕЛЕМЕНТА З ПОТРІЙНИМ ПОГЛИНАЮЧИМ ШАРОМ ДЛЯ ВИСОКОЇ ЕФЕКТИВНОСТІ ПЕРЕТВОРЕННЯ

Мохамед Меддах<sup>а</sup>, Окба Сайдані<sup>а</sup>, Зітуні Мессаї<sup>а</sup>, Рафік Зуахе<sup>б</sup>

Мохамед Меддах<sup>а</sup>, Юнес Белгумрі<sup>а</sup>

<sup>а</sup> *Лабораторія ЕТА, кафедра електроніки, технологічний факультет, Університет Мохамеда Ель Бачіра Ель Ібрагімі Бордж Бу Аррерідж-34030, Алжир*

<sup>б</sup> *Кафедра електроніки, технологічний факультет, Університет Мсіла, 28000, Алжир*

У цьому документі представлено комплексне моделювання впливу конфігурації потрійного поглинаючого шару в сонячному елементі на основі перовскіту з використанням програмного забезпечення SCAPS-1D під освітленням AM1.5. Змодельована структура містить шар поглиначача із цезію, олова та трійодиду германію (CsSn<sub>0.5</sub>Ge<sub>0.5</sub>I<sub>3</sub>), розміщеного між шарами оксиду індію, галію, цинку (IGZO) та Cu<sub>2</sub>O. Основною метою цього дослідження є підвищення ефективності перетворення електроенергії (PCE) шляхом оптимізації товщини кожного шару. Щоб перевірити наші результати моделювання, ми порівнюємо їх з експериментальними даними, отриманими з існуючої літератури, і спостерігаємо задовільну згоду між ними. Наші висновки показують, що максимального PCE 28% можна досягти, використовуючи конкретні значення товщини для кожного шару. Зокрема, визначено оптимальну товщину 20 нм для шару IGZO, 200 нм для шару Cu<sub>2</sub>O та 700 нм для шару перовскіту. Ці оптимізовані значення товщини призводять до значного покращення PCE сонячної батареї, досягаючи 29%. Це досягнення підкреслює ефективність запропонованої нами конфігурації потрійного поглинаючого шару та демонструє її потенціал для підвищення загальної продуктивності сонячної батареї на основі перовскіту. Загалом це дослідження дає цінну інформацію щодо оптимізації конфігурації шару поглиначача в перовскітних сонячних елементах, що призводить до підвищення ефективності перетворення електроенергії.

**Ключові слова:** перовскітний сонячний елемент; CsSn<sub>0.5</sub>Ge<sub>0.5</sub>I<sub>3</sub>; ефективність перетворення потужності; SCAPS-1D

## INVESTIGATIONS OF NONLINEAR OPTICAL PROPERTIES OF LITHIUM NIOBATE CRYSTALS

 Sharifa B. Utamuradova,  Zakirjan T. Azamatov,  Murodjon A. Yuldoshev\*,  
Nurlan N. Bazarbayev,  Abror B. Bakhromov

*Institute of Semiconductor Physics and Microelectronics, National University of Uzbekistan,  
20 Yangi Almazor st., Tashkent, 100057, Uzbekistan*

\*Corresponding Author e-mail: [murod.yuldoshev1993@gmail.com](mailto:murod.yuldoshev1993@gmail.com)

Received August 2, 2023; revised September 10, 2023; accepted September 14, 2023

The article is devoted to nonlinear effects in lithium niobate crystals. The possibility of using digital holographic interferograms obtained with the help of laser radiation of different duration at different moments of time for the reconstruction of dynamic phase changes is shown. Holograms were recorded on lithium niobate crystals doped with iron ions in various concentrations using He-Ne and He-Cd lasers, and the diffraction efficiency was calculated. Also, the effect of gamma radiation on the optical properties of LiNbO<sub>3</sub> and LiNbO<sub>3</sub>:Fe crystals was studied. At the same time, it was determined that the band gap of the samples decreases, as a result of which the refractive index, absorption coefficient and photorefractive sensitivity increase several times.

**Keywords:** *Ferroelectric crystals; Digital holographic interferometry; Diffraction efficiency; Photorefractive sensitivity*

**PACS:** 42.40.Eq, 42.40.Lx, 42.70.Mp

### INTRODUCTION

Among promising recording materials for creating holographic systems for optical information processing, a special place is occupied by ferroelectric crystals, for example, LiNbO<sub>3</sub> doped with iron ions in various concentrations [1–3]. Recording information in LiNbO<sub>3</sub>:Fe crystals is possible due to the photorefractive effect, which is interpreted mainly by the impurity photovoltaic mechanism, the change in the refractive index responsible for recording dynamic gratings that repeat the light grating, due to which the space charge grating is formed [4,5]. One of the promising directions for the practical use of doped photorefractive crystals is their use as optical memory elements based on local holographic gratings recorded by a laser, which can be repeatedly rewritten and stored.

If ordinary holography is a method of recording the wave front of an electromagnetic wave in an industrial form (on a photographic plate, thermoplastic, photorefractive material), then digital holography is a method of recording a wave front in digital form, followed by its restoration, storage, and transformation using computer programs.

Pure ferroelectric crystals are not highly sensitive to optical radiation. However, doping with transition metals, in particular iron ions, significantly increases their photosensitivity. The effect of doping on the sensitivity of LiNbO<sub>3</sub> crystals is described in detail in [6-8]. The use of transition metals as dopants is associated with their ability to reversibly donate electrons to the conduction band under the action of light [9–11]. An increase in the diffraction efficiency during the recording of holograms in a pure LiNbO<sub>3</sub> crystal and in crystals with various additives was shown in [6]. It can be said that there is a correlation between the absorption spectra and the recording sensitivity of crystals with various additives.

The sensitivity to an optically induced refractive index change can be expressed in terms of material parameters as follows.

$$\frac{dn_e}{dJ} = el \left( \frac{n_e^3}{2} \cdot \frac{r_{33}}{\epsilon_0 \epsilon_{33}} \right) \frac{\alpha\beta}{\hbar\omega}, \quad (1)$$

where  $dn_e/dJ$  is the energy sensitivity,  $el$  is the change in the electric dipole moment, the mechanism of which is different for different materials and experimental conditions.

For the most common case, the drift of photoexcited electrons in an internal or external electric field, the drift electron path length is  $l = \mu\tau E_0$ . The expression in brackets is due to the electro-optical effect. The expression  $\alpha\beta/\hbar\omega$  gives the number of excited centers or the number of photoelectrons in the conduction band. Alloying with transition metals, violation of stoichiometry, annealing in a reducing atmosphere, irradiation with  $\gamma$ -rays, application of an electric field makes it possible to significantly increase their photosensitivity. In addition, lithium niobate crystals make it possible to obtain new types of heterostructures due to their unique electro-optical properties [12].

The systematic study of radiation effects in lithium niobate began, in practice, from the moment the specific properties of photorefractive crystals were discovered. Especially, they appear in crystals doped with transition metals.

Doping with LiNbO<sub>3</sub> leads to a variety of radiation-induced effects, which include both bulk effects and effects arising during the formation of the component structure [13]. These effects can be used in lithium niobate-based thin-film optical devices as well as bulk acousto-optic modulators, which illustrate widely varying responses caused by radiation. The radiation sensitivity of LiNbO<sub>3</sub> has been determined both in pure and doped states. Depending on the field of application, LiNbO<sub>3</sub> can play the role of a sensitive radiation sensor or a radiation-resistant material used under radiation conditions [14].

### EXPERIMENTAL PART

In 2-exposure digital holographic interferometry, 2 wave fronts reconstructed from 2 digital holograms G1 and G2 are compared. G1 is a hologram of an unperturbed object and G2 is a hologram of an object with induced optical inhomogeneities. As a result of the addition of wave fronts, an interferogram is obtained, the position and curvature of the fringes of which makes it possible to control the phase changes of the object under study. Fig. 1. below shows the experimental scheme. Holograms were recorded digitally with a Nikon E885 digital camera. The lens was removed from the camera and the recording took place directly on the area of the CCD matrix with the number of pixels 1000×1000. The size of one pixel is 9×9 microns. The electronic shutter of the camera provided a minimum shutter speed of 1/12000 sec and was synchronized with the operation of the laser. The studies were carried out in the radiation of a ruby laser with Q-switching, pulse duration 60 ns, radiation energy per pulse 0.5 mJ.

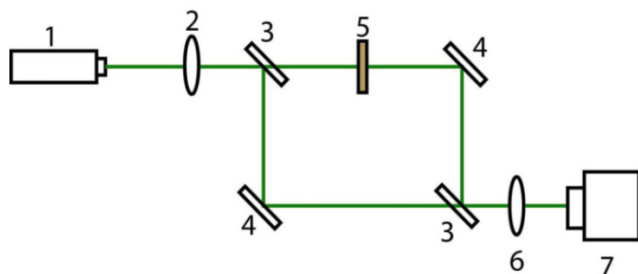


**Figure 1.** Optical scheme of the study. 1 - laser photograph input, 2 – focusing lens, 3 - beam splitter, 4 – mirror, 5 – sample, 6 - output lens, 7 – digital camera

Also, in experiments on the study of holographic recording in a LiNbO<sub>3</sub>:Fe crystal, the scheme presented in [15,16] was used.

Information was recorded using helium-cadmium (He-Cd,  $\lambda = 440$  nm) and helium-neon (He-Ne,  $\lambda = 630$  nm) lasers. The optical sensitivity of the crystal for a wavelength of  $\lambda = 440$  nm is very high. Reading information was carried out using a low-intensity helium-neon laser. The optical sensitivity of the crystal for a wavelength of  $\lambda = 630$  nm is very low, so the hologram does not disappear when information is read. As a result of the superposition of two plane waves in a crystal, an interference pattern appears in the form of light and dark lines. The  $\gamma$ -radiation power was  $\sim 106$  R/s. The crystals were irradiated using a <sup>60</sup>Co facility (Institute of Nuclear Physics, Academy of Sciences of the Republic of Uzbekistan). The absorption spectra were studied using a Shimadzu UV 3600 spectrometer. The surface morphology and elemental composition of the samples were studied using an EVO MA10 SEM (Carl Zeiss).

### RESULTS AND DISCUSSION

The structure of a pure lithium niobate crystal is formed by O<sub>6</sub> oxygen octahedral, which are connected to each other in such a way that they have common edges and sides [17]. On Fig. 2 shows an image of a pure lithium niobate crystal obtained using a scanning electron microscope and the results of elemental analysis.

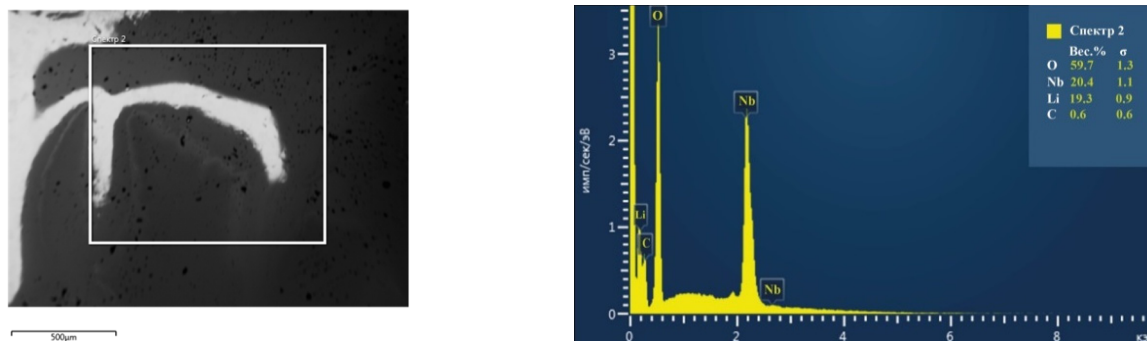


**Figure 2.** SEM image of a pure lithium niobate crystal and elemental analysis results

Elemental analysis results show that the amount of oxygen in the crystal is almost three times higher than that of niobium and lithium. This is fully consistent with the above opinion.

Plates made of a photorefractive crystal LiNbO<sub>3</sub>:Fe (0.01%) were used as objects of photography. Based on the recorded multicolor holograms, digital two-exposure interferometry methods were used to obtain digital interferograms of various stages of relaxation of the phase inhomogeneity recorded in the volume of a photorefractive LiNbO<sub>3</sub>:Fe

crystal. Based on the obtained interferograms, phase fronts were reconstructed, carrying quantitative information about changes in the samples under study.

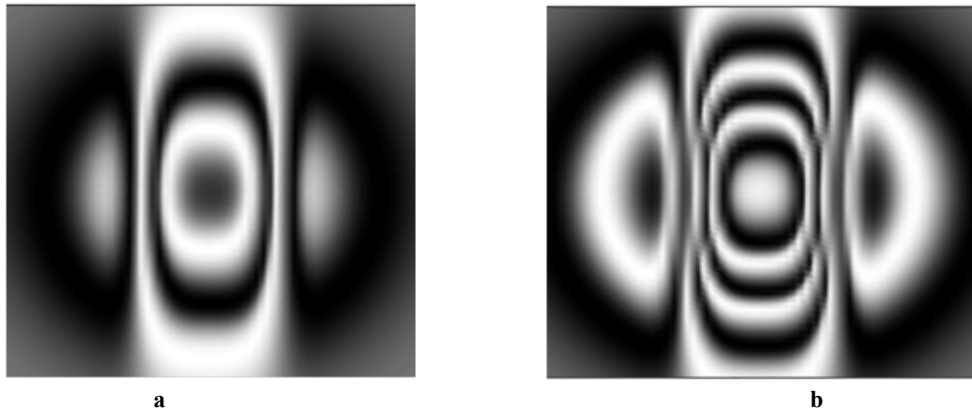


**Figure 3.** Changes in interference patterns at different exposures on photorefractive ones in  $\text{LiNbO}_3:\text{Fe}$  crystals

Phase inhomogeneity arising under the action of laser radiation in a photorefractive crystal is determined by the intensity of laser radiation  $I(t)$ , exposure time  $\tau$ , photorefractive sensitivity of the material  $K$  and absorption coefficient  $\alpha$ . Fig. 3 shows images of phase inhomogeneity in a photorefractive  $\text{LiNbO}_3:\text{Fe}$  crystal at different exposure times, corresponding to interference patterns in digital format, while the spatial distribution of laser radiation intensity is assumed to be Gaussian. The exposure time of the image shown in Fig. 3b, 3 times longer than the exposure time of the image shown in Fig. 3a. It can be seen that with increasing exposure time, the image of the phase inhomogeneity becomes more complicated, which manifests itself in the form of an increase in the number of interference fringes.

The algorithm for reconstructing digital interferograms from recorded holograms was as follows. If  $I(x,y)$  the intensity distribution in the hologram recording plane  $(x,y)$  is determined by the square of the modulus of the sum of the complex amplitudes of the object  $O(x,y)$  and reference  $R(x,y)$  waves, namely:

$$I(x,y) = |R(x,y)|^2 + |O(x,y)|^2 + R(x,y)O^*(x,y) + R^*(x,y)O(x,y) \quad (2)$$

Then the last two terms of equation (2) contain information corresponding to the amplitude and phase of the object wave. This information can be extracted using the Fourier transform method. After the transformation, we obtain the Fourier spectrum of the hologram with four localized spectra of spatial frequencies, which correspond to the terms of equation (2). The first two terms in (2) form the zeroth order of the spectrum, which is localized at the center of the two-dimensional Fourier plane. The third and fourth terms of Equation (2) form two conjugate spectra localized symmetrically with respect to the center. If one of the regions of the localized spectrum is selected (filtered) and then the inverse Fourier transform is applied, then the phase front of the object wave will be restored. In accordance with this algorithm, the hologram  $G1$  (of the unperturbed object) is taken in the first laser pulse, then the hologram  $G2$  (of the perturbed object) is taken in the next pulse, and an interferogram is constructed. Next, a phase unfolding algorithm similar to [16] is used, and the surface of the perturbed phase is reconstructed from the interferogram. Fig. 4a shows the obtained interferogram, and in Fig. 4b is a three-dimensional picture of the phase inhomogeneity recorded in the  $\text{LiNbO}_3:\text{Fe}$  (0.01%) crystal after 10 laser flashes. In this case, the crystal was at a distance of 2 cm from the focus of lens 2. The recorded inhomogeneity was gradually erased, and this relaxation process can be repeated.

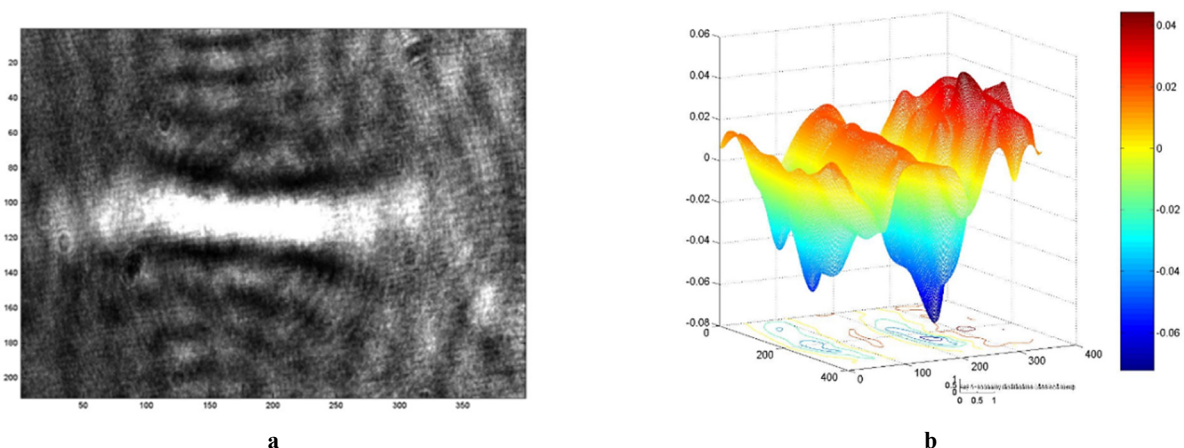


**Figure 4.** Interferogram and phase reconstruction of a photorefractive structure

Due to the presence of nonlinear effects in the lithium niobate crystal, this crystal can be used as a memory element. One of the requirements for a memory element is diffraction efficiency and photorefraction. The diffraction efficiency is experimentally defined as the ratio of the intensity of the diffracted readout beam to the intensity of the beam that has passed through the crystal when the hologram is not recorded in the crystal.

It is known that the use of transition metals as dopants is associated with their ability to reversibly donate d-electrons to the conduction band under the action of radiation. When a crystal is doped with  $Fe^{3+}$  ions, the absorption of light in it is caused by ionization. The light sensitivity of crystals doped with iron is determined by the concentration of  $Fe^{2+}$  ions. Upon photoexcitation,  $Fe^{2+}$  donates a photoelectron to the conduction band, which is captured by the  $Fe^{3+}$  ion in the unilluminated region during diffusion. Consequently, as the concentration of  $Fe^{2+}$  increases, the absorption at the wavelength  $\lambda$ , at which information is recorded, increases, which increases the sensitivity of the crystal to light.

Fig. 5 and Fig. 6 show experimental studies of the dependence of the influence of various concentrations of iron ions in  $LiNbO_3$  on the diffraction efficiency of holograms -  $\eta$ , recorded by a helium-neon laser -  $\lambda = 630$  nm and a helium-cadmium laser -  $\lambda = 440$  nm in the form of a plane wave front (sample 1 - 0.003 wt.% Fe, sample 2 - 0.005 wt.% Fe). Erasing was carried out with a helium-cadmium laser ( $\lambda = 440$  nm), since lithium niobate crystals doped with iron ions have high absorption in the blue frequency range. With an increase in the concentration of iron ions, as shown in Fig. 5 and Fig. 6, the photosensitivity of the crystal increases significantly.

As can be seen from Fig. 6, the photosensitivity in sample 2 is 7 times greater than in sample 1, and almost 2 times greater than in sample 1 when recording information at  $\lambda = 630$  nm, Fig. 5. For a wave with a wavelength of  $\lambda = 630$  nm obtained DE  $\eta = 31\%$ , and for the wavelength  $\lambda = 440$  nm -  $\eta = 34\%$ .

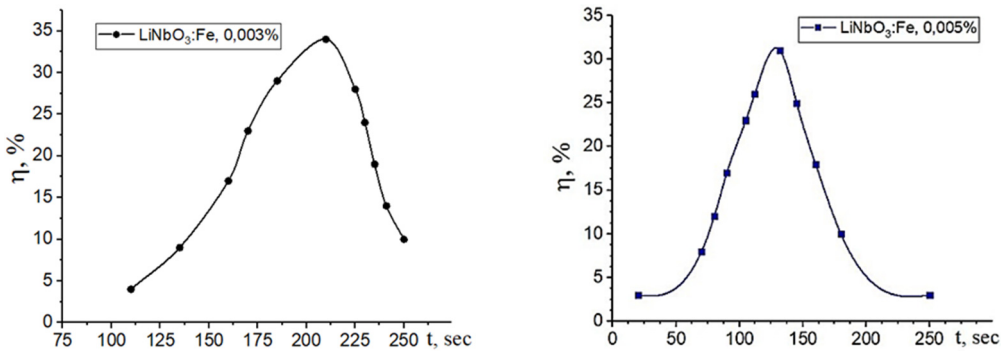


Figure 5. Experimental dependences of the diffraction efficiency of holograms on exposure:  $\lambda = 630$  nm (He-Ne)

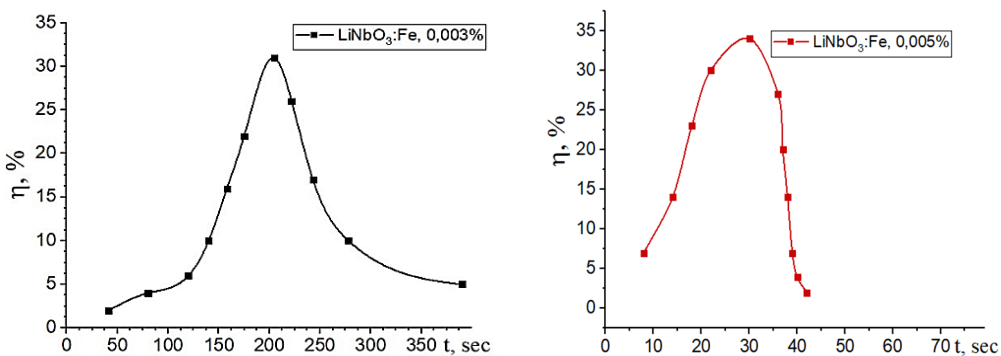


Figure 6. Experimental dependences of the diffraction efficiency of holograms on exposure:  $\lambda = 440$  nm (He-Cd)

In addition, when comparing the results obtained with He-Ne and He-Cd lasers, the photosensitivity for the first sample  $LiNbO_3:Fe$  0.003 wt.% practically does not change. But with an increase in the concentration of iron ions in lithium niobate to 0.005 wt.%, the light sensitivity of the crystal increases by almost 3 times, which leads to a decrease in the erasure time by almost 5 times.

The formed spatial interference pattern modulates the refractive index of the crystal, as a result of which a phase diffraction grating appears. Modulation of the refractive index is caused by the space charge field, through the electro-optical effect [1]. The appearance of a spatially inhomogeneous charge is associated with the redistribution of photoexcited carriers between impurity centers with a long capture time. Such a redistribution can be caused by the photovoltaic effect [5] and diffusion of carriers from the illuminated region of the crystal to the unilluminated one [6].

Next, we investigated the effect of laser and radiation, especially  $\gamma$ -radiation, on the photorefractive properties of  $LiNbO_3$  and  $LiNbO_3:Fe$  0.03 wt.% crystals. To study the effect of radiation, the samples were irradiated with  $\gamma$ -radiation with a dose in the range of  $10^3 - 10^8$  R. However, for  $LiNbO_3$  and  $LiNbO_3:Fe$  crystals at doses of  $10^3$  and  $10^8$  R, no spectral

changes were observed, but with an increase in the irradiation dose, the optical absorption edge shifted towards long waves. The band gap and absorption coefficients of the samples were calculated from the absorption spectra. The calculations showed that the band gap for the LiNbO<sub>3</sub> crystal was within 3.25–3.39 eV, and for the LiNbO<sub>3</sub>:Fe crystal it was 3.04–3.17 eV. The absorption coefficients were  $0.32 \div 2.06 \text{ mm}^{-1}$  for the LiNbO<sub>3</sub> crystal, and for the LiNbO<sub>3</sub>:Fe crystal they were  $2.03 \div 6.68 \text{ mm}^{-1}$ . Another important parameter is the change in the refractive indices, which were: 2.297–2.3182 for the LiNbO<sub>3</sub> crystal and 2.3285–2.3561 for the LiNbO<sub>3</sub>:Fe crystal. Calculations of the photorefractive sensitivity of materials - K show an increase of 9 times for the LiNbO<sub>3</sub> crystal and almost 2 times for the LiNbO<sub>3</sub>:Fe crystal.

## CONCLUSIONS

An analysis of the results shows the promise of using two-exposure digital holographic interferometry for direct dynamic measurement of phase inhomogeneities that arise in a strong laser field, and, consequently, for measuring the nonlinear refractive index, the photorefractive index of a material. An increase in the iron impurity content leads to a reduction in the erasing time of the holograms.

It has been established that the maximum diffraction efficiency of lithium niobate crystals doped with iron ions of various concentrations is  $\eta = 31\%$  for a wavelength of  $\lambda = 630 \text{ nm}$  and  $\eta = 34\%$  for a wavelength of  $\lambda = 440 \text{ nm}$ , and the photosensitivity increased by 3–7 once.

It was also found that the photorefractive sensitivity of the LiNbO<sub>3</sub> and LiNbO<sub>3</sub>:Fe samples depends on the concentration of the introduced impurity and the irradiation dose, and the photorefractive sensitivity of the crystals increases by a factor of 9, and the band gap varies from 3.04 to 3.39 eV in the dose range  $\gamma$ -irradiation  $10^4 \div 10^7 \text{ R}$ .

## ORCID

✉ Sharifa B. Utamuradova, <https://orcid.org/0000-0002-1718-1122>; ✉ Zakirjan T. Azamatov, <https://orcid.org/0000-0001-7074-9437>  
 ✉ Murodjon A. Yuldoshev, <https://orcid.org/0000-0002-9722-9439>; ✉ Abror B. Bakhromov, <https://orcid.org/0000-0001-8148-2467>

## REFERENCES

- [1] V.A. Barachevsky, "The current status of the development of light-sensitive media for holography (a review)," *Opt. Spectrosc.* **124**, 373–407 (2018). <http://dx.doi.org/10.1134/S0030400X18030062>
- [2] L. Dai, L. Wang, C. Liu, X. Han, Z. Yan, and Y. Xu, "OH absorption and holographic storage properties of Sc(0,1,2,3):Ru:Fe:LiNbO<sub>3</sub> crystals," *RSC Adv.* **8**, 5145–5150 (2018). <https://doi.org/10.1039/c7ra12606a>
- [3] L. Dai, C. Tan, L. Wang, X. Han, C. Liu, and Y. Xu, "Investigation on nonvolatile holographic storage properties in Hf:Ru:Fe:LiNbO<sub>3</sub> crystals as a function of Li composition," *Journal of Alloys and Compounds*, **753**, 407 (2018). <https://doi.org/10.1016/j.jallcom.2018.04.201>
- [4] M.H. Yükselci, D. Bulut, B.C. Ömür, A.A. Bozkurt, and C. Allahverdi, "Optical properties of iron-doped lithium niobate crystal depending on iron content and temperature," *Phys. Status Solidi B*, **251**, 1265–1269 (2014). <http://dx.doi.org/10.1002/pssb.201451071>
- [5] A.V. Syuy, N.V. Sidorov, M.N. Palatnikov, N.A. Teplyakova, D.S. Shtarev, and N.N. Prokopiv, "Optical properties of lithium niobate crystals," *Optik*, **156**, 239 (2018). <https://doi.org/10.1016/j.ijleo.2017.10.136>
- [6] N.V. Sidorov, L. A. Bobreva, N. Teplyakova, and G.M. Palatnikov, "Defect Complexes and Optical Properties of Doubly Doped Lithium Niobate Crystals," *Inorganic Materials*, **54**(10), 1009–1012 (2018). <http://dx.doi.org/10.1134/S0020168518100151>
- [7] E.M. de Miguel Sanz, M. Carrascosa, and L. Arizmendi. "Effect of the oxidation state and hydrogen concentration on the lifetime of thermally fixed holograms in LiNbO<sub>3</sub>:Fe," *Physical Review B* **65**(16). (2002). <http://dx.doi.org/10.1103/PhysRevB.65.165101>
- [8] Y.-Y. Li, H.-L. Chen, G.J. Chen, and W.-S. Hwang. "Investigation of the Defect Structure of Congruent and Fe-Doped LiNbO<sub>3</sub> Powders Synthesized by the Combustion Method," *Materials* **10**(4):380. (2017). <http://dx.doi.org/10.3390/ma10040380>
- [9] R. Inoue, S. Takahashi, Y. Kitanaka, and T. Oguchi, "Enhanced photovoltaic currents in strained Fe-doped LiNbO<sub>3</sub> films," *Physica Status Solidi (A) Applications and Materials*, **212**(12), (2015). <http://dx.doi.org/10.1002/pssa.201532398>
- [10] Y. Noguchi, R. Inoue, and M. Miyayama, "Electronic Origin of Defect States in Fe-Doped LiNbO<sub>3</sub> Ferroelectrics," *Advances in Condensed Matter Physics*, **2016**(4), 1–10. (2016). <http://dx.doi.org/10.1155/2016/2943173>
- [11] A.S. Pritulenko, A.V. Yatsenko, and S.V. Yevdokimov, "Analysis of the nature of electrical conductivity in nominally undoped LiNbO<sub>3</sub> crystals," *Crystallogr. Rep.* **60**, 267–272 (2015). <https://doi.org/10.1134/S1063774515020224>
- [12] Z.T. Azamatov, Sh.B. Utamuradova, M.A. Yuldoshev, and N.N. Bazarbaev. "Some properties of semiconductor-ferroelectric structures," *East Eur. J. Phys.* **2**, 187–190. (2023). <https://doi.org/10.26565/2312-4334-2023-2-19>
- [13] Y.-Y. Li, H.-L. Chen, G.-J. Chen, C.-L. Kuo, P.-H. Hsieh, and W.-S. Hwang, "Investigation of the defect structure of congruent and Fe-doped LiNbO<sub>3</sub> powders synthesized by the combustion method," *Materials*. **10**(4), 380 (2017). <https://doi.org/10.3390/ma10040380>
- [14] T. Volk, M. Wohlecke, *Lithium niobate, in: Defects, Photorefractive and Ferroelectric Switching.* (Springer, Berlin, 2008).
- [15] Z.T. Azamatov, M.A. Yuldoshev, and N.N. Bazarbaev, "Effect of gamma irradiation on optical properties of lithium niobate and LiNbO<sub>3</sub>:Fe crystals," *Izvestiya vuzov. Physics*, **2**, 106–113 (2023). <https://doi.org/10.17223/00213411/66/2/106>
- [16] R.A. Muminov, Z.T. Azamatov, N.A. Akbarova, V.I. Redkorechev, O.F. Tukfatullin, and I.A. Khusainov. "Effect of holographic coatings on the efficiency of silicon photoconverters," *Applied Solar Energy (English translation of Geliotekhnika)* **50**(3), 156–157 (2014). <https://doi.org/10.3103/S0003701X14030104>
- [17] A.A. Khruk, PhD. Thesis, I.V. Tananaev Institute of Chemistry and Technology of Rare Elements and Mineral Raw Materials, Kola Science Center RAS, 2015. (in Russian)



**ДОСЛІДЖЕННЯ НЕЛІНІЙНО-ОПТИЧНИХ ВЛАСТИВОСТЕЙ КРИСТАЛІВ НІОБАТУ ЛІТІЮ**

**Шаріфа Б. Утамурадова, Закірджан Т. Азаматов, Мураджон А. Юлдошев,**

**Нурлан Н. Базарбаєв, Аброр Б. Бахромов**

*Інститут фізики напівпровідників та мікроелектроніки Національного університету Узбекистану,  
Ташкент, Узбекистан*

Стаття присвячена нелінійним ефектам у кристалах ніобату літію. Показано можливість використання цифрових голографічних інтерферограм, отриманих за допомогою лазерного випромінювання різної тривалості в різні моменти часу, для реконструкції динамічних фазових змін. За допомогою He-Ne і He-Cd лазерів на кристалах ніобату літію, легованих іонами заліза в різних концентраціях, записували голограми та розраховували дифракційну ефективність. Також досліджено вплив гамма-випромінювання на оптичні властивості кристалів  $\text{LiNbO}_3$  та  $\text{LiNbO}_3:\text{Fe}$ . При цьому встановлено, що ширина забороненої зони зразків зменшується, внаслідок чого показник заломлення, коефіцієнт поглинання та фоторефрактивна чутливість зростають у кілька разів.

**Ключові слова:** сегнетоелектричні кристали; цифрова голографічна інтерферометрія; ефективність дифракції; фоторефрактивна чутливість

## CALCULATION OF THE DENSITY OF THE DISTRIBUTION OF ELECTRONIC STATES IN THE CONDUCTION BAND FROM THE FUNDAMENTAL ABSORPTION SPECTRA OF AMORPHOUS SEMICONDUCTORS

✉ **Rustamjon G. Ikramov**, ✉ **Khurshidbek A. Muminov\***, **Mashkhura A. Nuritdinova**,  
✉ **Bobur Q. Sultonov**, **Oybek T. Kholmirezayev**

*Namangan Engineering and Technology Institute, 7 Kosonsoy Street, Namangan 160115, Uzbekistan*

*\*Corresponding Author e-mail: [muminov\\_19912406@mail.ru](mailto:muminov_19912406@mail.ru)*

Received May 10, 2023; revised September 20, 2023; accepted September 23, 2023

The region of fundamental absorption in the optical spectra of amorphous semiconductors is theoretically studied using the Davis-Mott approximation according to the Kubo-Greenwood formula. As is known, three types of optical transitions of the electron can be observed in the fundamental absorption region; from the tail of the valence band to the conduction band, from the valence band to the conduction band and from the valence band to the tail of the conduction band. For all these electronic transitions, analytical expressions of the partial absorption spectra are obtained from two different types of the Kubo-Greenwood formula. The width of the optical mobility gap and the proportionality coefficient were determined in the analytical form of the interband absorption spectrum by fitting them to the experimental interband absorption spectrum. A new method is presented for calculating the density of distribution of electronic states in the conduction band of amorphous carbon based on the experimental interband absorption spectrum and the analytical expression of the Kubo-Greenwood formula written for the interband absorption spectrum.

**Keywords:** *Amorphous semiconductors; Optical absorption spectra; Davis-Mott approximation method; Kubo-Greenwood formula; Fundamental absorption spectrum; Partial absorption spectra; Interband absorption spectrum; Electronic state density distribution*

**PACS:** 61.43Dq, 68.43 Mn

### INTRODUCTION

The optical absorption coefficient of amorphous semiconductors is usually determined by the Kubo-Greenwood formula using the Davis-Mott approximation [1, 2]:

$$\alpha(\hbar\omega) = A \int g_V(\varepsilon) g_C(\varepsilon + \hbar\omega) \frac{d\varepsilon}{\hbar\omega} \quad (1)$$

or

$$\alpha(\hbar\omega) = A \int g_V(\varepsilon - \hbar\omega) g_C(\varepsilon) \frac{d\varepsilon}{\hbar\omega} \quad (2)$$

where  $A$  - is the coefficient of proportionality, independent of the energy ( $\hbar\omega$ ) of absorbed photons,  $g_V(\varepsilon)$ ,  $g_V(\varepsilon - \hbar\omega)$  and  $g_C(\varepsilon + \hbar\omega)$ ,  $g_C(\varepsilon)$  are the densities of the initial and final electronic states during optical transitions in valence band and conduction band, respectively.

It can be seen from Formulas (1), (2) that the values of the absorption coefficient strongly depend on the distribution of the density of electronic states involved in optical transitions. Formula (1) is used when the initial electronic states involved in optical transitions play the main role. Therefore, in [3], using Formula (1), the distributions of the density of electronic states in the valence band were determined. And then the main role is played, the final electronic state uses the Formula (2). From this it follows that, it is possible to analytically investigate the distribution of the density of electronic states of the valence band and the conduction band separately. Therefore, this paper proposes a new method for determining the distribution of the density of electronic states in the conduction band from the Kubo-Greenwood formula (2). Since the integrals in Formula (1) and (2) are indefinite, they give a general solution. It was shown in [4] that in order to obtain own solutions of the spectra of the optical absorption coefficient from the Kubo-Greenwood Formula, the indefinite integral in this formula must be written in a certain form, and then formula (1) takes the form:

$$\alpha(\hbar\omega) = A \int_{\varepsilon_0 - \hbar\omega}^{\varepsilon_0} g_V(\varepsilon) g_C(\varepsilon + \hbar\omega) \frac{d\varepsilon}{\hbar\omega} \quad (3)$$

where  $\varepsilon_0$  is the energy position of the intersection point of the exponentially decaying “tails” of allowed bands.

It is known that the energy of absorbed photons in the fundamental region is greater than the energy width ( $E_g < \hbar\omega$ ) of the mobility gap of amorphous semiconductors. It was shown in [5] that in amorphous semiconductors, upon absorption of photons with energies  $E > E_g$ , optical transitions of electrons from the “tail” of the valence band to

the conduction band, from the valence band to the conduction band, and from the valence band to the “tail” of the conduction band are simultaneously observed. Therefore, by adapting Formula (3) to the above optical transitions, we obtain:

$$\alpha(\hbar\omega) = A \int_{\varepsilon_0 - \hbar\omega}^{\varepsilon_0} g_V(\varepsilon) g_C(\varepsilon + \hbar\omega) \frac{d\varepsilon}{\hbar\omega} = A \left( \int_{\varepsilon_V}^{\varepsilon_0} g_V(\varepsilon) g_C(\varepsilon + \hbar\omega) \frac{d\varepsilon}{\hbar\omega} + \int_{\varepsilon_C - \hbar\omega}^{\varepsilon_V} g_V(\varepsilon) g_C(\varepsilon + \hbar\omega) \frac{d\varepsilon}{\hbar\omega} + \int_{\varepsilon_0 - \hbar\omega}^{\varepsilon_C - \hbar\omega} g_V(\varepsilon) g_C(\varepsilon + \hbar\omega) \frac{d\varepsilon}{\hbar\omega} \right) = \alpha_1(\hbar\omega) + \alpha_2(\hbar\omega) + \alpha_3(\hbar\omega) \tag{4}$$

where  $\varepsilon_V$  is the upper boundary of the valence band;  $\varepsilon_C$  is the lower boundary of the conduction band;  $\alpha_1(\hbar\omega)$ ,  $\alpha_2(\hbar\omega)$ ,  $\alpha_3(\hbar\omega)$  are partial absorption coefficients determined by optical transitions of electrons from the “tail” of the valence band to the conduction band, from the valence band to the conduction band (interband absorption spectrum), from the valence band to “tail” of the conduction band, respectively.

To calculate the partial spectra of fundamental absorption using Formula (4), the distributions of the density of electronic states in the valence band and in its tail, as well as in the conduction band and in its tail, must be known. Usually, in a theoretical study of optical absorption spectra, the density of electronic states of amorphous semiconductors at the boundaries of allowed bands is written with linear or parabolic distributions, and at the tails of allowed bands, with exponential distributions [6,7]. In [4], for these distributions, it was proposed:

$$g_V(\varepsilon) = N(\varepsilon_V) \left( \frac{\varepsilon_C - \varepsilon}{E_g} \right)^{n_1}, \quad n_1 = 1/2, 1 \quad \text{and} \quad g_V(\varepsilon) = N(\varepsilon_V) \exp(-\beta_1(\varepsilon - \varepsilon_V)), \tag{5}$$

$$g_C(\varepsilon) = N(\varepsilon_C) \left( \frac{\varepsilon - \varepsilon_V}{E_g} \right)^{n_2}, \quad n_2 = 1/2, 1 \quad \text{and} \quad g_C(\varepsilon) = N(\varepsilon_C) \exp(\beta_2(\varepsilon - \varepsilon_C)), \tag{6}$$

where  $\beta_1$  - and  $\beta_2$  - are the parameters that determine the slopes of the exponential tails of the valence and conduction bands,  $N(\varepsilon_V)$  and  $N(\varepsilon_C)$  are the effective densities of electronic states in the valence and conduction bands.

Substituting the distribution in Formulas (5) and (6) into Formula (4), for partial absorption spectra, we obtain: for interband electronic transitions at

$$n_1 = n_2 = 1/2$$

$$\alpha_2(\hbar\omega) = \frac{B}{4\hbar\omega E_g} \left[ 2(\hbar\omega - E_g) \sqrt{E_g \hbar\omega} - (E_g - \hbar\omega)^2 \operatorname{arctg} \left( \frac{E_g - \hbar\omega}{2\sqrt{E_g \hbar\omega}} \right) \right], \tag{7}$$

for  $n_1 = n_2 = 1$

$$\alpha_2(\hbar\omega) = \frac{B}{6\hbar\omega E_g^2} (\hbar\omega - E_g)(E_g^2 + 4\hbar\omega E_g + (\hbar\omega)^2), \tag{8}$$

For  $n_1 = 1, n_2 = 1/2$  и  $n_1 = 1/2, n_2 = 1$

$$\alpha_2(\hbar\omega) = \frac{2B}{15\hbar\omega \sqrt{E_g^3}} \left[ 5(\hbar\omega + E_g) (\sqrt{(\hbar\omega)^3} - \sqrt{E_g^3}) - 3(\sqrt{(\hbar\omega)^5} - \sqrt{E_g^5}) \right], \tag{9}$$

where  $B = AN(\varepsilon_V)N(\varepsilon_C)$ .

The results of calculation by Formulas (7)–(9) are shown in Fig. 1. Calculations were carried out for amorphous hydrogenated silicon  $B = 2.5 \cdot 10^5 \text{ cm}^{-1}$  and  $E_g = 1.8 \text{ eV}$  [1].

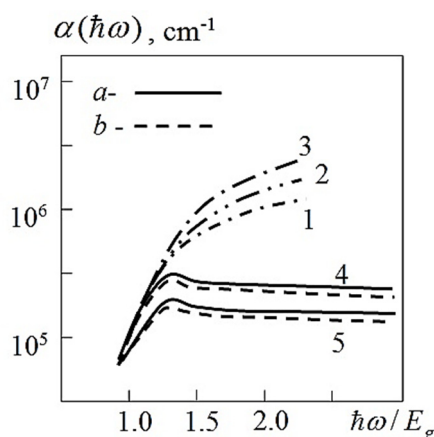


**Figure 1.** Partial spectra of fundamental absorption of amorphous semiconductors obtained by Formulas:

1 - at  $n_1 = n_2 = 1/2$  (7); 2 - at  $n_1 = n_2 = 1$  (8); 3 - at  $n_1 = 1, n_2 = 1/2$ ; or  $n_1 = 1/2, n_2 = 1$  (9) and obtained from Formulas (10) and (11) and from numerical calculations, when, 4 -  $n_1 = n_2 = 1$  and 5 - when  $n_1 = n_2 = 1/2$  electronic transitions from the tail of the valence band to the conduction band (a) and from the valence band to the “tail” of the conduction band (b).

Since at  $n_1 = n_2 = 1/2$  it is impossible to obtain an analytical expression for partial absorption spectra determined by optical transitions of electrons (from the “tail” of the valence band to the conduction band, from the valence band to the “tail” of the conduction band), they are determined using numerical calculations.

At  $n_1 = n_2 = 1/2$ , analytical expressions for partial absorption spectra determined by optical transitions of electrons from the “tail” of the valence band to the conduction band and from the valence band to the “tail” of the conduction band:

$$\alpha_1(\hbar\omega) = \frac{B \exp(-\beta_1(\varepsilon_0 - \varepsilon_V))}{E_g \hbar\omega \beta_1} \left[ \left( \frac{1}{\beta_1} + \hbar\omega \right) \exp(\beta_1(\varepsilon_0 - \varepsilon_V)) - \left( \varepsilon_0 - \varepsilon_V + \frac{1}{\beta_1} + \hbar\omega \right) \right], \quad (10)$$

$$\alpha_3(\hbar\omega) = \frac{B \exp(\beta_2(\varepsilon_0 - \varepsilon_C))}{E_g \hbar\omega \beta_2} \left[ \left( \frac{1}{\beta_2} + \hbar\omega \right) \exp(\beta_2(\varepsilon_C - \varepsilon_0)) - \left( \varepsilon_C - \varepsilon_0 + \frac{1}{\beta_2} + \hbar\omega \right) \right]. \quad (11)$$

The results of calculation by Formulas (10), (11) and by the method of approximate calculation at  $n_1 = n_2 = 1/2$  are shown in Fig. 1 (4- and 5- curve). The calculations were carried out for  $E_g = 1.8$  eV,  $\varepsilon_C - \varepsilon_0 = 0.7$  eV,  $\varepsilon_0 - \varepsilon_V = 1.1$  eV,  $\beta_1 = 16$  eV<sup>-1</sup> and  $\beta_2 = 22$  eV<sup>-1</sup>.

To calculate the absorption coefficient using the above method, taking into account (2), we write the integral in the form of a definite integral:

$$\alpha(\hbar\omega) = A \int_{\varepsilon_0}^{\varepsilon_0 + \hbar\omega} g_V(\varepsilon - \hbar\omega) g_C(\varepsilon) \frac{d\varepsilon}{\hbar\omega}. \quad (12)$$

Having adapted this Formula to the types of optical transitions of an electron, we divide it into partial absorption spectra:

$$\begin{aligned} \alpha(\hbar\omega) &= A \int_{\varepsilon_0}^{\varepsilon_0 + \hbar\omega} g_V(\varepsilon - \hbar\omega) g_C(\varepsilon) \frac{d\varepsilon}{\hbar\omega} = A \int_{\varepsilon_V + \hbar\omega}^{\varepsilon_0 + \hbar\omega} g_V(\varepsilon - \hbar\omega) g_C(\varepsilon) \frac{d\varepsilon}{\hbar\omega} + \\ &+ A \int_{\varepsilon_C}^{\varepsilon_0 + \hbar\omega} g_V(\varepsilon - \hbar\omega) g_C(\varepsilon) \frac{d\varepsilon}{\hbar\omega} + A \int_{\varepsilon_0}^{\varepsilon_C} g_V(\varepsilon - \hbar\omega) g_C(\varepsilon) \frac{d\varepsilon}{\hbar\omega} = \alpha_1(\hbar\omega) + \alpha_2(\hbar\omega) + \alpha_3(\hbar\omega) \end{aligned} \quad (13)$$

where  $\alpha_1(\hbar\omega)$ ,  $\alpha_2(\hbar\omega)$ ,  $\alpha_3(\hbar\omega)$  are partial fundamental absorption spectra.

From the calculation of the interband absorption coefficient according to Formula (13), the expressions are obtained: For  $n_1 = n_2 = 1/2$

$$\alpha_2(\hbar\omega) = \frac{B}{4\hbar\omega E_g} \left[ 2(\hbar\omega - E_g) \sqrt{E_g \hbar\omega} - (E_g - \hbar\omega)^2 \arctg \left( \frac{E_g - \hbar\omega}{2\sqrt{E_g \hbar\omega}} \right) \right], \quad (14)$$

For  $n_1 = n_2 = 1$ ,

$$\alpha_2(\hbar\omega) = \frac{B}{6\hbar\omega E_g^2} (\hbar\omega - E_g)(E_g^2 + 4\hbar\omega E_g + (\hbar\omega)^2), \quad (15)$$

$n_1=1, n_2=1/2$  and  $n_1=1/2, n_2=1$

$$\alpha_2(\hbar\omega) = \frac{2B}{15\hbar\omega \sqrt{E_g^3}} \left[ 5(\hbar\omega + E_g) \left( \sqrt{(\hbar\omega)^3} - \sqrt{E_g^3} \right) - 3 \left( \sqrt{(\hbar\omega)^5} - \sqrt{E_g^5} \right) \right]. \quad (16)$$

It can be seen that Formulas (7)-(9) and (14)-(16) are the same. This it follows that Formulas (3) and (12) can be used when determining the analytical expressions for the interband absorption coefficients using the Kubo-Greenwood formula.

Similarly, consider the calculation of  $\alpha_1(\hbar\omega)$  and  $\alpha_3(\hbar\omega)$  using Formula (13). Since at  $n_1 = n_2 = 1/2$  it is impossible to obtain an analytical expression for the spectral dependences of partial absorptions determined by optical transitions of electrons from the “tail” of the valence band to the conduction band, from the valence band to the “tail” of the conduction band, they were determined using numerical calculations.

The obtained analytical expressions for the partial absorption spectra  $n_1=n_2=1$  had the form:

$$\alpha_1(\hbar\omega) = \frac{B \exp(-\beta_1(\varepsilon_0 - \varepsilon_V))}{E_g \hbar\omega \beta_1} \left[ \left( \frac{1}{\beta_1} + \hbar\omega \right) \exp(\beta_1(\varepsilon_0 - \varepsilon_V)) - \left( \varepsilon_0 - \varepsilon_V + \frac{1}{\beta_1} + \hbar\omega \right) \right], \quad (17)$$

$$\alpha_3(\hbar\omega) = \frac{B \exp(\beta_2(\varepsilon_0 - \varepsilon_C))}{E_g \hbar\omega \beta_2} \left[ \left( \frac{1}{\beta_2} + \hbar\omega \right) \exp(\beta_2(\varepsilon_C - \varepsilon_0)) - \left( \varepsilon_C - \varepsilon_0 + \frac{1}{\beta_2} + \hbar\omega \right) \right]. \quad (18)$$

It can be seen from Formulas (10), (11) and (17), (18) that with the correctness of the chosen empirical model for the distribution of the density of electronic states in amorphous semiconductors and the limits of a definite integral in the Kubo–Greenwood formulas (3), (12), calculated partial absorption coefficients in the fundamental region will be the same.

### RESULTS AND DISCUSSION

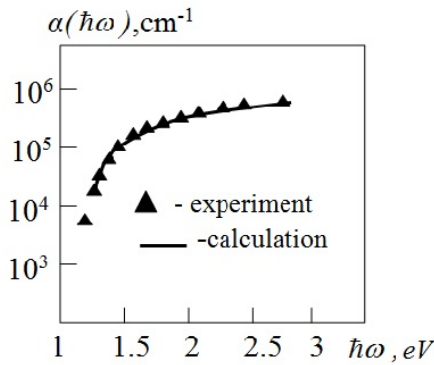


**Figure 2.** Interband absorption spectra of amorphous carbon (a-C): experimental and calculated by Formula (14) (solid line).

Figure 1 shows that the interband absorption spectrum plays the main role in the region of fundamental absorption, and at the edge of fundamental absorption, the values of the partial absorption spectra of the higher indicated optical transitions are almost equal [8]. It can be seen from Formulas (14)–(16) that in order to calculate the interband absorption coefficients, it is necessary to know the energy width of the mobility gap  $E_g$  and the coefficient of proportionality  $B$  in them. To determine these parameters, we use the experimental results for the interband absorption coefficient. In [9], the interband absorption spectrum of amorphous carbon is presented (Fig. 2).

Let us proceed to the calculation of the density of electronic states in the conduction band of amorphous carbon. To do this, from Formula (13) we select the interband absorption spectrum:

$$\alpha_2(\hbar\omega) = A \int_{\varepsilon_c}^{\varepsilon_v + \hbar\omega} g_v(\varepsilon - \hbar\omega) g_c(\varepsilon) \frac{d\varepsilon}{\hbar\omega}, \quad (19)$$

In [10], a Formula is given for the derivative of the integral of a function of two variables with respect to one variable:

$$\frac{d}{dy} \int_{\alpha(y)}^{\beta(y)} f(x, y) dx = \int_{\alpha(y)}^{\beta(y)} \frac{\partial f(x, y)}{\partial y} dx + \frac{\partial \beta(y)}{\partial y} f(\beta(y), y) - \frac{\partial \alpha(y)}{\partial y} f(\alpha(y), y), \quad (20)$$

Applying (20) to (19), we get:

$$\begin{aligned} \frac{\partial \alpha_2(\hbar\omega)}{\partial \hbar\omega} &= \frac{\partial}{\partial \hbar\omega} A \left( \int_{\varepsilon_c}^{\varepsilon_v + \hbar\omega} \frac{g_v(\varepsilon - \hbar\omega) g_c(\varepsilon)}{\hbar\omega} d\varepsilon \right) = \\ &= A \int_{\varepsilon_c}^{\varepsilon_v + \hbar\omega} g_c(\varepsilon) \frac{\partial}{\partial \hbar\omega} \frac{g_v(\varepsilon - \hbar\omega)}{\hbar\omega} d\varepsilon - \frac{\alpha(\hbar\omega)}{\hbar\omega} + \frac{A}{\hbar\omega} g_v(\varepsilon_v) g_c(\varepsilon_v + \hbar\omega). \end{aligned} \quad (21)$$

Let us substitute in (21) the distribution functions in the chosen model:

$$\alpha_2(\hbar\omega) = A \int_{\varepsilon_c}^{\varepsilon_v + \hbar\omega} N(\varepsilon_v) \left( \frac{\varepsilon_c - \varepsilon + \hbar\omega}{E_g} \right)^{\frac{1}{2}} N(\varepsilon_c) \left( \frac{\varepsilon - \varepsilon_c}{E_g} \right)^{\frac{1}{2}} \frac{d\varepsilon}{\hbar\omega}.$$

From here we obtain the derivative with respect to the photon energy

$$\begin{aligned} \frac{\partial \alpha_2(\hbar\omega)}{\partial \hbar\omega} &= \frac{B}{E_g} \int_{\varepsilon_c}^{\varepsilon_v + \hbar\omega} (\varepsilon - \varepsilon_v)^{\frac{1}{2}} \frac{\partial}{\partial \hbar\omega} \left( \frac{\varepsilon_c - \varepsilon + \hbar\omega}{\hbar\omega} \right)^{\frac{1}{2}} d\varepsilon + B \frac{\partial(\varepsilon_v + \hbar\omega)}{\partial \hbar\omega} \frac{(\varepsilon_c - \varepsilon_v - \hbar\omega + \hbar\omega)^{\frac{1}{2}} (\varepsilon_v + \hbar\omega - \varepsilon_v)^{\frac{1}{2}}}{E_g \hbar\omega} - \\ &- B \frac{\partial \varepsilon_c}{\partial \hbar\omega} \frac{(\varepsilon_c - \varepsilon_c + \hbar\omega)^{\frac{1}{2}} (\varepsilon_c - \varepsilon_v)^{\frac{1}{2}}}{E_g \hbar\omega} = \frac{B}{2E_g \hbar\omega} (E_g + \hbar\omega) \operatorname{arctg} \frac{E_g - \hbar\omega}{2\sqrt{E_g \hbar\omega}} - \frac{\alpha_2(\hbar\omega)}{\hbar\omega} + B \frac{(E_g \hbar\omega)^{\frac{1}{2}}}{E_g \hbar\omega} = \\ &= \frac{B}{2E \hbar\omega_g} (E_g + \hbar\omega) \operatorname{arctg} \frac{E_g - \hbar\omega}{2\sqrt{E_g \hbar\omega}} - \frac{\alpha_2(\hbar\omega)}{\hbar\omega} + \frac{B}{N(\varepsilon_c) \hbar\omega} \left( \frac{\hbar\omega}{E_g} \right)^{\frac{1}{2}} \end{aligned} \quad (22)$$

where

$$g_c(\varepsilon) = N(\varepsilon_c) \left( \frac{\varepsilon - \varepsilon_c}{E_g} \right)^{\frac{1}{2}} = N(\varepsilon_c) \left( \frac{\hbar\omega}{E_g} \right)^{\frac{1}{2}}. \quad (23)$$

It follows from (23) that  $\varepsilon - \varepsilon_c = \hbar\omega$ ,  $\varepsilon = \varepsilon_c + \hbar\omega$  this energy state is in the conduction band. Taking into account (23), we write (22)

$$\frac{\partial \alpha_2(\hbar\omega)}{\partial \hbar\omega} = \frac{B}{2E_g \hbar\omega} (E_g + \hbar\omega) \operatorname{arctg} \frac{E_g - \hbar\omega}{2\sqrt{E_g \hbar\omega}} - \frac{\alpha_2(\hbar\omega)}{\hbar\omega} + \frac{B}{N(\varepsilon_c) \hbar\omega} g_c(\varepsilon), \quad (24)$$

and find the distribution of the density of electronic states in the conduction band:

$$g_c(\varepsilon) = \frac{N(\varepsilon_c) \hbar\omega}{B} \left( \frac{\partial \alpha_2(\hbar\omega)}{\partial \hbar\omega} - \frac{B}{2E_g \hbar\omega} (E_g + \hbar\omega) \operatorname{arctg} \frac{E_g - \hbar\omega}{2\sqrt{E_g \hbar\omega}} + \frac{\alpha_2(\hbar\omega)}{\hbar\omega} \right), \quad (25)$$

Averaging the energy of absorbed photons and the interband absorption coefficient, we write (25) in the form

$$g_{Ci}(\varepsilon) = \frac{N(\varepsilon_c)(\hbar\omega_{i+1} + \hbar\omega_i)}{2B} \left( \frac{\alpha_2(\hbar\omega_{i+1}) - \alpha_2(\hbar\omega_i)}{\hbar\omega_{i+1} - \hbar\omega_i} - \frac{B}{E_g(\hbar\omega_{i+1} + \hbar\omega_i)} \left( E_g + \frac{\hbar\omega_{i+1} + \hbar\omega_i}{2} \right) \times \right. \\ \left. \times \operatorname{arctg} \frac{2E_g - (\hbar\omega_{i+1} + \hbar\omega_i)}{\sqrt{2E_g(\hbar\omega_{i+1} + \hbar\omega_i)}} + \frac{\alpha_2(\hbar\omega_{i+1}) + \alpha_2(\hbar\omega_i)}{\hbar\omega_{i+1} + \hbar\omega_i} \right), \quad (26)$$

where  $\alpha(\hbar\omega_i)$  and  $\hbar\omega_i$  are the experimental values of the interband absorption coefficient and the energy of absorbed photons, respectively. The effective value of the density of electronic states in the mobility zone  $N(\varepsilon_c) = 10^{21} \text{ eV}^{-1} \text{ cm}^{-3}$ .

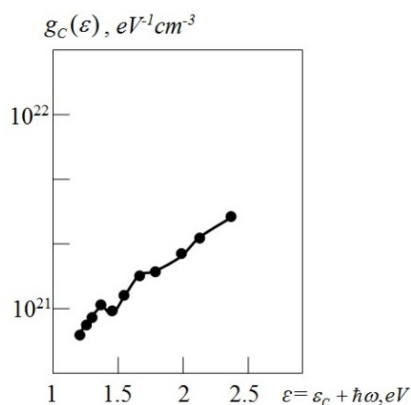


**Figure 3.** The distribution of the density of electronic states in the conduction band of amorphous carbon, obtained from the experimental spectrum of interband absorption

It can be seen from Formula (26) that the distributions of the density of electronic states in the conduction band should be overestimated from  $E_g$  and  $B$ . We determine them, assuming fitting parameters according to Formula (14), adapt the theoretically calculated spectra (solid line in Fig. 2) to the experimental spectra of interband absorption. The latest calculations showed that the best agreement between the calculation value of Formula (14) and the experimental results is obtained at  $E_g = 1.25 \text{ eV}$  and  $B = 6.1 \cdot 10^5 \text{ cm}^{-1}$ . Further calculations showed that these parameters do not have a very strong effect on the final result.

On Figure 3 presents the results of calculations performed with the substitution of experimental data for the interband absorption coefficient (Fig. 2) and the energy of absorbed photons into Formula (26), the density of electronic states in the conduction band of amorphous carbon.

## CONCLUSIONS

Thus, in this work, the region of fundamental absorption of the optical absorption coefficient of amorphous semiconductors has been theoretically investigated and the following results have been obtained:

1. The analytically calculated and experimental determination of the interband absorption spectra is adapted by considering the mobility gap and the proportionality factor in the analytically determined Formula for interband absorption as fitting parameters.
2. For the first time, a method is shown for determining the density of electronic states in the conduction band from the experimental spectrum of interband absorption of amorphous semiconductors.
3. A new Formula is found that determines the density of electronic states in the conduction band, from the Kubo-Greenwood formula written for the interband absorption spectrum of amorphous semiconductors.
4. The density of electronic states in the conduction band of amorphous carbon was determined from the experimental spectrum of interband absorption.

## ORCID

- Rustamjon G. Ikramov, <https://orcid.org/0000-0003-1629-1300>; 
 Khurshidbek X. Muminov, <https://orcid.org/0000-0001-6547-2592>;  
 Bobur Q. Sultonov, <https://orcid.org/0000-0002-6658-3072>

## REFERENCES

- [1] S. Zainobidinov, R.G. Ikramov, M.A. Nuritdinova, and R.M. Zhalalov, "Dependence of the Urbach energy on the Fermi level in a-Si:H films," *Ukr. J. Phys.* **53**(12), 1177-1180 (2008). <http://archive.ujp.bitp.kiev.ua/files/journals/53/12/531207p.pdf>
- [2] Z. Li, S.H. Lin, G.M. Qiu, J.Y. Wang, and Y.P. Yu, "A method for determining band parameters from the optical absorption edge of amorphous semiconductor: Application to a-Si:H," *Journal of applied physics* **124**, 025702 (2018). <https://doi.org/10.1063/1.5025920>

- [3] R.G. Ikramov, M.A. Nuriddinova, and Kh.A. Muminov, "Calculation of the density of electronic states in the valence band from the experimental spectrum of interband absorption of amorphous semiconductors," *Journal of Applied Spectroscopy*, **88**(3), 378-382 (2021). <https://doi.org/10.1007/s10812-021-01200-9>
- [4] R.G. Ikramov, A.A. Mamaxanov, M.A. Nuriddinova, R.M. Jalolov, Kh.M. Muminov, and B.Q. Sultonov, "Calculation of the interband absorption spectra of amorphous semiconductors using the Kubo-Greenwood formula," *Journal of Applied Science and Engineering*, **25**(5), 767-772 (2022). <https://doi.org/10.6180/jase.202210>
- [5] R.G. Ikramov, M.A. Nuriddinova, and Kh.A. Muminov, "A new method for determining the distribution of the density of electronic states in the tail of the valence band of amorphous solid solutions  $Se_xS_{1-x}$ ," *Optics and spectroscopy*, **129**(11), 1382-1386 (2021). <https://doi.org/10.21883/OS.2021.1151636.1949-21>
- [6] M. Brodsky, editor, *Amorphous semiconductors*, (Mir, Moscow, 1982)
- [7] D. Redfield, "Energy-band tails and the optical absorption edge; the case of a-Si:H," *Solid State Communications*, **44**, 1347-1349 (2014). [https://doi.org/10.1016/0038-1098\(82\)90890-0](https://doi.org/10.1016/0038-1098(82)90890-0)
- [8] S. Zainobinov, R.G. Ikramov, R.M. Zhalalov, and M.A. Nuriddinova, "Distribution of electron density of states in allowed bands and interband absorption in amorphous semiconductors," *Optics and Spectroscopy*, **110**(5), 762-766 (2011). <https://doi.org/10.1134/S0030400X11030271>
- [9] A.A. Pronkin, and A.V. Konstantinovskiy, "Absorption and optical gap width of  $\alpha$ -C films obtained by magnetron sputtering," *High Temp.* **53**(2), 312-314 (2015). <https://doi.org/10.1134/S0018151X15020212>
- [10] N. Bronshtein, and K.A. Semendyaev, *Handbook of Mathematics for Engineers and Technical University Students*, (Moscow, 1986). (in Russian)

### РОЗРАХУНОК ЩІЛЬНОСТІ РОЗПОДІЛУ ЕЛЕКТРОННИХ СТАНІВ У ЗОНІ ПРОВІДНОСТІ З ФУНДАМЕНТАЛЬНОГО СПЕКТРУ ПОГЛИНАННЯ АМОРФНИХ НАПІВПРОВІДНИКІВ

Рустамжон Г. Ікрамов, Хуршидбек А. Мумінов, Машхура А. Нурітдінова,  
Бобур Қ. Сутонов, Ойбек Т. Холмірзаєв

*Наманганський інженерно-технологічний інститут, вул. Косонсой, 7, Наманган 160115, Узбекистан*

Теоретично досліджено область фундаментального поглинання в оптичних спектрах аморфних напівпровідників з використанням наближення Девіса-Мотта за формулою Кубо-Грінвуда. Як відомо, в області фундаментального поглинання можна спостерігати три види оптичних переходів електрона; від хвоста валентної зони до зони провідності, від валентної зони до зони провідності та від валентної зони до хвоста зони провідності. Для всіх цих електронних переходів аналітичні вирази спектрів часткового поглинання отримані з двох різних типів формули Кубо-Грінвуда. Ширину забороненої зони оптичної рухливості та коефіцієнт пропорційності визначали в аналітичній формі спектра міжзонного поглинання шляхом їх підгонки до експериментального спектра міжзонного поглинання. Представлено новий метод розрахунку щільності розподілу електронних станів у зоні провідності аморфного вуглецю на основі експериментального спектра міжзонного поглинання та аналітичного виразу формули Кубо-Грінвуда, записаної для спектра міжзонного поглинання.

**Ключові слова:** аморфні напівпровідники; спектри оптичного поглинання; метод апроксимації Девіса-Мотта; формула Кубо-Грінвуда; фундаментальний спектр поглинання; часткові спектри поглинання; спектр міжзонного поглинання; електронний розподіл густини стану

## LATERAL PHOTOELECTRIC EFFECT IN IRON-SILICON DIOXIDE-COMPENSATED SILICON HYBRID STRUCTURES

✉ Eshkuvat U. Arzikulov<sup>a,\*</sup>, ✉ Alisher D. Nurimov<sup>a</sup>, F.A. Salakhitdinov<sup>a</sup>, U.A. Ashirov<sup>a</sup>, T.S. Sharafova<sup>a</sup>, A.Sh. Khujanov<sup>b</sup>, R.M. Usanov<sup>a</sup>

<sup>a</sup> Samarkand State University named after Sharof Rashidov, 140000, Samarkand, University Blvd. 15, Republic of Uzbekistan; e-mail: [rector1@samdu.uz](mailto:rector1@samdu.uz)

<sup>b</sup> Samarkand State University of Veterinary Medicine, Livestock and Biotechnologies, 140003, Samarkand, Mirzo Ulug'bek str. 77, Republic of Uzbekistan

\*Corresponding Author e-mail: [eshkuvata@gmail.com](mailto:eshkuvata@gmail.com); Tel.: (+998915389791)

Received August 6, 2023; revised September 21, 2023; accepted September 21, 2023

This article presents experimental results on the technology of obtaining and studying the lateral photoelectric effect (LPE) in hybrid structures (HS) of the Fe/SiO<sub>2</sub>/p-Si<B, Mn> and Fe/SiO<sub>2</sub>/n-Si<B, Mn> types. The technology for obtaining such HS consists of two parts: firstly, obtaining compensated (C), highly compensated (HC), and over-compensated (OC) samples of Si <B, Mn>. Secondly, obtaining HS Fe/SiO<sub>2</sub>/p-Si<B, Mn> and Fe/SiO<sub>2</sub>/n-Si<B, Mn>. Based on the results, it is shown that sufficiently good HS has been obtained. Experiments on the study of LPE have shown that in the studied HS there is a pronounced manifestation of the lateral photoelectric effect, the magnitude and nature of which strongly depend on the type of conductivity and resistivity of the compensated silicon. The observed features are explained by the fact that in C, HC, and OC silicon samples, impurities that create deep levels in the silicon band gap form various multi-charged complexes that modulate the energy band of silicon, which lead to significant changes in its physicochemical and generation-recombination properties, which underlies the observed effects. Based on the LPE studies, depending on the contact distance, it is possible to determine the numerical values of the diffusion lengths of the minor current carriers ( $L_p$  and  $L_n$ ), their lifetimes ( $\tau_p$  and  $\tau_n$ ), and diffusion coefficients ( $D_p$  and  $D_n$ ) on the substrate material.

**Keywords:** Lateral photo effect; Hybrid structure; Compensated silicon; Photovoltage; Diffusion; Evaporation; Oxide; p-n junction

**PACS:** 68.37.Ps; 68.65.Ac; 78.20.-e; 73.30.+y; 73.43.Qt; 81.10.Bk; 81.65.Cf

### INTRODUCTION

Although the discovery of LPE was first reported in 1930 by the German physicist Schottky [1], his pioneer in world literature is considered to be Wallmark, who published an article on this topic in 1957 [2]. Since then, LPE in semiconductor structures has been intensively studied due to its wide practical application in optoelectronic devices, especially as position-sensitive sensors, since the LPE arising in them varies linearly with the distance relative to the contacts. LPE occurs with uniform illumination of the p-n junction as a result of lateral diffusion and recombination of photogenerated electron-hole pairs [3-4]. A similar effect has also been studied in metal-semiconductor (MS) structures [5-10] and metal-oxide-semiconductor (MOS) [11-17]. In the last decade, so-called silicon-based hybrid structures, which are essentially MOS structures, have been intensively studied [19-23].

Analysis of existing works has shown that in the studied structures, low-resistance plates of monocrystalline silicon were mainly used as a semiconductor substrate with n- and p-types of conductivity: p-Si  $\rho = 4.5 \div 8.3 \Omega \times \text{cm}$  and n-Si  $\rho = 7.5 \div 80 \Omega \times \text{cm}$ , respectively [11, 12, 18, 22, 24-25]. Despite the existence of a number of studies devoted to the influence of the type of conductivity of substrates on their photovoltaic properties, there is currently no justification for the choice of substrate material.

In this connection, there is an interest in the use of C, HC and OC samples of monocrystalline silicon doped with various impurities as substrates in such structures by high-temperature diffusion. It is known that C, HC, and OC silicon samples have unique physical properties, namely, high photosensitivity in both the impurity and intrinsic spectral regions [26], infra-low-frequency oscillations of the photocurrent with a large amplitude [27-28], recombination waves [29-30], large positive and negative magnetoresistance [31-32], deep temperature and infrared quenching of photoconductivity [33-34], etc. In addition, the reproducible technology for producing compensated silicon with various impurities has reached its perfection and can be used as an additional degree of freedom both in controlling the parameters of the HS technology and in controlling the effects observed in them.

### RESULTS AND DISCUSSION

#### Technology for obtaining C, HC, and OC silicon samples

The production of HS consists of two stages. In the first stage, it is necessary to obtain C, HC, and OC silicon samples doped with manganese atoms by the high-temperature diffusion method. To do this, samples of  $8 \times 5 \times 0.5 \text{ mm}^3$  in the form of a parallelepiped with a crystallographic orientation [100] were cut from the original silicon plates of the



KDB-10 brand (boron-doped silicon with a specific electrical resistance of  $10 \Omega \times \text{cm}$  at room temperature) used in the electronics industry. To remove the damaged surface layer formed during plate cutting, the samples were first subjected to mechanical and then chemical treatment with HF:  $\text{HNO}_3$  etchant. The state of the surface of the initial substrate p-Si<B> after chemical cleaning was studied using AFM in static force mode (Fig. 1).

The surface texture of the p-Si<B> substrate was measured in an area with horizontal dimensions of  $60 \mu\text{m} \times 60 \mu\text{m}$  and vertical dimensions of 20 nm. Figure 1 on the left shows the image of the data obtained on the Z axis, and the image of the data obtained in the XY plane is placed on the right. The surface roughness parameters are given in Table 1.

Based on the results obtained, it can be said that the roughness parameters of the chemically treated surface show that such a surface is smooth enough to obtain HS. There are almost no hills or deep valleys on the surface. The results show that the chemical cleaning of the substrate p-Si<B> provides a smooth surface texture.

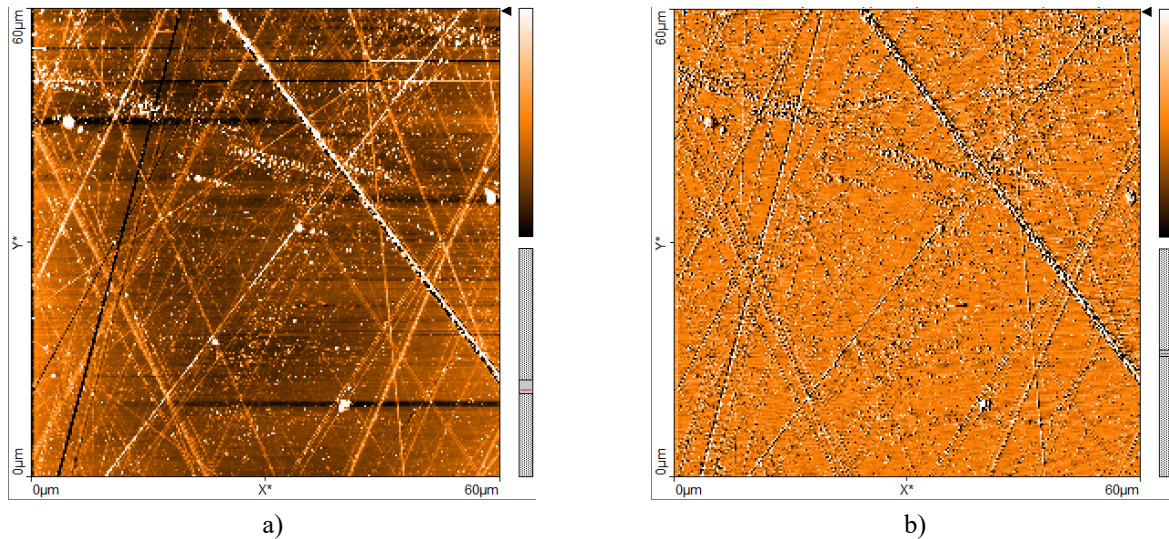


**Figure 1.** 2D AFM image of the surface of the initial samples p-Si<B> taken ( $60 \mu\text{m} \times 60 \mu\text{m}$ ) along the Z axis and along the XY plane in static force mode

High-temperature diffusion alloying of manganese into silicon was carried out according to a well-known technique [35]. The initial silicon samples with manganese impurities were placed in a pre-purified quartz ampoule and air was pumped out of the ampoule to a pressure of  $\sim 10^{-5}$  mm Hg. The diffusion of manganese into silicon was carried out in a horizontal furnace of the SOUL-4.0 type, which ensures the maintenance of a constant temperature with an accuracy of  $\pm 0.1^\circ\text{C}$  for two hours. The temperature in the working area of the furnace was additionally controlled using a type B thermocouple (a combination of platinum alloys (6% rhodium) or platinum (30% rhodium)).

**Table 1.** Roughness parameters of the p-Si<B> substrate and Fe layers.

Surface	$R_m$ , fm	$R_a$ nm	$R_q$ nm	$R_y$ nm	$R_p$ nm	$R_v$ nm
p-Si<B>	-41.355	1.528	3.327	145.71	104.73	-40.979
Fe	-19.009	26.446	33.783	254.31	167.74	-86.575

After the diffusion stage was completed, the samples were rapidly cooled at a rate of  $120\text{-}150^\circ\text{C/s}$  to a temperature of  $18^\circ\text{C}$ . To obtain samples with different values of electrical resistivity and types of conductivity, the diffusion temperature was varied in the range of  $1020\text{-}1060^\circ\text{C}$ . After the process of high-temperature diffusion, a manganese-enriched layer with a thickness of about 15-20 microns is formed on the surface of the samples. To remove this layer, the obtained samples were also subjected to mechanical and chemical treatment, as well as the original samples. To determine the main parameters (electrical resistivity ( $\rho$ ), concentration ( $n$ ) and mobility of current carriers ( $\mu$ )) the Hall effect method was used for both initial and doped samples [36]. This diffusion technology makes it possible to obtain C, HC and OC silicon samples doped with manganese with both p- and n-types of conductivity, with a resistivity in the range of  $\rho \approx 10^2 \div 10^5 \Omega \times \text{cm}$  at room temperature.

It is known that in C, HC and OC samples of silicon, the impurity atoms that create deep energy levels in its band gap in a charged state. The multiplicity of their charge depends on the degree of compensation. In addition, these charged atoms can combine into complex multicharged clusters, which, in turn, leads to noticeable changes in both the energy band of silicon and its generation-recombination parameters [26]. In the case of an impurity of manganese having a sufficiently large diffusion coefficient at high temperatures, its atoms can be in one- and two-times positively charged states, and can also be part of multicharged complexes of the type  $[\text{Mn}^+]^4$  [31], which, in turn, determines the basic physical properties of C, HC and OC Silicon samples, as well as HS, which they are part of. Thus, it can be concluded that the main parameters of C, HC and OC of silicon samples doped with manganese, as well as HS based on it, are

determined by the deep energy levels of the manganese atom in the silicon band gap. In addition, by regulating the diffusion temperature, the vapor pressure of the diffusant and the cooling rate of the samples, it is possible to control the basic physical parameters of C, HC and OC of silicon samples and HS based on it within a wide range [26].

### Technology for obtaining HS

At the second stage, it is necessary to obtain a HS of the Fe/SiO<sub>2</sub>/p(n)-Si<B, Mn> type. It has been shown that the properties of MOS HS are mainly determined by the thickness of the metal and oxide layers that provide tunneling of carriers through them. At the same time, it was found that the optimal thickness of the oxide layer is up to 5 nm, and the metal layer is 15 nm [24]. The growth of an oxide layer with a thickness of about 5 nm on the surface of diffusion-doped samples of n(p)-Si<B, Mn> was carried out according to the method described in the ref. [21, 41]. Then, layers of pure iron were obtained on the surface of purified and dried C, HC and OC samples of p(n)-Si<B, Mn> by thermal or electron beam evaporation in high vacuum [37]. The surface characteristics of the HS deposited by a thin layer of Fe were re-investigated using AFM in the static force mode (Figure 2).

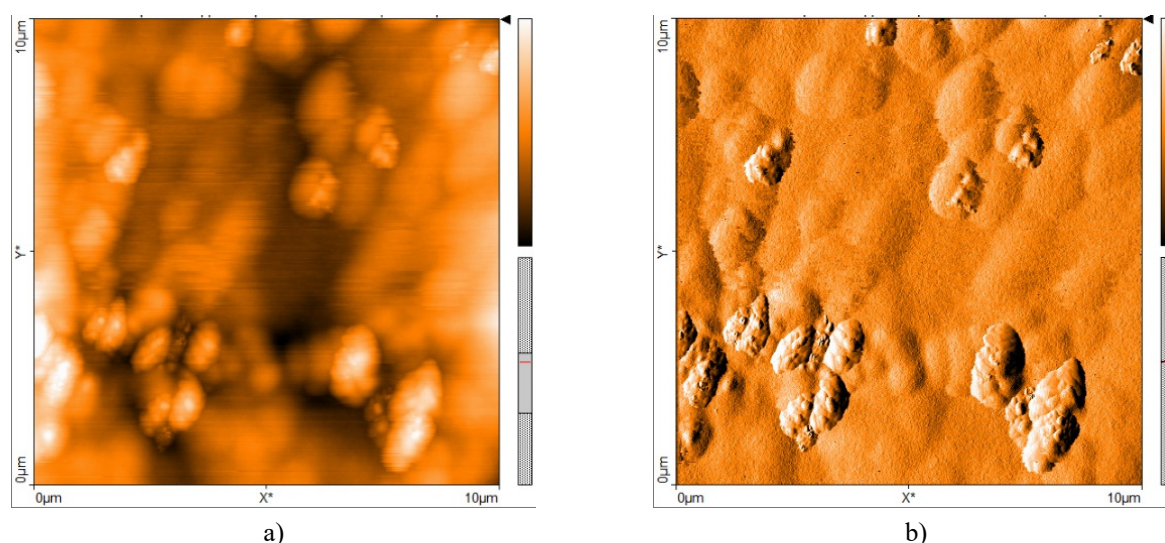


**Figure 2.** Two-dimensional AFM images of the surface (10 μm×10 μm) of the iron layer in the Fe/p-Si hybrid structure in the Z axis (a) and in the XY plane (b) obtained in the "static force mode"

As in Figure 1, the left part of the figure shows an image of the Z axis, and the right part shows an image of data in the XY plane. The surface of the Fe film has the shape of hills and valleys. The average roughness of the substrate decreased from -41 fm to -19 fm as a thin layer of Fe was deposited. At the same time, the average roughness increased from 1.5 nm to 26.4 nm. A decrease in the average roughness value from -41 fm to -19 fm and an increase in the mean square (RMS) roughness value of the substrate from 1.5 nm to 26.4 nm during the formation of a thin layer of iron means that during the formation of a thin layer of iron on the silicon surface, Fe pairs covered the porosity of the surface caused by chemical cleaning, but the average roughness increased due to uneven distribution porosity on the surface. If you pay attention to the image of the surface, you can see several roughness of the granular form. Such a sharp change in the RMS of irregularities can be explained by the formation of these grains. The peak height value increased from 104.7 nm to 167.74 nm, and the depression depth value increased from -41 nm to -86.575 nm. This can be explained by the inhomogeneous distribution of evaporated Fe over the silicon surface. This, in turn, provides an increase in the height of the peaks of the valley. As the surface roughness increases, the probability of adsorption of charged particles on the crystal film increases, which can be explained by the fact that high temperatures can stimulate the migration of grain boundaries [38]. In addition, at high temperatures they can diffuse and occupy the right place in the crystal lattice, and grains with lower surface energy will increase at high temperatures [39]. In addition, the surface roughness of conductive thin films has a significant effect on the electrical characteristics of electronic devices manufactured on their basis [40].

The experiments conducted to study the I-V characteristics showed that good HS were obtained. Figure 4 shows the I-V dependence for one of the obtained HS at different values of the external magnetic field. As can be seen from Figure 4, I-V dependence shows good rectifying properties of HS and has a significant negative magnetoresistance. Thus, we can say that on the basis of the described technology, it is possible to obtain sufficiently good HS with a Schottky barrier of the Fe/SiO<sub>2</sub>/p(n)-Si<B, Mn> type.

If we compare the images, then after the deposition of iron on a chemically treated silicon substrate, the grain size increased, which can be explained by the inhomogeneous distribution of iron atoms deposited on the surface during the evaporation of pure iron. However, the surface roughness can be analyzed based on the data obtained using AFM. Table 1 shows that initially the average roughness on the silicon substrate is about 1.5 nm, but after applying the iron layer, this value is 26.4 nm, which means that the surface roughness of the iron layer is significantly higher than the base. Comparing the values of the RMS, we can say that the roughness on the surface of the silicon base is due to the inhomogeneous

placement of Fe atoms on the silicon base, that is, the surface has a granular texture. In conclusion, we can say that the surface of the iron layer in the Fe/p-Si<B> HS has a high hardness and a granular surface. This kind of research provides a more complete understanding of the influence of shooting conditions and modes on the morphology of thin films and can help in adapting deposition parameters in accordance with the requirements of surface topography for electronic device applications.

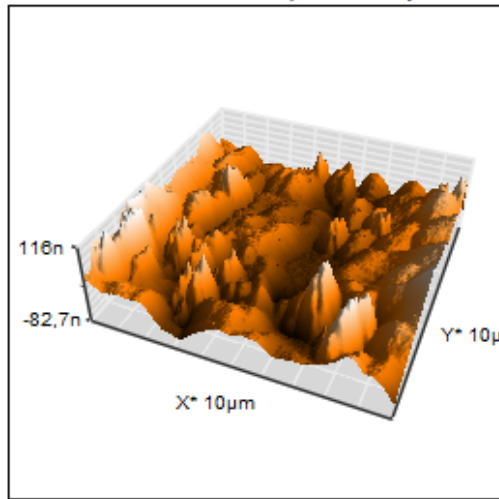


**Figure 3.** Three-dimensional images of the surface (10 μm×10 μm) of the iron layer in Fe/SiO<sub>2</sub>/p-Si HS

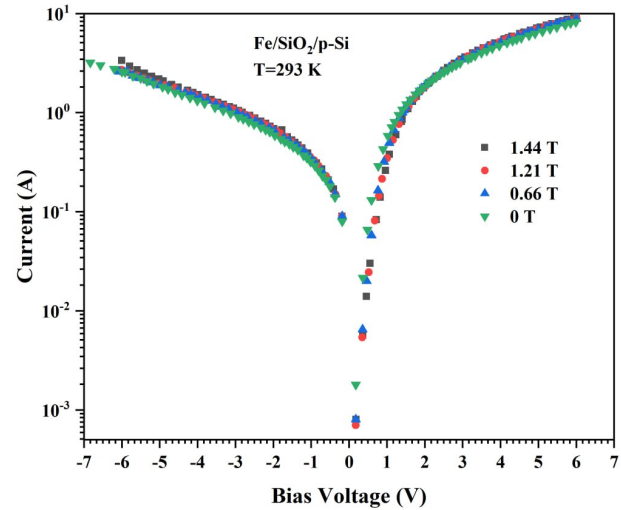


**Figure 4.** I-V dependence for one of the obtained HS Fe/SiO<sub>2</sub>/p-Si under an external magnetic field

### Lateral photoeffect in HS

The experimental setup described in [25] was used for the experimental study of LPE in the HS. Diode-pumped semiconductor lasers with wavelengths of 532 and 632 nm were used as a light source. Experiments conducted at T=293 K showed that pronounced LPE is observed in the studied HS and the value of lateral photovoltage (LPV) is higher than in the previously studied structures [2]. The sensitivity of the LPE is 1648.5 μV/mm. Figure 5 shows the dependence of the LPV on the distance between the contacts for HS based on the initial samples of p-Si<B>.

The electrical resistivity of the sample  $\rho = 10 \Omega \times \text{cm}$ , the wavelength and laser power  $\lambda = 632 \text{ nm}$  and 8 mW, respectively,  $T = 293 \text{ K}$ . As can be seen from Figure 5, the dependence of the LPV on the contact distance for the HS manufactured on the basis of the initial samples of p-Si <B> has a linear character, which corresponds to the results of theoretical [2, 3] and experimental studies [4]. We have studied the LPE in the HS Fe/SiO<sub>2</sub>/p-Si<B, Mn> and Fe/SiO<sub>2</sub>/n-Si<B, Mn> under the same conditions as in the HS manufactured on the basis of the initial samples of p-Si<B>. The results of the experiments are shown in Fig. 6. As can be seen from Figure 6, both Fe/SiO<sub>2</sub>/p-Si<B, Mn> and Fe/SiO<sub>2</sub>/n-Si<B, Mn> have LPE.

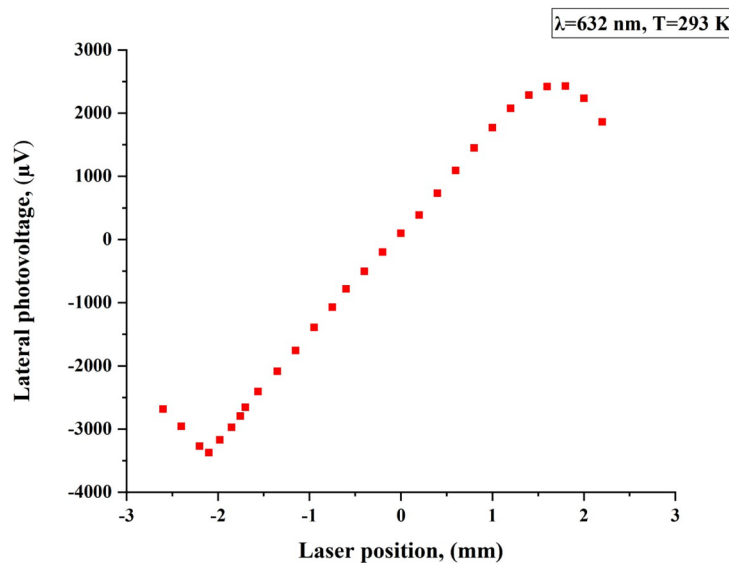


**Figure 5.** The dependence of the LPV on the distance between the contacts for the initial structure of p-Si<B>. Electrical resistivity of the sample  $\rho = 10 \text{ ohms} \times \text{cm}$ ,  $\lambda = 632 \text{ nm}$ ,  $T = 293 \text{ K}$ , laser power: 8 MW.

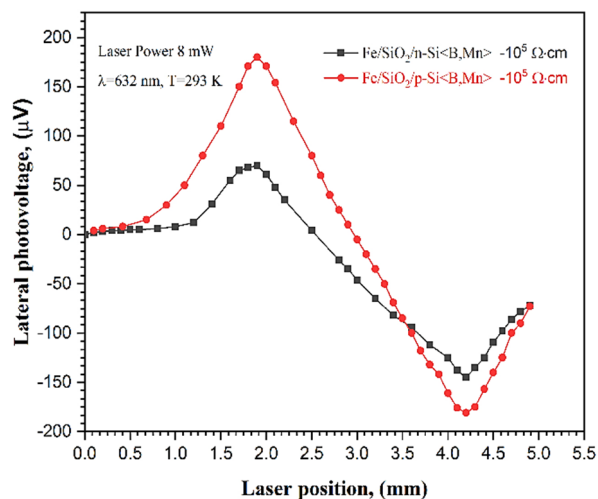


**Figure 6.** Dependence of the LPV on the distance between the contacts for the Fe/SiO<sub>2</sub>/p-Si<B, Mn> and Fe/SiO<sub>2</sub>/n-Si<B, Mn> HSs.

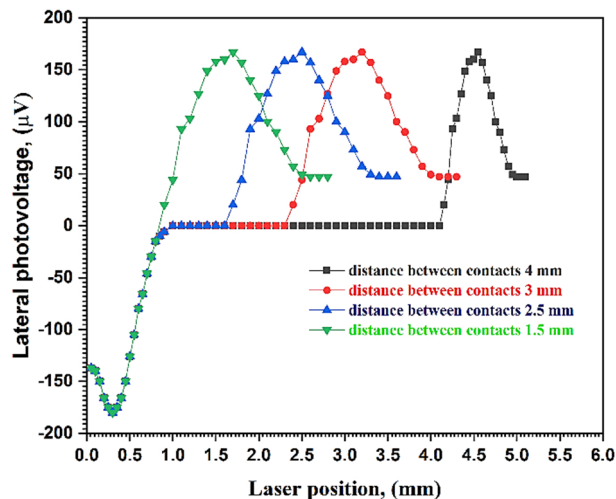


**Figure 7.** Dependence of the LPV on the distance between the contacts for the Fe/SiO<sub>2</sub>/p-Si<B, Mn> HS. Sample electrical resistivity is  $\rho = 1 \cdot 10^5 \Omega \times \text{cm}$ ,  $\lambda = 532 \text{ nm}$ ,  $T = 300 \text{ K}$ , Laser power: 8 mW.

When the type of conductivity of C, HC and OC of silicon samples is changed, an inversion of the LPV polarity is observed, which is explained by the fact that in the Fe/SiO<sub>2</sub>/n-Si<B, Mn> structure, the internal field of the transition is directed from silicon to a thin layer of iron, and in Fe/SiO<sub>2</sub>/p-Si<B, Mn> from the iron layer to silicon, which is due to the presence of interface states at the Fe/SiO<sub>2</sub>/Si<B, Mn> boundary [18]. For both structures, there is an extreme dependence of the LPV on the thickness of the Fe film with a maximum localized near  $\sim 5 \text{ nm}$ . It is assumed that in the Fe/SiO<sub>2</sub>/Si<B, Mn> HSs, due to the high resistivity of C, HC and OC silicon samples, the characteristics of the LPE are determined by the processes of lateral diffusion of excess photogenerated carriers drawn by the built-in barrier field from the silicon volume into the area adjacent to the Fe/SiO<sub>2</sub>/p-Si<B, Mn> interface and the role of the iron film is reduced only to the formation of bending zones in this region [18].

The observation of the linear dependence of the LPV on the position of the light spot in the studied structures can be understood if we assume that the metal film on the surface of the MOS structure serves only to create a surface bending of the zones into the silicon region adjacent to the SiO<sub>2</sub>/Si interface, and the process of LPV generation occurs in the near-surface region of silicon. Depending on the degree of curvature of the zones in the near-surface region of silicon, inversion layers, depletion or enrichment are formed, and the resulting transitions of the type p-n, p<sup>+</sup>p (n<sup>+</sup>n) or p<sup>+</sup>-p (n<sup>+</sup>-n) are responsible for the observed effects. At the same time, the excess concentrations of photogenerated carriers will be greater than the main ones in both the p-region and the n-region [2].

Usually, the LPV generated was measured at the contacts located on the side opposite to the illumination. However, it has recently been shown that the sensitivity of LPE in MS and MOS structures can be increased by lighting and placing contacts from the side of the metal film. For example, in Ti/Si and Co/Si structures, the sensitivity of the LPE measured from the metal side is 1.45 times higher than the similar characteristic measured from the silicon side [7, 8, 11, 12]. Based on theoretical calculations, it can be concluded that the use of metals with high output performance and high resistivity in MOS structures leads to an increase in LPE.

The study of the effect of the contact distance on the value of the LPV showed that with an increase in the distance between the contacts, starting from a certain distance from both contacts, the value of the LPV becomes zero (Figure 7). As the contacts approach each other, the area on which the LPV is zero decreases, and at a certain value of the contact distance, this area disappears altogether.

This phenomenon seems to be related to generation-recombination processes in a semiconductor substrate. When the distances between the contacts are greater than the diffusive length of the non-basic charge carriers, i.e.,  $d > L_p, L_n$ , the charge carriers formed under the action of light recombine without reaching the zone of action of the contact fields. When  $d$  becomes comparable to  $L_p, L_n$ , i.e., when the conditions  $d \sim L_p, L_n$  are met, most of the generated charge carriers reach the contact field area and thus contribute to the LPE. This fact shows that based on the study of the LPV value, depending on the contact distances, it is possible to determine the numerical values of the diffusion lengths of minor current carriers ( $L_p$  and  $L_n$ ), their lifetimes ( $\tau_p$  and  $\tau_n$ ) and diffusion coefficients ( $D_p$  and  $D_n$ ) on the substrate material.

To study the influence of the frequency of the radiation source on the magnitude and nature of the LPE, the dependences of the LPV of the studied structures on the frequency of radiation were removed (Figure 8). In our experiments, two diode-pumped semiconductor lasers with wavelengths of 532 and 632 nm and a power of 20 mW were used.

LPE has high sensitivity and linearity. The dependence of the LPE on the wavelength of laser radiation is shown in Fig. 8. As can be seen from Fig. 8, with an almost identical character, the change in the magnitude of the LFV and their magnitude depends on the wavelength. In addition, there is a significant asymmetry in the shape of the dependence of the

LPV on the contact distance. The value of the maximum LPV on the side of the negative electrode is significantly less than on the side of the positive electrode. For a red laser, these values are 300 and 210 mV, respectively. The value of the maximum LPV in the positive electrode for the red laser is almost 1.4 times greater than that of the green laser, at the same time, the value of this for the negative electrode is 1.2 times. This allows us to assume that for the study of LPE in Fe/SiO<sub>2</sub>/p-Si<B, Mn> HS, the most suitable laser wavelength is 632 nm, and LPE will increase with increasing laser radiation power in a certain range of power values and saturation is observed starting from a certain power value (Fig. 9). These results are in good agreement with the results of the study of LPE in Ni-SiO<sub>2</sub>-Si structures, where a laser with a wavelength of 632 nm is also suitable laser radiation for LPE [22].

The asymmetry of the shape of the LPV dependence on the contact distance is associated with an uneven distribution of charged impurity centers associated with manganese atoms. Since manganese in silicon is in a positively charged state, it is shifted towards the negative electrode under the action of the contact field, which leads to a decrease in the potential of the negative electrode. Figure 8 shows that the LPV value increases non-linearly with increasing laser power.

In the initial phase of the dependence, with laser power in the range of 0-6 mW, the LPV grows quasi-linearly, in the power range of 7-10 mW, the LPV grows very quickly and, starting from 11 mW, its growth slows down and reaches saturation, starting from 12 mW. In a certain wavelength range of laser radiation and at high power, repeated excitation of electron-hole pairs is possible. When the saturation state is reached, the LPV value does not change with increasing laser power. The LPV value at saturation depends on the laser frequency. Apparently, this is due to the possibility of multiple excitations of electron-hole pairs for different photons. Although the number of photogenerated electron-hole pairs increases with increasing laser power, the number of electrons that can be transferred by the built-in internal electric field is limited. The LPV value reaches saturation when the rate of generation of electron-hole pairs is equal to the rate of their recombination. Consequently, the LPV cannot increase indefinitely with increasing laser power. This is indirect evidence that the LPV is mainly due to electron diffusion, and not temperature effects.

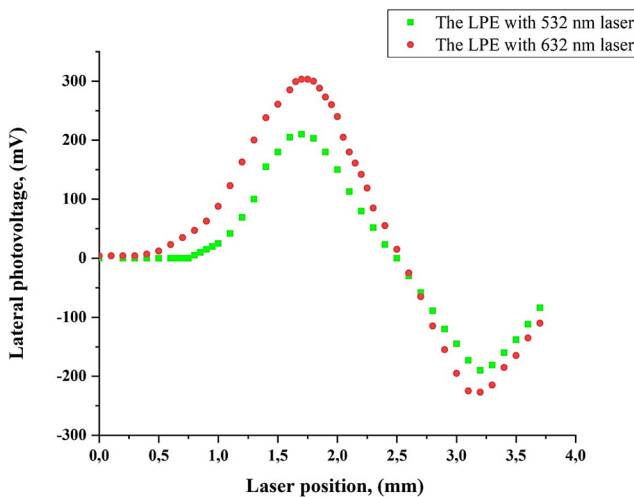


**Figure 8.** The dependence of the LPV on the wavelength of laser radiation with a power of 8 mW in HS Fe/SiO<sub>2</sub>/p-Si<B, Mn>. The electrical resistivity of the sample  $\rho = 1 \times 10^2 \Omega \times \text{cm}$ ,  $T = 293 \text{ K}$

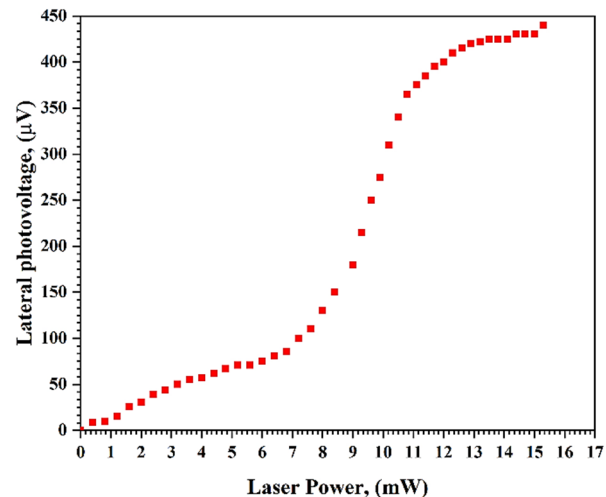


**Figure 9.** The dependence of the LPV on the laser power in the Fe/SiO<sub>2</sub>/n-Si<B, Mn> HS. The electrical resistivity of the samples  $\rho = 1 \times 10^5 \Omega \times \text{cm}$ ,  $T = 293 \text{ K}$

The dependence of the LPV on the power of laser radiation, shown in Fig. 9, can be interpreted as follows. At low laser powers, the number of photogenerated pairs is small and their number increases linearly with increasing laser power, which corresponds to the linear growth of the LPV. Starting from a certain value of the laser radiation power, the number of generated carrier pairs increases non-linearly. This is due to the fact that at high laser radiation powers, it is possible to re-excite electron-hole pairs, which undoubtedly leads to a rapid increase in LPV. When the saturation state is reached, the LPV value does not change with increasing laser power. The LPV value at saturation depends on the laser frequency. Apparently, this is due to the possibility of multiple excitations of electron-hole pairs for different photons. Although the number of photogenerated electron-hole pairs increases with increasing laser power, the number of electrons that can be transferred by the built-in internal electric field is limited. The LPV value reaches saturation when the rate of generation of electron-hole pairs is equal to the rate of their recombination. Consequently, the LPV cannot increase indefinitely with increasing laser power. This is indirect evidence that LPV is mainly caused by electron diffusion, and not by temperature effects [18].

### CONCLUSIONS

In this paper, the technology of obtaining HS of the Fe/SiO<sub>2</sub>/p-Si<B, Mn> and Fe/SiO<sub>2</sub>/n-Si<B, Mn> types and LPE in them is investigated.

Based on the results obtained, it can be concluded that the technology described by us allows obtaining fairly good HS. Experiments on the study of LPE have shown that a pronounced manifestation of LPV is observed in the studied HS.

In these HS, LPE is observed and the nature of the change in LPV depends on the contact distance, wavelength and power of the laser radiation.

Based on the LPV study, depending on the contact distance, it can be said that it is possible to determine the numerical values of the diffusion lengths of minor current carriers ( $L_p$  and  $L_n$ ), their lifetimes ( $\tau_p$  and  $\tau_n$ ) and diffusion coefficients ( $D_p$  and  $D_n$ ) on the substrate material.

The nature of the change and the magnitude of the LPV depend on the concentration of charge carriers and the type of conductivity C, HC and OC of silicon samples. The observed features in HS are explained by the fact that in C, HC and OC silicon samples, impurities that create deep levels in the silicon band gap form various multicharged complexes that modulate the energy band of silicon, which underlies the observed effects in C, HC and OC silicon samples and HS based on them.

**Author Contributions:** Conceptualization, A.E.U. and S.F.A.; methodology, A.E.U. and S.F.A.; software, N.A.D. and A.U.A.; validation, S.T.S. and U.R.M.; formal analysis, S.T.S. and U.R.M.; R.; writing - review and editing, A.E.U., N.A.D.; writing – original draft preparation, A.E.U.

**Funding:** This research received no external funding.

**Data Availability Statement:** The data may partially be available through direct contact with the relevant authors.

**Conflicts of Interest:** The authors declare no conflict of interest.

#### ORCID

©Eshkuvat U. Arzikulov, <https://orcid.org/0000-0001-9179-3402>; ©Alisher D. Nurimov, <https://orcid.org/0009-0008-1291-3380>

#### REFERENCES

- [1] J. Henry, and J. Livingstone, “Improved position-sensitive detectors using high resistivity substrates,” *J. Phys. D: Appl. Phys.* **41**, 165106 (2008). <https://doi.org/10.1088/0022-3727/41/16/165106>
- [2] S.Q. Xiao, H. Wang, Z.C. Zhao, Y.Z. Gu, Y.X. Xia, and Z.H. Wang, “The Co-film-thickness dependent lateral photoeffect in Co-SiO<sub>2</sub>-Si metal-oxide-semiconductor structures,” *Opt. Express*. **16**, 3798-3806 (2008). <https://doi.org/10.1364/OE.16.003798>
- [3] C.Q. Yu, H. Wang, S.Q. Xiao, and Y.X. Xia, “Direct observation of lateral photovoltaic effect in nano-metal films,” *Opt. Express*, **17**, 21712-21722 (2009). <https://doi.org/10.1364/OE.17.021712>
- [4] S. Wang, W. Wang, L. Zou, X. Zhang, J. Cai, Z. Sun, B. Shen, and J. Sun, “Magnetic Tuning of the Photovoltaic Effect in Silicon-Based Schottky Junctions,” *Adv. Mater.* **26**(47), 8059–8064 (2014). <https://doi.org/10.1002/adma.201403868>
- [5] S.H. Wang, X. Zhang, L.K. Zou, J. Zhao, W.X. Wang, and J.R. Sun, “Lateral resistance reduction induced by the light-controlled leak current in silicon-based Schottky junction,” *Chin. Phys. B*, **24**(10), 107307 (2015). <https://doi.org/10.1088/1674-1056/24/10/107307>
- [6] S.Q. Xiao, H. Wang, C.Q. Yu, Y.X. Xia, J.J. Lu, Q.Y. Jin, and Z.H. Wang, “A novel position-sensitive detector based on metal-oxide-semiconductor structures of Co-SiO<sub>2</sub>-Si,” *New Journal of Physics*, **10**(3), 033018 (2008). <https://doi.org/10.1088/1367-2630/10/3/033018>
- [7] C. Yu, and H. Wang, “Large Lateral Photovoltaic Effect in Metal-(Oxide-) Semiconductor Structures,” *Sensors*, **10**, 10155-10180 (2010). <https://doi.org/10.3390/s101110155>
- [8] L. Chi, P. Zhu, H. Wang, X. Huang, and X. Li, “A high-sensitivity position-sensitive detector based on Au-SiO<sub>2</sub>-Si structure,” *J. Opt.* **13**(1), 015601 (2010). <https://doi.org/10.1088/2040-8978/13/1/015601>
- [9] J.P. Cascales, I. Martínez, D. Díaz, J.A. Rodrigo, and F.G. Aliev, “Transient lateral photovoltaic effect in patterned metal-oxide-semiconductor films,” *Applied Physics Letters*, **104**(23), 231118 (2014). <https://doi.org/10.1063/1.4882701>
- [10] S. Liu, X. Xie, and H. Wang, “Lateral photovoltaic effect and electron transport observed in Cr nano-film,” *Opt. Express*, **22**, 11627–11632 (2014). <https://doi.org/10.1364/OE.22.011627>
- [11] I.A. Bondarev, M.V. Raustkii, and A.S. Tarasov, “Lateral photovoltaic effect in silicon-based hybrid structures under external magnetic field,” *Materials Science in Semiconductor Processing*, **167**, 107786-107795 (2023). <https://doi.org/10.1016/j.mssp.2023.107786>
- [12] X. Wang, B. Song, M. Huo, Y. Song, Z. Lv, Y. Zhang, Y. Wang, et al., “Fast and sensitive lateral photovoltaic effects in Fe<sub>3</sub>O<sub>4</sub>/Si Schottky junction,” *RSC Advances*, **5**(80), 65048–65051 (2015). <https://doi.org/10.1039/c5ra11872g>
- [13] X. Huang, C. Mei, J. Hu, D. Zheng, Z. Gan, P. Zhou, and H. Wang, “Potential Superiority of p-Type Silicon-Based Metal–Oxide–Semiconductor Structures Over n-Type for Lateral Photovoltaic Effects,” *IEEE Electron Device Letters*, **37**(8), 1018–1021 (2016). <https://doi.org/10.1109/led.2016.2577700>
- [14] T.A. Pisarenko, V.V. Korobtsov, A.A. Dimitriev, V.V. Balashev, V.V. Zheleznov, and A.A. Yakovlev, “Giant lateral photovoltaic effect in the TiO<sub>2</sub>/SiO<sub>2</sub>/p-Si heterostructure,” *St. Petersburg Polytechnic University Journal. Physics and Mathematics*, **15**, 32-37 (2022).
- [15] M.C. Özdemir, Ö. Sevgili, I. Orak, and A. Turut, “Determining the potential barrier presented by the interfacial layer from the temperature induced I-V characteristics in Al/p-Si Structure with native oxide layer,” *Mater. Sci. Semicond. Process*, **125**, 105629 (2021). <https://doi.org/10.1016/j.mssp.2020.105629>
- [16] A. Ashery, M.M. Elnasharty, I.M. El Radaf, “Current Transport and Dielectric Analysis of Ni/SiO<sub>2</sub>/p-Si Diode Prepared by Liquid Phase Epitaxy,” *Silicon*, **14**, 153–163 (2022). <https://doi.org/10.1007/s12633-020-00808-4>
- [17] A. Ashery, M.M. Elnasharty, A.A. Khalil, and A.A. Azab, “Negative resistance, capacitance in Mn/SiO<sub>2</sub>/p-Si MOS structure,” *Mater. Res. Express*, **7**, 085901 (2020). <https://doi.org/10.1088/2053-1591/aba818>
- [18] X. Ling, P.F. Zhu, K. Song, and X. Li, “The lateral photovoltaic effect in the Ni-SiO<sub>2</sub>-Si structure with bias,” *Research Square*, 1-19 (2023). <https://doi.org/10.21203/rs.3.rs-2903257/v1>
- [19] N.N.K. Reddy, S. Godavarthi, K.M. Kumar, V.K. Kummara, S.V.P. Vattikuti, H.Sh. Akkera, Y. Bitla, et al., “Evaluation of temperature dependent electrical transport parameters in Fe<sub>3</sub>O<sub>4</sub>/SiO<sub>2</sub>/n Si metal–insulator semiconductor (MIS) type Schottky

- barrier heterojunction in a wide temperature range,” J. Mater. Sci. Mater. Electron. **30**, 8955–8966 (2019). <https://doi.org/10.1007/s10854-019-01223-1>
- [20] N.V. Volkov, M.V. Rautskii, A.S. Tarasov, I.A. Yakovlev, I.A. Bondarev, A.V. Lukyanenko, S.N. Varnakov, and S.G. Ovchinnikov, “Magnetic field-driven lateral photovoltaic effect in the Fe/SiO<sub>2</sub>/p-Si hybrid structure with the Schottky barrier,” Physica E Low Dimens. Syst. Nanostruct. **101**, 201–207 (2018). <https://doi.org/10.1016/j.physe.2018.03.027>
- [21] M.K. Bakhadyrkhanov, N.F. Zikrillaev, S.B. Isamov, and S.V. Koveshnikov, in: *Photoelectrical Phenomenon in Silicon with multicharged nanostructures*, (Technical University press, Tashkent, Uzbekistan, 2017). pp. 252-254.
- [22] E.U. Arzikulov, and I.P. Parmankulov, “Vibrations of Photocurrent Induced by IR Light in Silicon with Quantum Dots,” Surf. Eng. Appl. Electrochem. **44**, 504–507 (2008). <https://doi.org/10.3103/S1068375508060148>
- [23] M.K. Bakhadyrkhanov, K.S. Ayupov, G.Kh. Mavlyanov, and S.B. Isamov, “Negative Magnetoresistance in Silicon with Manganese Atom Complexes [Mn<sup>+</sup>]<sup>4</sup>,” Semicond. **44**, 1145–1148 (2010). <https://doi.org/10.1134/S106378261009006X>
- [24] E.U. Arzikulov, and J.T. Ruzimurodov, “Magnetic Resistance of Silicon Specimens with Manganese Impurities,” J. Commun. Technol. Electron. **52**, 1049–1053 (2007). <https://doi.org/10.1134/S1064226907090148>
- [25] M.K. Bakhadyrkhanov, S.B. Isamov, N.F. Zikrillaev, and E.U. Arzikulov, “Infrared Quenching of Photoconduction in Silicon with Multicharge Manganese Clusters,” Surf. Eng. Appl. Electrochem. **49**, 308–311 (2013). <https://doi.org/10.3103/S1068375513040029>
- [26] M.K. Bakhadyrkhanov, G.K. Mavlonov, S.B. Isamov, Kh.M. Iliev, K.S. Ayupov, Z.M. Saparniyazova, and S.A. Tacilin, “Transport properties of silicon doped with manganese via low-temperature diffusion,” Inorg. Mater. **47**, 479–483 (2011). <https://doi.org/10.1134/S0020168511050062>
- [27] M. Mebarki, A. Layadi, A. Guittoum, A. Benabbas, B. Ghebouli, M. Saad, and N. Menni, “Structural and electrical properties of evaporated Fe thin films,” Appl. Surf. Sci. **257**(16), 7025–7029 (2011). <https://doi.org/10.1016/j.apsusc.2011.02.114>
- [28] Y. Lin, J. Xie, H. Wang, Y. Li, C. Chavez, S. Lee, S.R. Foltyn, et al., “Green luminescent zinc oxide films prepared by polymer-assisted deposition with rapid thermal process,” Thin Solid Films. **492**(1-2), 101–104 (2005). <https://doi.org/10.1016/j.tsf.2005.06.060>
- [29] Z.B. Fang, Z.J. Yan, Y.S. Tan, X.Q. Liu, and Y.Y. Wang, “Influence of post-annealing treatment on the structure properties of ZnO films,” Appl. Surf. Sci. **241**(3-4), 303–308 (2005). <https://doi.org/10.1016/j.apsusc.2004.07.056>

#### ЛАТЕРАЛЬНИЙ ФОТОЕЛЕКТРИЧНИЙ ЕФЕКТ У КРЕМНІЄВИХ ГІБРИДНИХ СТРУКТУРАХ ЗАЛІЗО-ДІОКСИД КРЕМНІЮ

Ешкуват У. Арзікулов<sup>а</sup>, Алішер Д. Нурімов<sup>а</sup>, Ф.А. Салахітдінов<sup>а</sup>, У.А. Аширов<sup>а</sup>,  
Т.С. Шарафова<sup>а</sup>, А.С. Худжанов<sup>б</sup>, Р.М. Усанов<sup>а</sup>

<sup>а</sup> Самаркандський державний університет імені Шарофа Рашидова,  
м. Самарканд, Університетський бульвар 15, 140000, Республіка Узбекистан

<sup>б</sup> Самаркандський державний університет ветеринарної медицини, тваринництва і біотехнологій,  
м. Самарканд, вул. Мірзо Улуг Бек 77, 140003, Республіка Узбекистан

У статті наведено експериментальні результати з технології отримання та дослідження латерального фотоелектричного ефекту (ЛФЕ) в гібридних структурах типу (ГС) Fe/SiO<sub>2</sub>/p-Si<B, Mn> та Fe/SiO<sub>2</sub>/n-Si<B, Mn>. Технологія отримання таких ГС складається з двох частин: по-перше, отримання компенсованих (К), висококомпенсованих (ВК) і надкомпенсованих (НК) зразків Si<B, Mn>. По-друге, отримання HS Fe/SiO<sub>2</sub>/p-Si<B, Mn> і Fe/SiO<sub>2</sub>/n-Si<B, Mn>. На основі результатів показано, що було отримано достатньо хороший ГС. Експерименти по вивченню ЛФЕ показали, що в досліджуваних ГС спостерігається виражений прояв латерального фотоелектричного ефекту, величина і характер якого сильно залежать від типу провідності та питомого опору компенсованого кремнію. Спостережувані особливості пояснюються тим, що в зразках кремнію К, ВК та НК домішки, які створюють глибокі рівні в забороненій зоні кремнію, утворюють різноманітні багатозарядні комплекси, які модулюють енергетичну зону кремнію, що призводить до суттєвих змін його фізико-хімічних та генераційно-рекомбінаційних властивостей, що лежить в основі спостережуваних ефектів. На основі досліджень ЛФЕ залежно від контактної відстані можна визначити чисельні значення дифузійних довжин другорядних носіїв струму ( $L_p$  та  $L_n$ ), їх час життя ( $\tau_p$  та  $\tau_n$ ) та коефіцієнтів дифузії ( $D_p$  та  $D_n$ ) на матеріалі підкладки.

**Ключові слова:** латеральний фотоелектричний ефект; гібридна структура; компенсований кремнію; фотонапруга; дифузія; випаровування; оксид; p-n перехід

## INVESTIGATION OF THE MAGNETIC PROPERTIES OF SILICON DOPED WITH RARE-EARTH ELEMENTS

 **Khodjakbar S. Daliev**<sup>a#</sup>,  **Zavkiddin E. Bahronkulov**<sup>b\*</sup>,  **Jonibek J. Hamdamov**<sup>b#</sup>

<sup>a</sup> Branch of the Federal State Budgetary Educational Institution of Higher Education “National Research University MPEI”,  
1 Yogdu st., Tashkent, Uzbekistan

<sup>b</sup> Institute of Semiconductor Physics and Microelectronics at the National University of Uzbekistan,  
20 Yangi Almazar st., Tashkent, 100057, Uzbekistan

\*Corresponding Author e-mail: [zbahronkulov@inbox.ru](mailto:zbahronkulov@inbox.ru)

Received July 24, 2023; revised September 13, 2023; accepted September 15, 2023

This article discusses the electrical properties of silicon doped with rare earth elements (REE). Atoms of rare earth elements (REE) diffused onto the surface of the silicon substrate. To measure the electrical parameters, samples of n-Si, n-Si<Lu>, n-Si<Er> and n-Si<Gd> were prepared and their electrical properties were determined using the Hall effect, four-probe and thermal probe methods. The studies were carried out in the temperature range 77÷300 K. The samples were ohmically contacted using a mixture of 1% Sb + 99% Au for measurement on the HMS500 instrument. The specific resistance of the samples in layers, the concentration of charge carriers, and the mobility of the samples were also studied by the magnetoresistance method. The electrical parameters of the samples were measured on an Ecopia Hall effect measuring system (HMS5000).

**Key words:** Silicon; Lutetium; Rare earth elements; Magnetoresistive; Diffusion; Magnetic field; Temperature

**PACS:** 78.30.Am

### INTRODUCTION

At present, special attention is paid to the study of the nature of defects formed by the introduction of atoms of rare earth elements (REE) into semiconductor single crystals by the diffusion method. A lot of scientific work is being done on the formation of a deep energy level in silicon, which is the main material of semiconductor devices, its doping with additives that allow changing its properties, and the study of their resistance to heat and radiation [8-9].

Modern microelectronics main material silicon that it was due to, silicon in single crystal defects appear to be such as technological processes to study is very important. The physical and optical parameters of silicon doped with hafnium and lanthanum have been studied [1,5,6].

As is known, the first single crystals used for the manufacture of semiconductor devices are not without defects. Point and volume distortions of the crystal lattice occur in a single crystal even during its growth. In subsequent device manufacturing processes, these defects are filled with other defects in various parts of the semiconductor structure. In recent years, there has been a sharp increase in interest in semiconductor materials with special properties. Doping with rare earth elements is more widely used to obtain such materials. This is due to the use of silicon doped with these compounds in special semiconductor devices, for example, various types of photoreceptors, solar cells, high-radiation and thermally stable devices. In addition, most of the experiments were carried out using the Hall effect, and the sensitivity of measuring electrical conductivity, magnetic susceptibility, and other measurement methods is relatively low.

### MATERIALS AND METHODS

Investigate for the Czochralski method grown n - type ( $\rho=40 \Omega \times \text{cm}$ ) dimensions  $7 \times 6 \times 1 \text{ cm}^3$ , to the (111) surface suitable silicon from a single crystal was used. Source diffusion was created by sputtering metallic lutetium (purity ~ 99.99).

Propagation from making the first silicon into monocrystals mechanic and chemical processing considering VUP-4 device using single crystal silicon on the surface of lutetium atoms high vacuum ( $10^{-6} \text{ mmHg.}$ ) under sprayed Use of quartz glass high vacuum ampoule received. The diffusion method has been used in many studies to study the properties of silicon with rare earth elements, transition elements, and refractory elements [1-7].

Distribution at high temperature 1523 K oven SUOL-0.4 30 hours of use time between was spent. From spreading after the samples have cooled rapidly. After diffusion annealing samples repeatedly washed in hydrofluoric acid, aqua regia, and also in a boiling mixture  $\text{H}_2\text{O}_2$ : HCl. Such washing usually allows almost completely remove the source of diffusion remaining on the surface of the sample [2-5].

After this edge of the sample cleaned to a depth of ~ 10  $\mu\text{m}$ , significantly greater than the diffusion depth. The profile was determined by etching thin layers (in 1HF:50HNO<sub>3</sub> solution) and measuring surface resistance of a four-probe sample method, as well as the method Hall effect using Van der Pauw probes. Samples on the device HMS 500 measure for a mixture of 1% Sb + 99% Au received through an ohmic contact. The 175 Lu isotope was deposited onto the surface of a silicon sample. After diffusion and subsequent washes, as well as in the process of removing the layers, X-ray



diffraction of samples was carried out to control the uniformity of alloying. The electrical parameters of the samples were determined using the Hall effect. Input concentration for the experiment: n-Si<Er> ( $N_{Er} = 2.3 \times 10^{17} \text{ cm}^{-3}$ ), n-Si<Lu> ( $N_{Lu} = 2.43 \times 10^{14} \text{ cm}^{-3}$ ) and n-Si<Gd> ( $N_{Gd} = 1 \times 10^{16} \text{ cm}^{-3}$ ). samples are prepared.

### RESULTS AND DISCUSSION

In this work, we studied the magnetic field dependences of the magnetoresistive effect and the Hall effect in silicon doped with Er, Gd, and Ho. Doping with rare earth elements (REE) was carried out in the process of growing from a melt according to the Czochralski method. The magnetic field dependences of the magnetoresistance (MR) and the Hall effect were studied in a constant magnetic field up to 1.4 T in the temperature range 20–300 K. The study of the temperature dependence of the Hall mobility  $\mu_H(T)$  showed that in samples doped with REE, its value was ~10–20% lower than in the control material, which indicates that additional scattering of charge carriers occurs in Si<REE> due to the inclusion of lanthanides.

The magnetic field dependences of the magnetoresistive of the control undoped single crystals over the entire temperature range have a close to quadratic  $(\Delta\rho/\rho_0) \sim b_r (\mu_H B)^\gamma$ , where  $\gamma=1.8-1.9$ , dependence on the magnetic field. At  $T = 300 \text{ K}$ , REE doping did not change the general form of the dependence of magnetoresistive on the magnetic field, although the magnitude of the magnetoresistive effect decreased significantly. At liquid nitrogen temperature in Si<REE> in a weak magnetic field ( $B < 0.5 \text{ T}$ ), the magnetoresistive effect is negative and reaches its maximum value in a field  $B \approx 0.25 \text{ T}$ . Negative magnetoresistive in fields  $B > 0.3 \text{ T}$  begins to decrease and passes into the region of positive magnetoresistance. A further decrease in temperature to 20 K leads to the disappearance of the negative MR and the appearance of a positive magnetoresistive, despite the fact that the charge transfer mechanism has not changed. Immediately after growth, lanthanides in silicon show no electrical activity. However, later studies did not confirm this assumption. Samples magnet resistance magnet in the field  $\frac{\Delta\rho}{\rho_0} \sim b_r (\mu_H B)^\gamma$  expression via connected [10-16]. Here  $\rho$  - comparison resistance  $b_r$ - magnetic resistance  $\mu_H$ - magnetic field constant, B - magnetic field induction.

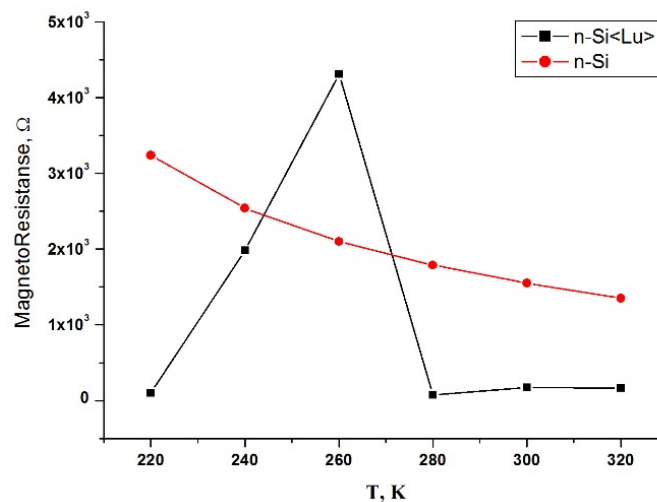


Figure 1. T =220÷320 K magnetic resistance to temperature depending on: n-Si (control) (1); n-Si <Lu> (2).

In Figure 1, the red line is lutetium doped with silicon, the black line is the control sample. As can be seen from the figure, the magnetic resistance of a single crystal of silicon (control sample) in the temperature range 220÷320 K practically did not change.

The magnetic resistance of a silicon sample doped with lutetium (n- Si<Lu>) increased from 101 Ω to 4308 Ω in the temperature range 220÷260 K, decreased from 4308 Ω to 87 Ω in the temperature range 260÷280 K, increased from 87 Ω to 175 Ω in the temperature range 280÷300 K and after 300 K the value has not changed. It was noticed that the magnetic resistance of the control sample decreased exponentially from 3249 Ω to 1349 Ω in the temperature range 220-260 K. As can be seen from Fig. 1, lutetium atoms have influenced the magnetic resistance of single-crystal silicon. The resistivity of our lutetium-doped silicon sample increased dramatically below 220 K. Since the lutetium-silicon alloy is being studied for the first time, the magnetoresistance compared with samples of silicon with rare earth elements.

Throughout the studied range of magnetic fields, the criterion of a classically weak ( $\mu_H B \ll 1$ ) magnetic field was fulfilled, and the value of the magnetoresistance coefficient lay within the range  $b = 0.2...0.4$ , which is close to the theoretical value of b characteristic of scattering charge carriers by acoustic phonons background  $b_t^{phon} = 0.27$ . The slightly overestimated value of b may be caused by the additional contribution of the geometric effect to the magnetoresistance due to the short-circuiting of the Hall emf by current contacts. The sample resistance in the absence of a magnetic field is due to both the scattering of charge carriers by acoustic phonons and their scattering by magnetic clusters with a random orientation of magnetic moments. According to the giant magnetoresistive model, an external magnetic field orients the magnetic moments of clusters in the direction of the field, which leads to a decrease in the

scattering of charge carriers (resistance of the sample), i.e. to negative magnetoresistive. The smallness of the negative magnetoresistance in the studied Si<REE> samples is due to the fact that the conditions for observing a giant magnetoresistive are far from optimal, when the sizes of isolated magnetic clusters and the distance between them is of the order of the mean free path of the carriers.

On Fig. 2 shows a graph of the temperature dependence of conductivity. The red line is an n-Si sample (control), and the black line is a single crystal of silicon doped with lutetium (n-Si<Lu>). The mobility of the control sample in the range of 220÷320 K did not change. In a sample of single-crystal silicon (n-Si<Lu>) doped with lutetium, the electron mobility increased by  $3 \times 10^9 \text{ cm}^2/\text{Vs}$  in the range 220÷240 K, decreased by  $5.35 \times 10^{19} \text{ cm}^2/\text{Vs}$  at 240÷260 K, increased by  $1.13 \times 10^{19} \text{ cm}^2/\text{Vs}$  in the temperature range 260÷280 K and after 280 K coincided with the control sample.

As a result of our studies in Fig. 3 it is established that single-crystal silicon doped with rare-earth elements does not change the general form of the dependence of magnetic resistance on the magnetic field at  $T = 300 \text{ K}$ . At the same time, due to the uneven distribution of lutetium atoms in a single crystal of silicon, the magnetic resistance coefficient of the sample was higher than the theoretical value. As can be seen from Fig. 3, the magnetic resistance of silicon samples doped with rare earth elements in a weak magnetic field ( $B < 0.5 \text{ T}$ ) at liquid nitrogen temperature has a negative value and reaches a maximum value in the field  $B \approx 0.25 \text{ T}$ .  $B > 0.3 \text{ T}$  changed to a positive value. This indicates that the Hall constant in rare earth doped silicon is almost positive.

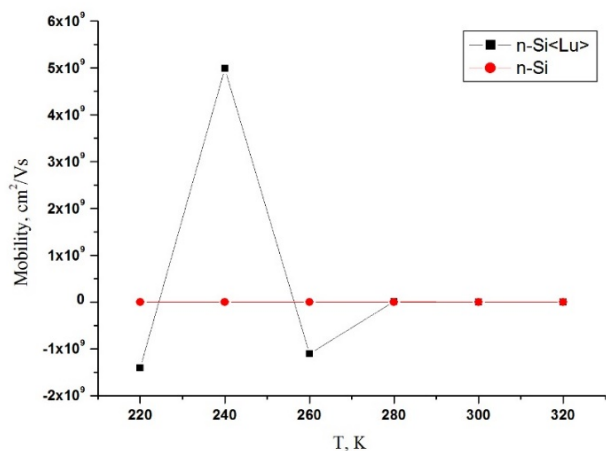


Figure 2.  $T = 220 \div 320 \text{ K}$  mobility to temperature depending on: n-Si (1); n-Si<Lu> (2)

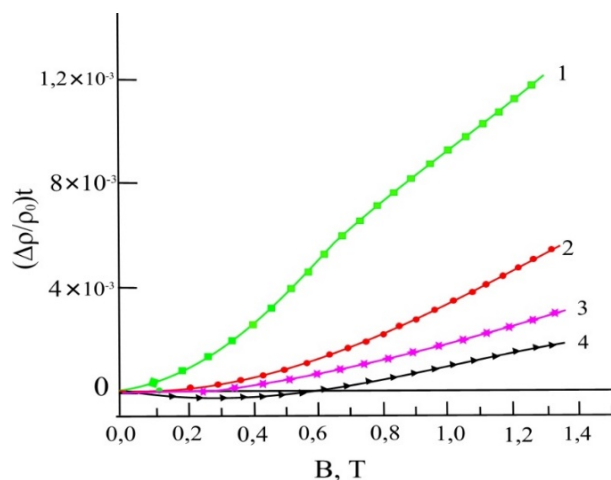


Figure 3. Room temperature control n - Si (1); n - Si<Gd> (2); n-Si<Er> (3); and n-Si<Lu> (4), magnet resistance magnet samples in the field dependence

The magnetic resistance of silicon samples doped with rare earth elements at 77 K is evidenced by the nature of the dependence of the magnetic resistance on the magnetic field (Fig. 4). This resistance is the algebraic sum of the measured positive and negative component values:

$$\Delta\rho_{\Sigma} = \Delta\rho_{-} + \Delta\rho_{+}$$

The closest to optimal conditions for observing negative MR due to scattering by magnetic clusters are realized in samples doped with erbium at a concentration of  $2.3 \times 10^{17} \text{ cm}^{-3}$ . A decrease in the REE concentration leads to a decrease in the size of lanthanide inclusions and, ultimately, to a decrease in the negative MR (see Fig. 4).

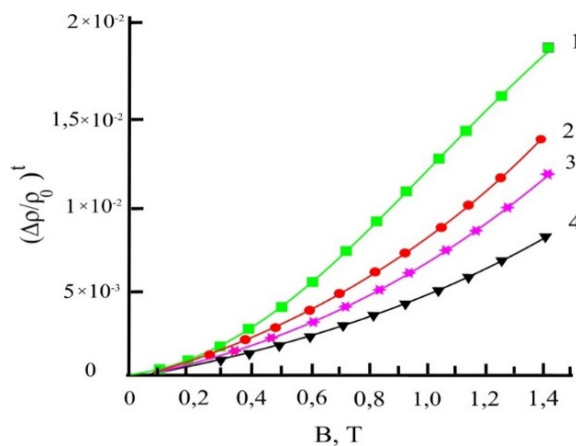


Figure 4. At a temperature of 77÷300 K, control n - Si (1); n - Si <Gd> (2); n - Si <Er> (3); and n - Si <Lu> (4) samples magnet resistance magnet in the field dependence.

An additional confirmation of this mechanism of the negative component of the MR at  $B < 0.6$  T can be the independence of the Hall constant on the magnitude of the magnetic field, which is not typical for the band transfer mechanism and "traditional" mechanisms of scattering of charge carriers, for which the Hall factor decreases with increasing magnetic field in classical magnetic fields.

The results of studies carried out at temperatures of 300 and 77 K show that single crystals of silicon with rare earth elements do not change their general properties at both temperatures. According to the results obtained, it was found that the Si <Lu> sample is more resistant to magnetism than the Si <Er> and Si <Gd> samples.

### CONCLUSIONS

A temperature graph of the magnetic resistance of samples doped with lutetium (n- Si <Lu>) has been obtained. Such a conclusion can be drawn from the analysis of the obtained results.

1. Magnetic aging of lutetium-doped silicon (n- Si <Lu>) and control (n- Si) samples at room and nitrogen temperatures was studied for the first time.

2. After alloying single-crystal silicon with lutetium atoms, it was found for the first time that the magnetic resistance does not change at room temperature and changes at nitrogen temperature.

3. Samples in a weak magnetic field ( $B < 0.5$  T) The magnetic resistance of silicon samples doped with Lu, Er and Gd elements at liquid nitrogen temperature has a negative value and reaches a maximum value in a field  $B \approx 0.25$  T.

This indicated that the Hall constant in silicon doped with Lu, Er and Gd elements is positive.

4. In the temperature range of 77-300K, it was established that the resistance of n-Si<Lu> samples to a magnetic field is higher than that of n-Si<Er> and n-Si<Gd> samples.

### ORCID

✉ Khodjakbar S. Daliev, <https://orcid.org/0000-0002-2164-6797>; ✉ Zavkiddin E. Bahronkulov, <https://orcid.org/0009-0002-9843-8344>

✉ Jonibek J. Hamdamov, <https://orcid.org/0000-0003-2728-3832>

### REFERENCES

- [1] Sh.B. Utamuradova, Kh.S. Daliev, E.K. Kalandarov, and Sh.Kh. Daliev, "Features of the behavior of lanthanum and hafnium atoms in silicon," *Technical Physics Letters*, **32**(6), 469–470 (2006). <https://doi.org/10.1134/S1063785006060034>
- [2] Kh.S. Daliev, Sh.B. Utamuradova, I.Kh. Khamidzhonov, A.Zh. Akbarov, I.K. Mirzairova, and Zh. Akimova, "Thermally Induced Deep Centers in Silicon Doped with Europium or Lanthanum," *Inorganic Materials*, **37**(5), 436–438 (2001). <https://doi.org/10.1023/A:1017556212569>
- [3] K.P. Abdurakhmanov, Sh.B. Utamuradova, Kh.S. Daliev, S.G. Tadjy-Aglaeva, and R.M. Érgashev, "Defect-formation processes in silicon doped with manganese and germanium," *Semiconductors*, **32**(6), 606–607 (1998). <https://doi.org/10.1134/1.1187448>
- [4] K.P. Abdurakhmanov, Kh.S. Daliev, Sh.B. Utamuradova, and N.Kh. Ochilova, "On defect formation in silicon with impurities of manganese and zinc," *Applied Solar Energy* (English translation of *Geliotekhnika*), **34**(2), 73–75 (1998).
- [5] Sh.B. Utamuradova, A.V. Stanchik, and D.A. Rakhmanov, "X-Ray Structural Investigations Of n-Si<Pt> Irradiated with Protons," *East Eur. J. Phys.* **2**, 201 (2023). <https://doi.org/10.26565/2312-4334-2023-2-21>
- [6] Sh.B. Utamuradova, and D.A. Rakhmanov, "Effect of Holmium Impurity on the Processes of Radiation Defect Formation in n-Si<Pt>," *Annals of the University of Craiova, Physics*, **32**, 132–136 (2022). [https://cis01.central.ucv.ro/pauc/vol/2022\\_32/15\\_PAUC\\_2022\\_132\\_136.pdf](https://cis01.central.ucv.ro/pauc/vol/2022_32/15_PAUC_2022_132_136.pdf)
- [7] Sh.B. Utamuradova, Kh.S. Daliev, Sh.Kh. Daliev, and K.M. Fayzullaev, "Influence of chromium and iron atoms on defect formation processes in silicon," *Applied Physics*, (6), 90 (2019). <https://applphys.orion-ir.ru/appl-19/19-6/PF-19-6-90.pdf> (in Russian)
- [8] Sh.B. Utamuradova, D.A. Rakhmanov, A.S. Doroshkevich, Z. Slavkova, and M.N. Ilyina, "Impedance spectroscopy of p-Si<Pt>, p-Si<Cr> irradiated with protons," *Advanced Physical Research*, **5**(1), 5–11 (2023). [http://jomardpublishing.com/UploadFiles/Files/journals/APR/V5N1/Utamuradova\\_et\\_al.pdf](http://jomardpublishing.com/UploadFiles/Files/journals/APR/V5N1/Utamuradova_et_al.pdf)
- [9] Sh.B. Utamuradova, Sh.Kh. Daliev, A.V. Stanchik, and D.A. Rakhmanov, "Raman spectroscopy of silicon, doped with platinum and irradiated by protons," *E3S Web of conferences*, **402**, 14014 (2023). [https://www.e3s-conferences.org/articles/e3sconf/abs/2023/39/e3sconf\\_transsiberia2023\\_14014/e3sconf\\_transsiberia2023\\_14014.html](https://www.e3s-conferences.org/articles/e3sconf/abs/2023/39/e3sconf_transsiberia2023_14014/e3sconf_transsiberia2023_14014.html)
- [10] M.S. Sercheli, and C. Rettori, "Magnetic properties of a-Si films doped with rare-earth elements," *Physical review B, Condensed matter*, **68**, 174418 (2003). <http://dx.doi.org/10.1103/PhysRevB.68.174418>
- [11] J. Wen, N. Li, P. Lin, Y. Han, G. Chen, L. Bai, S. Guo, et al., "Electronic, magnetic and photocatalytic properties of Si doping in g-ZnO monolayer with point defects," *Physica E: Low-dimensional Systems and Nanostructures*, **134**, 114913 (2021). <https://doi.org/10.1016/j.physe.2021.114913>
- [12] J.H. Park, H. Takagi, K. Nishimura, H. Uchida, M. Inoue, J.H. Park, J.K. Cho, "Magneto-optic spatial light modulators driven by an electric field," *J. Appl. Phys.* **93**, 8525–8527 (2003). <https://doi.org/10.1063/1.1557836>
- [13] P.S. Kireev, *Semiconductor Physics*, 2nd ed. (Mir, Moscow, 1978).
- [14] A. Telegin, and Y. Sukhorukov, "Magnetic Semiconductors as Materials for Spintronics," *Magnetochemistry*, **8**(12), 173 (2022). <https://doi.org/10.3390/magnetochemistry8120173>
- [15] Y.P. Sukhorukov, N.N. Loshkareva, A.V. Telegin, E.V. Mostovshchikova, V.L. Kuznetsov, A.R. Kaul, A.N. Vinogradov, "IR radiation modulator based on the effect of magnetotransmission in lanthanum manganite operating near room temperature," *Tech. Phys. Lett.* **29**, 904–906 (2003). <https://doi.org/10.1134/1.1631359>
- [16] H.S. Nalva, *Handbook of Thin Film Materials: Nanomaterials and Magnetic Thin Films*, Vol. 5, (Academic Press, 2002). ISBN 9780125129084

**ДОСЛІДЖЕННЯ МАГНІТНИХ ВЛАСТИВОСТЕЙ КРЕМНІЮ ЛЕГОВАНОГО  
РІДКОЗЕМЕЛЬНИМИ ЕЛЕМЕНТАМИ****Ходжакбар С. Далієв<sup>а</sup>, Завкідін Е. Бахронкулов<sup>б</sup>, Джонібек Дж. Хамдамов<sup>б</sup>**<sup>а</sup> Філія ФДБУ «Національний дослідницький університет МПЕІ»,

Йогду, 1, Ташкент, Узбекистан

<sup>б</sup> Інститут фізики напівпровідників та мікроелектроніки Національного університету Узбекистану,  
100057, Ташкент, Узбекистан, вул. Янги Алмазар, 20

У цій статті розглядаються електричні властивості кремнію, легованого рідкоземельними елементами (РЗЕ). Атоми рідкоземельних елементів (РЗЕ) дифундували на поверхню кремнієвої підкладки. Для вимірювання електричних параметрів були підготовлені зразки n-Si, n-Si<Lu>, n-Si<Er> і n-Si<Gd> та визначені їх електричні властивості за допомогою ефекту Холла, чотирізондового та термічного зондового методів. Дослідження проводили в інтервалі температур 77÷300 К. Омічний контакт зразків створювали сумішшю 1% Sb + 99% Au для вимірювання на приладі HMS500. Також питомий опір зразків у шарах, концентрацію носіїв заряду та рухливість зразків досліджували методом магнітоопору. Електричні параметри зразків вимірювали за допомогою системи вимірювання ефекту Холла Есорія (HMS5000).

**Ключові слова:** кремній; лутецій; рідкоземельні елементи; магніторезистивний; дифузія; магнітне поле; температура

## ENHANCING THE PERFECTION OF A SILICON CRYSTAL DOPED WITH NICKEL AND ZINC IMPURITIES

 **Daryabay M. Esbergenov**<sup>a\*</sup>,  **Elmira M. Naurzalieva**<sup>b</sup>, **Sabirbay A. Tursinbaev**<sup>a</sup>

<sup>a</sup> Nukus State Pedagogical Institute Named After Ajiniyaz, Nukus, Republic of Karakalpakstan

<sup>b</sup> Nukus Branch of Tashkent University of Information Technologies Named After al-Khwarizmi, Republic of Karakalpakstan

\*Corresponding Author e-mail: [edaryabay@gmail.com](mailto:edaryabay@gmail.com)

Received October 4, 2023; revised October 27, 2023; accepted November 10, 2023

This research paper presents the findings of an investigation into the interaction between zinc (Zn) and nickel (Ni) impurity atoms within a silicon (Si) matrix, which were doped sequentially in various combinations. The characterization techniques employed for this study encompass X-ray diffraction and IR-Fourier spectrometry. It is noteworthy that the degree of crystallinity exhibited by the silicon lattice, subject to the introduction of Zn and Ni impurities, is contingent upon the methodology employed for impurity incorporation. The results of this study reveal a distinctive trend in the optical properties of these doped silicon samples. Specifically, upon the introduction of Zn atoms into silicon that was pre-doped with Ni (Si<Ni, Zn>), there is a concomitant reduction in the concentration of optically active oxygen atoms. Remarkably, this alteration in the dopant composition leads to a marked enhancement in the transparency of the silicon crystal. In stark contrast, when the doping sequence is reversed (Si<Ni, Zn> Ni>), an opposing effect is observed, resulting in a diminishment of crystal transparency. These findings underscore the intricate interplay between the introduced impurity atoms, the dopant sequence, and their collective impact on the optical properties of the silicon matrix. Such insights contribute to our comprehension of the nuanced behavior of doped silicon and have implications for applications requiring tailored optical characteristics in semiconductor materials.

**Keywords:** Silicon; Zinc; Nickel; Diffusion; X-ray diffraction spectrum; IR transmission

**PACS:** 42.55.Ye, 61.72.Yx, 61.72.Tt

### INTRODUCTION

Over the past few decades, extensive research has been conducted worldwide to investigate the behavior of defects in semiconductors and elucidate the mechanisms underlying their formation. Additionally, significant efforts have been directed towards the simultaneous mitigation of undesirable defects [1-9]. The scientific community has developed models to expound upon a diverse array of phenomena, encompassing topics such as the profile characteristics of dopants, conditions governing diffusion doping, non-equilibrium effects induced by chemical reactions or radiation-induced damage, diminishment in the electrical activation of dopant impurities due to the creation of impurity phases, clusters, and complexes involving other impurities, as documented in references [6-8]. Furthermore, research has probed the phenomenon of dopant accumulation at the interfaces and surfaces of semiconductor materials. The realm of transition metal impurities in silicon (Si) has been a subject of long-standing investigation, yielding a comprehensive understanding of the properties and electrophysical parameters of isolated atoms [9]. However, relatively limited attention has been directed towards the study of complexes involving atoms of multiple elements that facilitate the nucleation of precipitates [10, 11]. Transition element impurities, known for their ability to introduce deep energy levels within the band gap of silicon, exhibit remarkable mobility. Consequently, the mechanisms governing the motion of impurity atoms are contingent upon the doping methodology employed for their incorporation into the primary crystal matrix. The heightened mobility of these impurities engenders interactions with other uncontrolled impurities present in silicon, thereby giving rise to the formation of impurity pairs.

In light of these considerations, the investigation of defect formation processes in silicon doped with multiple impurity atoms of transition elements, specifically Ni and Zn, and their responses to various influencing factors, such as the interaction between technological and uncontrolled impurity defects in silicon [12], assumes paramount importance. Furthermore, understanding the impact of thermal and radiation-induced defects on the development of a defect structure in silicon when doped with Ni and Zn impurities emerges as a significant research challenge. These circumstances necessitate the exploration of novel theoretical and practical methodologies aimed at uncovering the mechanisms governing the formation and reconfiguration of structural defect complexes at the atomic level, thereby facilitating precise control over the properties of silicon doped with diverse impurities.

Consequently, the primary objective of this study was to delve into the defect structure and its interplay with technological impurities in the presence of rapidly diffusing transition elements, Ni and Zn, within the silicon lattice. To achieve this, we employed IR-Fourier spectroscopy and X-ray diffraction analysis.

### MATERIAL AND METHOD

For the experiments we used samples of n-type silicon grown by the Czochralski method with a resistivity of 100 Ohm·cm. In these samples, the phosphorus concentration was about  $\sim 10^{13}$  cm<sup>-3</sup>, the oxygen concentration

was  $\sim 10^{17} \text{ cm}^{-3}$ . During the diffusion of impurity atoms, metal Zn and Ni with a purity of 99.99% were deposited on the cleaned surface of the samples in vacuum. Doping of silicon samples with impurities was carried out by the thermal diffusion method in quartz ampoules evacuated to vacuum, in the temperature range from  $T=1000^\circ\text{C}$  to  $1100^\circ\text{C}$  for  $t = 1-5 \text{ h}$ . As a result, 3 groups of silicon samples were obtained:

I) the first group was characterized by separate diffusions of impurities of nickel and zinc atoms into the initial silicon (samples Si<P,Ni> and Si<P,Zn>);

II) the second group was obtained by diffusion of zinc atoms into silicon preliminarily doped with impurities of nickel atoms (samples Si<P,Ni,Zn>);

III) the third group was obtained by diffusion of nickel atoms into silicon preliminarily doped with impurities of zinc atoms (samples Si<P,Zn,Ni>).

Structural studies of the samples were carried out on a third-generation X-ray diffractometer of the Empyrean Malvern PANalytical L.T.D. type. (CuK $\alpha$  radiation,  $\lambda = 0.15418 \text{ nm}$ ) according to the  $\omega$ -2 $\theta$  scheme in the step-by-step scanning mode with a monochromator in the range  $2\theta =$  from  $15^\circ$  to  $140^\circ$  continuously with a scanning speed of  $0.33 \text{ deg/min}$  and an angular step of  $0.0200 \text{ (deg)}$ . The IR absorption spectrum of the samples was recorded using an FSM-1202 IR-Fourier spectrometer at room temperature.

### DESCRIPTION AND ANALYSIS OF RESULTS

After diffusion with Ni and Zn impurities, the values of the resistivity of the initial silicon changed significantly (Table 1). The table shows that in the overcompensated samples p-Si<P,Ni,Zn>  $\rho$  decreases, and in the samples p-Si<P,Zn,Ni>  $\rho$  increases. Such a difference in the value of  $\rho$  shows that the concentration of electroactive Ni atoms in p-Si<P,Ni,Zn> is higher than in p-Si<P,Zn,Ni> samples.

**Table 1.** The values of the resistivity of the samples

Samples	Technology of doping	Diffusion Mode	Conductivity type	$\rho$ (Ohm·cm)
Si<P>	–	–	N	100
Si<P, Ni>	Spraying	T=1200 $^\circ$ C, t=2 h	N	305
Si<P, Zn>	Spraying		p	121
Si<P, Ni, Zn>	Consistently: Ni - deposition, Zn - sputtering		p	64.3
Si<P, Zn, Ni>	Consistently: Zn - sputtering, Ni - deposition		p	200

In our previous works [12, 13], using capacitive spectroscopy and the photoconductivity method, we identified the energy spectra of deep levels (DL) created by Ni and Zn atoms in Si upon their diffusion introduction and showed that in n-Si<P, Ni> DL  $E_C - 0.42 \text{ eV}$ ,  $E_V + 0.17 \text{ eV}$  are formed; in p-Si<Zn>, the DL  $E_V + 0.28 \text{ eV}$ ,  $E_C - 0.55 \text{ eV}$  are formed, and in the simultaneous doping of p-Si<P, Ni+Zn>, a new DL  $E_C - 0.25 \text{ eV}$  is formed;

After recording the IR absorption spectra in polished samples in the range from  $1000$  to  $1100 \text{ cm}^{-1}$ , the concentrations of optically active oxygen atoms  $N_O^{opt}$  and carbon  $N_C^{opt}$  were calculated. To calculate the concentration of optically active oxygen atoms  $N_O^{opt}$  and carbon  $N_C^{opt}$ , formulas (1, 2) were used.

$$N_O^{opt} = 3,3 \cdot 10^{17} \cdot \frac{1}{d} \ln \frac{I_0}{I}, \quad (1)$$

$$N_C^{opt} = 1,1 \cdot 10^{17} \cdot \frac{1}{d} \ln \frac{I_0}{I}, \quad (2)$$

where  $I_0$  – is the intensity of the incident light;  $I$  – the intensity of the transmitted light;  $d$ – is the sample thickness.

On Fig. 1 shows typical IR absorption spectra of optically active oxygen in samples: Si<P>; n-Si<P, Ni>; p-Si<P, Zn>; p-Si<P, Zn, Ni>; p-Si<P, Ni, Zn>, from which it can be seen that the oxygen band and the carbon band are visible in the region of wave numbers  $k = 1100 \text{ cm}^{-1}$  ( $9.1 \mu\text{m}$ ). Analysis of IR absorption in the region of  $1100 \text{ cm}^{-1}$  showed that in all silicon samples doped with nickel and zinc, there is a decrease in optically active oxygen  $N_O^{opt}$  and carbon  $N_C^{opt}$  within 20-40%. This can be explained by the difference between the limiting solubility of nickel and zinc in silicon at  $1200^\circ\text{C}$ , which, according to the data of [12,15,16], is  $N_{prev}^{Ni} \sim 10^{17} \text{ cm}^{-3}$  and  $N_{prev}^{Zn} \sim 10^{16} \text{ cm}^{-3}$  electrically active nickel and zinc  $N_{e.a.}^{Ni} \sim 10^{14} \text{ cm}^{-3}$  and  $N_{e.a.}^{Zn} \sim 10^{15} \text{ cm}^{-3}$ , respectively. This difference between  $N_{prev}$  and  $N_{e.a}$  is apparently due to the precipitation of some part of the dissolved nickel and zinc atoms on some sinks or the binding of Ni and Zn into neutral complexes, for example, such as Ni-O, Ni-C, Zn-O and Zn-C.

If we pay attention to the Si<Ni> samples, the IR band at  $1100 \text{ cm}^{-1}$  is shifted down, which indicates a loss of transparency of the crystal itself. According to the authors of [17], the opacity of Si<Ni> samples is associated with the arrangement of interstitial inactive nickel atoms: during quenching, clusters form and the sample becomes opaque.

It is also assumed that the temperature interval and time at which diffusion of nickel atoms into silicon is carried out leads to the dissolution of any kind of defective associations, precipitates of the second phase, accumulations of impurities, including nickel atoms and their uniform distribution in the silicon lattice, and rapid quenching Si<Ni> samples after diffusion leads to freezing of such a finely dispersed state of Ni atoms in the Si lattice [18–20].

In the case of Si<Zn> samples, a decrease in optically active oxygen of ~10-15% is observed, but without loss of transparency. This is most likely due to site substitutions of zinc atoms in the silicon crystal.

Interesting phenomena occur when Zn atoms are introduced into Si with pre-doped nickel atoms (Si<Ni, Zn>). Along with a decrease in the concentration of optically active oxygen atoms, the transparency of the crystal also improves, while in samples with the reverse combination of doping (Si<Zn, Ni>), the opposite effect is observed (Fig. 1, curves 4 and 5).

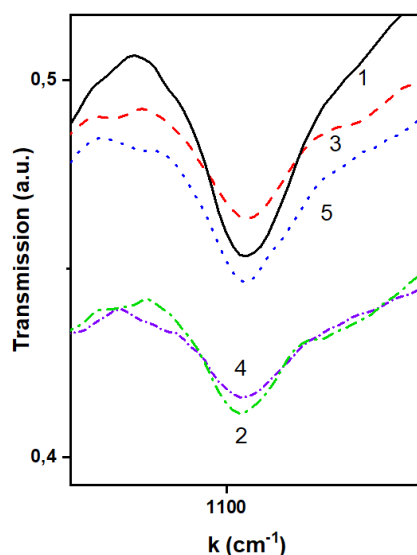


**Figure 1.** IR transmission spectrum of optically active oxygen in silicon:  
 1-Si<P>; 2-Si<Ni>; 3-Si<Zn>; 4-Si<Zn, Ni>; 5-Si<Ni, Zn>

To elucidate the cause of this phenomenon, an additional structural analysis of the samples was carried out. Fig. 2 shows the X-ray diffraction spectra of the main reflection Si (111) of samples Si<P>, n-Si<Ni>, n-Si<Zn>, n-Si<Zn, Ni>, n-Si<Ni, Zn>.

The maximum intensity of the Si (111) reflection and the small width (FWHM) testify to the high perfection of the silicon crystal structure, since the intensity of the main reflection indicates the number of atoms in the lattice site of the crystal. It can be seen from Fig. 2 that the intensity in the X-ray diffraction spectrum of silicon after doping with Ni atoms decreased by a factor of 10. This indicates that the periodicity of the crystal lattice is destroyed and the Ni atoms are in the interstitial position, which also underlies the results of IR absorption. But in the p-Si<P, Zn> single crystal, the intensity of the Si(111) reflection decreased insignificantly. It is known from the literature that Zn atoms mainly diffuse into crystal lattice sites.

After indexing the X-ray diffraction pattern of a substance with a cubic lattice, the crystal period is easily determined by formula (3)

$$a_{Si} = \frac{\lambda}{2\sin\theta} \sqrt{h^2 + k^2 + l^2}, \quad (3)$$

The average crystallite size was estimated using the Scherrer formula [21]

$$D = \frac{k\lambda}{\beta\cos\theta}, \quad (4)$$

where k- is the Scherrer coefficient (equal to 0.9),  $\lambda$  is the X-ray wavelength,  $\beta$  is the full width at half maximum (FWHM) of the crystalline peaks in radians,  $\theta$  is the Bragg angle of the diffraction peak, D is the grain size (in nm). The size of subcrystallites estimated from the width of this peak was  $D_{Si} \approx 24.55$  nm.

It can be seen from the Fig. 2 that the samples of the II-group (n-Si<Ni, Zn>) show the highest intensity, while the samples of the III-group (n-Si<Zn, Ni>) give the lowest intensity. This indicates that silicon sequentially doped with Ni and Zn impurities has a high degree of crystallinity, which depends on the intensity. The shift of the intensity of X-rays towards smaller scattering angles shows the microdistortion of the silicon crystal with an increase in the lattice constant d. If the position of the breakline is shifted without loss of intensity, then this indicates a uniform distortion of the crystal lattice [14].

The table lists the positions of the Si(111) peak and the average subcrystallite size of a silicon single crystal. Table 2 shows that the samples n-Si<Ni>, n-Si<Ni, Zn> and n-Si<Zn> cause inhomogeneous microdistortion, which reduces the

size of the silicon subcrystallite. In the case of n-Si<Ni, Zn> samples, the silicon crystal lattice is distorted uniformly, but the crystallite size increases by 30 nm relative to the original sample.

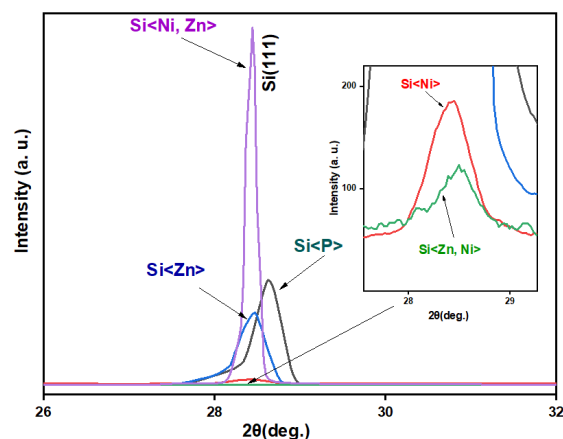


**Figure 2.** X-ray diffraction spectrum of silicon doped with nickel and zinc at various doping technologies

**Table 2.** Main parameters of X-ray diffraction pattern

Samples	Peak position 2θ, deg.	Average size of Si subcrystallite, nm
Si<P>	28.62±0.05	24.55±0.01
Si<P, Ni>	28.40±0.03	15.56±0.01
p-Si<P, Zn>	28.43±0.02	22.53±0.01
p-Si<P, Ni, Zn>	28.43±0.01	54.89±0.01
p-Si<P, Zn, Ni>	28.47±0.02	20.59±0.01

Comparing the obtained experimental data on IR absorption with the results of X-ray diffraction analysis of Si<Ni, Zn> samples, the increase in intensity can be explained by two circumstances: 1) high-temperature diffusion of zinc atoms serves as annealing for Si<Ni> samples, in which various kinds of defect states formed begin to decompose and redistribute, gathering on some sinks 2) Zn atoms, being located at the nodes of the silicon crystal, fill the vacant places by the mechanism  $V + Zn = Zn_{int}$ , thereby improving the periodicity of the crystal lattice.

## CONCLUSION

The findings obtained through IR-Fourier spectrometry and X-ray diffraction analysis reveal the strong influence of the silicon doping process with nickel and zinc impurities on the initial silicon structure. Specifically, it is evident that silicon subjected to sequential doping with Ni and Zn impurities exhibits a notably enhanced crystal perfection. A noteworthy observation is the reduction in the concentration of optically active oxygen atoms, which ranges from 15% to 30%, contingent on the concentration levels of nickel and zinc atoms during the high-temperature diffusion process. Moreover, across all samples, a consistent decrease in the concentration of optically active oxygen and carbon atoms has been observed. This phenomenon is attributed to the formation of electrically neutral complexes, namely Ni-O, Ni-C, Zn-O, and Zn-C.

## ORCID

©Daryabay M. Esbergenov, <https://orcid.org/0000-0002-7544-4031>; ©Elmira M. Naurzalieva, <https://orcid.org/0000-0002-5110-1851>

## REFERENCES

- [1] N.A. Sobolev, "Defect engineering in the implantation technology of silicon light-emitting structures with dislocation luminescence," *Physics and Technology of Semiconductors*, **44**(1), 3-25 (2010). (in Russian)
- [2] B. Al-Aderah, A. Obeidat, and J. Talla, "Influence of transition metal defects on electronic and magnetic properties of bulk silicon: Ab-initio simulation," *Materials Today Communications*, 105415 (2023). <https://doi.org/10.1016/j.mtcomm.2023.105415>
- [3] F. Rortais, C. Vergnaud, C. Ducruet, C. Beigné, A. Marty, J.-P. Attané, J. Wdziez, et al., "Electrical spin injection in silicon and the role of defects," *Physical Review B*, **94**(17), 174426 (2016). <https://doi.org/10.1103/PhysRevB.94.174426>
- [4] V.A. Pilipenko, V.A. Gorushko, A.N. Petlitskiy, V.V. Ponaryadov, A.S. Turtsevich, and S.V. Shvedov, "Methods and mechanisms of gettering silicon structures in the production of integrated circuits," *Technology and design in electronic equipment*, 2-3, 43-57 (2013). [http://nbuv.gov.ua/UJRN/TKEA\\_2013\\_2-3\\_9](http://nbuv.gov.ua/UJRN/TKEA_2013_2-3_9). (in Russian)
- [5] Y. Yoshida, and G. Langouche, editors, *Defects and impurities in silicon materials* (Springer, Berlin, 2015).
- [6] R.C. Newman, "Oxygen Carbon Nitrogen and Hydrogen in Silicon," in: *Proceedings of the Second Symposium on Defects in Silicon: Defects in Silicon II*, edited by W.M. Bullis, U. Gösele, and F. Shimura, vol. **91-1**, (Electrochemical Society, Pennington, NJ, 1991), pp. 271-285.
- [7] S.Z. Zainabidinov, and A.O. Kurbanov, "Atomic clusters of nickel impurity and their influence on the recombination properties of silicon," *Vestnik MGTU im. N.E. Bauman. Ser. Natural sciences*, **2**, 81-93 (2019). (In Russian)



- [8] H.C. Sio, et al. "Fluorine passivation of defects and interfaces in crystalline silicon," ACS Applied Materials & Interfaces, **13**(27), 32503-32509 (2021). <https://doi.org/10.1021/acsami.1c07221>
- [9] E.B. Yakimov, "Metal Impurities and Gettering in Crystalline Silicon," in: Handbook of Photovoltaic Silicon, edited by D. Yang, (Springer, Berlin, Heidelberg, 2019). [https://doi.org/10.1007/978-3-662-56472-1\\_23](https://doi.org/10.1007/978-3-662-56472-1_23)
- [10] S. Binetti, S. Pizzini, E. Leoni, R. Somaschini, A. Castaldini, and A. Cavallini, "Optical properties of oxygen precipitates and dislocations in silicon," Journal of applied physics, **92**(5), 2437-2445 (2002). <https://doi.org/10.1063/1.1497450>
- [11] F.E. Rougieux, H.T. Nguyen, D.H. Macdonald, B. Mitchell, and R. Falster, "Growth of oxygen precipitates and dislocations in Czochralski silicon," IEEE Journal of photovoltaics, **7**(3), 735-740 (2017). <https://doi.org/10.1109/JPHOTOV.2017.2678840>
- [12] S.S. Nasriddinov, and D.M. Esbergenov, "Kinetics of formation of complex defects in silicon doped with zinc and nickel," European Science Review, 1-2, 40-45 (2022). <https://doi.org/10.29013/ESR-22-1.2-40-45>
- [13] Zh.Zh. Khamdamov, and D.M. Esbergenov, "Study of the gettering property of Ni impurity in silicon doped with Zn impurity," in: *Modern trends in the development of semiconductor physics: achievements, problems and prospects" II international scientific conference*, (Tashkent, 2022). pp. 51-52. (in Russian)
- [14] D. Bouhafs, N. Khelifati, Y. Kouhlane, and R.S. Kaddour, "Activation of electrical defects under Rapid Thermal Annealing in Cz-silicon for solar cells application," Mater. Res. Express, **6**, 055907 (2019). <https://doi.org/10.1088/2053-1591/aadcc8>
- [15] S.N. Dobryakov, B.V. Kornilov, and V.V. Privezentsev, Russ. Microelectron. **36**, pp. 203 2007. (in Russian)
- [16] V. Privezentsev, "Defects in zinc doped silicon studied on base of X-ray diffuse scattering analysis," Phys. Status Solidi C, **6**(8), 1897-1900 (2009). <https://doi.org/10.1002/pssc.200881472>
- [17] S.Z. Zainabiddinov, and Kh.S. Daliev, *Defect formation in silicon*, (Tashkent State University, 1993). (in Russian)
- [18] L. Scheffler, V.I. Kolkovsky, and J. Weber, AIP Conf. Proc. **1583**, 85-89 (2014). <https://doi.org/10.1063/1.4865610>
- [19] S.S. Nasriddinov, and D.M. Esbergenov, "A Study of Complex Defect Formation in Silicon Doped with Nickel," Russian Physics Journal, **65**(9), 1559-1563 (2023). <https://doi.org/10.1007/s11182-023-02801-x>
- [20] K. Matsukawa, K. Shirai, H. Yamaguchi, and H. Katayama-Yoshida, "Diffusion of transition-metal impurities in silicon," Physica B: Condensed Matter, **401-402**, 151-154 (2007). <https://doi.org/10.1016/j.physb.2007.08.134>
- [21] A.S. Vorokh, "Scherrer formula: estimation of error in determining small nanoparticle size," Nanosystems: physics, chemistry, mathematics, **9**(3), 364-369 (2018).

#### ПІДВИЩЕННЯ ДОСКОНАЛОСТІ КРИСТАЛУ КРЕМНІЮ, ЛЕГОВАНОГО ДОМІШКАМИ НІКЕЛЮ ТА ЦИНКУ

Дар'ябай М. Есбергенов<sup>а</sup>, Ельміра М. Наурзалієва<sup>б</sup>, Сабірбай А. Турсібасєв<sup>а</sup>

<sup>а</sup> Державний педагогічний інститут імені Аджиніяза, м. Нукус, Республіка Каракалпакстан

<sup>б</sup> Філія Ташкентського університету інформаційних технологій імені аль-Хорезмі, Нукус, Республіка Каракалпакстан

Ця дослідницька стаття представляє результати дослідження взаємодії між домішковими атомами цинку (Zn) і нікелю (Ni) у кремнієвій (Si) матриці, які були леговані послідовно в різних комбінаціях. Методи визначення характеристик, використані для цього дослідження, охоплюють рентгенівську дифракцію та ІЧ-Фур'є-спектрометрію. Слід зазначити, що ступінь кристалічності, який демонструє решітка кремнію, за умови введення домішок Zn і Ni, залежить від методології, яка використовується для включення домішок. Результати цього дослідження показують відмінну тенденцію в оптичних властивостях цих легованих зразків кремнію. Зокрема, при введенні атомів Zn в кремній, попередньо легований Ni (Si<Ni, Zn>), відбувається супутне зниження концентрації оптично активних атомів кисню. Примітно, що ця зміна складу допantu призводить до помітного підвищення прозорості кристала кремнію. На відміну від цього, коли послідовність легування змінюється (Si<Ni, Zn> Ni>), спостерігається протилежний ефект, що призводить до зменшення прозорості кристала. Ці висновки підкреслюють складну взаємодію між введеними атомами домішок, послідовністю допantів та їхнім сукупним впливом на оптичні властивості кремнієвої матриці. Такі ідеї сприяють нашому розумінню нюансів поведінки легованого кремнію та мають наслідки для застосувань, які вимагають індивідуальних оптичних характеристик у напівпровідникових матеріалах.

**Ключові слова:** кремній; цинк; нікель; дифузія; рентгенівський дифракційний спектр; ІЧ-пропускання

## THE MECHANISM OF THE FORMATION OF BINARY COMPOUNDS BETWEEN Zn AND S IMPURITY ATOMS IN Si CRYSTAL LATTICE

✉ Nurulla F. Zikrillaev, ✉ Maruf K. Khakkulov, ✉ Bobir O. Isakov\*

Tashkent State Technical University, University St., 2, 100095, Tashkent, Uzbekistan

Corresponding Author e-mail: [bobir6422isakov@gmail.com](mailto:bobir6422isakov@gmail.com)

Received October 3, 2023; revised October 26, 2023; accepted November 7, 2023

The paper presents the results of an experimental study of surface morphology, elemental composition, electrophysical and optical properties of Si samples earlier doped with impurity atoms of Zn and S. The results of the study revealed a sufficient concentration of Zn and S elements on Si surface after diffusion (3.1% and 2.6% by weight, respectively). After additional thermal treatment at different temperatures, i.e., at 850°C and 875°C, the samples of I group have regained their initial parameters. However, it's noteworthy that the mobility of charge carriers in group I samples was comparatively lower than that in group II samples allegedly under the influence of Zn and S binary molecules. After additional heat treatment of all samples at a temperature of 875°C, the authors have studied optical absorption coefficients. And their band gap energies were determined using the Tauc Plot method. According to the results of the study, the optical band gaps in group II and III samples were 1.12 eV, whereas the band gap energy in group I samples after additional thermal treatment at a temperature of 875 °C turned out to be 1.31 eV. Having theoretically calculated the band gap by applying Vegard's law, the authors suggested that the new structure must be of  $\text{Si}_{0.92}\text{ZnS}_{0.08}$  - type.

**Keywords:** Resistivity, Silicon, Impurity atoms, Binary compound, Diffusion, Mobility of charge carriers, Concentration of charge carriers

**PACS:** 61.72.uf, 68.43.Jk

### 1. INTRODUCTION

Wide-bandgap semiconductor compounds have over recently become a new opportunity for perspective optical research and application development. An increased interest in ZnS-type semiconductor compounds in recent years was largely due to its application in optical electronic devices such as light-emitting diodes, flat panel displays, non-linear optical devices, sensors, lasers as well as photocatalysis [1-5]. Due to large band gap values, these materials are likely to be proper source for the production of LEDs [6,7]. However, engineering single crystalline samples of ZnS-type binary semiconductor compounds is both technologically and materially expensive. The authors in [8,10] are said to have engineered the islets of GaSb binary compounds on the surface of Si by using the diffusion technique, thus theoretically justifying and practically calculating the band gap energy and lattice parameters of the novel compound. Therefore, the proper technology is in place so that one can actually engineer ZnS binary compounds in single crystalline Si, thus allowing to obtain novel types of materials by applying the diffusion technique.

Therefore, it is of both scientific and practical importance to form ZnS semiconductor compounds in silicon crystal lattice and study its fundamental parameters. It is known that the ZnS semiconductor is mainly formed in one of cubic sphalerite ( $E_g=3,54$  eV [1-7]) or hexagonal wurtzite ( $E_g=3,8\div 3,91$  eV [1-7]) structures.

### 2. MATERIALS AND METHODS

A single crystalline silicon wafer grown by the Chokhralskiy method, doped with phosphorus impurity atoms, with a specific resistance of  $\sim 100 \Omega\cdot\text{cm}$  was chosen as a starting material (the concentration oxygen  $\text{NO}\sim 10^{17} \text{ cm}^{-3}$ ). The silicon wafer was cut in geometry of  $1\times 4\times 8 \text{ mm}^3$  and the surface of the samples was subjected to mechanical treatment and chemical cleansing. Afterwards, the Zn and S were diffused in into samples during the two-stage process. The samples were divided into three groups:

The group 1 samples: in the first stage, S atoms were diffused into silicon samples at a temperature of  $T=1250^\circ\text{C}$  for  $t=10$  hours, while in the second stage, Zn atoms were diffused at a temperature of  $T=1200^\circ\text{C}$  for  $t=1$  hour;

The group 2 samples: in the first stage, S atoms were diffused into the silicon samples at a temperature of  $T=1250^\circ\text{C}$  for a period of  $t=10$  hours, while in the second stage, the samples were additional annealed at a temperature of  $T=1200^\circ\text{C}$  for a period of  $t=1$  hour;

The group 3 samples: in the first stage, pure silicon samples without inclusions were annealed at a temperature of  $T=1250^\circ\text{C}$  for  $t=10$  hours, in the second stage, Zn impurity atoms were diffused at a temperature of  $T=1200^\circ\text{C}$  for a period of  $t=1$  hour.

After diffusion, the samples were repeatedly additionally subjected to mechanical treatment and chemically cleansed. The elemental analysis of the samples was done using an Energy-Dispersive X-ray spectrometer (EDS - Oxford Instrument) - Aztec Energy Advanced X-ray SDD scanning electron microscope (SEM) (Fig. 1), optical analysis was obtained on a Shimadzu UV-1900i spectrophotometer. After that, the samples were additional annealed step by step at temperatures of 600, 700, 800, 825, 850, 875, 900, 950 and  $1000^\circ\text{C}$ , and after each additional annealing, the

electrophysical properties of the samples were measured on HLS-3000 Ecopia Hall Effect Measurement System. All measurements were made at 300°K, i.e., the room temperature.

### 3. RESULTS AND DISCUSSION

#### 3.1. Element analysis

Elemental analysis of samples was done after two-stage diffusion.

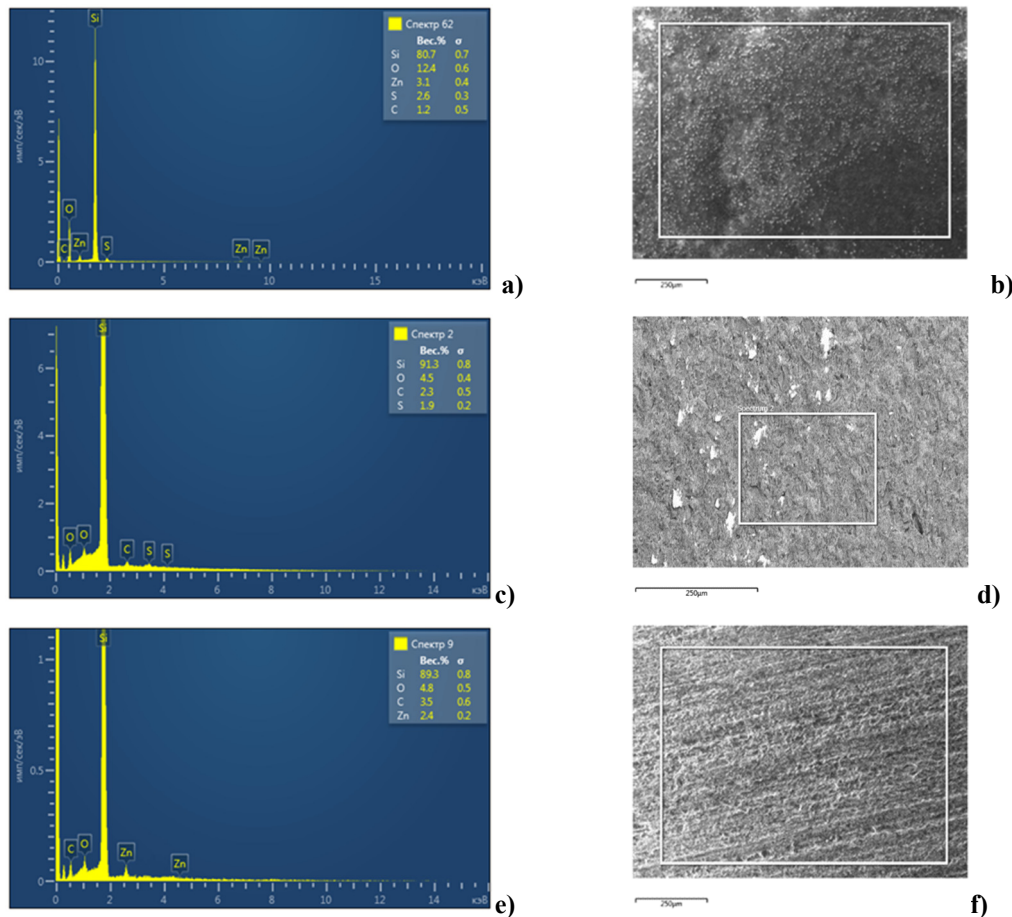


**Figure 1.** Elemental analysis and SEM images of the surface of the samples:  
a), c), e) elemental composition of group I, II, III samples, respectively;  
b), f), d) SEM images of the surface of samples of groups I, II, III, respectively

As can be seen from Figure 1-a), Si, O, C, Zn, and S were detected in 80.7, 12.4, 1.2, 3.1, and 2.6 mass fractions in the samples belonging to group I, respectively. In Figure 1-b), Si, O, C, S in the samples of group II were determined in 91.3, 4.5, 2.3, and 1.9 mass fractions, respectively. In Figure 1-c), in the samples of group III, Si, O, C, Zn were detected in 89.3, 4.8, 3.5 and 2.4 mass fractions, respectively. It is noteworthy, that the amount of oxygen detected in samples of group I and III are were almost equal to each other. However, the amount of oxygen detected in the samples belonging to group I appears to be significantly higher than the amount of oxygen detected in the samples of group II and III. The reason for this can be explained by the fact that Zn and S atoms on the surface of silicon must have attracted and bonded the oxygen previously contained in silicon.

#### 3.2. Electrophysical analysis

Electrophysical properties [11-12] of the samples after two-stage diffusion were studied, and their results are presented in Table 1.

**Table-1.** Electrophysical parameters of the samples after the diffusion process

Samples	Conductivity type	Resistance $\rho$ , $\Omega \cdot \text{cm}$	Mobility of charge carriers $\mu$ , $\text{cm}^2/(\text{V} \cdot \text{s})$	Concentration of charge carriers $n$ or $p$ , $\text{cm}^{-3}$
Starting silicon sample	$n$	108.71	1243	$4.6 \times 10^{13}$
Group I samples, i.e., Si<S, Zn>	$p$	9.05	292	$2.36 \times 10^{15}$
Group II samples, i.e., Si<S>	$n$	2.01	946	$3.29 \times 10^{15}$
Group III samples, i.e., Si<Zn>	$p$	4.98	209	$6.0 \times 10^{15}$

As can be seen from Table 1, the resistivity of the group I samples is 4.5 times greater than the resistivity of the Group II samples, and almost twice bigger than the resistivity of the group III samples. This can be explained by the mutual neutralization of Zn and S impurity atoms in the group I samples. It is known that in the silicon crystal lattice, S atoms form 2 donor energy levels ( $E_c - 0.26$  eV and  $E_c - 0.48$  eV) and they usually manifest themselves in three different states: 1–neutral ( $S^0$ ), 2– one electron leaves, and the atom turns into a singly positively charged ion ( $S^+$ ), 3 –two electrons leave, and the atom turns into a doubly positively charged ion ( $S^{++}$ ).

In their turn, Zn impurity atoms create 2 acceptor energy levels ( $E_v + 0.26$  eV and  $E_v + 0.55$  eV, respectively) in the silicon crystal lattice, and they manifest themselves in three different states: 1–neutral ( $Zn^0$ ), 2–accepts an electron, and the atom turns into a singly negatively charged ion ( $Zn^-$ ), 3 - accepts two electrons, and the atom turns into a doubly negatively charged ion ( $Zn^{--}$ ).

If the above two last mechanisms take place, the positive and negative ions of S and Zn impurity atoms in the silicon crystal lattice begin to attract each other. In this case, since the molar mass of Zn atom is 2 times larger than the molar mass of S atom, the attraction of a positively charged S ion to the negatively charged Zn ion is probably stronger. But one needs to create certain thermodynamic conditions to ensure that S and Zn ions migrate in the silicon crystal lattice subsequently forming a ZnS-molecule. For this purpose, the samples were additionally annealed at various temperatures for the same time duration. Afterwards, we have determined their electrophysical properties (Table 2).

**Table 2.** Electrophysical parameters ( $\rho, \mu, n$ ) of the samples after additional thermal treatment at various temperatures.

$T, ^\circ\text{C}$	samples	600	700	800	825	850	875	900	950	1000
$t$ (hours)		1	1	1	1	1	1	1	1	1
$\rho, \Omega \cdot \text{cm}$	I-group	9,85	10	27,8	85,5	92,3	150	129	112	63
	II-group	2,1	2,06	2,04	2,05	2,1	2,2	2,4	2,5	2,7
	III group	5,15	5,21	5,32	5,33	5,41	5,61	5,71	6,2	7,2
$\mu, \text{cm}^2/(\text{V} \cdot \text{s})$	I-group	285	240	443	324	783	810	57	276	335
	II-group	924	920	921	923	923	927	931	940	964
	III-group	198	196	194	197	195	198	202	207	211
$n, p$ ( $\text{cm}^{-3}$ )	I group	$2,2 \cdot 10^{15}$	$2,6 \cdot 10^{15}$	$5,7 \cdot 10^{14}$	$2,3 \cdot 10^{14}$	$8,6 \cdot 10^{13}$	$5,1 \cdot 10^{13}$	$8,5 \cdot 10^{14}$	$2 \cdot 10^{14}$	$2,9 \cdot 10^{14}$
	II group	$3,2 \cdot 10^{15}$	$3,3 \cdot 10^{15}$	$3,3 \cdot 10^{15}$	$3,3 \cdot 10^{15}$	$3,2 \cdot 10^{15}$	$3,1 \cdot 10^{15}$	$2,8 \cdot 10^{15}$	$2,7 \cdot 10^{15}$	$2,4 \cdot 10^{15}$
	III group	$6,1 \cdot 10^{15}$	$6,1 \cdot 10^{15}$	$6,0 \cdot 10^{15}$	$5,9 \cdot 10^{15}$	$5,9 \cdot 10^{15}$	$5,6 \cdot 10^{15}$	$5,4 \cdot 10^{15}$	$4,9 \cdot 10^{15}$	$4,1 \cdot 10^{15}$
Type of conductivity	I group	$p$	$p$	$p$	$p$	$n$	$n$	$p$	$p$	$p$
	II group	$n$	$n$	$n$	$n$	$n$	$n$	$n$	$n$	$n$
	III group	$p$	$p$	$p$	$p$	$p$	$p$	$p$	$p$	$p$

As can be seen from Table 2, the Group 3 samples were additional annealed step by step at temperatures of 600, 700, 800, 825, 850, 875, 900, 950 and 1000°C and their resistivity ( $\rho, \Omega \cdot \text{cm}$ ), charge carriers mobility ( $\mu, \text{cm}^2/(\text{V} \cdot \text{s})$ ), charge carriers' concentrations ( $n, p, \text{cm}^{-3}$ ), and the conductivity type were subsequently determined. As can be seen from Table-2, the results of electrophysical measurements in Group I samples annealed at temperatures  $T=850^\circ\text{C}$  and  $T=875^\circ\text{C}$  are rather anomalous. The rest of the results obey the known rules of physics due to which we will only discuss the results in the Group I sample annealed at temperatures  $T=850^\circ\text{C}$  and  $T=875^\circ\text{C}$ . The conductivity is  $n$ -type, the resistivity is 92.3 and 150  $\Omega \cdot \text{cm}$ , respectively, the concentration of charge carriers is  $8.6 \times 10^{13}$  and  $5.1 \times 10^{13} \text{ cm}^{-3}$ , respectively, the mobility of charge carriers is 783 and 810  $\text{cm}^2/(\text{V} \cdot \text{s})$ . From these results, one can conclude that the parameters in Group I samples regain their original values. When it comes to discussing the mobility of charge carriers, it can be seen that mobility parameters do not completely regain their initial value at these temperatures. Assuming that the mobility of charge carriers in  $n$ -type ZnS compound semiconductor is  $\sim 200 \text{ cm}^2/(\text{V} \cdot \text{s})$ , it can be said that the mobility of charge carriers of the initial silicon decreases due to forming of Zn and S compounds in the bulk of silicon. That is, the formation of the ZnS molecules in the silicon crystal lattice can be explained based on the results shown in Figure 2 below.

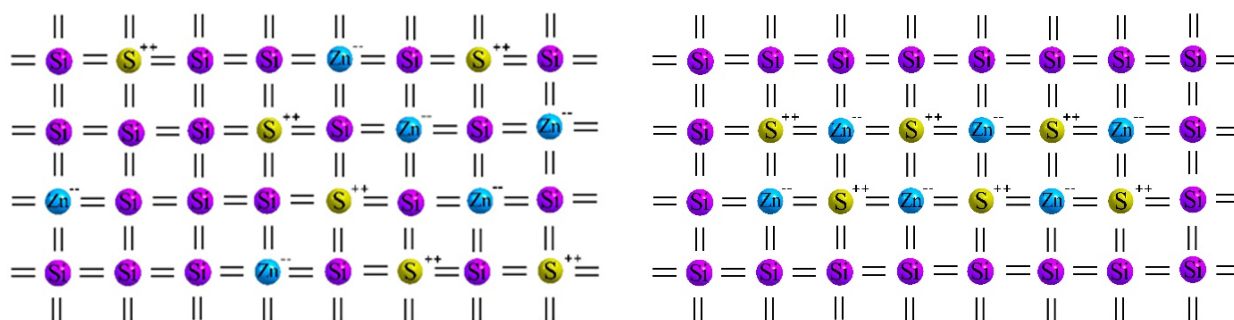


**Figure 2.** Zn and S atoms in the silicon monocrystal lattice:  
a) before additional thermal treatment; b) after additional thermal treatment.

### 3.3. Optical analysis

One of the most preferred methods for determining the band gap of semiconductors is optical absorption method. There are no special requirements for the shape and geometry of samples under investigation, and the accuracy level of the measurement is sufficiently high.

The technique consists in the behavior of light whereby a certain portion of the monochromatic light beam directed at the surface of a semiconductor sample is reflected from the surface, a certain portion passes through the bulk of the sample, while the rest is absorbed in the bulk of a semiconductor material. As a result, the light intensity decreases. The relative change in the light intensity per unit volume is called the absorption coefficient. The value of the absorption coefficient depends on the wavelength ( $\lambda$ ) of the incident radiation, and the function is called the absorption spectrum.

Absorption coefficient can be calculated based on the measurement of reflectance ( $R$ ) and transmittance ( $T$ ) using the following formula:

$$\alpha = \frac{1}{d} \ln \frac{(1-R)^2}{T} \quad (1)$$

where  $d$  is the sample thickness,  $R$  is the reflection coefficient,  $T$  is the light transmission coefficient. The Formula (1) is valid at  $T < 10\%$ . If  $T > 10\%$ , the relation (2) hereunder should be used to calculate the absorption coefficient:

$$T = \frac{(1-R)^2 \exp(-\alpha d)}{1-R^2 \exp(-2\alpha d)} \quad (2)$$

The absorption spectra of the samples were received using a Shimadzu UV-1900i -type spectrometer, and the optical band gaps of the samples were determined using the Tauc plot's method [11] (Figure-3). Before the UV-1900i measurements, all samples were had a thickness of  $d \sim 200 \mu\text{m}$ .

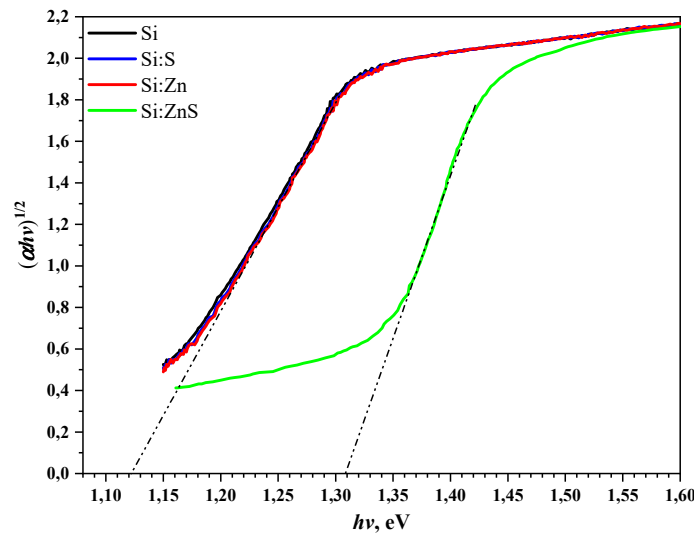


Figure 3. Optical band gaps of the samples

Figure 3 shows the measurement results of samples belonging to Group III, reference sample and Group I samples after additional thermal treatment at  $T=875 \text{ }^\circ\text{C}$ . As can be seen from Figure 3, optical band gaps of samples belonging to Group II and III and the reference sample are almost the same, that is  $\sim 1.12 \text{ eV}$ . The optical band gap of Group I samples after additional thermal treatment at temperature  $T=875 \text{ }^\circ\text{C}$  was  $\sim 1.31 \text{ eV}$ . Taking into account that the band gap energy of ZnS semiconductor at temperature  $T=300 \text{ }^\circ\text{K}$  is  $\sim 3.54 \text{ eV}$ , the results are assumably indicative of the formation of ZnS binary molecules in the silicon crystal lattice.

Based on the measurement results and applying reciprocal calculation of Vegard's law [12] we will calculate the portion of each Si and ZnS in  $\text{Si}_{1-x}\text{ZnS}_x$  compound.

$$E_{g,A_{1-x}B_x} = (1-x) \cdot E_{g,A} + x \cdot E_{g,B} \rightarrow E_{g,\text{Si}_{1-x}\text{ZnS}_x} = (1-x) \cdot E_{g,\text{Si}} + x \cdot E_{g,\text{ZnS}} \quad (3)$$

where  $x$  is the molar fraction of the substance,  $E_{g,\text{Si}_{1-x}\text{ZnS}_x}$  is the band gap of the newly formed structure i.e.,  $E_{g,\text{Si}_{1-x}\text{ZnS}_x} = 1.31 \text{ eV}$ ,  $E_{g,\text{Si}}$  - the band gap of silicon which is  $E_{g,\text{Si}} = 1.12 \text{ eV}$  and  $E_{g,\text{ZnS}}$  is the band gap of ZnS, equal to  $E_{g,\text{ZnS}} = 3.54 \text{ eV}$  (the band gap of ZnS of cubic sphalerite structure). We will calculate the value of the unknown coefficient  $x$  in equation 3 based on the above information. According to the calculations, it was found that  $x \approx 0.08$ . Therefore, it can be said that the band gap energy of the newly engineered structure formed in silicon is equal to  $1.31 \text{ eV}$ .

#### 4. CONCLUSION

The results of electrophysical and optical experiments showed that after two-stage diffusion of Zn and S into a monocrystalline silicon sample these elements incidentally do not form a compound in silicon due to the fact that both Zn and S are not deep-level creating impurities. To achieve that certain thermodynamic conditions are required to be in place in order to ensure forming bonds between these impurities in the silicon crystal lattice. The measured electrophysical results show that the formation of ZnS binary compounds was negatively affected by the low temperature when the samples of Group I were additionally annealed in the temperature range of 600–800°C, and the ZnS binary compounds began to form when additionally annealed in the temperature range of 800–850°C. ZnS binary compounds are fully formed under additional thermal treatment in the temperature range of 850–900°C, while in the temperature range of 900–1000 °C, ZnS binary compounds must have dissociated into atoms again. This conclusion was confirmed by the surface morphological and elemental analysis of the samples, as well as the results of optical measurements.

#### ORCID

©Nurulla F. Zikrillayev, <https://orcid.org/0000-0002-6696-5265>; ©Maruf K. Khakkulov, <https://orcid.org/0009-0006-2629-220X>  
 ©Bobir O. Isakov, <https://orcid.org/0000-0002-6072-3695>

#### REFERENCES

- [1] J. McCloy, and R. Tustison, *Chemical vapor deposited zinc sulfide*, (SPIE The International Society for Optical Engineering, Bellingham, Washington USA, 2013).
- [2] J. Liu, and S. Yue, "Fabrication of ZnS layer on silicon nanopillars surface for photoresistor application," *Chemical Physics Letters*, **801**, 139716 (2022). <https://doi.org/10.1016/j.cplett.2022.139716>
- [3] J. Kang, J.-S. Park, P. Stradins, and S.-H. Wei, "Nonisovalent Si-III-V and Si-II-VI alloys: Covalent, ionic, and mixed phases," *Physical Review B*, **96**, 045203 (2017). <https://doi.org/10.1103/PhysRevB.96.045203>
- [4] V.H. Choudapura, S.B. Kapatkara and A.B. Raju, "Structural and optoelectronic properties of zinc sulfide thin films synthesized by co-precipitation method," *Acta chemica IASI*, **27**(2), 287-302 (2019). <https://doi.org/10.2478/achi-2019-0018>
- [5] H.J. Xu, H.S. Jia, Z.T. Yao, and X.J. Lia, "Photoluminescence and I–V characteristics of ZnS grown on silicon nanoporous pillar array," *J. Mater. Res.* **23**(1), 121–126 (2008). <https://doi.org/10.1557/JMR.2008.0005>
- [6] J. Diaz-Reyes, R.S. Castillo-Ojeda, R. Sanchez-Espindola, M. Galvan-Arellano, and O. Zaca-Moran, "Structural and optical characterization of wurtzite type ZnS," *Current Applied Physics*, **15**, 103e109 (2015). <http://dx.doi.org/10.1016/j.cap.2014.11.012>
- [7] M. Özkan, N. Ekem, S. Pat, M.Z. and Balbağ, "ZnS thin film deposition on Silicon and glass substrates by Thermionic vacuum Arc," *Materials Science in Semiconductor Processing*, **15**, 113–119 (2012). <https://doi.org/10.1016/j.mssp.2011.07.004>
- [8] X.M. Iliyev, S.B. Isamov, B.O. Isakov, U.X. Qurbonova, and S.A. Abduraxmonov, "A surface study of Si doped simultaneously with Ga and Sb," *East Eur. J. Phys.* **3**, 303 (2023). <https://doi.org/10.26565/2312-4334-2023-3-29>
- [9] X.M. Iliyev, V.B. Odzhaev, S.B. Isamov, B.O. Isakov, B.K. Ismaylov, K.S. Ayupov, S.I. Hamrokulov, and S.O. Khasanbaeva, "X-ray diffraction and raman spectroscopy analyses of GaSb-enriched Si surface formed by applying diffusion doping technique," *East Eur. J. Phys.* **3**, 363 (2023), <https://doi.org/10.26565/2312-4334-2023-3-38>
- [10] D.C. Onwudiwe, J.O. Adeyemi, R.T. Papane, F.F. Bobinihi, and E. Hosten, "Synthesis, optical and structural characterisation of ZnS nanoparticles derived from Zn(II) dithiocarbamate complexes," *Open Chemistry*, **19**, 1134–1147 (2021). <https://doi.org/10.1515/chem-2021-0094>
- [11] N.F. Zikrillayev, G.A. Kushiev, S.V. Koveshnikov, B.A. Abdurakhmanov, U.K. Qurbonova, and A.A. Sattorov, "Current status of silicon studies with Ge<sub>x</sub>Si<sub>1-x</sub> binary compounds and possibilities of their applications in electronics," *East Eur. J. Phys.* **3**, 334 (2023). <https://doi.org/10.26565/2312-4334-2023-3-34>
- [12] N.F. Zikrillayev, G.A. Kushiev, S.I. Hamrokulov, and Y.A. Abduganiev, "Optical Properties of Ge<sub>x</sub>Si<sub>1-x</sub> Binary Compounds in Silicon," *Journal of Nano- and Electronic Physics*, **15**(3), (2023). [https://doi.org/10.21272/jnep.15\(3\).03024](https://doi.org/10.21272/jnep.15(3).03024)
- [13] W. Macyk, "How to Correctly Determine the Band Gap Energy of Modified Semiconductor Photocatalysts Based on UV–Vis Spectra," *J. Phys. Chem. Lett.* **9**, 6814–6817 (2018). <https://doi.org/10.1021/acs.jpcclett.8b02892>
- [14] M. Merli, and A. Pavese, "Beyond the Vegard's law: solid mixing excess volume and thermodynamic potentials prediction, from end-members," *Physics Letters A*, **384**(2), 126059 (2020). <https://doi.org/10.1016/j.physleta.2019.126059>

#### МЕХАНІЗМ УТВОРЕННЯ БІНАРНИХ СПОЛУК МІЖ ДОМІШКОВИМИ АТОМАМИ Zn ТА S У КРИСТАЛІЧНІЙ ГРАТЦІ Si

Нурулла Ф. Зікріллаєв, Маруф К. Хаккулов, Бобір О. Ісаков

Ташкентський державний технічний університет, Узбекистан, 100095, м. Ташкент, вул. Університетська, 2

У статті наведено результати експериментального дослідження морфології поверхні, елементного складу, електрофізичних і оптичних властивостей зразків Si, раніше легованих домішковими атомами Zn і S. Результати дослідження виявили достатню концентрацію елементів Zn і S на поверхні Si після дифузії (3,1% і 2,6% мас. відповідно). Після додаткової термічної обробки при різних температурах, тобто при 850°C і 875°C, зразки I групи відновили вихідні параметри. Проте варто відзначити, що рухливість носіїв заряду в зразках I групи була порівняно нижчою, ніж у зразках II групи нібито під впливом бінарних молекул Zn і S. Після додаткової термічної обробки всіх зразків при температурі 850°C автори досліджували коефіцієнти оптичного поглинання. Їхню енергію забороненої зони було визначено за допомогою методу Tauc Plot. За результатами дослідження встановлено, що ширина забороненої зони в зразках II та III групи становила 1,12 еВ, тоді як у зразках групи I після додаткової термічної обробки при температурі 850°C енергія забороненої зони виявилася 1,31 еВ. Теоретично розрахувавши ширину забороненої зони за допомогою закону Вегарда, автори припустили, що нова структура має бути типу Si<sub>0,92</sub>ZnS<sub>0,08</sub>.

**Ключові слова:** титомий опір; кремній; домішкові атоми; бінарна сполука; дифузія, рухливість носіїв заряду; концентрація носіїв заряду

## EVOLUTION OF MECHANICAL PROPERTIES OF Pb–Sb–Sn–As–Se GRID ALLOYS FOR LEAD-ACID BATTERIES DURING NATURAL AGING

 Victor O. Dzenzerskiy,  Serhii V. Tarasov,  Olena V. Sukhova\*,  Volodymyr A. Ivanov

*Institute of Transport Systems and Technologies of National Academy of Sciences of Ukraine*

*5, Pisarzhevsky St., Dnipro, 49005, Ukraine*

\*Corresponding Author: [sukhovaya@ukr.net](mailto:sukhovaya@ukr.net)

Received October 1, 2023; revised November 1, 2023; accepted November 10, 2023

This study is devoted to the investigation of mechanical properties of a series of low-antimony Pb–Sb–Sn–As–Se grid alloys for lead-acid batteries in as-cast condition and after natural aging during storage. Mechanical properties were characterized by ultimate tensile strength, yield strength, elongation, and Young's modulus determined at room temperature using TIRAtest 2300 and P-0.5 universal testing machines. For most investigated as-cast alloys, an increase in ultimate tensile strength is accompanied by an increase in elongation. Within the temperature range between 70 °C and 150 °C, higher heating temperature of a casing mold does not markedly affect average elongation but causes the slight decrease (by ~4 %) in average ultimate tensile strength. When aged during storage for 30–33 days, the Pb–Sb–Sn–As–Se grid alloys, attain higher values of ultimate tensile strength, yield strength, and Young's modulus but lower values of elongation. This is due to precipitation of second-phase particles from lead-based solid solution oversaturated by antimony, arsenic, and selenium. The most noticeable effect of strengthening is observed during first five days of natural aging.

**Keywords:** *Lead-acid batteries, Low-antimony Pb–Sb–Sn–As–Se grid alloys, Natural aging during storage, Tensile tests, Ultimate tensile strength, Yield strength, Elongation, Young's modulus*

**PACS:** 61.82.Bg, 61.66.Dk, 62.20.-x, 62.20.Fe, 62.20.Mk, 64.70.Dv, 81.70.Bt, 81.40.Cd, 81.40.Lm

For many years, the most common battery chemistries used for lead-acid batteries were the high-antimony lead alloy compositions. Antimony gave to the pure lead strength, good castability and high performance on charge-discharge characteristics [1-4]. The concentrations of antimony to lead were initially in the 4–12 wt.% range [5-9]. But most battery manufacturers tried to minimize the antimony addition especially in batteries for stationary applications. High-antimony grids have higher hydrogen evolution (which also accelerates as the battery ages), and thus greater outgassing and higher maintenance costs. These problems are caused by the dissolution of antimony from positive electrode and its deposition or plating on negative electrode. This leads to lower charge voltage, a high discharge rate, increased water loss of the battery and therefore a short lifetime [10-14].

Using alloying elements, the antimony content of grid alloys can be reduced to the level that the drawbacks of low antimony are almost eliminated, but the positive effects are mainly retained [15-20]. Nowadays the grids for lead-acid batteries are made from lead antimony alloys together with minor additions of elements such as Sn, As, and Se [21-27]. These are added to confer properties such as grain refinement, castability and performance characteristics to the grids.

Adding antimony to produce hypoeutectic lead antimony alloys also ensures hardening of lead. The alloys containing 6 wt.% Sb appears to undergo optimum hardening, but the alloys with 2 wt.% Sb and less harden comparatively slow [28,29]. Antimony in low-antimony lead alloys has difficulty in precipitating and therefore substantially remains in solution through the casting, working process and aging period. Therefore, small amounts of arsenic and selenium retain beneficial characteristics of high-antimony alloys, such as the precipitation hardening effect, increasing supersaturation of antimony in lead when its concentration is relatively low (<2 wt.%). Additional alloying elements typically produce a fine and homogenize distribution of precipitation [27]. But only when the alloys are heat treated the alloys strengthen on aging due to formation of metastable arsenic- or selenium-bearing nuclei which facilitate the antimony precipitation process [30-32].

Heat treatment of the low-antimony lead alloys is performed under time and temperature conditions which do not result in a conventional solution treatment effect [33-40]. Solution treatment requires diffusion-controlled dissolution of the already precipitated antimony-rich phase. Such processes are slow since they depend on the solid-state movement of individual atoms from one crystal site to the next [41-45]. Strengthening occurs after quenching when the super-saturated solution precipitates in a form which strains the alloy crystal lattice and inhibits dislocation motion [46-51].

In alloys of the lead-antimony system, the initial hardening produced by alloying is quickly followed by softening as the coarse structure is formed during storage. The effects of tin, arsenic, and selenium on low-antimony Pb–Sb alloys were investigated by some authors [29,32], but there is not complete research about the influence of these additives on the evolution of the tensile properties of Pb–Sb–Sn–As–Se alloys from as-cast condition and under natural aging during storage. The purpose of this paper is to achieve the mechanical strength within aging times suitable for storage using the combination of alloying elements such as antimony, tin, arsenic, and selenium with lead to manufacture lead-acid battery grids with low antimony contents (<1.77 wt.%), which show the necessary grid quality.

## MATERIALS AND METHODS

Commercial Pb–Sb–Sn–As–Se grid alloys for lead-acid batteries received from *Westa* ISI Corp. (City of Dnipro, Ukraine) were used in this research. The chemical composition of the studied castings is presented in Table 1. The alloys were composed of Sb (1.55–1.77 wt.%); Sn (0.11–0.17 wt.%); As (0.097–0.13 wt.%); Se (0.018–0.025 wt.%); impurities, such as Cu, Bi, Ag, S, Fe, Ni, Cd, and Zn (in descending order), (0.0217–0.0533 wt.% altogether); Pb – the remainder. The chemical analysis of elements present in the castings was performed using an ARL 3460 optical emission spectrometer. The Pb–Sb–Sn–As grid alloys were prepared in the melting pot of *Wirtz* manufacturing book mold grids casting machine (the USA). The melts at temperatures of 440–460 °C were poured into a casting mold preheated in the temperature range between 70 °C and 150 °C. The temperatures of the mold were controlled using chromel-alumel thermocouple.

Mechanical properties of the as-cast Pb–Sb–Sn–As–Se grid alloys used in this study were assessed in terms of ultimate tensile strength ( $\sigma_U$ ) and elongation ( $\gamma$ ). The tensile tests were performed at room temperature in P-0.5 tensile testing machine providing controlled uniformly increasing tension force. The specimens flat in the cross section which had a thickness of 0.3 cm, a total length of 6.0 cm, and a gage length of 4.5 cm (prepared according to DSTU 11701-84) were stretched up to failure. Six tests were conducted for each alloy composition and the average values were reported. The measurements were presented with their standard error of 2–8 %. In the results section, the mean curves determined from tensile tests are shown.

The as-cast Pb–Sb–Sn–As–Se alloys were put into storage where they naturally aged at room temperature for 30-33 days. Determination of the tensile properties was made 1 day after casting and then at intervals of 3–4 days. After each interval of aging time, six specimens in a row were exerted for tensile tests carried out on TIRAtest 2300 universal testing machine. Altogether were tested sixty specimens broken into 10 sets of 6 specimens each. Tensile experiments were carried out on the flat specimens at room temperature with a crosshead speed of 10 mm/min. Tensile force was applied stepwise with a step of 100 N until the stress part of stress-strain diagrams started falling back down slowly. As the load was applied, the stress and strain experienced by the test specimen were captured digitally and graphed. Values of ultimate tensile strength ( $\sigma_U$ ), yield strength ( $\sigma_Y$ ), and Young's modulus ( $Y$ ) were determined from plotted stress-strain diagrams. The data obtained were each calculated from an average of six specimens with error 3–5 %.

## RESULTS AND DISCUSSION

The studied as-cast Pb–Sb–Sn–As–Se grid alloys consist of two phases, namely primary dendrites of  $\alpha$ -Pb solid solution and  $\beta$ -Sb phase formed at the boundaries of  $\alpha$ -phase [1-3]. In the investigated compositional range, the influence of major alloying elements on ultimate tensile strength and elongation is quite irregular (Table 1). These irregularities are believed to be more experimental errors than significant variations in the properties of the alloys. But in general, ultimate tensile strength increases with increasing arsenic content. Most alloys become more ductile when become stronger. The combination of high ultimate tensile strength and high elongation ensures high toughness of the Pb–Sb–Sn–As–Se grid alloys. Meanwhile, increasing content of impurities in the investigated Pb-based alloys leads to a decrease in their elongation. This is because impurities segregate at grain boundaries of  $\alpha$ -Pb phase forming brittle secondary phases. Also, there are more interfaces between the phases which hinder the dislocation motion [35].

**Table 1.** The mechanical properties of the as-cast Pb–Sb–Sn–As–Se grid alloys for lead-acid batteries

Casting No.	Chemical composition, wt.%					$\sigma_U$ , MPa	$\gamma$ , %
	Sb	Sn	As	Se	Impurities		
952	1.62	0.14	0.10	0.021	0.0549	22.3	6.7
433	1.55	0.12	0.10	0.020	0.0533	25.5	8.7
980	1.58	0.13	0.11	0.018	0.0480	25.8	9.5
827	1.64	0.14	0.11	0.023	0.0452	26.3	9.7
696	1.77	0.13	0.10	0.024	0.0318	26.3	9.7
870	1.67	0.15	0.11	0.022	0.0314	26.8	9.7
836	1.61	0.13	0.11	0.025	0.0527	27.0	9.5
146	1.65	0.11	0.11	0.023	0.0270	29.4	13.9
202	1.66	0.13	0.12	0.022	0.0258	29.9	12.6
137	1.56	0.14	0.11	0.023	0.0212	30.4	15.4
150	1.70	0.11	0.12	0.023	0.0269	30.4	15.6
152	1.63	0.17	0.11	0.022	0.0217	30.4	16.0
0005	1.68	0.15	0.13	0.024	0.0291	31.7	12.4
<b>Average</b>	<b>1.64±0.04</b>	<b>0.13±0.01</b>	<b>0.11±0.01</b>	<b>0.022±0.001</b>	<b>0.0361±0.0113</b>	<b>27.9±2.3</b>	<b>11.4±2.7</b>

The ultimate tensile strength data show a decrease with increasing heating temperature of casting mold in the range between 70 °C and 110 °C, followed by practically constant or slightly decreasing values at temperatures upwards of 110 °C (Fig. 1a). Tensile strength results on as-cast specimens tend to be influenced by imperfections, such as microscopic cracks or cavities which weaken castings produced at the mold temperatures above 110 °C due to slower cooling rate. These defects create a weak point where a crack can initiate. The experimental data indicate some



irregularities in elongation behavior although this characteristic is usually affected by casting imperfections to a greater degree than the ultimate tensile strength (Fig. 1b).

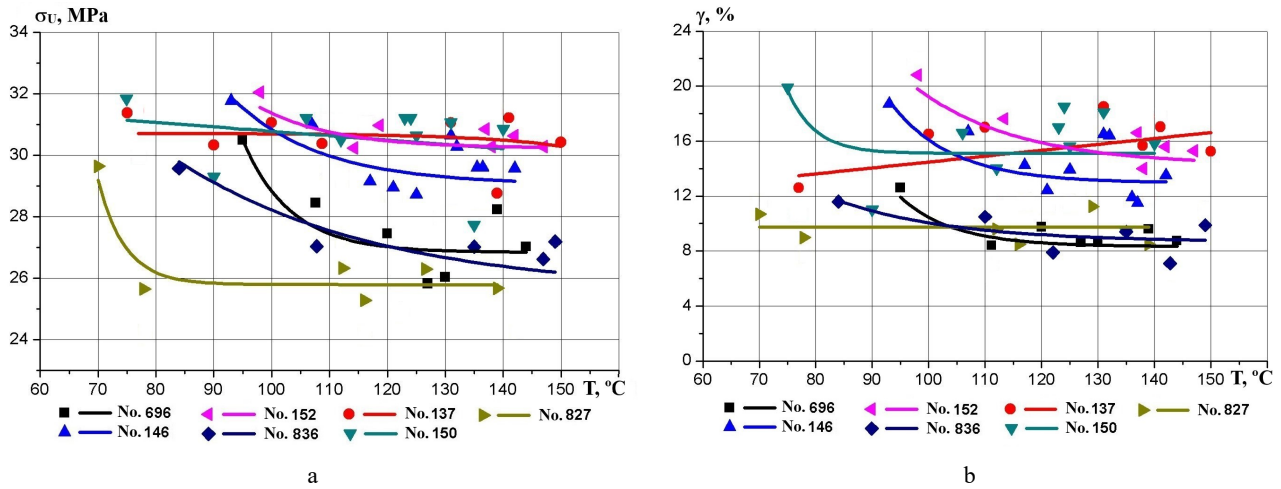


**Figure 1.** Effect of heating temperature of casting mold on tensile properties of castings: a – ultimate tensile strength; b – elongation

Based on the tensile test results, average curves for a set of specimens in the as-cast condition are calculated and a linear trend line is given for the subsequent analysis of the influence of heating temperature of casting mold on tensile properties, as shown in Fig. 2. The data confirm that the tensile strength is lowered (Fig. 2a), although the elongation of the alloys is not appreciably affected by heating temperature (Fig. 2b). With mold temperature increasing from 75 °C to 150 °C, average tensile strength decreases from 29.8 MPa to 28.5 MPa (by ~4 %). The temperature dependence of ultimate tensile strength is approximately 0.017 MPa/°C. It is possible that changes in ultimate tensile strength behavior may be attributed to the fact that cooling rate of the as-cast specimens decreases as a heating temperature of casting mold increases. Aside from deleterious effect of casting flaws, the slower cooling rate also produces coarser microstructure of the alloys, weakening them in ultimate tensile strength, while not appreciably affecting their elongation to failure. Besides, in slow cooling the lead grains tend to push the major alloying elements and impurities to the grain boundaries which is the lowest energy condition. These elements at the grain boundaries still provide dislocation blocking, but not so well as uniformly dispersed ones. The residual internal stresses cause tensile strength tests to give lower values. Meanwhile, considering instability of tensile properties at heating temperatures below 110 °C, a mold during casting should be preheated over the temperature range of 110 °C to 150 °C despite the slight deterioration in average values of ultimate tensile strength.

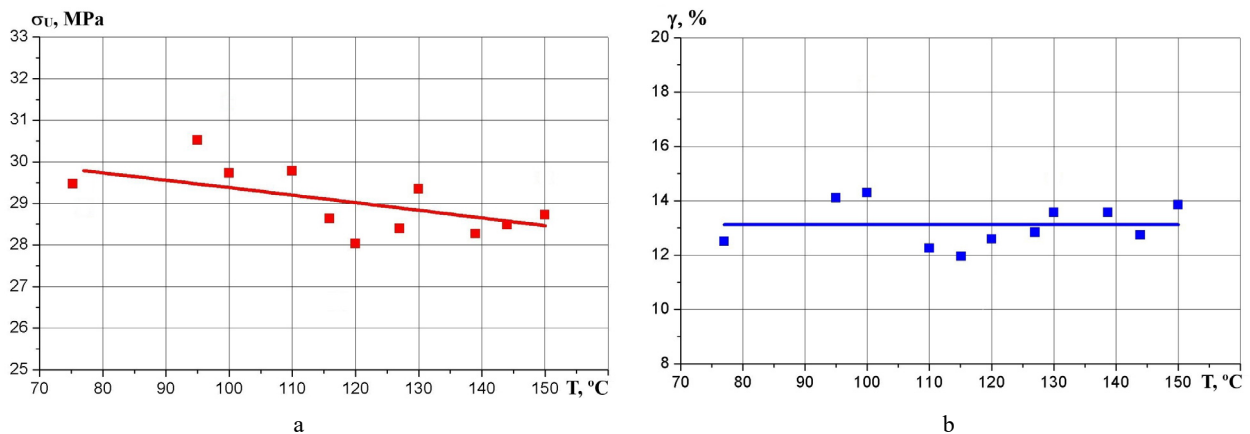


**Figure 2.** Average values of tensile properties vs. heating temperature of casting mold: a – ultimate tensile strength; b – elongation

The mechanical properties of the Pb–Sb–Sn–As–Se alloys are dependent not only on the heating temperature of casting mold but also on the time of natural aging during storage after cooling to room temperature. The casting conditions assure oversaturation of lead-rich  $\alpha$ -phase in the structure of the alloys which is sufficient for age-strengthening. Fig. 3 shows the effects of room temperature storage on the aging characteristics of the alloys identified by changes with time in the ultimate tensile strength and the elongation determined using P-0.5 tensile testing machine. Some alloys experienced up to a 40-% increase in ultimate tensile strength (from 22–32 MPa to 30–44 MPa) during 33 days of storage after casting. All aging curves have the same characteristic shape since strengthening occurs in two stages: at first rapid strengthening during the first 5 days, followed by a much longer period of gradual strengthening

(Fig. 3a). This process is mainly attributed to the precipitation of the finely dispersed antimony in the supersaturated lead-rich matrix [29,30]. What is more, the best strengthening results are obtained with alloys of higher selenium and arsenic contents. As known, these additional alloying elements produce a fine and homogenize distribution of precipitates [27]. The smaller grains have the larger area of grain boundaries that inhibit dislocation motion. Therefore, reducing the grain size increases the available nucleation sites for precipitated antimony.

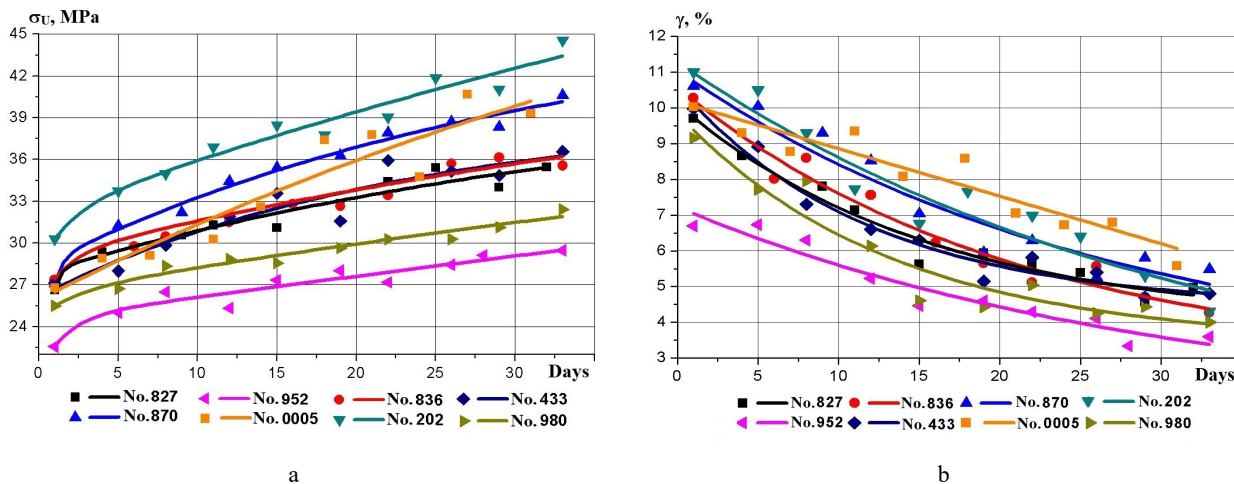


Figure 3. Effect of aging time on tensile properties of castings: a – ultimate tensile strength; b – elongation

The aging effect of the Pb–Sb–Sn–As–Se alloys during storage also results in a decrease in the elongation (Fig. 3b). Depending on castings composition, elongation reduces by 50–57 % (from 7–11 % to 3.5–5.1 %) after 33 days of storage. Such behavior can be explained by precipitation of supersaturated lead-based solid solution which makes the alloys lattice distortion and hinders dislocation motion. The casting No. 0005 combining a sufficient tensile strength with the highest elongation of any contains simultaneously the highest amounts of arsenic (0.13 wt.%) and selenium (0.024 wt.%) (Table 1). This alloy undergoes precipitation strengthening due to antimony as well as other minor alloying elements, particularly arsenic and selenium, forming particles within the lattice of the casting. The grids produced contain a higher volume of second-phase particles which inhibit dislocation and grain boundary movement and thus make the grids more stable.

Average values of the ultimate tensile strength and elongation for the investigated castings are plotted in the graphs of Fig. 4. As expected, ultimate tensile strength raises from 26.7 MPa to 37.0 MPa (by ~40 %), but elongation reduces from 9.7 % to 4.5 % (by ~2 times) after 33 days of aging. Aging time dependence of the ultimate tensile strength is 0.39 MPa/day, whereas the elongation's dependence is 0.54 %/day. Thus, as the ultimate tensile strength increases, the alloys tend to become more brittle and less prone to tension, as shown by the decreased elongation to failure. But for grid alloys, the increase in ultimate tensile strength might be of greater importance than the decrease in elongation which accompanies the aging processes.

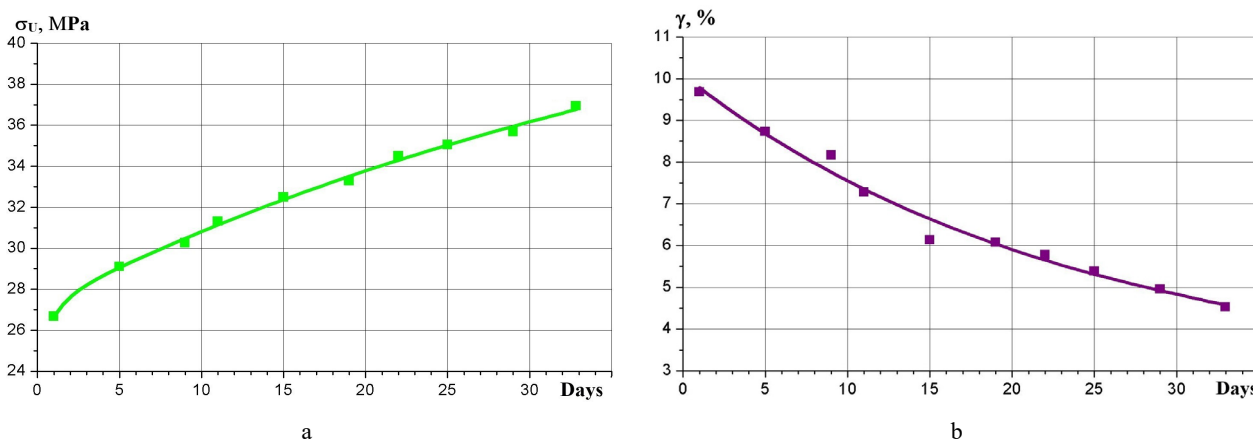


Figure 4. Average values of tensile properties vs. aging time: a – ultimate tensile strength; b – elongation

Fig. 5 illustrates typical stress-strain diagrams that use data from tensile tests performed in TIRAtest 2300 universal testing machine (exemplified by six specimens aged for 14 days). All curves display a linear elastic range where the stress and strain are proportional to each other and a gradually rising part (without pronounced yield plateau) where specimens undergo plastic deformation.

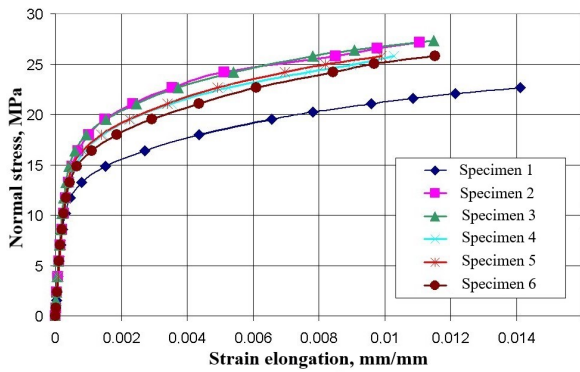


Figure 5. Typical stress-strain curves for tensile tests on 6 specimens aged for 14 days

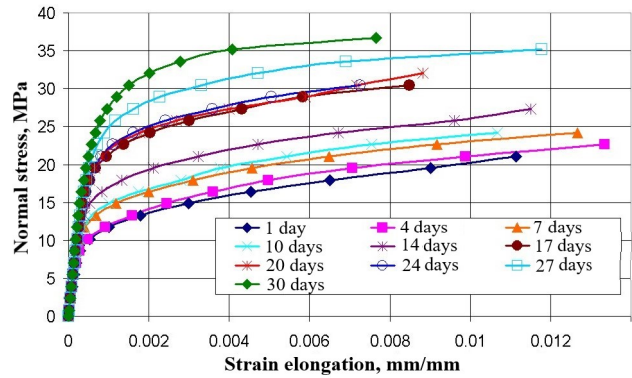
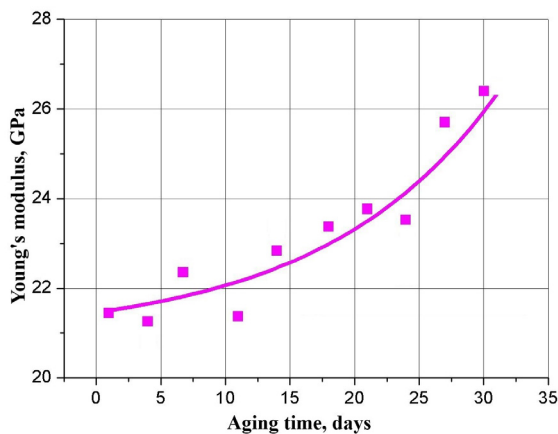
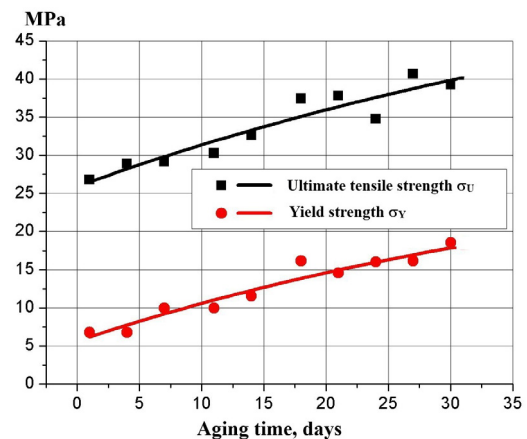


Figure 6. Stress-strain diagrams averaged over 10 sets of 60 specimens aged for 1–30 days

The slope of a linear region of the stress-strain graphs increases with prolonging aging time during storage, which evidences the improvement of elastic properties (Fig. 6). Besides, the curves have a larger elastic region where the stress-strain relationship is linear, so the stress at which specimens deform plastically increases. The lift height of the stress-strain graphs increases with aging time which means that the studied Pb–Sb–Sn–As–Se alloys become stronger. These observations are confirmed by calculated average values of Young's modulus, yield strength, and ultimate tensile strength as functions of aging time (Fig. 7). After 30 days of aging, the values of Young's modulus raise from 21.5 MPa to 26.4 MPa (by ~23 %) (Fig. 7a), yield strength and tensile strength increase correspondingly from 7 MPa to 18 MPa (by 2.4 times) and from 27 MPa to 39 MPa (by ~44 %) (Fig. 7b). Experimental data also show a distinct parallelism between the yield strength and ultimate tensile. Both curves rise steadily as the aging time is increased up to 30 days. Elongation decreases from 10 % to 5.3 % (by 47 %), which is in good agreement with results shown in Fig. 4b.



a



b

Figure 7. Average values of tensile properties vs. aging time: a – Young's modulus; b – yield strength and ultimate tensile

A higher Young's modulus indicates that the investigated Pb–Sb–Sn–As–Se alloys become stiffer after natural aging and require higher force to be deformed. The yield strength is most affected by the second-phase particles precipitated during aging because they inhibit dislocation and grain boundary movement and decrease permanent deformation of the alloys when stresses exceed the yield strength. As the number of second-phase particles is increased by longer aging time, the yield strength reaches a highest value. The ultimate tensile data confirm the results obtained in other mechanical tests on P-0.5 tensile testing machine (Fig. 4a). The yield strength is proportionally lower than the ultimate tensile strength during the studied period of natural aging. This is due to the grain structure and second-phase particle distribution in the structure of the alloys. Lower amounts of alloying elements are present in solution which precipitate as second-phase particles within the lead matrix. This location of the precipitates is less effective in increasing the yield strength by blocking the motion of dislocations within the grains.

### CONCLUSIONS

In this study, the effects of alloying elements, casting conditions and aging time during storage on the tensile properties of the Pb–Sb–Sn–As–Se grid alloys were investigated. From the experimental results and their analysis, the following conclusions can be made. Ultimate tensile strength and elongation results for the alloys in as-cast condition are quite irregular, but in general do not change greatly with changing composition within the range of Sb (1.55–

1.77 wt.%); Sn (0.11–0.17 wt.%); As (0.097–0.13 wt.%); Se (0.018–0.025 wt.%); impurities (0.0217–0.0533 wt.%); Pb – the remainder. Most of the as-cast Pb–Sb–Sn–As–Se alloys simultaneously combine enhanced values of ultimate tensile strength and elongation, which made them valuable for structural grid components that experience high dynamic loads. Increase in a heating temperature of casting mold causes the slight decrease in the tensile strength but does not significantly affect the elongation. Pouring of the molten metal into a casting mold preheated in the temperature range between 110 °C and 150 °C was found to be effective in stabilizing the tensile properties of the studied grid alloys.

The storing of Pb–Sb–Sn–As–Se alloys for 30–33 days does not weaken them in any degree. Due to natural aging the structure of the alloys undergoes microscopic changes that increase both the yield strength and the ultimate tensile strength, simultaneously increasing Young's modulus and decreasing elongation. The strongest effect of strengthening is observed during the first 5 days of natural aging. Thus, the investigated alloys strengthen rather rapidly so that the grids can be utilized in a short period of time after production without excessively long aging time or artificial aging.

The work was performed within the framework of research projects of National Academy of Sciences of Ukraine No. 1.3.6.18 “Development of new methods and improvement of known ones to investigate mechanics of transport and energetic systems” (2017-2021) and No. 1.3.6.22 “Development of mathematical models and investigation of ground transport and energetic systems” (2022-2026).

#### ORCID

©Victor O. Dzenzerskiy, <https://orcid.org/0000-0002-9722-1920>; ©Sergei V. Tarasov, <https://orcid.org/0000-0002-9254-1503>  
 ©Olena V. Sukhova, <https://orcid.org/0000-0001-8002-0906>; ©Volodymyr A. Ivanov, <http://orcid.org/0009-0008-9836-6508>

#### REFERENCES

- [1] S. Guruswamy, *Engineering Properties and Applications of Lead Alloys*, (CRC Press, New York, 2000). <https://doi.org/10.1201/9781482276909>
- [2] D.A.J. Rand, T. Moseley, J. Garche, and C.D. Parker, *Valve-Regulated Lead-Acid Batteries*, (Elsevier, Amsterdam, 2004). <https://doi.org/10.1016/B978-0-444-50746-4.X5000-4>
- [3] A.H. Seikh, E.-S.M. Sherif, S.M.A. Khan Mohammed, M. Baig, M.A. Alam, and N. Alharthi, *PLOS One*. **13**(4), 1 (2018). <https://doi.org/10.1371/journal.pone.0195224>
- [4] H.T. Liu, C.X. Yang, H.H. Liang, J. Yang, and W.F. Zhou, *J. Power Sources*. **103**(2), 173 (2002). [https://doi.org/10.1016/S0378-7753\(01\)00839-4](https://doi.org/10.1016/S0378-7753(01)00839-4)
- [5] W.-B. Cai, Y.-Q. Wan, H.-T. Liu, and W.-F. Zhou, *Chin. J. Chem.* **14**(2), 138 (1996). <https://doi.org/10.1002/cjoc.19960140208>
- [6] T. Hirasawa, K. Sasaki, M. Taguchi, and H. Kaneko, *J. Power Sources*. **85**(1), 44 (2000). [https://doi.org/10.1016/S0378-7753\(99\)00380-8](https://doi.org/10.1016/S0378-7753(99)00380-8)
- [7] M. Viespoli, A. Johanson, A. Alvaro, B. Nyhus, A. Sommacal, and F. Berto, *Mater. Sci. Eng. A* **744**, 365 (2019). <https://doi.org/10.1016/j.msea.2018.12.039>
- [8] T. Gancarz and W. Gasior, *J. Chem. Eng. Data*. **63**(5), 1471-1479 (2018). <https://doi.org/10.1021/acs.jced.7b01049>
- [9] S.E. Kisakurek, *J. Mater. Sci.* **19**(7), 2289-2305 (1984). <https://doi.org/10.1007/BF01058106>
- [10] R.D. Prengaman, *J. Power Sources*. **67**(1-2), 267-278 (1997). [https://doi.org/10.1016/S0378-7753\(97\)02512-3](https://doi.org/10.1016/S0378-7753(97)02512-3)
- [11] K. Sawai, Y. Tsuboi, Y. Okada, M. Shiomi, and S. Osumi, *J. Power Sources*. **179**(2), 799-807 (2008). <https://doi.org/10.1016/j.jpowsour.2007.12.106>
- [12] D.A.J. Rand, D.P. Boden, C.S. Lakshmi, R.R. Nelson, and R.D. Prengaman, *J. Power Sources*. **107**(2), 280-300 (2002). [https://doi.org/10.1016/S0378-7753\(01\)01083-7](https://doi.org/10.1016/S0378-7753(01)01083-7)
- [13] R.D. Prengaman, *J. Power Sources*. **95**(1-2), 224-233 (2001). [https://doi.org/10.1016/S0378-7753\(00\)00620-0](https://doi.org/10.1016/S0378-7753(00)00620-0)
- [14] A.G. Gad Allah, H.A.A. El-Rahman, S.A. Salih, and M.A. El-Galil, *J. Appl. Electrochem.* **22**(6), 571-576 (1992). <https://doi.org/10.1007/BF01024099>
- [15] H. Li, W.X. Guo, H.Y. Chen, D.E. Finlow, H.W. Zhou, C.L. Dou, G.M. Xiao, S.G. Peng, W.W. Wei, and H. Wang, *J. Power Sources*. **191**(1), 111-118 (2009). <https://doi.org/10.1016/j.jpowsour.2008.10.059>
- [16] R.K. Shervedani, A.Z. Isfahani, R. Khodavisy, and A. Hatefi-Mehrjardi, *J. Power Sources*. **164**(2), 890-895 (2007). <https://doi.org/10.1016/j.jpowsour.2006.10.105>
- [17] M. Matrakova, A. Aleksandrova, P. Nikolov, O. Saoudi, and L. Zerroual, *Bulg. Chem. Commun.* **52**(A), 74-79 (2020). [https://doi.org/10.34049/bcc.52.A.232\\_74](https://doi.org/10.34049/bcc.52.A.232_74)
- [18] S. Khatbi, Y. Gouale, S. Mansour, A. Lamiri, and M. Essahli, *Port. Electrochim. Acta*. **36**(2), 133-146 (2018). <https://doi.org/10.4152/pea.201802133>
- [19] Y.B. Zhou, C.X. Yang, W.F. Zhou, and H.T. Liu, *J. Alloys Compd.* **365**(1-2), 108-111 (2004). [https://doi.org/10.1016/S0925-8388\(03\)00649-2](https://doi.org/10.1016/S0925-8388(03)00649-2)
- [20] B. Yang, C. Xianyu, Y. Shaoqiang, L. Wei, D. Changsong, and Y. Geping, *J. Energy Storage*. **25**, 100908 (2019). <https://doi.org/10.1016/j.est.2019.100908>
- [21] Z. Ghasemi and A. Tizpar, *Int. J. Electrochem. Sci.* **2**, 700-720 (2007). [https://doi.org/10.1016/S1452-3981\(23\)17106-9](https://doi.org/10.1016/S1452-3981(23)17106-9)
- [22] Z. Ghasemi and A. Tizpar, *Int. J. Electrochem. Sci.* **3**, 727-745 (2008). [https://doi.org/10.1016/S1452-3981\(23\)15476-9](https://doi.org/10.1016/S1452-3981(23)15476-9)
- [23] Z. Ghasemi and A. Tizpar, *Appl. Surf. Sci.* **252**(10), 3667-3672 (2006). <https://doi.org/10.1016/j.apsusc.2005.05.043>
- [24] D. Slavkov, B.S. Haran, B.N. Popov, and F. Fleming, *J. Power Sources*. **112**(1), 199-208 (2002). [https://doi.org/10.1016/S0378-7753\(02\)00368-3](https://doi.org/10.1016/S0378-7753(02)00368-3)
- [25] E. Rocca, G. Bourguignon, and J. Steinmetz, *J. Power Sources*. **161**(2), 666-675 (2006). <http://dx.doi.org/10.1016/j.jpowsour.2006.04.140>
- [26] C.S. Lakshmi, J.E. Manders, and D.M. Rice, *J. Power Sources*. **73**(1), 23-29 (1998). [https://doi.org/10.1016/S0378-7753\(98\)00018-4](https://doi.org/10.1016/S0378-7753(98)00018-4)

- [27] M.T. Wall, Y. Ren, T. Hesterberg, T. Ellis, and M.L. Young, J. Energy Storage. **55**, 105569 (2022). <https://doi.org/10.1016/j.est.2022.105569>
- [28] S. O'Dell, G. Ding, and S. Tewari, Metall. Mater. Trans. A **30**(8), 2159-2165 (1999). <https://doi.org/10.1007/s11661-999-0027-7>
- [29] N. Ryoichi, Bull. Univ. Osaka Prefect. A **16**(1), 145-157 (1967). <http://doi.org/10.24729/00008892>
- [30] S. El-Gamal, Gh. Mohammed, and E.E. Abdel-Hady, Am. J. Mater. Sci. **5**(5), 97-105 (2015). <https://doi.org/10.5923/j.materials.20150505.01>
- [31] M.M. El-Sayed, F. Abd El-Salam, R. Abd El-Hasseb, and M.R. Nagy, Phys. Status Solidi. A **144**(2), 329-334 (1994). <https://doi.org/10.1002/pssa.2211440211>
- [32] J.P. Hilger, J. Power Sources. **53**(1), 45-51 (1995). [https://doi.org/10.1016/0378-7753\(94\)01977-4](https://doi.org/10.1016/0378-7753(94)01977-4)
- [33] G.S. Al-Ganainy, M.T. Mostafa, and F. Abd El-Salam, Physica. B **348**(1-4), 242-248 (2004). <https://doi.org/10.1016/j.physb.2003.11.096>
- [34] O.V. Sukhova and Yu.V. Syrovatko, Metallofiz. Noveishie Technol. **33**(Special Issue), 371-378 (2011). (in Russian)
- [35] I.M. Spiridonova, E.V. Sukhovaya, and V.P. Balakin, Metallurgia. **35**(2), 65-68 (1996).
- [36] R.D. Prengaman, J. Power Sources. **53**(2), 207-214 (1995). [http://dx.doi.org/10.1016/0378-7753\(94\)01975-2](http://dx.doi.org/10.1016/0378-7753(94)01975-2)
- [37] I. Spiridonova, O.V. Sukhova, and A. Vashchenko, Metallofiz. Noveishie Technol. **21**(2), 122-125 (1999).
- [38] G.S. Al-Ganainy, M.T. Mostafa, and M.R. Nagy, Phys. Stat. Sol. A **165**(1), 185-193 (1998). [https://doi.org/10.1002/\(SICI\)1521-396X\(199801\)165:1<185::AID-PSSA185>3.0.CO;2-M](https://doi.org/10.1002/(SICI)1521-396X(199801)165:1<185::AID-PSSA185>3.0.CO;2-M)
- [39] O.V. Sukhova, V.A. Polonsky, and K.V. Ustinova, Vopr. Khimii Khimicheskoi Tekhnologii. **3**, 46-52 (2019). <http://dx.doi.org/10.32434/0321-4095-2019-124-3-46-52>. (in Ukrainian)
- [40] Y. Zhang, K. Shimizu, X. Year, K. Kusumoto, and V.G. Efremenko, Wear. **390-391**, 135-145 (2017). <https://doi.org/10.1016/j.wear.2017.07.017>
- [41] O.V. Sukhova and K.V. Ustinova, Funct. Mater. **26**(3), 495-506 (2019). <https://doi.org/10.15407/fm26.03.495>
- [42] E. Gullian, L. Albert, and J.L. Caillerie, J. Power Sources. **116**(1-2), 185-192 (2003). [http://dx.doi.org/10.1016/S0378-7753\(02\)00705-X](http://dx.doi.org/10.1016/S0378-7753(02)00705-X)
- [43] O.V. Sukhova, V.A. Polonsky, and K.V. Ustinova, Voprosy Khimii i Khimicheskoi Tekhnologii. **6**, 77-83 (2018). <https://doi.org/10.32434/0321-4095-2018-121-6-77-83>. (in Ukrainian)
- [44] S.I. Ryabtsev, V.A. Polonsky, and O.V. Sukhova, Mater. Sci. **56**(2), 263-272 (2020). <https://doi.org/10.1007/s11003-020-00428-8>
- [45] O.V. Sukhova, Phys. Chem. Solid St. **22**(1), 110-116 (2021). <https://doi.org/10.15330/pcss.22.1.110-116>
- [46] L. Albert, A. Goguelin, and E. Jullian, J. Power Sources. **78**(1-2), 23-29 (1999). [https://doi.org/10.1016/S0378-7753\(99\)00006-3](https://doi.org/10.1016/S0378-7753(99)00006-3)
- [47] O.V. Sukhova and V.A. Polonsky, East Eur. J. Phys. **3**, 5-10 (2020). <https://doi.org/10.26565/2312-4334-2020-3-01>
- [48] O.V. Sukhova, Probl. At. Sci. Technol. **4**, 77-83 (2020). <https://doi.org/10.46813/2020-128-077>
- [49] D.M. Rosa, J.E. Spinelli, I.L. Ferreira, and A. Garcia, Metall. Mater. Trans. A **39**(9), 2161-2174 (2008). <https://doi.org/10.1007/s11661-008-9542-1>
- [50] O.V. Sukhova, V.A. Polonsky, and K.V. Ustinova, Mater. Sci. **55**(2), 285-292 (2019). <https://doi.org/10.1007/s11003-019-0030-2>
- [51] V.A. Dzenzerskiy, V.F. Bachev, V.A. Polonskiy, S.V. Tarasov, Yu.I. Kazacha, V.A. Ivanov, and A.A. Kostina, Metallofiz. Noveishie Technol. **36**(2), 259-273 (2014). <https://doi.org/10.15407/mfint.36.02.0259>

### ЗМІНА МЕХАНІЧНИХ ВЛАСТИВОСТЕЙ СПЛАВІВ Pb–Sb–Sn–As–Se ДЛЯ СТРУМОВІДВОДІВ СВИНЦЕВО-КИСЛОТНИХ БАТАРЕЙ ПІД ЧАС ПРИРОДНОГО СТАРІННЯ

Віктор О. Дзензерський, Сергій В. Тарасов, Олена В. Сухова, Володимир А. Іванов

*Інститут транспортних систем і технологій Національної Академії наук України*

*49005, Україна, м. Дніпро, вул. Писаржевського, 5*

Роботу присвячено дослідженню механічних властивостей низькосурм'яних Pb–Sb–Sn–As–Se сплавів для струмовідводів свинцево-кислотних батарей у литому стані та після природного старіння під час зберігання на складі. З використанням універсальних розтяжних машин TIRAtest 2300 і P-0.5 визначено межі міцності на розтяг, межі плинності, подовження і модуль Юнга за кімнатної температури. Для більшості досліджених сплавів у литому стані збільшення межі міцності на розтяг супроводжується збільшенням подовження. Підвищення температури нагріву ливарної форми в температурному інтервалі 70–150 °C практично не впливає на середні значення подовження сплавів, але незначно знижує їх середню межю міцності на розтяг (на ~4%). Внаслідок старіння під час зберігання на складі впродовж 30–33 діб спостерігається підвищення значень межі міцності на розтяг, межі плинності і модуля Юнга, але зниження значень подовження сплавів Pb–Sb–Sn–As–Se для струмовідводів. Такі зміни пов'язані з виділенням частинок вторинних фаз з твердого розчину на основі свинцю, пересиченого сурмою, миш'яком і селеном. Найбільший зміцнювальний ефект спостерігається впродовж перших п'яти діб природного старіння.

**Ключові слова:** свинцево-кислотні батареї; низькосурм'яні Pb–Sb–Sn–As–Se сплави для струмовідводів; природне старіння під час зберігання; випробування на розтяг; межа міцності на розтяг; межа плинності; подовження; модуль Юнга

## STUDY OF THE MOBILITY AND ELECTRICAL CONDUCTIVITY OF CHROMIUM SILICIDE

✉ Makhmudhodzha Sh. Isaev<sup>a</sup>, Tokhirjon U. Atamirzaev<sup>b</sup>, Mukhammadsodik N. Mamatkulov<sup>c</sup>,  
Uralboy T. Asatov<sup>c</sup>, Makhmudjon A. Tulametov<sup>c</sup>

<sup>a</sup> National University of Uzbekistan, Tashkent, Uzbekistan

<sup>b</sup> Namangan Engineering Construction Institute, Namangan, Uzbekistan

<sup>c</sup> Tashkent Institute of Chemical Technology, Tashkent, Uzbekistan

\*Corresponding Author e-mail: [isayevmahmud02@gmail.com](mailto:isayevmahmud02@gmail.com)

Received August 8, 2023; revised September 16, 2023; accepted September 18, 2023

The temperature dependence of the mobility in chromium silicides in the temperature range of 80 ÷ 780 K was studied. The mobility gradually increases to a temperature of 350 K, then it saturates in the temperature range of 350 ÷ 450 K, then gradually decreases. It is shown that the mobility depends on the scatter of charge of carriers on a crystal lattice, impurity ions, dislocations, and silicide inclusions. The frequency of collisions is proportional to  $T^{3/2}$ , and the mobility varies with temperature as  $T^{-3/2}$ . At high temperatures, phonons may be considered as “frozen” defects and collision frequency with its will proportional to  $T$ . The temperature dependences of the electrical conductivity in this temperature range were also studied. Areas with negative and positive temperature coefficients are revealed.

**Keywords:** Diffusion; Associate; Lifetime; Film; Acceptor center; Radioactive isotope; Distribution; Mobility; Resistivity; Diffusion coefficient; Enthalpy

**PACS:** 71.20. – b, 71.28. + d

### INTRODUCTION

The use of diffusion-doped single-crystal silicon to produce Schottky diodes, sandwich photoresistors, infrared sensors, thermal sensors, and solar cells is an urgent task today [1-3]. A well-developed technology for growing single-crystal silicon, a fundamentally new technology for creating low-dimensional objects in silicon, modifying properties by various methods, as well as discovering new physical phenomena in the near-surface region that are not typical for bulk silicon, attracts close attention of researchers as an active material for the needs of micro- and nanotechnology [4,5].

Currently, transition metal silicides are becoming the base material for new, promising technological schemes of future generations due to their resistance to aggressive media and high-temperature treatments [6-9]. Therefore, a comprehensive study of the mechanism of the entry of impurities into the bulk of the crystal and their interaction with both the matrix atoms of the crystal and technological impurities is relevant. From this point of view, the study of the formation of silicides in the surface region of silicon during diffusion doping and the development of new semiconductor devices based on them is of particular scientific importance in the context of the creation of new materials for micro- and nanoelectronics.

Therefore, in this work, we investigated the mobility of charge carriers and electrical conductivity, which are necessary in studying the mechanism of current flow through chromium silicides.

### MATERIALS AND METHODS

Chromium has a large diffusion coefficient in silicon, so the diffusion method of doping was used. This method has a number of other advantages: 1) relative simplicity of technology; 2) the possibility of studying the influence of annealing temperature on the initial parameters of the crystal; 3) the ability to regulate the concentration of electrically active chromium atoms by changing the temperature. [10, 11]. For doping, single-crystal silicon samples of the KDB-10 and KEF-20 brands grown by the Czochralski method were used. Samples in the form of a parallelepiped with dimensions of  $2 \times 2 \times 10 \text{ mm}^3$ ,  $3 \times 5 \times 16 \text{ mm}^3$  were cut out from single crystal ingots. The samples were degreased and subjected to chemical etching in a 1HF:5HNO<sub>3</sub> solution for 1÷2 minutes, washed in deposited water, and dried at a temperature not exceeding 373 K.

Ampoules with silicon samples and powders of chromium atoms were evacuated to a vacuum of ~0.133 Pa and sealed. The ampoules were placed in a horizontal furnace and annealed at a temperature of 1123 ÷ 1323 K for 30 ÷ 80 minutes. After annealing, the samples were quenched at a rate of 150 K/s. Using the methods of helium ion back scattering spectrometry [12], X-ray photoelectron spectrometry, the formation of new chemical compounds was proved: mono-, di- higher chromium silicides. Electrical conductivity and mobility were measured by classical methods [13-15].

### RESULTS AND DISCUSSION

In Fig. 1 the temperature dependence of the mobility of charge carriers is given. As can be seen from this figure, the mobility increases smoothly up to a temperature of 350 K, then it saturates in the temperature range of 350 ÷ 450 K, then gradually decreases. Mobility is a characteristic that depends on the scattering of current carriers.

Carriers scatter for various reasons: on vibrations of atoms of the crystal lattice, on impurity ions, when colliding with each other, on neutral impurities, on crystal imperfections, such as dislocations, boundaries of crystal grains, boundaries of silicide inclusions, etc. Thus, the frequency of collisions of carriers with scattering centers will be the sum of the frequencies of collisions with various kinds of defects.

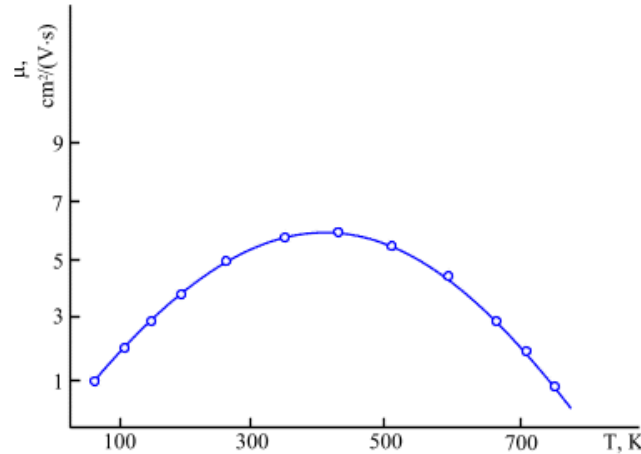


Figure 1. Temperature dependence of mobility in Si<Cr> samples

Carriers scatter for various reasons: on vibrations of atoms of the crystal lattice, on impurity ions, when colliding with each other, on neutral impurities, on crystal imperfections, such as dislocations, boundaries of crystal grains, boundaries of silicide inclusions, etc. Thus, the frequency of collisions of carriers with scattering centers will be the sum of the frequencies of collisions with various kinds of defects.

In different temperature regions, the role of collisions of various kinds is not the same. Scattering of carriers occurs as a result of thermal vibrations of atoms. The cross section associated with thermal vibrations of atoms and leading to scattering of the carrier is proportional to the square of the amplitude of thermal vibrations, which in turn is proportional to the energy  $kT$ . In this case, the effective frequency of carrier collisions will be proportional to the cross section of scattering centers and the velocity of carriers moving between them:  $\langle v_H \rangle \sim \sqrt{T}$ . Thus, the frequency of atomic vibrations is proportional to  $T^{3/2}$ , and the mobility varies with temperature as  $T^{-3/2}$ . At sufficiently high temperatures, the phonon velocity is  $10^5$  cm/s, and the current carrier velocity is  $10^7$  cm/s. Therefore, for current carriers, phonons are practically “frozen” lattice defects. The frequency of collisions with these “frozen” defects will be proportional to their number, i.e.  $T$ .

In Si<Cr> samples, in the near-surface region with a thickness of 35  $\mu\text{m}$ , when carriers are scattered by impurity ions, the mobility increases with increasing temperature, then it reaches saturation, and at high temperatures, when scattering occurs mainly on phonons, the mobility decreases.

Typical temperature dependences of electrical conductivity for chromium silicides are shown in Fig. 2.

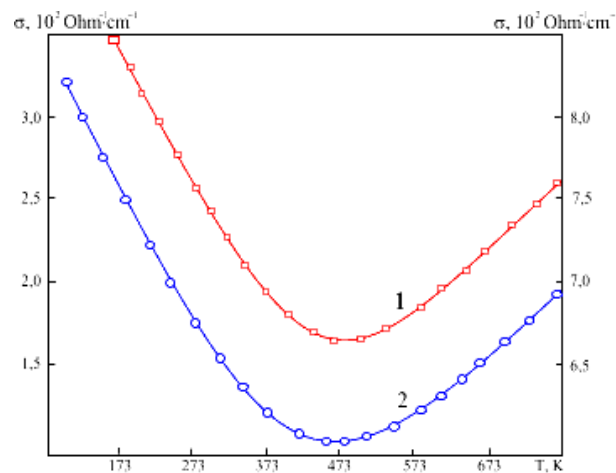


Figure 2. Temperature dependence of electrical conductivity of chromium silicides: 1– for CrSi; 2–for CrSi<sub>2</sub>

It can be seen from the figure that both for CrSi and CrSi<sub>2</sub> there are three regions. The first section is the temperature range 73 ÷ 423 K, where the electrical conductivity decreases linearly with increasing temperature. The second section is the temperature range 423 ÷ 523 K, where the electrical conductivity almost does not change. The third section is the

temperature range  $523 \div 773$  K, where the electrical conductivity increases linearly with increasing temperature. In the first region, chromium silicide behaves metal-like, having a negative temperature coefficient.

In the third section, the temperature dependence of chromium silicide is similar to that of a semiconductor (positive temperature coefficient). The electrical conductivity of chromium monosilicide is about 6-7 times greater than that of disilicide, which is explained by the difference in the number of charge carriers.

The decrease in electrical conductivity in the first section is due to the increased scattering of electrons on lattice phonons, on the boundaries of crystal grains, on crystal imperfections, on impurity ions, and so on. It should be noted that the role of collisions of various kinds is not the same in different temperature regions. In our crystals, the main role is played by scattering by vibrations of lattice atoms and by the boundaries of crystal grains.

## CONCLUSIONS

Diffusion doping of silicon with chromium revealed a near-surface region  $35 \mu\text{m}$  thick, where chromium silicides are formed. The temperature dependences of the mobility of current carriers and the electrical conductivity of the silicide layer of the crystal were experimentally studied in the temperature range  $350 \div 780$  K. It was shown that the mobility increases smoothly up to 350 K, then saturates, then gradually decreases.

The reasons for this dependence are indicated. Three segments were revealed in the temperature dependence of mobility: the first segment is the temperature range  $77 \div 423$  K, where the electrical conductivity linearly decreases with increasing temperature. The second section is the temperature range  $423 \div 523$  K, where the electrical conductivity does not change. The third section is the temperature range of  $523 \div 773$  K, where the electrical conductivity of the linear increases with increasing temperature, the conductivity increases linearly with increasing temperature. Such a temperature dependence of the electrical conductivity is explained by the difference in the type of scattering in different temperature regions.

## ORCID

✉ Makhmudhodzha Sh. Isaev, <https://orcid.org/0009-0007-9559-5834>

## REFERENCES

- [1] M.Sh. Isaev, A.G. Gaibov, and A.A. Eshkulov, "Investigation of parameters of Schottky diodes based on chromium silicides," *Journal of Physics: Conference Series*, **1679**, 022029 (2020). <https://doi.org/10.1088/1742-6596/1679/2/022029>
- [2] Sh.B. Utamuradova, A.V. Stanchik, D.A. Rakhmanov, A.S. Doroshkevich, and K.M. Fayzullaev, *New Materials, "X-Ray Structural Analysis of n-Si<Cr>, Irradiated with Alpha Particles," Compounds and Applications*, **6**(3), 214 (2022). [http://jomardpublishing.com/UploadFiles/Files/journals/NMCA/V6N3/Utamuradova\\_et\\_al.pdf](http://jomardpublishing.com/UploadFiles/Files/journals/NMCA/V6N3/Utamuradova_et_al.pdf)
- [3] D. Nematov, Kh. Kholmurodov, A. Stanchik, K. Fayzullaev, V. Gnatovskaya, and T. Kudzoev, "On the Optical Properties of the  $\text{Cu}_2\text{ZnSn}[\text{S}_{1-x}\text{Se}_x]_4$  System in the IR Range," *Trends in Sciences*, **20**(2), 4058 (2023). <https://doi.org/10.48048/tis.2023.4058>
- [4] S.A. Muzafarova, Sh.B. Utamuradova, A.M. Abdugafurov, K.M. Fayzullaev, E.M. Naurzalieva, and D.A. Rakhmanov, "Characteristics of X-ray and gamma radiation detectors based on polycrystalline CdTe and CdZnTe films," *Applied Physics*, **4**, 81 (2021). <https://applphys.orion-ir.ru/appl-21/21-4/PF-21-4-81.pdf> (in Russian)
- [5] D. Nematov, Kh. Kholmurodov, A. Stanchik, K. Fayzullaev, V. Gnatovskaya, and T. Kudzoev, "A DFT Study of Structure, Electronic and Optical Properties of Se-Doped Kesterite  $\text{Cu}_2\text{ZnSnS}_4$  (CZTSSe)," *Letters in Applied NanoBioScience*, **12**(3), 67 (2023). <https://doi.org/10.33263/LIANBS123.067>
- [6] A.S. Achilov, R.R. Kabulov, S.B. Utamuradova, and S.A. Muzafarova, "Effect of temperature on the current transfer mechanism in the reverse I-V characteristics of the n-CdS/i-CdS<sub>x</sub>Te<sub>1-x</sub>/p-CdTe heterostructure," *Modern Physics Letters B*, 2350162, (2023). <https://doi.org/10.1142/S0217984923501622>
- [7] B.I. Boltaks, M.K. Bakhadyrkhanov, S.M. Gorodetsky, and G.S. Kulikov, *Compensated silicon*, (Nauka, Leningrad, 1972). (in Russian)
- [8] M. Isaev, A. Gaibov, A. Eshkulov, and P. Saidachmetov, "Formation of Nanosized Films of Chromium Silicides on Silicon Surface," in: *XIV International Scientific Conference "INTERAGROMASH 2021"*, (2022), pp. 1031-1041. [https://doi.org/10.1007/978-3-030-80946-1\\_93](https://doi.org/10.1007/978-3-030-80946-1_93)
- [9] M.Sh. Isaev, Sh.G. Norov, and A.D. Mazhidov, "Study of galvanomagnetic properties of the surface layer of diffusion-doped silicon," *Electronic Processing of Materials*, **42**(6), 80 (2006). <https://eom.ifa.md/ru/journal/shortview/848>. (in Russian)
- [10] N.A. Turgunov, E.Kh. Berkinov, and R.M. Turmanova, "Accumulations of impurity Ni atoms and their effect on the electrophysical properties of Si," in: *E3S Web of Conferences*, **402**, 14018 (2023). <https://doi.org/10.1051/e3sconf/202340214018>
- [11] Sh.B. Utamuradova, Sh.Kh. Daliev, K.M. Fayzullaev, D.A. Rakhmanov, and J.Sh. Zarifbayev, *New Materials, Compounds and Applications*, **7**(1), 37 (2023). [http://jomardpublishing.com/UploadFiles/Files/journals/NMCA/V7N1/Utamuradova\\_et\\_al.pdf](http://jomardpublishing.com/UploadFiles/Files/journals/NMCA/V7N1/Utamuradova_et_al.pdf)
- [12] Y.Y. Kryuchkov, V.M. Malyutin, V.F. Pichugin, and V.V. Sohoreva, "Development and application of fast ion backscattering spectroscopy methods for analyzing the composition and structure of ion-irradiated dielectric layers," *Bulletin of the Tomsk Polytechnic University. Georesource Engineering*, **303**(3), 12 (2000). <https://cyberleninka.ru/article/n/razrabotka-i-primeneniemetodov-spektroskopii-obratnogo-rasseyaniya-bystryh-ionov-dlya-analiza-sostava-i-struktury-ionno-obluchennyh>. (in Russian)
- [13] S.B. Utamuradova, A.V. Stanchik, and D.A. Rakhmanov, "X-Ray Structural Investigations Of n-Si Irradiated with Protons," *East European Journal of Physics*, **2**, 201 (2023). <https://doi.org/10.26565/2312-4334-2023-2-21>
- [14] Sh.B. Utamuradova, A.V. Stanchik, K.M. Fayzullaev, and B.A. Bakirov, "Raman scattering of light by silicon single crystals doped with chromium atoms," *Applied Physics*, **2**, 33 (2022). [https://applphys.orion-ir.ru/appl-22/22-2/PF-22-2-33\\_RU.pdf](https://applphys.orion-ir.ru/appl-22/22-2/PF-22-2-33_RU.pdf) (in Russian)
- [15] N.A. Turgunov, E.K. Berkinov, and D.K. Mamajonova, "Decay of Impurity Clusters of Nickel and Cobalt Atoms in Silicon under the Influence of Pressure," *Journal of Nano- and Electronic Physics*, **13**(5), 1 (2021). [https://doi.org/10.21272/jnep.13\(5\).05006](https://doi.org/10.21272/jnep.13(5).05006)



**ДОСЛІДЖЕННЯ РУХОМОСТІ ТА ЕЛЕКТРОПРОВІДНОСТІ СИЛІЦИДУ ХРОМУ**  
**Махмудходжа Ш. Ісаєв<sup>a</sup>, Тохірджон У. Атамірзаєв<sup>b</sup>, Мухаммадсодік Н. Маматкулов<sup>c</sup>,**  
**Уралбой Т. Асатов<sup>c</sup>, Махмуджон А. Туламетов<sup>c</sup>**

<sup>a</sup> Національний університет Узбекистану, Ташкент, Узбекистан

<sup>b</sup> Наманганський інженерно-будівельний інститут, Наманган, Узбекистан

<sup>c</sup> Ташкентський хіміко-технологічний інститут, Ташкент, Узбекистан

Досліджено температурну залежність рухливості в силіцидах хрому в інтервалі температур  $80 \div 780$  К. Рухливість поступово зростає до температури 350 К, потім насичується в діапазоні температур  $350 \div 450$  К, потім поступово зменшується. Показано, що рухливість залежить від розкиду носіїв заряду на кристалічній решітці, домішкових іонів, дислокацій та силіцидних включень. Частота зіткнень пропорційна  $T^{3/2}$ , а рухливість змінюється залежно від температури як  $T^{-3/2}$ . При високих температурах фонони можна розглядати як «заморожені» дефекти, а частота зіткнень з їх волі пропорційна  $T$ . Досліджено також температурні залежності електропровідності в цьому діапазоні температур. Виявлено ділянки з негативними та позитивними температурними коефіцієнтами.

**Ключові слова:** дифузія; асоціат; час життя; плівка; акцепторний центр; радіоактивний ізотоп; розподіл; рухливість, питомий опір; коефіцієнт дифузії; ентальпія

## STRUCTURE DETERMINATION AND DEFECT ANALYSIS n-Si<Lu>, p-Si<Lu> BY RAMAN SPECTROMETER METHODS

✉ Khodjakbar S. Daliev<sup>a</sup>, ✉ Sharifa B. Utamuradova<sup>b</sup>, ✉ Zavkiddin E. Bahronkulov<sup>b\*</sup>,  
✉ Alisher Kh. Khaitbaev<sup>c</sup>, ✉ Jonibek J. Hamdamov<sup>b</sup>

<sup>a</sup> Branch of the Federal State Budgetary Educational Institution of Higher Education “National Research University MPEI”,  
1 Yogdu st., Tashkent, Uzbekistan

<sup>b</sup> Institute of Semiconductor Physics and Microelectronics at the National University of Uzbekistan,  
20 Yangi Almazar st., Tashkent, 100057, Uzbekistan

<sup>c</sup> National University of Uzbekistan, Tashkent, Uzbekistan

\*Corresponding Author e-mail: [zbahronkulov@inbox.ru](mailto:zbahronkulov@inbox.ru)

Received August 9, 2023; revised September 13, 2023; accepted September 15, 2023

In this work, lutetium-doped silicon samples were studied using the Raman scattering method. Registration and identification of both crystalline and amorphous phase components in the samples was carried out. There is some violation in the spectra of Raman scattering of light samples of silicon doped with lutetium in comparison with the original sample. It was found that the intensity of Raman scattering of doped samples is 2-3 times higher than the scattering from silicon. The comparison is carried out for the intensities associated with the intensities of the single-phonon line of the silicon substrate. This effect of the Raman spectra in the range  $930\text{ cm}^{-1} - 1030\text{ cm}^{-1}$  appearing in this range is similar to the data reduction for multiphonon propagation on silicon. For the obtained images (n-Si<Lu> and p-Si<Lu>), the bands in the atomic range of combinatorial scattering have a mixed broad and oval background in the range from  $623\text{ cm}^{-1}$  to  $1400\text{ cm}^{-1}$ . This background can change the shape of the observed bands.

**Keywords:** Silicon; Lutetium; Raman spectroscopy; Diffusion; Doping; Temperature

**PACS:** 78.30.Am

### INTRODUCTION

Modern world scientific and technological progress is largely determined by the development of electronics, the achievements of which directly depend on the success of fundamental sciences, primarily solid-state physics and semiconductor physics [1]. Recent advances in these areas are related to the physics of low-dimensional structures and the creation of technologies for obtaining nanostructures with fundamentally new functionality for nano- and optoelectronics, communications, new technologies, measuring equipment, etc. Structured silicon is currently of great interest, since Si itself is an extremely promising material not only for electronics, but also for optoelectronics and solar cells [2,5]. In this regard, studies of the formation of low-dimensional objects and the study of their influence on the electrophysical, optical, photoelectric, and magnetic properties of semiconductors are topical tasks of today [4,6-8]. In the last two decades, Raman spectroscopy (Raman Spectroscopy) has been widely used to study the structure and dynamics of solids. Raman spectroscopy is one of the most powerful analytical methods, when analyzing the chemical and phase state of various objects and their structure and when researching and developing new semiconductor materials, composites, superconductors. Raman scattering has become a standard tool for studying silicon and nanostructured silicon for many years [5,13,14]. Raman studies of nanomaterials provide us with information about energy dispersion, structure, bonding, and disorder [3,16]. In this work, we present the spectra of one- and two-phonon Raman scattering of light from single-crystal silicon doped with lutetium (Lu) atoms.

### MATERIALS AND METHODS

Samples of n-Si and p-Si with initial resistivity from  $0.3$  to  $100\ \Omega\cdot\text{cm}$  were chosen for the study. The samples were doped with Lu impurities sequentially by the thermal diffusion method. Before alloying, the samples were subjected to chemical cleaning and etching, while the oxide layers were removed from the surface of the samples using an HF solution. After thermal degassing of the samples, high-purity (99.999%) Lu impurity films were deposited on clean Si surfaces using vacuum deposition. Vacuum conditions in the volume of the working chamber of the order of  $10^{-6} - 10^{-8}$  Torr were provided by an oil-free vacuum pumping system.

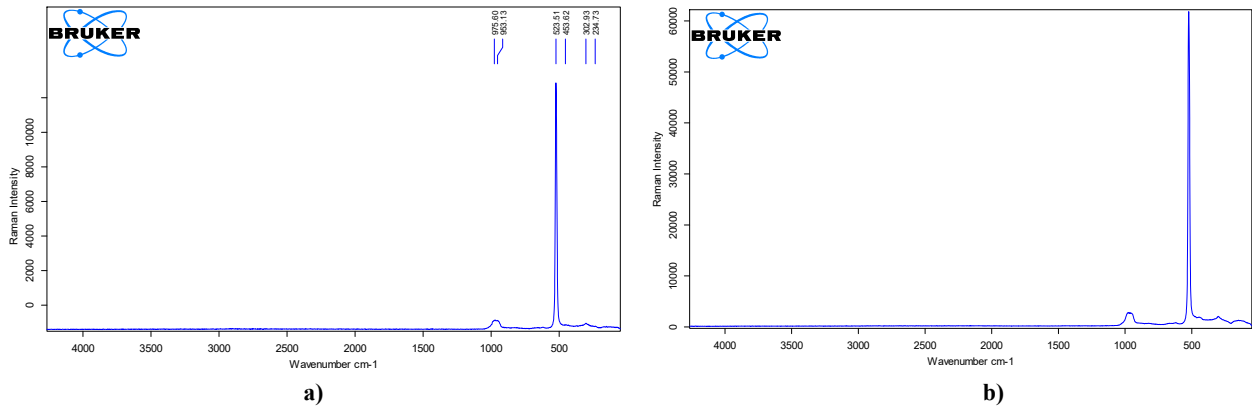
Before diffusion annealing, the samples were placed in evacuated quartz ampoules. The diffusion of Lu impurities into the Si bulk was ensured by heating the deposited samples in a diffusion furnace at a temperature of  $1250^\circ\text{C}$  for 30 hours followed by rapid cooling. To study the interaction of impurity atoms in silicon, it is necessary not only to uniformly dope the material, but also to maximize the concentration [9,10,17].

The Raman spectra were obtained using a SENTERRA II Bruker Raman spectrometer. This fully automated instrument combines excellent sensitivity with a high resolution of  $4.0\text{ cm}^{-1}$ . Sunterra's calibration was automatic and tied to NIST standards, acetaminophen and silicon, resulting in a wavelength measurement accuracy of  $0.2\text{ cm}^{-1}$ . The

experiments were carried out with a laser with a wavelength  $\lambda_0 = 532$  nm, maximum power  $P_{\max} = 25$  mW, acquisition time 100 s, and summation of two spectra. This device makes it possible to obtain spectra in the range from 50 to 4265  $\text{cm}^{-1}$ . The Raman spectra were specially processed in order to be able to compare the intensity ratios between the samples. Before normalizing the spectra at the peak at 522  $\text{cm}^{-1}$ , which corresponded to the most intense peak in the spectral region 4265-50  $\text{cm}^{-1}$ , we subtracted the baseline for each spectrum [11].

Mathematical data preprocessing included offset and cosmic ray removal, baseline correction, and intensity normalization. The intensity of the one-phonon silicon line “523  $\text{cm}^{-1}$ ” was chosen as a condition for normalization, and the value equal to 1 was chosen. Preliminary processing was carried out using the OPUS 8.5 program (Senterra II, Bruker, Germany). The measured spectra for materials with high  $\kappa$  were compared with the data obtained for n-Si and p-Si.

Samples: n-Si, p-Si and lutetium-doped silicon, n-Si<Lu>, p-Si<Lu> were characterized by Raman spectroscopy.



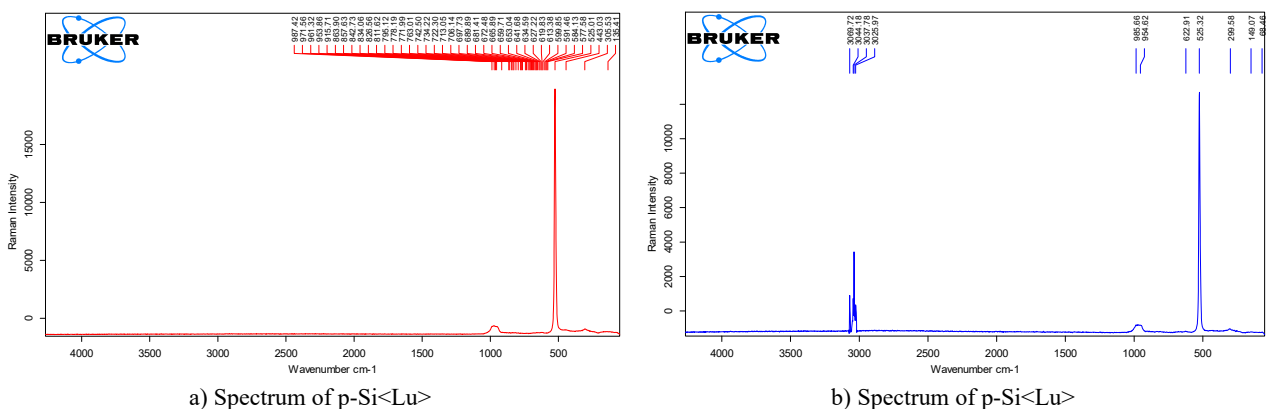
**Figure 1.** Raman spectrum measured for n-Si and p-Si samples, excitation wavelength 532 nm  
 a) n-Si spectrum; b) p-Si spectrum

Figure 1 shows the data collected for n-Si and p-Si samples. In the studied spectra are present as signals modeling a single-phonon silicon line. The following bands can be recognized in the spectrum (except for the Si “523  $\text{cm}^{-1}$ ” line):

- (I) faint band peaking around 230  $\text{cm}^{-1}$ ;
- (II) relatively strong propagation of the band from 300  $\text{cm}^{-1}$  to the one-phonon Si line ( $\sim 550$   $\text{cm}^{-1}$ );
- (III) band with one maximum at about 623  $\text{cm}^{-1}$ ;
- (IV) a broad band with a maximum at about 810  $\text{cm}^{-1}$ ;
- (V) relatively average band spread from 930  $\text{cm}^{-1}$  to 1030  $\text{cm}^{-1}$ ;

The Raman spectra measured for silicon wafers doped with Lu (n-Si<Lu> and p-Si<Lu>) are shown in Fig. 2. The two most important similarities observed for both semiconductor materials can be distinguished without detailed analysis:

- (I) the absence of the so-called bosonic band;
- (II) the presence of a band between 930  $\text{cm}^{-1}$  and 1030  $\text{cm}^{-1}$  in the literature is attributed to multiphonon scattering generated in a silicon substrate [12].



**Figure 2.** Raman spectrum measured for n-Si<Lu> and p-Si<Lu> samples, excitation wavelength 532 nm

Analysis of the Raman spectrum taken for reference samples of n-Si and p-Si (Fig. 1). The band located between 930  $\text{cm}^{-1}$  and 1030  $\text{cm}^{-1}$  refers to multiphonon scattering generated in the silicon substrate [12]. The first feature that appears in the spectra recorded for silicon wafers doped with Lu (n-Si<Lu> and p-Si<Lu>) (Fig. 2) is a significant signal below 300  $\text{cm}^{-1}$ . This corresponds to the boson band recorded for excitation with visible Raman scattering [15]. The absence of a relatively strong band in the Raman shift range between 930  $\text{cm}^{-1}$  and 1030  $\text{cm}^{-1}$  is attributed to second-order scattering in doped silicon also observed for both impurity layers (n-Si<Lu> and p-Si<Lu>). The spectra obtained for n-Si<Lu> and p-Si<Lu> contain not only broad bands, but also narrow lines; the full width at half-height of these

lines is about  $1 \text{ cm}^{-1}$ . This suggests fluctuations in crystal structures as the origin of these lines. Amorphous structures generate bands with a half-width on the order of  $10 \text{ cm}^{-1}$ . The appearance of the first line in the scattering observed for both semiconductors has a maximum of about  $300 \text{ cm}^{-1}$ . The broad band merged with the one-phonon Si line begins between  $305 \text{ cm}^{-1}$  and  $440 \text{ cm}^{-1}$  and is much narrower than the main band. This is followed by a lower growth in the range of  $420 \text{ cm}^{-1}$ – $500 \text{ cm}^{-1}$ . In the Raman shift range of  $500 \text{ cm}^{-1}$  and  $540 \text{ cm}^{-1}$ , the single-phonon Si line dominates in the Raman spectrum. One narrow line peaking at  $395 \text{ cm}^{-1}$  and a slightly wider band peaking at  $452 \text{ cm}^{-1}$  appear in the spectrum of the obtained composites. The next two bands appearing in the Raman spectra have maxima at  $622 \text{ cm}^{-1}$  and  $680 \text{ cm}^{-1}$ . A maximum of  $622 \text{ cm}^{-1}$  corresponds to an unconsolidated structure, and  $680 \text{ cm}^{-1}$  corresponds to a densified structure. The next band present in the Raman spectra, registered for composites, has a maximum at about  $780 \text{ cm}^{-1}$ . The intensity of the band related to the intensity of the one-phonon Si line in the case of composites is approximately two times greater than that for silicon. The following features can be distinguished in the range of the Raman shift from  $930 \text{ cm}^{-1}$ – $1030 \text{ cm}^{-1}$ .

The Raman spectra recorded for n-Si<Lu> and p-Si<Lu> show a broad oval background that ranges from  $623 \text{ cm}^{-1}$ – $1400 \text{ cm}^{-1}$ . The bands described earlier appear against this background. In this case, the Raman scattering signals do not have the typical shape of the observed band for the Si layer and are assigned to multiphonon scattering from the silicon substrate [12]. It is possible that the band assigned to multiphonon scattering is modified and partially masked by the broad background. The last two bands that can be recognized in the spectra measured for the obtained composites have maxima around  $1070 \text{ cm}^{-1}$  and  $1200 \text{ cm}^{-1}$ . The band with the maximum at  $1070 \text{ cm}^{-1}$  has a symmetrical shape. The group with a maximum at  $1200 \text{ cm}^{-1}$  seems asymmetric. The tail of this band reaches  $1400 \text{ cm}^{-1}$ . The maxima of these bands reported in the literature are approximately  $1075 \text{ cm}^{-1}$  and  $1200 \text{ cm}^{-1}$ , respectively.





### CONCLUSIONS

In this work, samples of n-Si, p-Si were studied, as well as samples doped with lutetium, n-Si<Lu>, p-Si<Lu>, according to the data obtained, were characterized using Raman spectroscopy. Raman spectra of doped n-Si<Lu> and p-Si<Lu> samples were compared with silicon. It was found that the intensity of Raman scattering of doped samples is 2-3 times higher than the scattering from silicon. The comparison was made for intensities related to the intensity of the single-phonon line of the silicon substrate.

The last thing to sum up is the behavior of the Raman spectra in the range  $930 \text{ cm}^{-1}$ – $1030 \text{ cm}^{-1}$ . The band appearing in this range is similar to the reduction of data for multiphonon scattering on silicon.

For the obtained n-Si<Lu> and p-Si<Lu> samples, the bands in this range of Raman scattering are shifted with a broad and oval background in the range from  $623 \text{ cm}^{-1}$ – $1400 \text{ cm}^{-1}$ . This background can change the shape of the observed bands.

### ORCID

-  Khodjakbar S. Daliev, <https://orcid.org/0000-0002-2164-6797>; 
  Sharifa B. Utamuradova, <https://orcid.org/0000-0002-1718-1122>  
 Zavkiddin E. Bahronkulov, <https://orcid.org/0009-0002-9843-8344>; 
  Alisher Kh. Khaitbaev, <https://orcid.org/0000-0001-9892-8189>  
 Jonibek J. Hamdamov, <https://orcid.org/0000-0003-2728-3832>

### REFERENCES

- [1] S.B. Utamuradova, S.Kh. Daliev, S.A. Muzafarova, and K.M. Fayzullaev, "Effect of the Diffusion of Copper Atoms in Polycrystalline CdTe Films Doped with Pb Atoms," *East Eur. J. Phys.* 3, 385 (2023), <https://doi.org/10.26565/2312-4334-2023-3-41>
- [2] B.E. Egamberdiev, Sh.B. Utamurodova, S.A. Tachilin, M.A. Karimov, K.Yu. Rashidov, A.R. Kakhramonov, M.K. Kurbanov, *et al.*, *Applied Solar Energy*, **58**(4), 490 (2022). <https://doi.org/10.3103/S0003701X22040065>
- [3] S.B. Utamuradova, S.Kh. Daliev, E.M. Naurzalieva, X.Yu. Utemuratova, "Investigation of Defect Formation in Silicon Doped with Silver and Gadolinium Impurities by Raman Scattering Spectroscopy," *East Eur. J. Phys.* 3, 430 (2023), <https://doi.org/10.26565/2312-4334-2023-3-47>
- [4] N.F. Zikrilliev, G.A. Kushiev, S.V. Koveshnikov, B.A. Abdurakhmanov, U.K. Qurbonova, and A.A. Sattorov, "Current Status of Silicon Studies with Ge<sub>x</sub>Si<sub>1-x</sub> Binary Compounds and Possibilities of Their Applications in Electronics," *East Eur. J. Phys.* 3, 334 (2023), <https://doi.org/10.26565/2312-4334-2023-3-34>
- [5] Sh.B. Utamuradova, A.V. Stanchik, K.M. Fayzullaev, and B.A. Bakirov, "Raman scattering of light by silicon single crystals doped with chromium atoms," *Applied Physics*, (2), 33–38 (2022). [https://applphys.orion-ir.ru/appl-22/22-2/PF-22-2-33\\_EN.pdf](https://applphys.orion-ir.ru/appl-22/22-2/PF-22-2-33_EN.pdf)
- [6] Sh.B. Utamuradova, and D.A. Rakhmanov, "Effect of Holmium Impurity on the Processes of Radiation Defect Formation in n-Si<Pt>," *Annals of the University of Craiova, Physics*, **32**, 132–136 (2022). [https://cis01.central.ucv.ro/pauc/vol/2022\\_32/15\\_PAUC\\_2022\\_132\\_136.pdf](https://cis01.central.ucv.ro/pauc/vol/2022_32/15_PAUC_2022_132_136.pdf)
- [7] M.B. Gongalsky, N.V. Pervushin, D.E. Maksutova, U.A. Tsurikova, P.P. Putintsev, O.D. Gyuppenen, Y.V. Evstratova, *et al.*, "Optical Monitoring of the Biodegradation of Porous and Solid Silicon Nanoparticles," *Nanomaterials*, **11**, 2167 (2021) <https://doi.org/10.3390/nano11092167>
- [8] Z.T. Azamatov, Sh.B. Utamuradova, M.A. Yuldoshev, and N.N. Bazarbaev. "Some properties of semiconductor-ferroelectric structures," *East Eur. J. Phys.* 2, 187-190 (2023), <https://doi.org/10.26565/2312-4334-2023-2-19>
- [9] Kh.S. Daliev, Sh.B. Utamuradova, I.Kh. Khamidzhonov, A.Zh. Akbarov, I.K. Mirzairova, and Zh. Akimova, "Thermally Induced Deep Centers in Silicon Doped with Europium or Lanthanum," *Inorganic Materials*, **37**(5), 436-438 (2001). <https://doi.org/10.1023/A:1017556212569>
- [10] K.P. Abdurakhmanov, Sh.B. Utamuradova, Kh.S. Daliev, S.G. Tadjy-Aglavaeva, and R.M. Érgashev, "Defect-formation processes in silicon doped with manganese and germanium," *Semiconductors*, **32**(6), 606–607 (1998). <https://doi.org/10.1134/1.1187448>

- [11] M. Borowicz, W. Latek, A. Rzdokiewicz, A. Laszcz, Czerwinski, and J. Ratajczak, "Deep ultraviolet Raman investigation of silicon oxide: thin film on silicon substrate versus bulk material," *Advances in Natural Sciences: Nanoscience and Nanotechnology*, **3**, 045003 (2012). <https://doi.org/10.1088/2043-6262/4/045003>
- [12] P.A. Temple, and C.E. Hathaway, "Multiphonon Raman spectrum of silicon," *Physical Review B*, **7**(8), 3685–3697 (1973). <https://doi.org/10.1103/PhysRevB.7.3685>
- [13] A.G. Revesz, and H.L. Hughes, "The structural aspects of non-crystalline SiO<sub>2</sub> films on silicon: a review," *Journal of Non-Crystalline Solids*, **328**(1-3), 48–63 (2003). [https://doi.org/10.1016/S0022-3093\(03\)00467-8](https://doi.org/10.1016/S0022-3093(03)00467-8)
- [14] K.J. Kingma, and R.J. Hemley, "Raman spectroscopic study of microcrystalline silica," *American Mineralogist*, **79**(3-4), 269-273 (1994). [https://pubs.geoscienceworld.org/msa/ammin/article-pdf/79/3-4/269/4209223/am79\\_269.pdf](https://pubs.geoscienceworld.org/msa/ammin/article-pdf/79/3-4/269/4209223/am79_269.pdf)
- [15] G.E. Walrafen, Y.C. Chu, and M.S. Hokmabadi, "Raman spectroscopic investigation of irreversibly compacted vitreous silica," *The Journal of Chemical Physics*, **92**(12), 6987–7002 (1990). <https://doi.org/10.1063/1.458239>
- [16] B. Champagnon, C. Martinet, M. Boudeulle, D. Vouagner, C. Coussa, T. Deschamps, and L. Grosvalet, "High pressure elastic and plastic deformations of silica: in situ diamond anvil cell Raman experiments," *Journal of Non-Crystalline Solids*, **354**(2-9), 569–573 (2008). <https://doi.org/10.1016/j.jnoncrysol.2007.07.079>
- [17] Sh.B. Utamuradova, Kh.S. Daliev, E.K. Kalandarov, and Sh.Kh. Daliev, "Features of the behavior of lanthanum and hafnium atoms in silicon," *Technical Physics Letters*, **32**(6), 469–470 (2006). <https://doi.org/10.1134/S1063785006060034>

**ВИЗНАЧЕННЯ СТРУКТУРИ ТА АНАЛІЗ ДЕФЕКТІВ n-Si<Lu>, p-Si<Lu>  
ЗА ДОПОМОГОЮ РАМАНІВСЬКОЇ СПЕКТРОСКОПІЇ**

**Ходжакбар С. Далієв<sup>а</sup>, Шаріфа Б. Утамурадова<sup>б</sup>, Завкіддін Е. Бахронкулов<sup>б</sup>,  
Алішер Х. Хаїтбаєв<sup>с</sup>, Джонібек Дж. Хамдамов<sup>б</sup>**

<sup>а</sup> Філія ФДБУ «Національний дослідницький університет МПЕІ», Йогду, 1, Ташкент, Узбекистан



<sup>б</sup> Інститут фізики напівпровідників та мікроелектроніки Національного університету Узбекистану,  
100057, Ташкент, Узбекистан, вул. Янги Алмазар, 20

<sup>с</sup> Національний університет Узбекистану, Ташкент, Узбекистан

У даній роботі методом комбінаційного розсіяння досліджено леговані лютетієм зразки кремнію. Проведено реєстрацію та ідентифікацію компонентів як кристалічної, так і аморфної фаз у зразках. Спостерігається деяке порушення в спектрах комбінаційного розсіювання світла зразків кремнію, легованого лютетієм, порівняно з вихідним зразком. Встановлено, що інтенсивність комбінаційного розсіювання легованих зразків у 2-3 рази перевищує розсіювання кремнію. Порівняння проведено для інтенсивностей, пов'язаних з інтенсивностями однофононої лінії кремнієвої підкладки. Цей ефект спектрів комбінаційного розсіювання в діапазоні 930 см<sup>-1</sup> – 1030 см<sup>-1</sup>, що з'являється в цьому діапазоні, подібний до зменшення даних для розповсюдження мультифононів на кремнії. Для отриманих зображень (n-Si<Lu> і p-Si<Lu>) смуги в атомному діапазоні комбінаторного розсіяння мають змішаний широкий і овальний фон в діапазоні від 623 см<sup>-1</sup> до 1400 см<sup>-1</sup>. Цей фон може змінювати форму спостережуваних смуг.

**Ключові слова:** кремній; лютетій; раманівська спектроскопія; дифузія; легування; температура

## INFLUENCE OF SILICON CHARACTERISTICS ON THE PARAMETERS OF MANUFACTURED PHOTONICS CELLS

 Mykola S. Kukurudziak<sup>a,b,\*</sup>,  Volodymyr M. Lipka<sup>a,b</sup>

<sup>a</sup> Rhythm Optoelectronics Shareholding Company, Holovna str. 244, 58032, Chernivtsi, Ukraine

<sup>b</sup> Yuriy Fedkovych Chernivtsi National University, Kotsyubyns'kogo str. 2, 58012, Chernivtsi, Ukraine

\*Corresponding Author e-mail: [mykola.kukurudzyak@gmail.com](mailto:mykola.kukurudzyak@gmail.com)

Received October 15, 2023; revised October 28, 2023; accepted November 22, 2023

The paper investigates the influence of the electrophysical characteristics of silicon on the final parameters of photoelectronic elements using *p-i-n* photodiodes as an example. It has been found that photodiode samples made on the basis of silicon with a higher resistivity are more prone to the formation of inversion channels at the oxide-semiconductor interface. Also, the dark current and responsivity of such photodiodes reach saturation at a lower voltage. It has also been shown that silicon-based photodiodes with a longer lifetime of non-basic charge carriers have lower dark current values. It has been shown that products with crystallographic orientation [111] have a much lower density of surface dislocations after technological operations than in the case of silicon with orientation [100]. It was also found that materials with different crystallographic orientations have different phosphorus diffusion coefficients. It has been experimentally established that a silicon oxide film grows faster on the surface of crystallographic orientation silicon [111] than on the surface of crystallographic orientation silicon [100]. This is due to the difference in the surface density of silicon atoms inherent in different crystallographic planes.

**Keywords:** Silicon; Photodiode; Responsivity; Dark current; Dislocations; Crystallographic orientation

**PACS:** 61.72.Ji, 61.72.Lk, 85.60.Dw

Semiconductor photovoltaic devices with *p-n* junctions are becoming increasingly popular. For example, they are used in automation, telemechanics, various protective devices, control and measuring equipment, surveillance and guidance circuits, etc. [1]. The emergence of new and improved sources of monochromatic radiation modulated by frequencies in the hundreds and thousands of megahertz, as well as new types of photoelectric semiconductor devices capable of converting an optical signal into an electrical signal, has made it possible to realize many tasks of opto- and photoelectronics.

In recent decades, researchers have paid special attention to the development and production of photodetectors for near-infrared spectral range detection. The manufacture of perfect photo receivers (PR) for this wavelength region remains an urgent scientific and technical task. One of the first issues to be solved in the design and manufacture of photodetectors is the choice of the base semiconductor material. Today, the most commonly used photodetectors are *p-n* junction photodetectors based on  $A_3B_5$  compounds, in particular GaAs, as well as Ge or Si. The choice of material depends primarily on the type of their spectral responsivity characteristic. For example, for wide-band GaAs ( $E_g = 1.42$  eV), the spectral response shifts towards short wavelengths, since photons with higher energy (short-wave radiation) are required to create electron-hole pairs and, accordingly, the photocurrent [2]. For semiconductors with a small band gap, such as Ge ( $E_g = 0.66$  eV), the spectral response is shifted to the long-wave region ( $\lambda_m = 1.54$   $\mu\text{m}$ ) [3, 4]. In narrow bandgap semiconductors, electron-hole pairs can occur under the influence of photons with lower energy (long-wave radiation).

The dependence of the light absorption coefficient on the wavelength has an impact on the appearance of the spectral response and the location of the maximum. For semiconductors with a sharp dependence of the absorption coefficient on the wavelength (Ge), the maximum of the spectral response for different types of devices usually occurs at the same wavelength regardless of the technology. For semiconductors with a less sharp dependence of the absorption coefficient, such as Si, the maximum spectral response, depending on the design of the photodetector and the technology used, can vary in a wide range from  $\lambda = 0.6$   $\mu\text{m}$  up to the intrinsic absorption edge of  $\lambda = 1.1$   $\mu\text{m}$  [5].

Comparing the capabilities of Si and GaAs materials, we can see that the main influence on the spectral characteristic is due to differences in the mechanism of light absorption. GaAs is characterized by a sharp edge of the main absorption band and a weak dependence of the absorption coefficient on the wavelength in the range of  $\lambda = 0.4 - 0.9$   $\mu\text{m}$ . In this regard, in GaAs photonics cells, the photocurrent value is determined mainly by the base (depth of the *p-n* junction) of the device. Therefore, by changing the thickness of the base, it is possible to change the shape of the spectral response of these photodetectors. In turn, for silicon PRs, the shift in the maximum of the spectral response can be realized both by changing the thickness of the base and by changing the diffusion lengths of non-main charge carriers in the base. By keeping the thickness of the silicon photo receivers base constant and changing the diffusion length of non-basic charge carriers in the source material, it is possible to change the maximum of the spectral curve both in absolute value and in wavelength. The described capabilities of silicon photodetectors to detect wavelengths of a wide range have led to their widespread use in solving photoelectronics problems. In addition to the above, important factors in the use of silicon as the main

material not only for photoelectronics but also for solid-state electronics in general are its widespread use and high manufacturability [6, 7]. In particular, silicon ranks second in terms of its prevalence on Earth: about 27.6 % of the mass of the Earth's crust, about 17 % of the mass of the lithosphere, and about 7 % of the mass of the core (Fig. 1). Note that the mass fraction of silicon in the universe is less than 0.1% [8].

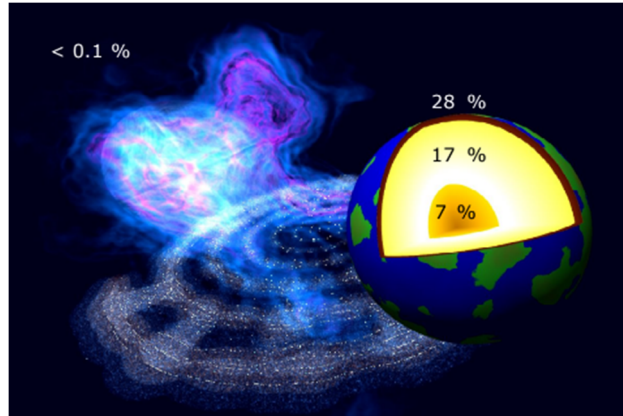


**Figure 1.** The abundance (in mass %) of silicon in the universe and in the planet Earth

It should be noted that the choice of the base material for the manufacture of photodetectors is not limited to the choice of semiconductor, as there are a number of other parameters of semiconductor ingots or wafers that should be taken into account when designing. These parameters include the type of conductivity, resistivity, density of structural defects, lifetime of minority charge carriers, crystallographic orientation, etc. The ability to estimate the requirements of material parameters, in particular silicon, for the manufacture of specific types of photodetectors is an important and relevant scientific and technical task. A review of the literature shows that most of the works are devoted to the production of defect-free silicon ingots [9], and the influence of growth or acquired defects in the semiconductor material on the parameters of the resulting electronics elements [10, 11]. Also, many works are devoted to the study of technological processes or modes on the parameters of final products, but no works on the influence of the parameters of the source silicon on the parameters of the final photodetectors have been found. Accordingly, the aim of this work is to study the dependence of the final parameters of silicon photodiodes on the electrophysical characteristics of the source silicon.

### EXPERIMENTAL

The research was carried out on the example of silicon four-element *p-i-n* photodiodes (PD) with guard ring (GR) designed to detect radiation with a wavelength of  $\lambda_{op}=1064$  nm. Two different materials with different electrophysical parameters were chosen for comparison. The first material was single-crystal dislocation-free *p*-type FZ-Si with orientation [111], resistivity at  $\rho \approx 16\text{-}20$  k $\Omega$ ·cm and life time of minority charge carriers at  $\tau \approx 1.1\text{-}1.3$  ms (PD<sub>[111]</sub>). Another material was single-crystal dislocation-free *p*-type FZ-Si with orientation [100], resistivity at  $\rho \approx 45\text{-}55$  k $\Omega$ ·cm and life time of minor charge carriers at  $\tau \approx 2.2\text{-}2.4$  ms (PD<sub>[100]</sub>). The devices were prepared using diffusion planar technology in a single process cycle under the same conditions. The PDs technological route consisted of a complex of four thermal operations and three photolithographies: semiconductor substrates were oxidized according to the principle of dry-wet-dry oxidation; photolithography was carried out to create windows for phosphorus diffusion; diffusion of phosphorus (predeposition) to the front side to create *n*<sup>+</sup>-type responsive elements (RE) and GR; driving-in of phosphorus to redistribute the alloying impurity and increase the depth of the *n*<sup>+</sup>-*p* junction; diffusion of boron to the reverse side of the substrate to create a *p*<sup>+</sup>-type ohmic contac; photolithography for creating contact windows; sputtering of Cr-Au on the front and back sides, separation of pastes into crystals by scraping or cutting with a disk with an external diamond edge. The thickness of the final photodiode crystals reached 390-400 microns. The parameters of the obtained devices were compared.

After oxidation and each subsequent thermal operation, the high-frequency volt-farad (*C-V*) characteristics of the metal-oxide-semiconductor-structures were measured at a frequency of 30 kHz, which made it possible to predict the final parameters of the products.

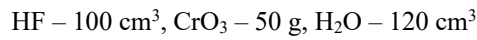
An important parameter of multi-element PDs with GR is the resistance of the isolation of the REs and the GR ( $R_{con}$ ), the decrease of which leads to an increase in the photocoupling coefficient and dark currents. This parameter characterizes the presence of inversion conduction channels at the Si-SiO<sub>2</sub> interface. Determination of insulation resistance of REs and GR was carried out according to the method given in [3] with  $U_{bias}=2$  V and load resistance  $R_l=10$  k $\Omega$ .

The dark current ( $I_d$ ) and *I-V* characteristics of PDs were measured using a hardware-software complex implemented on the basis of the Arduino platform, an Agilent 34410A digital multimeter and a Siglent SPD3303X programmable power source, which were controlled by a personal computer using software created by the authors in the LabView environment (dark current density  $J_d$  is given).

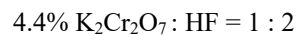
Monitoring of current monochromatic pulse responsivity ( $S_{pulse}$ ) was carried out by method of comparing responsivity of the investigated PD with a reference photodiode certified by the respective metrological service of the company. Measurements were performed when illuminating the PD with a radiation flux of a power of not over  $1 \cdot 10^{-3}$  W; load resistance across the responsive element  $R_l = 10$  k $\Omega$ , at the bias voltages of  $U_{bias} = 2-120$  V and pulse duration  $\tau_i = 500$  ns. The spectral characteristics of photodiode responsivity ( $S(\lambda)$ ) at different bias voltages are also obtained. The measurement was carried out using the KSVU-23 automated spectral complex.

The capacitance of REs ( $C_{RE}$ ) was determined at a  $U_{bias} = 2-120$  V

To investigate the defective structure of the substrates with [111] orientation, chemical treatment was performed in selective Sirtle's etchant [12] with the following composition:



To investigate the defective structure of the substrates with [100] orientation, chemical treatment was performed in selective Secko's etchant [13] with the following composition:



Then the surface was examined in microscopes of different magnifications. The number of dislocations was calculated by the metallographic method [14].

The growth rate of  $\text{SiO}_2$  on substrates of different crystallographic orientation has been investigated. The thickness of the oxide films was measured by the ellipsometric method. The depth of the diffusion layer ( $x_{n+p}$ ) of phosphorus was also compared at the same diffusion durations. Determination of the depth of the  $p-n$  junction was performed by spherical grinding.

## RESULTS OF THE RESEARCH AND THEIR DISCUSSION

### A) Study of $C-V$ characteristics and insulation resistance between responsive elements and guard ring

As mentioned above,  $C-V$  characteristics were monitored after each thermal operation. After thermal oxidation and subsequent heat treatments, the silicon substrates with lower resistivity ( $\text{PD}_{[111]}$ ) had a classic volt-faradic characteristic curve for  $p$ -type material (Fig. 2, curve 1). As for the substrates with a higher resistivity ( $\text{PD}_{[100]}$ ), a slight inverted characteristic curve was observed after the first thermal operation (Fig. 2, curve 2). After boron diffusion, a complete inverted  $C-V$  characteristics was observed (Fig. 2, curve 3).

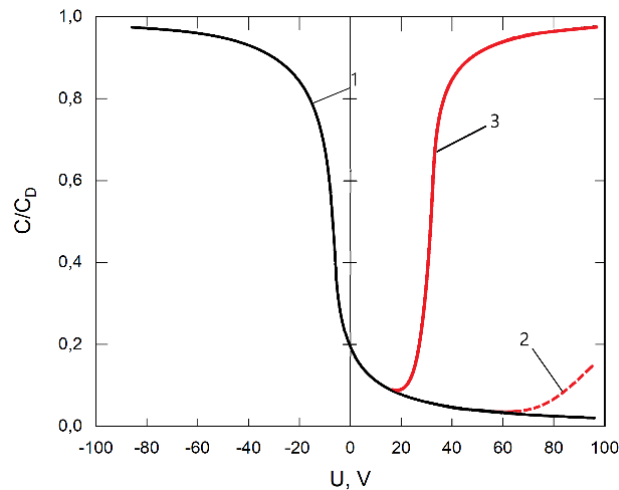


**Figure 2.**  $C-V$  characteristics of PDs:

1 - characteristic of  $\text{PD}_{[111]}$ ; 2 - characteristic of  $\text{PD}_{[100]}$  after oxidation; 3 - characteristic of  $\text{PD}_{[100]}$  after diffusion of boron

The inversion of the  $C-V$  characteristics indicated the presence of inversion layers at the Si-SiO<sub>2</sub> interface. Technological reasons for the appearance of inversion layers are improper chemical treatment of substrates, the presence of alkali metal impurities in deionized water, quartz dishes, or a quartz reactor and carrier gases. The deterioration of the characteristics after boron diffusion is caused by the redistribution and diffusion of impurities in SiO<sub>2</sub> to the Si-SiO<sub>2</sub> interface introduced during thermal operations due to the high total duration of heat treatment [15, 16]. Silicon for  $\text{PD}_{[100]}$  is more prone to the formation of inversion layers, since in this case a smaller amount of impurity is required to change the surface conductivity to the opposite one, unlike a material with a lower resistivity.

The parameter that is a vivid quantitative characteristic of the presence of conductive inversion channels at the Si-SiO<sub>2</sub> interface is  $R_{con}$ . Measurements showed that samples  $\text{PD}_{[111]}$  had  $R_{con} \approx 3.9-5.5$  M $\Omega$  and samples  $\text{PD}_{[100]}$  had  $R_{con} \approx 0.7-1.1$  M $\Omega$ . As indicated above,  $R_{con}$  of  $\text{PD}_{[100]}$  is much lower than of  $\text{PD}_{[111]}$ , as evidenced by the  $C-V$ -characteristics. In case of difficulty or impossibility of manufacturing PDs with low  $R_{con}$  due to the formation of



surface inversion channels, it is worth forming surface areas of leakage channel restriction isotypic with the substrate material between the REs and GR of the photodiodes [17]. This is especially important when using silicon with a  $\rho \geq 20 \text{ k}\Omega$ .

### B) Study of dark currents of photodiodes

The  $I$ - $V$ -characteristics of photodiodes were obtained (Fig. 3).

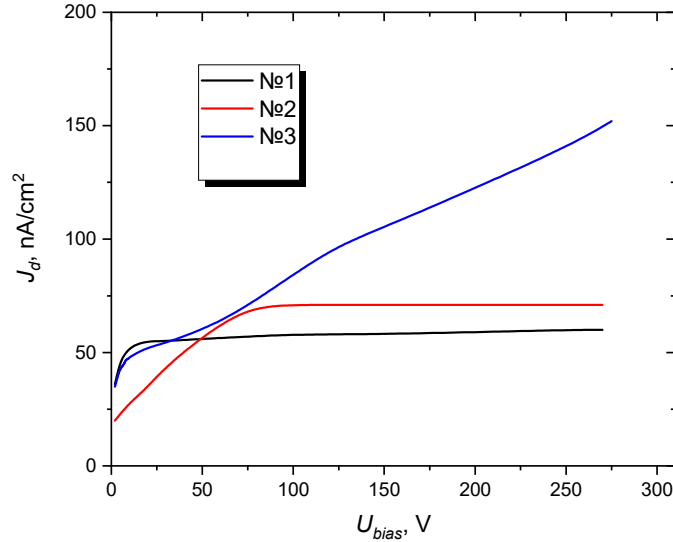


**Figure 3.**  $I$ - $V$ -characteristics of PDs: 1, 3 - characteristic of PD<sub>[100]</sub>; 2 - characteristic of PD<sub>[111]</sub>

The volt-ampere characteristic curves for PD<sub>[111]</sub> were typical for all samples from the experimental batch with some variation in  $J_d$  (curve 1, Fig. 3). The dark currents for PD<sub>[111]</sub> at  $U_{bias}=2 \text{ V}$  reached  $J_d=52\text{-}78 \text{ nA/cm}^2$ , and at  $U_{bias}=120 \text{ V}$   $J_d=156\text{-}208 \text{ nA/cm}^2$ .

In the case of PD<sub>[100]</sub>, a slightly different picture was observed. For some PDs, the characteristic of curve type 1 of Fig. 3 was inherent, and for the other part, the characteristic of curve type 3 of Fig. 3. As for the samples with the  $I$ - $V$ -characteristic of curve type 1, in this case, the value of the dark current reached slightly lower values than in PD<sub>[111]</sub> (at voltages above the saturation voltage), since in PD<sub>[111]</sub> the initial lifetime of minority charge carriers of the material is much higher, and the generation component of the dark current ( $I_d^G$ ) is inversely proportional to the  $\tau$  [11]:

$$I_d^G = e \frac{n_i}{2\tau} W_i A_{RE} \quad (1)$$

where  $n_i$  is own concentration of charge carriers in the substrate;  $e$  is the charge of the electron;  $A_{RE}$  is effective area of RE;  $W_i$  is space charge region (SCR) width.

It is also worth noting that curve 1 of  $I$ - $V$  characteristic reaches saturation at  $U_{bias}=10\text{-}15 \text{ V}$ , in contrast to curve 2, which reaches saturation at  $U_{bias}=70\text{-}80 \text{ V}$ . This can be explained by the fact that the SCR of PD<sub>[100]</sub> stretches over the entire thickness of the substrate (not including the diffusion length of minority charge carriers) at lower bias voltages, since the PD<sub>[100]</sub> material has a much higher resistivity, and the  $W_i$  is directly proportional to the  $\rho$  [18]:

$$W_i = \frac{\sqrt{\rho U_{bias}}}{3} \times 10^{-4} \quad (2)$$

It should be added that in some samples of the PD<sub>[100]</sub> type, an increase in the dark current was observed with an increase in the reverse bias voltage over the entire measurement range (curve 3 of Fig. 3). To determine the reasons for the increase in dark current, it was decided to examine the surface of such PDs for surface structural defects. For this purpose, selective etching of the samples was performed (Fig. 4a, b). For comparison, PD<sub>[111]</sub> was also treated in a selective etchant (Fig. 4c, d).

It should be noted that in both cases studied, the silicon substrates were doped with the same phosphorus concentration in a single technological cycle. However, as can be seen from Fig. 4a, b, the surface of PD<sub>[111]</sub> had a much lower surface density of dislocations than PD<sub>[100]</sub>. The density of dislocations of PD<sub>[111]</sub> in the  $n^+$ -regions reached  $N_{dis} \approx 2 \cdot 10^3\text{-}2 \cdot 10^3 \text{ cm}^{-2}$ , and in the  $p$ -regions  $N_{dis} \approx 50\text{-}90 \text{ cm}^{-2}$ . In the case of the  $n^+$ -regions of PD<sub>[100]</sub>, the determination of the dislocation density is complicated due to the high density of dislocations and the merging of their dislocation lines and grids, but it can be estimated that in this case  $N_{dis} \approx 10^9\text{-}10^{11} \text{ cm}^{-2}$ . As for the  $p$ -regions of PD<sub>[100]</sub>, in this case  $N_{dis} \approx 1 \cdot 10^5\text{-}2 \cdot 10^5 \text{ cm}^{-2}$ . Note that the increased density of dislocations provokes an increase in the surface generation component of the dark current ( $I_d^{surf}$ ) [19]:

$$I_d^{surf.} = \frac{e N_{ss} v_{drift} \sigma_{ss} A_{p-n}}{2} \quad (3)$$

where  $\sigma_{ss}$  is capture cross-sectional area;  $N_{ss}$  – density of surface states;  $A_{p-n}$  - is the area that contributes to the surface component of the dark current;  $v_{drift}$  – is the average relative (relative to the center of re-combination) velocity of thermal charge carriers.

The influence of these defects and their number on  $I_d$  can be explained in several ways. First, the presence of dislocations can lead to the appearance of levels in the band gap due to the elastic stress fields associated with dislocations; these structural defects can serve as carrier recombination centers. The presence of recombination centers in the depleted region of the  $p-n$  junction will be manifested in an increase in the generation currents at the reverse bias on the PD. Secondly, dislocations can accumulate impurities due to their elastic fields. Decorated dislocations that cross the  $p-n$  junction lead to the appearance of a high density of generation-recombination centers in the spatial charge region. This again leads to an increase in the generation currents at the reverse bias [20, 21]. This situation was observed in some products of the PD<sub>[100]</sub> type.

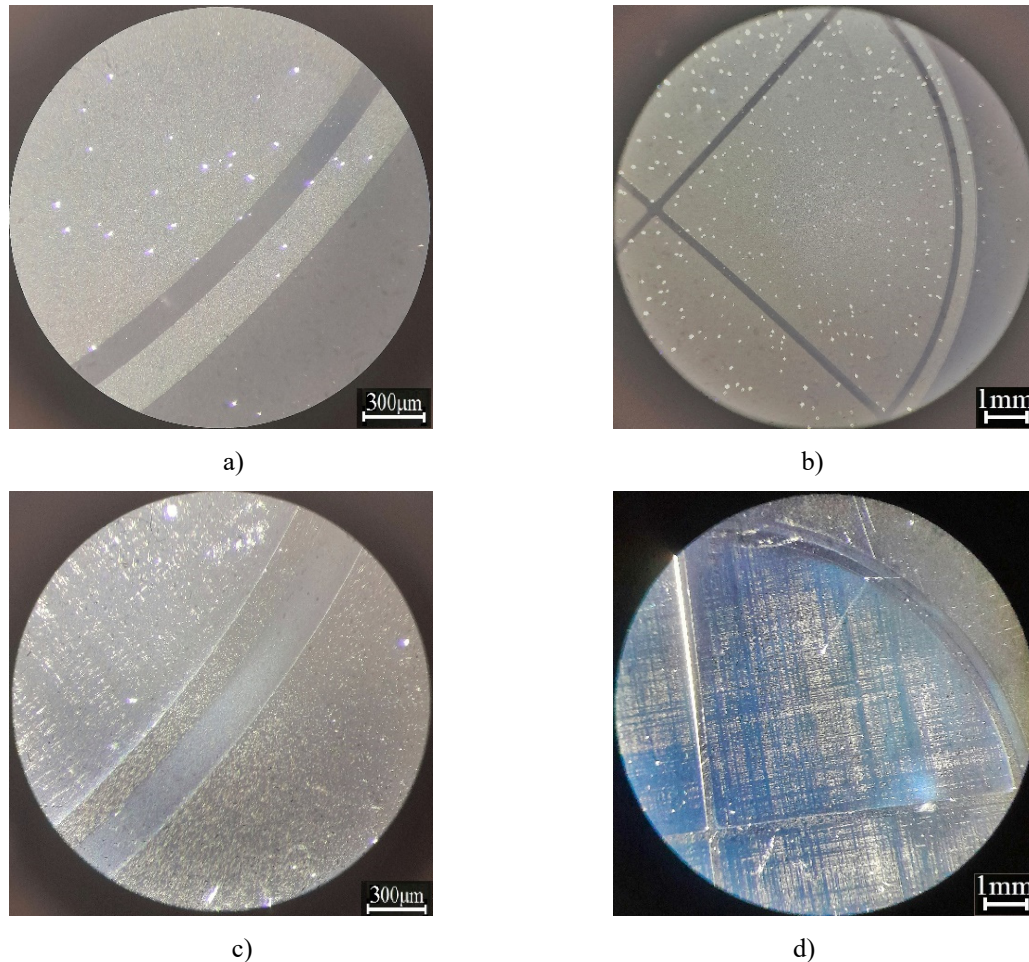


**Figure 4.** Image of the PD surface after selective etching in the dark field: a, b) PD<sub>[111]</sub>; c, d) PD<sub>[100]</sub>

We also investigated the value of the dark currents of the guard rings ( $J_{GR}$ ). It was found that the dark current of the PD<sub>[100]</sub> guard ring was significantly higher than that of the PD<sub>[111]</sub>. At  $U_{bias}=120$  V  $J_{GR}=288-432$   $\mu\text{A}/\text{cm}^2$  in PD<sub>[100]</sub> and  $J_{GR}=3.6-22$   $\mu\text{A}/\text{cm}^2$  in PD<sub>[111]</sub>. The increase in the guard ring currents in the case of PD<sub>[100]</sub> is caused by the presence of inversion channels at the interface between the Si-SiO<sub>2</sub> phases, which provokes an increase in currents when the SCR expands with an increase in the bias voltage.

**B) Investigation of current monochromatic pulse responsivity of photodiodes.**

The graph of  $S_{pulse}(U_{bias})$  for both photodiode variants was obtained (Fig. 5). Figure 5 shows that the  $S_{pulse}(U_{bias})$  dependence curve of PD<sub>[100]</sub> reaches saturation faster (at  $U_{bias}=7-9$  V) than the PD<sub>[111]</sub> curve (at  $U_{bias}=70-80$  V). This is due to the fact that in PD<sub>[100]</sub>, as mentioned above, the SCR stretches to its maximum width at lower bias voltages, respectively, the charge carrier collection coefficient, which depends on  $W_i$ , reaches saturation also at lower  $U_{bias}$ , and the responsivity, being directly proportional to the charge carrier collection coefficient, also reaches saturation at lower bias voltages [22]:

$$S_{\lambda} = (1 - R)TQ\alpha_{p-n} \frac{\lambda}{1.24}, \tag{4}$$

where  $R$  is the anti-reflective coating reflection coefficient;  $T$  is the transmission coefficient of the input window or optical filter;  $Q$  is the quantum output of the internal photoeffect;  $\alpha_{p-n}$  is the collection coefficient of minor charge carriers generated by radiation in the active region of the photodiode.

Fig. 6a shows that the maximum of the spectral characteristic ( $S_m$ ) of PD<sub>[111]</sub> shifts towards longer wavelengths with increasing bias voltage. This is caused by the expansion of the SCR with increasing reverse voltage, and when the  $W_i$  reaches saturation, no further shift of the maximum occurs. In the case of PD<sub>[100]</sub>, a different picture was observed (Fig. 6b): even at low bias voltages, the maximum of the characteristic is at its maximum value of wavelengths and does not shift with increasing voltage due to the high diffusion length of non-basic charge carriers and the maximum charge carrier collection coefficient even at two volts.

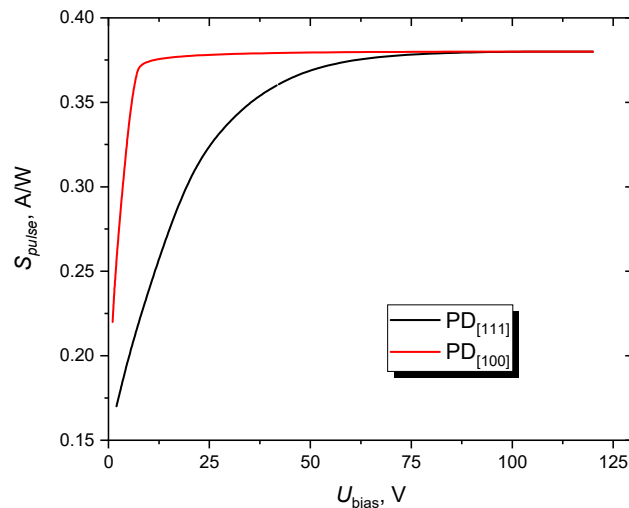


Figure 5. The graph of  $S_{pulse}(U_{bias})$  PD<sub>[100]</sub> and PD<sub>[111]</sub>

The spectral characteristics of the photodiode's responsivity are also obtained (Fig. 6).

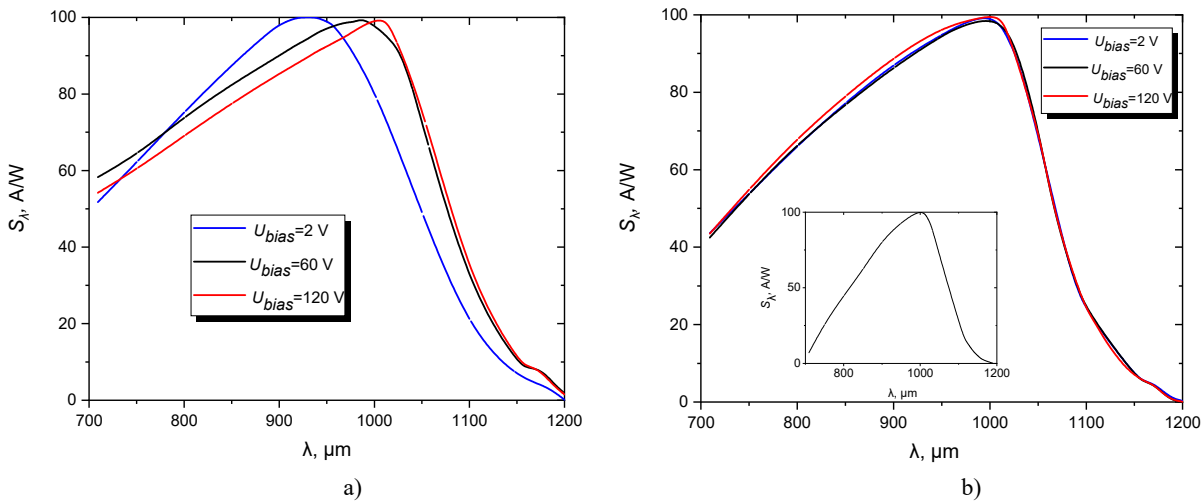


Figure 6. Spectral characteristics of the photodiodes responsivity: a) PD<sub>[111]</sub>; b) PD<sub>[100]</sub>; inset in figure (b) is spectral characteristic of PD<sub>[100]</sub> with a short-wave minimum of the spectral characteristic of about  $\lambda = 700$  nm

Note that in Fig. 6a and 6b the short-wave responsivity is different. For example, at  $\lambda = 700$  nm,  $S_\lambda = 0.5S_m - 0.6S_m$  for PD<sub>[111]</sub>, and for PD<sub>[100]</sub>  $S_\lambda = 0.4S_m$ . The change in the short-wave resistivity and the shift of the short-wave minimum of the spectral characteristic can be explained by the change in the depth of the  $n^+p$  junction ( $x_{n+p}$ ). Indeed, when measuring the  $x_{n+p}$ , it was seen that in PD<sub>[111]</sub>  $x_{n+p} = 4-4.2$   $\mu\text{m}$ , and in PD<sub>[100]</sub>  $x_{n+p} = 5.8-6$   $\mu\text{m}$ . Accordingly, as depth of the  $n^+p$  junction decreases, the influence of background radiation and short-wave responsivity increases. This is due to the fact that with a decrease in the wavelength of radiation, the depth of its absorption decreases, and in  $p-i-n$  PDs, the formation of photocurrent occurs during the generation of charge carriers in the high-resistance  $p$ -region. And in the case of PD<sub>[100]</sub>, a larger range of wavelengths is absorbed by the  $n^+$ -region due to the higher depth of the  $p-n$  junction. In particular, in some samples of the PD<sub>[100]</sub> type, a shift of the short-wave minimum of the spectral characteristic to 700 nm was observed (Fig.6b-inset). Note that the different depths of the diffusion layer in the two cases may be due to the difference in phosphorus diffusion coefficients for different crystallographic orientations.

**B) Investigation of the growth rate of SiO<sub>2</sub> on the surface of different types of silicon**

During the phosphor deposition operation, a anti-reflective SiO<sub>2</sub> is grown on the surface of the REs that meets the minimum reflection condition (5) [23]:

$$\frac{\lambda}{4} = nd_{SiO_2}, \tag{5}$$

where  $\lambda$  is the working wavelength;  $n$  the refractive index of SiO<sub>2</sub>;  $d_{SiO_2}$  is the thickness of the anti-reflective film.

For the working wavelength of the described photodiodes, the anti-reflective oxide should be  $d_{SiO_2} \approx 0.18-0.19 \mu\text{m}$  [24]. When studying the thickness of the grown anti-reflective oxide in the two studied variants of photodiodes, it was found that the thickness of SiO<sub>2</sub> in PD<sub>[111]</sub> reaches  $d_{SiO_2} \approx 0.183 \mu\text{m}$ , and in PD<sub>[100]</sub> reaches  $d_{SiO_2} \approx 0.17 \mu\text{m}$ . Presumably, the different growth rate of the oxide film is caused by the different surface concentration of silicon atoms ( $n$ ) for different crystallographic orientations, since it can be assumed that the growth rate will increase with increasing surface concentration of atoms. To test this, we calculated the surface concentrations of silicon atoms for different crystallographic orientations. The surface concentration of atoms of different crystallographic planes of silicon can be visually estimated from Fig. 7a.

The surface concentration (the number of atoms per unit area) of atoms is calculated by the formula [25]:

$$n = \frac{N}{S}, \tag{6}$$

where  $N$  is the number of atoms that are completely contained in a unit cell of a two-dimensional surface lattice;

$S$  is the area of the unit cell.

Let's calculate the value of  $n$  for plane (100). Plane (100) in the diamond structure is a two-dimensional square lattice with Si atoms in the nodes. The side of the square (the elementary cell of a two-dimensional lattice) is equal to half the diagonal of the face (Fig. 7b). A unit cell of the lattice contains one atom, since 1/4 of the atoms from each of the four atoms at the vertices of the square fall into the unit cell. So, the number of atoms per unit area of the plane (100) will be:

$$n_{(100)} = \frac{1}{(a\sqrt{2}/2)^2} = 6.78 \cdot 10^{14} \text{ cm}^{-2} \tag{7}$$

where  $a$  is silicon lattice period.

For plane (111), the two-dimensional lattice is hexagonal (graphene structure). An elementary cell is a rhombus with side length  $a$  (angle 60°) and containing two Si atoms (Fig. 7b). Thus, the number of atoms per unit area of the plane (111) will be:

$$n_{(111)} = \frac{1}{a^2\sqrt{3}/2} = 7.83 \cdot 10^{14} \text{ cm}^{-2}. \tag{8}$$

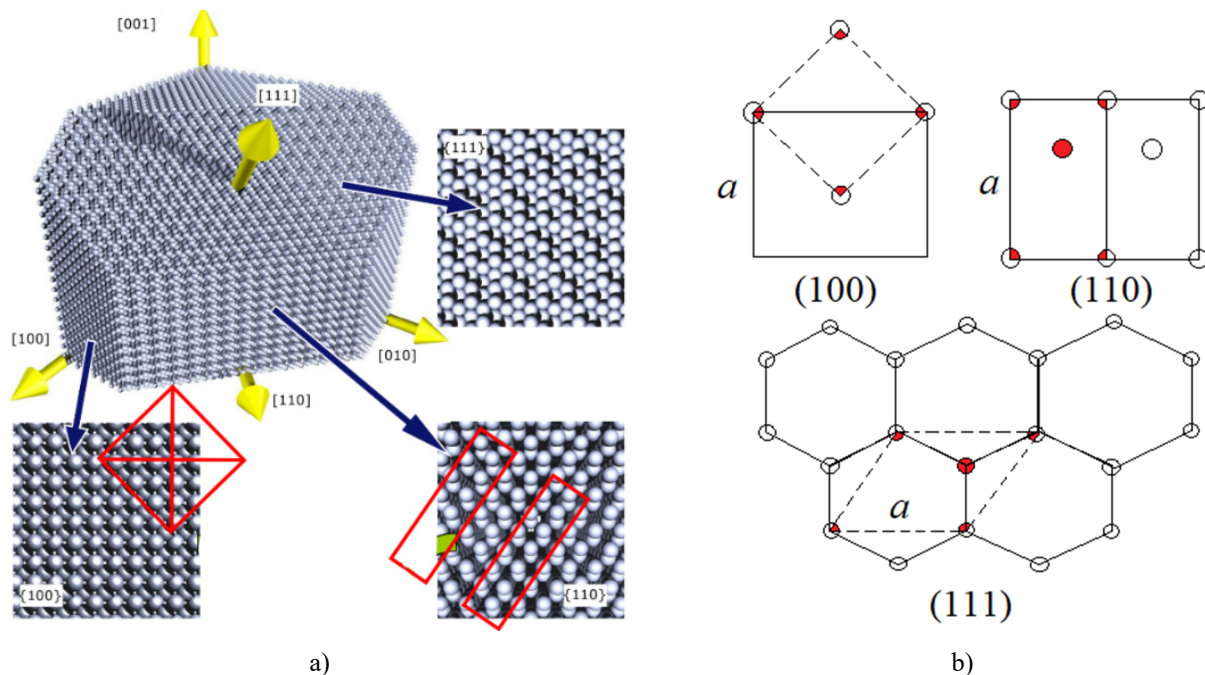


**Figure 7.** A schematic representation of the density of silicon atoms inherent in different crystallographic planes: a) schematic illustration of an ingot; b) number of atoms in unit cells

For clarity, the surface density of silicon atoms for plane (110) is also shown. In the case of plane (110), a two-dimensional lattice is a rectangular lattice containing two atoms in a unit cell (Fig. 7b). The unit cell of the lattice is a

rectangle whose larger side is equal to the lattice constant  $a$ , and the other side is half the diagonal of the face of the elementary cube of the structure. Thus, the number of atoms per unit area of the plane (110) will be:

$$n_{(110)} = \frac{1}{a^2\sqrt{2}/2} = 9.59 \cdot 10^{14} \text{ cm}^{-2}. \quad (9)$$

As can be seen from the calculations, the surface density of silicon atoms for different crystallographic planes is different, respectively, with an increase in the density of atoms, the growth rate of the oxide film increases.

As described in the paper, the final parameters of electronics elements, in particular photodiodes, depend on electrophysical parameters and the type of silicon used.

## CONCLUSIONS

The influence of the electrophysical characteristics of silicon on the final parameters of photoelectronic elements on the example of  $p$ - $i$ - $n$  photodiodes is investigated. The following conclusions have been made:

1. Photodiodes made on the basis of silicon with a higher resistivity are more prone to the formation of inversion channels at the oxide-semiconductor interface. Samples with higher resistivity of the base material have lower insulation resistance between responsive elements.
2. The dark current and photosensitivity of such photodiodes reach saturation at a lower voltage.
3. Silicon-based photodiodes with a longer lifetime of non-basic charge carriers have lower values of dark currents.
4. Products with crystallographic orientation [111] have a much lower density of surface dislocations after technological operations than in the case of silicon with orientation [100].
5. Silicon of different crystallographic orientations has different phosphorus diffusion coefficients. This was established by determining the depth of charging of the diffusion layer of phosphorus at the same diffusion time.
6. Silicon oxide film grows faster on the surface of crystallographic orientation silicon [111] than on the surface of crystallographic orientation silicon [100]. This is due to the difference in the surface density of silicon atoms inherent in different crystallographic planes.

## ORCID

©Mykola S. Kukurudziak, <https://orcid.org/0000-0002-0059-1387>; ©Volodymyr M. Lipka, <https://orcid.org/0009-0001-4419-3356>

## REFERENCES

- [1] M.K. Bakhadyrkhanov, S.B. Isamov, Z.T. Kenzhaev, D. Melebaev, K.F. Zikrillayev, and G.A. Ikhtiyarova, *Applied Solar Energy*, **56**, 13 (2020). <https://doi.org/10.3103/S0003701X2001003X>
- [2] H. Helmers, E. Lopez, O. Höhn, D. Lackner, J. Schön, M. Schauerte, and A.W. Bett, *Physica status solidi – Rapid Research Letters*, **15**(7), 2100113 (2021). <https://doi.org/10.1002/pssr.202100113>
- [3] M. Kukurudziak, *Radioelectronic and Computer Systems*, **105**(1), 92 (2023). <https://doi.org/10.32620/reks.2023.1.07>
- [4] A.V. Fedorenko, *Technology and design in electronic equipment*, **17**(3–4), 17 (2020). <https://doi.org/10.15222/TKEA2020.3-4.17> (in Ukrainian)
- [5] W.J. Westerveld, M. Mahmud-Ul-Hasan, R. Shnaiderman, V. Ntziachristos, X. Rottenberg, S. Severi, and V. Rochus, *Nature Photonics*, **15**(5), 341-345 (2021). <https://doi.org/10.1038/s41566-021-00776-0>
- [6] A. Müller, M. Ghosh, R. Sonnenschein, and P. Woditsch, *Materials Science and Engineering: B*, **134**(2-3), 257 (2006). <https://doi.org/10.1016/j.mseb.2006.06.054>
- [7] C. Ballif, F.J. Haug, M. Boccard, P.J. Verlinden, and G. Hahn, *Nature Reviews Materials*, **7**(8), 597 (2022). <https://doi.org/10.1038/s41578-022-00423-2>
- [8] X. Pan, S. Li, Y. Li, P. Guo, X. Zhao, and Y. Cai, *Minerals Engineering*, **183**, 107600 (2022). <https://doi.org/10.1016/j.mineng.2022.107600>
- [9] U. Hilleringmann, Wiesbaden: Springer Fachmedien Wiesbaden, 5-20 (2023). [https://doi.org/10.1007/978-3-658-41041-4\\_2](https://doi.org/10.1007/978-3-658-41041-4_2)
- [10] B. Son, Y. Lin, K.H. Lee, Q. Chen, and C.S. Tan, *Journal of Applied Physics*, **127**(20), 203105 (2020). <https://doi.org/10.1063/5.0005112>
- [11] M.S. Kukurudziak, *Journal of nano- and electronic physics*, **14**(4), 04015 (2022). [https://doi.org/10.21272/jnep.14\(4\).04015](https://doi.org/10.21272/jnep.14(4).04015)
- [12] E. Sirtl, and A. Adler, *Z. Metallk.*, **119**, 529 (1961).
- [13] F.A. Abdullin, and V.E. Pautkin, in: *2019 IEEE International Seminar on Electron Devices Design and Production (SED)*, 2023. <https://doi.org/10.1109/SED.2019.8798467>
- [14] S.N. Knyazev, A.V. Kudrya, N.Y. Komarovskiy, Y.N. Parkhomenko, E.V. Molodtsova, and V.V. Yushchuk, *Modern Electronic Materials*, **8**(4), 131 (2022). <https://doi.org/10.3897/j.moem.8.4.99385>
- [15] V.M. Lytvynenko, I.M. Vikulin, *Bulletin of the Kherson National Technical University*, (1), 46 (2018). (in Ukrainian)
- [16] Yu.O. Kruglyak, and M.V. Strikha, *Sensor Electronics and Microsystem Technologies*, **16**(2), 5 (2019). <https://doi.org/10.18524/1815-7459.2019.2.171224> (in Ukrainian)
- [17] M.S. Kukurudziak, *Journal of nano- and electronic physics*, **14**(1), 01023 (2022). [https://doi.org/10.21272/jnep.14\(1\).01023](https://doi.org/10.21272/jnep.14(1).01023)
- [18] V.A. Bruk, V.V. Garshenin, and A.I. Kurnosov, *Production of semiconductor devices: Textbook*. ed. 3rd, revision and supplement. (Vysshaya Shkola, Moscow, 1973). (in Russian)
- [19] M.S. Kukurudziak, and E.V. Maistruk, *Semicond. Sci. Technol.*, **38**, 085007 (2023). <https://doi.org/10.1088/1361-6641/acdf14>
- [20] K. Ravey, *Defects and impurities in semiconductor silicon*, (Trans.), edited by G.N. Gorina, (Mir, Moscow, 1984). (in Russian).
- [21] M.S. Kukurudziak, *Semiconductor Physics, Quantum Electronics & Optoelectronics*, **25**(4), 385 (2022). <https://doi.org/10.15407/spqeo25.04.385>

- [22] V.P. Maslov, A.V. Sukach, V.V. Tetyorkin, M.Yu. Kravetskyi, N.V. Kachur, E.F. Wenger, and A.V. Fedorenko, *Optoelectronics and Semiconductor Technology*, **53**, 188 (2018). (in Ukrainian)
- [23] S.B. Khan, S. Irfan, Z. Zhuanghao, and S.L. Lee, *Materials*, **12**(9), 1483 (2019). <https://doi.org/10.3390/ma12091483>
- [24] M.S. Kukurudziak, *East Eur. J. Phys.* **2**, 289 (2023), <https://doi.org/10.26565/2312-4334-2023-2-33>
- [25] P. Haas, F. Tran, and P. Blaha, *Physical Review B*, **79**(8), 085104. <https://doi.org/10.1103/PhysRevB.79.085104>

#### ВПЛИВ ХАРАКТЕРИСТИК КРЕМНІЮ НА ПАРАМЕТРИ ВИГОТОВЛЕНИХ ЕЛЕМЕНТІВ ФОТОЕЛЕКТРОНІКИ

Микола С. Кукурудзяк<sup>a,b</sup>, Володимир М. Ліпка<sup>a,b</sup>



<sup>a</sup> АТ «Центральне конструкторське бюро Ритм», 58032, м. Чернівці, вул. Головна, 244, Україна

<sup>b</sup> Чернівецький національний університет імені Юрія Федьковича, 58002, м. Чернівці, вул. Коцюбинського, 2, Україна

В статті досліджено вплив електрофізичних характеристик кремнію на кінцеві параметри елементів фотоелектроніки на прикладі *p-i-n* фотодіодів. Під час досліджень встановлено, що зразки фотодіодів виготовлені на основі кремнію з вищим питомим опором більш схильні до утворення інверсійних каналів на межі розділу оксид-напівпровідник. Також темновий струм та фоточутливість таких фотодіодів виходять в насичення при нижчій напрузі. Також побачено, що фотодіоди на основі кремнію із вищим часом життя неосновних носіїв заряду володіють нижчими значеннями темнових струмів. Досліджено, що вироби із кристалографічною орієнтацією [111] володіють значно нижчою густиною поверхневих дислокацій після технологічних операцій, ніж в випадку кремнію з орієнтацією [100]. Також встановлено, що матеріал різної кристалографічної орієнтації має різні коефіцієнти дифузії фосфору. Експериментально встановлено що плівка оксиду кремнію росте швидше на поверхні кремнію кристалографічної орієнтації [111], ніж на поверхні кремнію кристалографічної орієнтації [100]. Це спричинено відмінністю в поверхневій густині атомів кремнію притаманній різним кристалографічним площинам.

**Ключові слова:** кремній; фотодіод; чутливість; темновий струм; дислокації; кристалографічна орієнтація

## ON THE PROPERTIES OF THE Si-SiO<sub>2</sub> TRANSITION LAYER IN MULTILAYER SILICON STRUCTURES

 Shakhrukh Kh. Daliev<sup>#</sup>,  Fayzulla A. Saparov\*

*Institute of Semiconductor Physics and Microelectronics at the National University of Uzbekistan,  
20 Yangi Almazar st., Tashkent, 100057, Uzbekistan*

*\*Corresponding Author e-mail: sfa@inbox.ru, #e-mail: shakhrukh@mail.ru*

Received July 28, 2023; revised September 15, 2023; accepted September 18, 2023

Capacitance spectroscopy was used to study the capacitive-voltage characteristics of multilayer structures with a Si-SiO<sub>2</sub> transition layer in Al-SiO<sub>2</sub>-n-Si type samples fabricated by the thermal oxidation of a semiconductor. It is shown that the inhomogeneous distribution of the density of surface states is a localized electroactive center at the very semiconductor-dielectric interface, due to over-barrier charge emission or thermal ionization of impurity centers.

**Keywords:** MDS structure; Silicon; Transition layer; Interface; Temperature; Dielectric layer

**PACS:** 78.30.Am.

### INTRODUCTION

An integral part of most modern semiconductor devices is silicon MDS or MOS structures. Given that the physical processes occurring on the semiconductor-insulator transition layer have a significant impact on the performance of semiconductor devices. Layers of amorphous silicon dioxide grown on silicon by thermal oxidation satisfy most of the requirements listed above. At the same time, the technological modes of its production easily fit into the existing technological processes for the production of semiconductor devices and integrated circuits. The foregoing made SiO<sub>2</sub> films the most common material for creating passivating and insulating layers in semiconductor instrumentation. Analysis of the dielectric and transition layers of Si-SiO<sub>2</sub> may eventually prove useful for constructing theoretical or computer simulations of impurity states [1,12]. To solve it, it is necessary to have information about the nature of electron and hole trapping centers (trapping centers). One of the important features of semiconductors is that their electrical and optical properties can differ significantly depending on the state of the surface and change with its various processing (grinding, etching), and changes in environmental parameters. The common cause of these phenomena is that in a limited crystal there arise not only quantum states of electrons moving in the bulk of the crystal, but also additional states in which the electrons are localized on the very surface of the crystal. Accordingly, in addition to the volume energy levels that form the energy zones of an infinite crystal, there appear local energy levels located near the surface itself [1,2,13].

The presence of local surface energy levels leads to the fact that electrons and holes can "stick" to the surface, forming a surface electric charge. In this case, an induced charge equal in magnitude and opposite in sign appears in the volume under the surface, i.e. enriched or depleted near-surface layers appear. The appearance of such layers explains the influence of the surface on the equilibrium properties of semiconductors (electrical conductivity, work function, contact potential difference, etc.). Based on these results, our goal is to obtain cheap microchips.

### MATERIALS AND METHODS

To experimentally study the effect of Si-SiO<sub>2</sub> transition layers on the capacitance-voltage characteristics in three-layer structures, we used the most widely used in microelectronics metal-dielectric-semiconductor structures of the Al-SiO<sub>2</sub>-n-Si type, fabricated by the thermal oxidation of silicon KEF-5 with crystallographic orientation  $\langle 100 \rangle$ . To form MDS structures, aluminum field electrodes 0.8 mm in diameter were deposited on the SiO<sub>2</sub> film by thermal deposition in vacuum. The contact to the semiconductor substrate was also made of aluminum. For comparison, different methods were used [2,3,14] and to study the effect of transition layers, measurements of capacitance-voltage characteristics were carried out (Fig. 1). Measurements of the dielectric constant were carried out in the range from 30°C to 200°C and a voltage sweep in the range from -10 to 8 V. The films have a specific resistance  $\rho = 10^{13} \dots 10^{16}$  Ohm cm, a breakdown field strength  $E = (1 \dots 3) \cdot 10^6$  V/cm. The value of the relative permittivity for different layers  $\epsilon = 5 \dots 12$ .

### RESULTS AND DISCUSSION

The obtained characteristics strongly depend both on the technological regimes for the manufacture of layered structures and on the impurity content in the starting materials. It is shown that the best characteristics are achieved at an annealing temperature from 650°C to 900°C, but for a dielectric, the tangent of the angle increases to 0.1, but the insulating properties of the films also deteriorate. These data are also confirmed by the results obtained by other authors [4-6].

On the whole, the Si-SiO<sub>2</sub> structure is characterized by the presence of mechanical stresses in it. Mechanical stresses already arise in a non-oxidized silicon wafer during processing of its upper and lower surfaces in different ways. In the case of growing oxide on one of the surfaces of a semiconductor wafer, mechanical stresses can be significant. This is primarily due to the difference (almost an order of magnitude) in the coefficient of linear expansion of silicon materials, since the oxide film is grown (or deposited) at an elevated temperature. The cooling of the Si-SiO<sub>2</sub> structure leads to the appearance of mechanical stresses, and, consequently, causes deformation of the structure (the SiO<sub>2</sub> film is compressed, and the surface part of the Si plates is stretched). The cause of the occurrence of mechanical stresses can also be the difference in the structure of the materials of the semiconductor and dielectric.

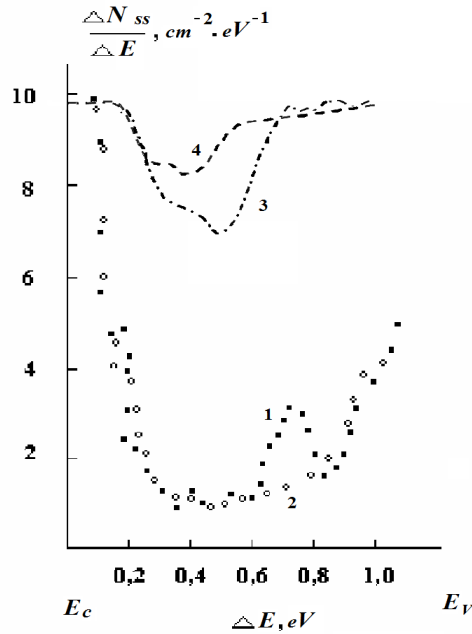


Figure 1. Capacitance-voltage characteristics of 1 - Si, 3 - SiO<sub>x</sub>, 2 – 4 after TA

Let us briefly consider the main characteristics of the semiconductor-insulator transition layer. The capacitance-voltage characteristics of MDS structures with Si-SiO<sub>2</sub> transition layers do not differ significantly from the C-V characteristics for silicon. From a comparison of the obtained C-V characteristics with the calculated one, the surface charge Q and the density of surface states N<sub>ss</sub> at the semiconductor-dielectric interface were determined (Fig. 2). For our structures obtained at a temperature of about 200°C, the minimum density N<sub>ss</sub> for the <100> silicon orientation was  $\approx 2 \cdot 10^{10} \text{ cm}^{-2} \text{ eV}^{-1}$ , and for <111> N<sub>ss</sub>  $\approx 1.2 \cdot 10^{10} \text{ cm}^{-2} \text{ eV}^{-1}$ . Such differences in the values of N<sub>ss</sub> are explained by different values of the activation energy and the number of free bonds of atoms for different orientations of the crystal surface [7,15].

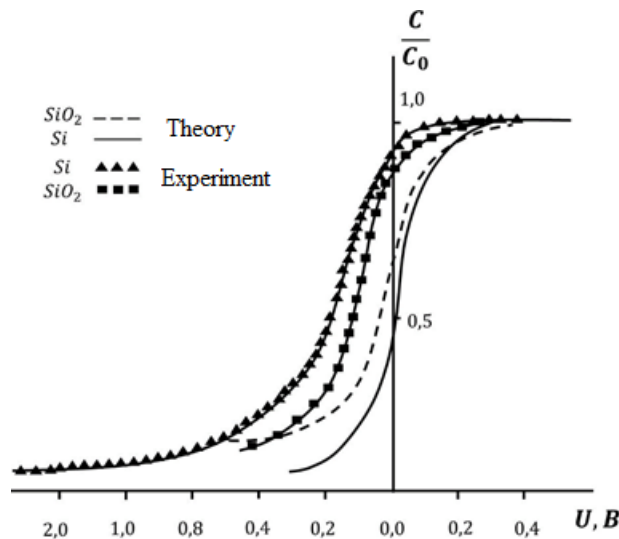
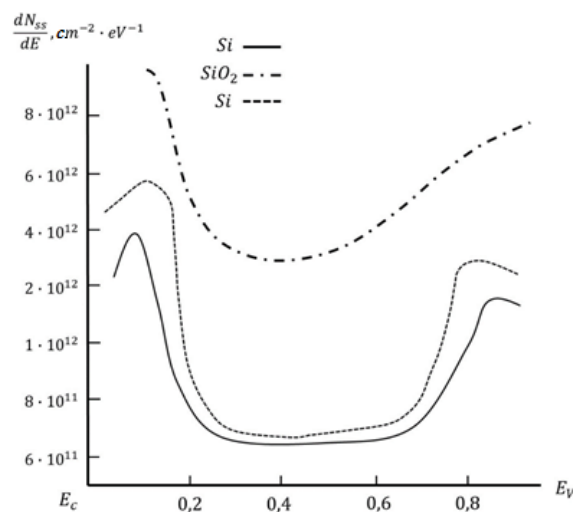


Figure 2. Theoretical and experimental capacitance-voltage characteristics of silicon structures normalized to the capacitance value of the dielectric layer



Comparative detailed analysis of the theoretical and experimental methods showed that the formulation of the density of surface states near the inversion region of the C-V characteristics, as well as not far from the region of strong enrichment. To describe the properties of the interface, the three-layer model is most often used [6,9], in which the semiconductor-dielectric system is divided into three regions qualitatively different in their properties: the region of regular SiO<sub>2</sub> and single-crystal Si, the transition region of the non-stoichiometric composition of SiO<sub>2</sub> and the regions of deformed SiO<sub>2</sub> attached to it and cushioned Si [1,10]. The thickness of the SiO<sub>2</sub> layer is 0.6 ÷ 2 μm and depends on the pre-treatment of the silicon substrate and the oxidation mode. The disordered layers of Si and SiO<sub>2</sub> applied to this region are characterized by an increased content of various kinds of defects and mechanical stresses caused by different coefficients of thermal expansion of the SiO<sub>2</sub> layer and the silicon substrate [8,16]. It is the region of the nonstoichiometric composition of SiO<sub>2</sub> and the regions of disordered SiO<sub>2</sub> and Si adjacent to it that in this model are united under the concept of an interface, and the defects contained in these regions determine its electrophysical characteristics. [6,11]. The energy state density distributions at the Si-SiO<sub>2</sub> interface over the band gap of silicon are shown in Fig.3. As for Si-SiO<sub>2</sub> structures, the density of states is minimal near the middle of the band gap and increases near the edges of the C- and V- bands. The value of the maximum density N<sub>ss</sub>, in accordance with [3,17], depends both on the orientation of the substrate and on the conditions for obtaining the dielectric layer.



**Figure 3.** Sample-averaged distribution of the density of surface states over the band gap of a semiconductor and dielectric

It can be seen from the figure that the smallest scatter of the obtained data takes place in the energy range from  $E_c - 0.2$  eV to  $E_c - 0.75$  eV. Significant scatter of values for MIS structures, fabricated and previously obtained results [3,11]. This, according to the authors of [5,6], is a consequence of optical inactive oxygen and the presence of local spatial inhomogeneities in the distribution of the surface charge on the Si – SiO<sub>2</sub> transition layer and the fluctuations of the surface potential associated with them. It is in this energy range that a good uniformity of the results of all measurements is observed. Meanwhile, a rather large spread in the values of the averaged values of the density of surface states near the edges of the energy bands is synchronously observed. It is possible that from Figure 3, in the energy range from  $E_c$  to  $E_c - 0.2$  eV and from  $E_c - 0.75$  eV to  $E_v$ , this spread reaches 30%. In our opinion, the reason for this scatter of data may be as follows. As the enrichment voltage applied to the structure decreases, the electrons localized on the surface states begin to be ejected into the conduction band due to thermal generation. In this case, the probability of their recapture is high, since the concentration of electrons near the interface is rather high [3,8].

### CONCLUSIONS

From the experimentally observed characteristics, an important point here is the way holes appear in the dielectric, since the heights of the Al-SiO<sub>2</sub> and Si-SiO<sub>2</sub> barriers are large in order to appear by hole tunneling. Consequently, the center localized on the semiconductor-insulator transition layer itself is responsible for the inhomogeneous distribution of the density of surface states. As for Si-SiO<sub>2</sub> elements, this is typical for electrical conductivity due to above-barrier charge emission or thermal ionization of impurity centers [11,18]. In the absence of voltage on the structure and at low depleting voltages, the indicated center is neutral. At sufficiently high inversion voltages, the center is ionized, releasing electrons localized on it, which are captured by the charge of the inversion layer, reducing the rate of its formation. With full ionization of the center, the charge of the inversion layer increases due to the thermal generation of minor charge carriers, which leads to a further decrease in the measured capacitance of the structure [8,19,20]. Based on the above, it can be assumed that the experimentally observed, dielectric parameters of the Si-SiO<sub>2</sub> elements studied by us are close to the characteristics of silicon MDS structures, and even better in a number of parameters. The low-temperature technology for producing oxide films makes it possible to use these materials to create MIS structures based on multicomponent semiconductors, for which high-temperature treatment is undesirable.

### Acknowledgment

The authors are grateful to the Director of the Research Institute of Semiconductor Physics and Microelectronics, Doctor of Physical and Mathematical Sciences, Prof. Sh.B. Utamuradova for assistance in conducting experiments and discussing the results.

### ORCID

©Shakhrukh Kh. Daliev, <https://orcid.org/0000-0001-7853-2777>; ©Fayzulla A. Saparov, <https://orcid.org/0009-0001-4291-1334>

### REFERENCES

- [1] Sh. B. Utamuradova, Kh. S. Daliev, E. K. Kalandarov, and Sh. Kh. Daliev, "Features of the behavior of lanthanum and hafnium atoms in silicon," *Technical Physics Letters*, **32**(6), 469–470 (2006). <https://doi.org/10.1134/S1063785006060034>
- [2] Yu.S. Chistov, and V.F. Synorov, *Physics of MOS structures*, (State publishing house, Voronezh VSU, 1989).
- [3] Sh. Kh. Daliev, and F.A. Saparov, "Influence of the interface on the electrical characteristics of MIS structures," *The European science review*, **1-2**, 31-35 (2022). <https://doi.org/10.29013/ESR-22-1.2-31-35>
- [4] Sh.D. Kurmashev, I.M. Vikulin, and S.V. Lenkov, "Silicon MIS structures with oxides of rare earth elements as a dielectric," *Technology and design in electronic equipment*, **6**, 6-8 (2001). <http://dspace.nbuv.gov.ua/handle/123456789/70884> (in Russian)
- [5] P. Borowicz, P. Latek, W. Rzdokiewicz, A. Łaszcz, A. Czerwinski, and J. Ratajczak, "Deep-ultraviolet Raman investigation of silicon oxide: thin film on silicon substrate versus bulk material," *Advances in Natural Sciences: Nanoscience and Nanotechnology*, **3**, 045003 (2012). <https://iopscience.iop.org/article/10.1088/2043-6262/4/045003>
- [6] L.S. Berman, E.I. Belyakova, L.S. Kostina, E.D. Kim, and S.C. Kim, "Analysis of charges and surface states at the interfaces between semiconductor - dielectric - semiconductor structures," *Physics and technology of semiconductors*, **34**(7), 814-817 (2000). <https://journals.ioffe.ru/articles/viewPDF/37188> (in Russian)
- [7] B.I. Boltaks, *Diffusion in semiconductors*, (State publishing house of physical and mathematical literature, Moscow, 1971).
- [8] Sh.B. Utamuradova, A.V. Stanchik, K.M. Fayzullaev, and B.A. Bakirov, "Raman scattering of light by silicon single crystals doped with chromium atoms," *Applied Physics*, (2), 33–38 (2022). [https://applphys.orion-ir.ru/appl-22/22-2/PF-22-2-33\\_RU.pdf](https://applphys.orion-ir.ru/appl-22/22-2/PF-22-2-33_RU.pdf) (in Russian)
- [9] Sh.B. Utamuradova, Kh.S. Daliev, Sh.Kh. Daliev, and K.M. Fayzullaev, *Applied Physics*, **6**, 90 (2019). <https://applphys.orion-ir.ru/appl-19/19-6/PF-19-6-90.pdf> (in Russian)
- [10] W. Kaiser, P.H. Keck, and C.F. Lange, "Infrared absorption and oxygen content in silicon and germanium," *Phys. Rev.* **101**, 1264-1268 (1956). <https://journals.aps.org/pr/abstract/10.1103/PhysRev.101.1264>
- [11] Sh.Kh. Daliev, F.A. Saparov, and F. Umarov, "Influence of thermal field treatments on the volt-farad characteristics of MDS structures," *Science and World, International scientific journal.* **2**, 10(98), 8-11 (2021). [http://scienceph.ru/f/science\\_and\\_world\\_no\\_10\\_98\\_october\\_vol\\_ii.pdf](http://scienceph.ru/f/science_and_world_no_10_98_october_vol_ii.pdf) (in Russian)
- [12] Sh.B. Utamuradova, Sh.Kh. Daliev, K.M. Fayzullaev, D.A. Rakhmanov, and J.Sh. Zarifbayev, "Raman Spectroscopy of Defects in Silicon Doped with Chromium Atoms," *New materials, compounds and applications*, **7**, 1, 37-43 (2023). [http://jomardpublishing.com/UploadFiles/Files/journals/NMCA/V7N1/Utamuradova\\_et\\_al.pdf](http://jomardpublishing.com/UploadFiles/Files/journals/NMCA/V7N1/Utamuradova_et_al.pdf)
- [13] Sh.B. Utamuradova, Sh.Kh. Daliev, D. A. Rakhmanov, A. S. Doroshkevich, V.A. Kinev, O.Yu. Pomamareva, M.N. Mirzayev, and R.Sh. Isayev, "Ir – Spectroscopy of n-Si<Pt> Irradiated with Protons," *Advanced Physical research*, **5**(2), 73-80 (2023). [http://jomardpublishing.com/UploadFiles/Files/journals/APR/V5N2/Utamuradova\\_et\\_al.pdf](http://jomardpublishing.com/UploadFiles/Files/journals/APR/V5N2/Utamuradova_et_al.pdf)
- [14] Sh.B. Utamuradova, Sh.Kh. Daliev, A.V. Stanchik, and D.A. Rakhmanov, "Raman spectroscopy of silicon, doped with platinum and irradiated by protons," *E3S Web of conferences*, **402**, 14014(1-9) (2023). <https://doi.org/10.1051/e3sconf/202340214014>
- [15] Sh.B. Utamuradova, A.V. Stanchik, and D.A. Rakhmanov, *East Eur. J. Phys.* **2**, 201 (2023). <https://doi.org/10.26565/2312-4334-2023-2-21>
- [16] Kh.S. Daliev, Sh.B. Utamuradova, O.A. Bozorova, Sh.Kh. Daliev, "Joint effect of Ni and Gf impurity atoms on the silicon solar cell photosensitivity," *Applied Solar Energy (English translation of Geliotekhnika)*, **41**(1), 80–81 (2005). [https://www.researchgate.net/publication/294234192\\_Joint\\_effect\\_of\\_Ni\\_and\\_Gf\\_impurity\\_atoms\\_on\\_the\\_silicon\\_solar\\_cell\\_photosensitivity](https://www.researchgate.net/publication/294234192_Joint_effect_of_Ni_and_Gf_impurity_atoms_on_the_silicon_solar_cell_photosensitivity)
- [17] Sh.B. Utamuradova, and D.A. Rakhmanov, "Effect of Holmium Impurity on the Processes of Radiation Defect Formation in n-Si<Pt>," *Annals of the University of Craiova, Physics*, **32**, 132–136 (2022). [https://cis01.central.ucv.ro/pauc/vol/2022\\_32/15\\_PAUC\\_2022\\_132\\_136.pdf](https://cis01.central.ucv.ro/pauc/vol/2022_32/15_PAUC_2022_132_136.pdf)
- [18] Sh.B. Utamuradova, D.A. Rakhmanov, A.S. Doroshkevich, Z. Slavkova, and M.N. Ilyina, "Impedance spectroscopy of p-Si<Pt>, p-Si<Cr> irradiated with protons," *Advanced Physical Research*, **5**(1), 5–11 (2023). [http://jomardpublishing.com/UploadFiles/Files/journals/APR/V5N1/Utamuradova\\_et\\_al.pdf](http://jomardpublishing.com/UploadFiles/Files/journals/APR/V5N1/Utamuradova_et_al.pdf)
- [19] Kh.S. Daliev, Sh.B. Utamuradova, O.A. Bozorova, and Sh.Kh. Daliev, "Joint influence of impurity atoms of nickel and hafnium on photosensitivity of silicon solar cells," *Geliotekhnika*, (1), 85–87 (2005).
- [20] S.I. Vlasov, and F.A. Saparov, "Effect of pressure on the electric properties of passivating coatings based on lead borosilicate glasses," *Surface Engineering and Applied Electrochemistry*, **47**(4), 338-339 (2011). <http://dx.doi.org/10.3103%2FS1068375511040156>

### ПРО ВЛАСТИВОСТІ ПЕРЕХІДНОГО ШАРУ Si-SiO<sub>2</sub> У БАГАТОШАРОВИХ КРЕМНІЄВИХ СТРУКТУРАХ

Шахрух Х. Далієв, Файзулла А. Сапаров

Інститут фізики напівпровідників і мікроелектроніки Національного університету Узбекистану,  
100057, Ташкент, Узбекистан, вул. Янги Алмазар, 20

Методом ємнісної спектроскопії досліджено вольт-ємнісні характеристики багат шарових структур з перехідним шаром Si-SiO<sub>2</sub> у зразках типу Al-SiO<sub>2</sub>-n-Si, виготовлених термічним окисленням напівпровідника. Показано, що неоднорідний розподіл щільності поверхневих станів є локалізованим електроактивним центром на самій межі розділу напівпровідник-діелектрик внаслідок надбар'єрної емісії заряду або термічної іонізації домішкових центрів.

**Ключові слова:** структура MDS; кремній; перехідний шар; інтерфейс; температура; діелектричний шар

## ELECTRONIC STRUCTURE CALCULATION OF $\alpha$ -Al<sub>2</sub>X<sub>3</sub> SYSTEM (X = O, S) BASED ON r++SCAN FUNCTIONAL

 **Muhammad R. Ramadhan<sup>a</sup>, Salwa A. Khansa<sup>a</sup>, Q. Zulindra<sup>a</sup>, Dian P. Handayani<sup>a</sup>,  
Nina A. Wardani<sup>a</sup>,  Fahmia Astuti<sup>b\*</sup>**

<sup>a</sup> Department of Chemical Engineering, Faculty of Industrial Engineering, UPN Veteran Yogyakarta, 55283 Sleman, Indonesia

<sup>b</sup> Department of Physics, Faculty of Science and Data Analytics, Institut Teknologi Sepuluh Nopember, 60111 Surabaya, Indonesia

\*Corresponding Author e-mail: [fahmia@physics.its.ac.id](mailto:fahmia@physics.its.ac.id)

Received September 25, 2023; revised October 11, 2023; accepted October 31, 2023

Due to the necessity of reducing the reliance on fossil fuels, several systems are considered to be alternative and/or additional support for the existing battery material. In this report, structural and electronic properties of aluminium oxide (Al<sub>2</sub>O<sub>3</sub>) and aluminium sulfide (Al<sub>2</sub>S<sub>3</sub>) with hexagonal symmetry ( $\alpha$ -phase), are investigated by utilizing density functional theory technique based on r++SCAN functional. The calculated lattice parameter and insulating gap for both systems are well matched with previous experimental studies and display higher accuracy compared to the results from local density approximation (LDA) and generalized gradient approximation (GGA) studies. The calculated insulating gap values are 10.3 eV and 4.1 eV for  $\alpha$ -Al<sub>2</sub>O<sub>3</sub> and  $\alpha$ -Al<sub>2</sub>S<sub>3</sub> respectively. For  $\alpha$ -Al<sub>2</sub>O<sub>3</sub> system, we observed hybridized s-p-d orbital of Al-O in the conduction states, consistent with the interpretation of past X-ray Absorption Near Edge Structure (XANES) data. Finally, the bulk and young modulus for  $\alpha$ -Al<sub>2</sub>O<sub>3</sub> are determined to be 251 GPa and 423 GPa which is very close to the known experimental values of 280 GPa and 451 GPa.

**Keywords:** DFT; meta-GGA; r++SCAN;  $\alpha$ -Al<sub>2</sub>O<sub>3</sub>,  $\alpha$ -Al<sub>2</sub>S<sub>3</sub>

**PACS:** 31.15.E-, 31.15.eg, 31.15.es

### INTRODUCTION

Recently, global interest is increasing for the development of renewable energy storage material that is clean and affordable, leading to the reduction of reliance on fossil energy. Battery technology based on lithium ion is one of the most researched for the energy storage system. However, due to the current technological advancement, the power density and life cycle of lithium-ion battery does not meet the current global needs [1,2]. This situation motivates many researchers to design an alternative to the lithium-ion battery [3,4]. One such system is the aluminium-based sulfide battery, Al<sub>2</sub>S<sub>3</sub>, that has been attracted interest recently due to its promising characteristics to achieve low-cost and high-performance energy storage system [5]. It was observed from the experimental studies that Al<sub>2</sub>S<sub>3</sub> is stable in P6<sub>1</sub> space group symmetry (the so-called  $\alpha$ -phase) [6]. On the other aspect, similar  $\alpha$ -phase system based on aluminium, Al<sub>2</sub>O<sub>3</sub>, is also utilized to support the existing lithium-based battery material by coating its surface to improve the electrochemical performance and cycling capacity of the battery [7,8].

Both structure of  $\alpha$ -Al<sub>2</sub>O<sub>3</sub> and  $\alpha$ -Al<sub>2</sub>S<sub>3</sub> can be described based on the hexagonal crystal axes, in which both systems contain 12 Al atoms and 18 O or S atoms. For  $\alpha$ -Al<sub>2</sub>O<sub>3</sub>, the lattice parameters of  $a = 4.756 \text{ \AA}$  and  $c = 12.982 \text{ \AA}$  is observed at 4.5 K by using Bragg backscattering method [9]. Whereas the lattice parameter for Al<sub>2</sub>O<sub>3</sub> is calculated to be  $a = 6.438 \text{ \AA}$  and  $c = 17.898 \text{ \AA}$  from a single crystal x-ray diffraction (XRD) refinement [6]. From its electronic properties, both systems are insulating and confirmed experimentally by optical spectroscopy for  $\alpha$ -Al<sub>2</sub>O<sub>3</sub> [10] and photoconductivity experiment for  $\alpha$ -Al<sub>2</sub>S<sub>3</sub> [11].

Several theoretical studies have been reported for both of the systems. For  $\alpha$ -Al<sub>2</sub>O<sub>3</sub> system, it was initially investigated by Xu *et al.*, that an indirect insulating gap of 6.29 eV is obtained from local density approximation (LDA) of density functional theory (DFT) calculation [12]. Following this result, further studies using generalized gradient approximation (GGA) suggested similar insulating gap albeit with direct gap characteristics [13]. Considering that the experimental gap is reported to be 8.8 eV, the calculated values based on LDA and GGA functionals are underestimated [14,15]. Higher gap values can be obtained by employing hybrid functionals such as B3LYP (8.5 eV) and HSE (9.2 eV) [16,17]. For  $\alpha$ -Al<sub>2</sub>S<sub>3</sub> system, GGA-PBE functional gives a gap value of  $\sim 3 \text{ eV}$  [18], while hybrid functional of HSE06 gives a higher gap at 4.95 eV [19]. From those theoretical results, the lower gap values from the semilocal functional such as LDA and GGA can be increased by using hybrid functional such as B3LYP and HSE. However, hybrid functional is also known to be very expensive from the perspective of computational resource, making it difficult to utilize this functional on more complex DFT calculation such as surface dynamic and/or atomic substitution effect. Thus, semilocal functional is preferably used for those type of calculation [20], while ignoring the facts that insulating gap is severely underestimated. Based on those facts, more DFT studies with more efficient functional is still required.

Recently, the meta-GGA functional which obeys all 17 known constraints of for the exact exchange-correlation (XC) at semilocal level named SCAN (strongly constrained appropriately normed), attract wide interest due to its accuracy

on predicting different type of materials [21]. Lane *et al.*, report a proper insulating gap values on the Mott-insulator of La<sub>2</sub>CuO<sub>4</sub> without any additional parameter [22]. Our group also successfully describe the most realistic structure of superhard material B<sub>4</sub>C from the perspective of both electronic and elastic characteristics [23]. Other successful implementation of SCAN is also reported for the problematic germanium atom, in which 0.57 eV gap is opened, contrary to the metallic behavior observed when using GGA-PBE functional [24]. Furthermore, the composite structure made from Si and Ge atom can also be properly described when discussing its composition effects on the calculated gap [25]. However, SCAN functional is also known to suffers numerical instability which leads to the increasing computational cost making it closer to the inefficiency level of hybrid functional [26]. To remedy this, regularized SCAN (rSCAN) functional is developed by Bartok and Yates, which reduces the number of satisfied constraints (13 out of 17 exact constraints) [27]. Further investigation based on rSCAN shows a reduced accuracy compared to the original SCAN functional [28]. To improve this situation, Furness *et al.*, modifies the rSCAN functional and introduces three new functionals with increasing adherence to the constraint named r++SCAN, r<sup>2</sup>SCAN, and r<sup>4</sup>SCAN [29]. Out of those three new functionals, r<sup>2</sup>SCAN is the one that is recommended by the author, to achieve balance between accuracy and numerical performance. Later study by Kingsbury *et al.*, confirm the robustness of r<sup>2</sup>SCAN calculation's time with the caveat that the calculated band gap is smaller and larger lattice volumes are obtained for many strongly-bound structures [30]. The fact that r<sup>2</sup>SCAN functional predicts larger lattice parameters can also be seen on the original report by Furness *et al.*, where the r<sup>2</sup>SCAN has a tendency to overestimate lattice parameters for a system that consists 2 elements such as LiCl, LiF, MgO, NaCl, NaF and SiC. For those type of systems, r++SCAN is actually superior in terms of predicting lattice parameters and achieves the accuracy level of SCAN functional (Furness *et al.*, 2022).

Following those results, we chose r++SCAN functional to investigate the electronic structure of  $\alpha$ -Al<sub>2</sub>O<sub>3</sub> and  $\alpha$ -Al<sub>2</sub>S<sub>3</sub> and try to provide more insight on the application of SCAN-type functionals to different type of materials.

### COMPUTATIONAL METHODOLOGY

All calculations were conducted based on Quantum Espresso (QE) v.7.0 package [31,32]. The chosen functional for exchange-correlation is r++SCAN which is provided via Libxc v.6.0.0 [33]. The pseudopotential that considers additional kinetic term for the electron density are based on Yao *et al.* [24]. Both  $\alpha$ -Al<sub>2</sub>O<sub>3</sub> and  $\alpha$ -Al<sub>2</sub>S<sub>3</sub> are optimized using the kinetic energy cut-off of 80 Rydberg (Ry) to accommodate a denser fast fourier transform (FFT) grids that is necessary for this type of functional. The chosen value for the kinetic energy cut-off is determined by looking into the relation between calculated total energy and its kinetic energy cut-off as depicted in Fig. 1.

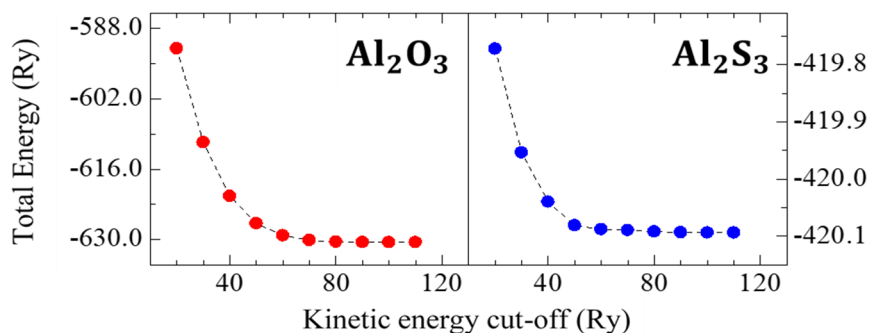


**Figure 1.** Calculated total energy of Al<sub>2</sub>O<sub>3</sub> and Al<sub>2</sub>S<sub>3</sub> with respect to kinetic energy cut-off

Brillouin zone of  $\alpha$ -Al<sub>2</sub>O<sub>3</sub> ( $\alpha$ -Al<sub>2</sub>S<sub>3</sub>) system is considered within the automatic k-points arrangement of  $9 \times 9 \times 3$  ( $6 \times 6 \times 2$ ). Then, we expand the k-points to  $18 \times 18 \times 6$  ( $12 \times 12 \times 4$ ) for the density of states calculations. The electronic and structural optimization is conducted following the convergence criteria of  $1 \times 10^{-6}$  Ry,  $1 \times 10^{-5}$  Ry/Bohr, and  $5 \times 10^{-1}$  kbar for the energy, force and pressure respectively. These convergence criteria show good consistencies for both electronic and structural parameters of both systems. LDA and GGA-PBE functionals are also used for the structural, electronic, and elastic properties following same k-points arrangements and convergence criteria, with reduced kinetic energy cut-off. The elastic parameters of bulk ( $B$ ) and young ( $E$ ) modulus of  $\alpha$ -Al<sub>2</sub>O<sub>3</sub> is calculated based on Voigt-Reuss-Hill approximation as implemented in thermo\_pw v.1.6.0. package by utilizing the optimized crystal structure from the initial calculation, and fixed the atomic positions.

### RESULTS AND DISCUSSION

Optimized structures for both systems are described in Fig. 2 and its calculated values are summarized in Table 1. For comparison, we also include the calculated lattice parameter values from LDA and GGA-PBE functional [35,36]. For  $\alpha$ -Al<sub>2</sub>O<sub>3</sub> system, the calculated lattice parameter of  $a$  and  $c$ -values based on r++SCAN functional are 4.781 Å and 13.022 Å. These values are 0.52 % and 0.31 % higher compared to the experimental result [9]. Reported calculated values based on LDA functional are 0.98 % and 1.0 % smaller, while GGA-PBE functional lattice parameters ( $a$  and  $c$ ) are overestimated by either 0.59 % and 0.66 % [35], or 1.03 % and 1.02 % [36]. The difference on the reported GGA-PBE

results could be very likely due to the different initial calculation's condition (kinetic energy cut-off, sampling k-points, convergence criteria, DFT-code, etc.). Similar situation is observed for  $\alpha$ -Al<sub>2</sub>S<sub>3</sub> system, where the difference between our calculated results and the experimental data are 0.67 % and 0.50 % higher for *a* and *c*-lattice parameter. The LDA functional underestimate the lattice parameter by 1.71 % and 1.27 %, while the GGA-PBE functional overestimate the lattice parameters by 1.88 % and 0.89 %. Looking into those results, the r++SCAN functional gives a better estimation on the lattice parameters for both  $\alpha$ -Al<sub>2</sub>O<sub>3</sub> and  $\alpha$ -Al<sub>2</sub>S<sub>3</sub> system, albeit with a slightly overestimated lattice parameter that is also previously reported on different systems [29]. The better accuracy on estimating the lattice parameter by this type of functional is due to its capability to describe the atomic-bonding interaction properly [21].

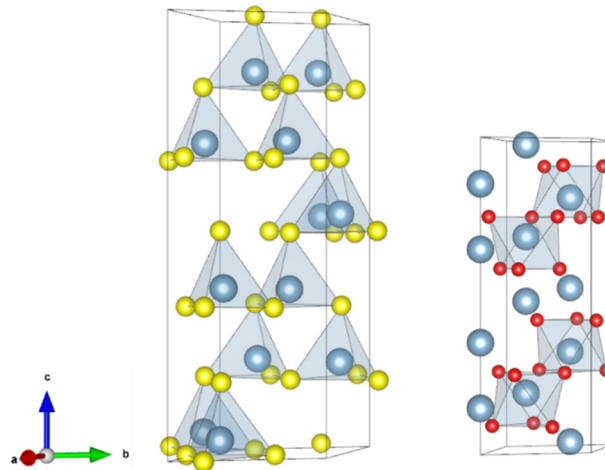


**Figure 2.** Optimized structure of  $\alpha$ -Al<sub>2</sub>S<sub>3</sub> and  $\alpha$ -Al<sub>2</sub>O<sub>3</sub>. Red and yellow balls indicate S and O atom, while silver balls show the coordinate for Al atom. The drawings are produced by VESTA software [34]

**Table 1.** Optimized lattice parameter of  $\alpha$ -Al<sub>2</sub>O<sub>3</sub> and  $\alpha$ -Al<sub>2</sub>S<sub>3</sub>

	LDA	GGA-PBE	r++SCAN	Experiment
		$\alpha$ -Al <sub>2</sub> O <sub>3</sub>		
<i>a</i> (Å)	4.709 <sup>a</sup>	4.784 <sup>a</sup> 4.805 <sup>b</sup>	4.781	4.756 <sup>c</sup>
<i>c</i> (Å)	12.846 <sup>a</sup>	13.068 <sup>a</sup> 13.116 <sup>b</sup>	13.022	12.982 <sup>c</sup>
<i>V</i> (Å <sup>3</sup> )	246.740 <sup>a</sup>	259.072 <sup>a</sup> 262.252 <sup>b</sup>	257.787	254.338 <sup>c</sup>
		$\alpha$ -Al <sub>2</sub> S <sub>3</sub>		
<i>a</i> (Å)	6.330 <sup>d</sup>	6.562 <sup>d</sup>	6.473	6.438 <sup>e</sup>
<i>c</i> (Å)	17.660 <sup>d</sup>	18.054 <sup>d</sup>	17.970	17.898 <sup>e</sup>
<i>V</i> (Å <sup>3</sup> )	612.808 <sup>d</sup>	673.386 <sup>d</sup>	652.080	640.206 <sup>e</sup>

<sup>a</sup>Ref. 35 <sup>b</sup>Ref. 36 <sup>c</sup>Ref. 9 <sup>d</sup>This work <sup>e</sup>Ref. 6

We further analyze both system from density of states (DOS) and partial density of states (PDOS) calculations. It was known from previous studies that the calculated gap of a system depends on the functional. Our calculated data shows that the  $\alpha$ -Al<sub>2</sub>O<sub>3</sub> have an insulating gap of 10.3 eV. This value is actually larger compared to the optical gap (8.8 eV) and the value provided by SCAN functional (7.2 eV) with the same calculation's condition. Similar situation is also reported by Swathilakshmi *et al.*, where the r<sup>2</sup>SCAN band gap gives larger value compared to SCAN functional for oxide system such as V<sub>2</sub>O<sub>5</sub>, CrO<sub>3</sub>, MnO, and Fe<sub>2</sub>O<sub>3</sub> [37]. Even by changing the exchange-part to the more accurate r<sup>4</sup>SCAN functional, we also observed similar ~10 eV gap for  $\alpha$ -Al<sub>2</sub>O<sub>3</sub>. The fact that similar trend (r++SCAN gives larger gap compared to SCAN) is observed on the oxide system, we believe that more detailed study needs to be addressed for this type of system in the future. Other possibilities that the 8.8 eV gap obtained from the experiment are considered to be an optical gap in which by definition is lower than the fundamental gap estimated by DFT calculation. Nevertheless, the DOS general characteristics for  $\alpha$ -Al<sub>2</sub>O<sub>3</sub> is the same with previous study based on GGA-PBE functional, with the valence states are dominated by oxygen and the conduction states mainly originated from aluminium as shown in Fig. 3(a). Looking into its orbital contribution on Fig. 3(c,d), we observe that the conduction states are originated from the hybridized states between s-p-d orbitals of Al-O. This is actually differs with what is shown from the previous GGA-PBE result, where only s and p-orbital that is observed [35], but consistent with the interpretation of experimental XANES data, where the distorted nature of the Al-O octahedral structure allowed such hybridization (s-p-d) to be exist [38].

Moving on to the  $\alpha$ -Al<sub>2</sub>S<sub>3</sub> system, the calculated insulating gap by using r++SCAN functional is 4.1 eV, which is very close to the experimental value of 4.2 eV. The DOS general characteristic for both conduction and the highest valence states is dominated by sulfur. This calculated value significantly improves the results obtained from the PBE (2.72 eV and  $\sim$ 3 eV) and LDA (2.51 eV) functionals [18]. As the gap value given by hybrid functional HSE06 is 4.95 eV [19], r++SCAN functional seems to improve the accuracy of HSE06. However, the experimental 4.2 eV gap is considered to be an optical instead of fundamental gap that is calculated from DFT technique. Thus, one can always argue that r++SCAN functional slightly underestimates the insulating gap of  $\alpha$ -Al<sub>2</sub>S<sub>3</sub>. While the trend of r++SCAN functional calculated gap in respect to the reported hybrid functional seems to be differs for both  $\alpha$ -Al<sub>2</sub>O<sub>3</sub> and  $\alpha$ -Al<sub>2</sub>O<sub>3</sub> system (higher in  $\alpha$ -Al<sub>2</sub>O<sub>3</sub> and lower in  $\alpha$ -Al<sub>2</sub>O<sub>3</sub>), note that the SCAN-type functional is a “parameter-free” calculation (additional parameter are set without any reference to the real systems) while hybrid functional depends on the adjusted mixing parameter (exact Hartree-Fock exchange) that differs on different systems and need to be adjusted accordingly. Therefore, whether r++SCAN functional gives a better electronic structure prediction compared to the reported hybrid functional is still an open question.

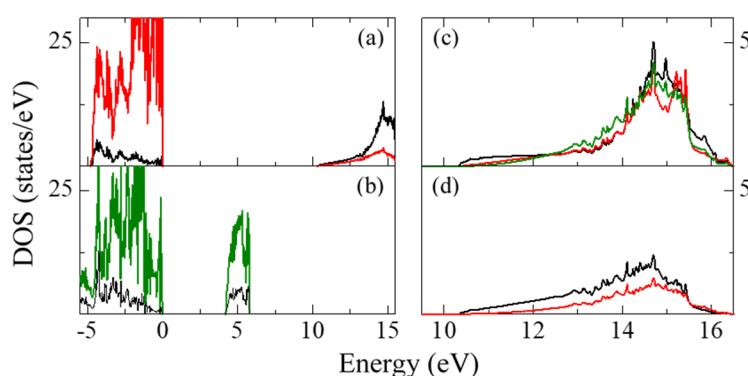


**Figure 3.** Density of states for (a)  $\alpha$ -Al<sub>2</sub>O<sub>3</sub> and (b)  $\alpha$ -Al<sub>2</sub>S<sub>3</sub>. Black solid lines indicate Al electronic states, while blue and green lines indicate O and S electronic states. The highest valence state energy for each system is defined as 0 eV. (c) Orbital contribution of s (black), p (red), and d-orbitals (green) for Al atom (d). Orbital contribution of s (black) and p-orbitals (red) for O atom

Finally, we discuss about the calculated elastic parameters of  $\alpha$ -Al<sub>2</sub>O<sub>3</sub> and  $\alpha$ -Al<sub>2</sub>S<sub>3</sub> and compare to the previous study based on PBE functional and known experimental data. All calculated elastic parameters are summarized in Table 2. For  $\alpha$ -Al<sub>2</sub>O<sub>3</sub> system, r++SCAN functional overestimates the elastic constants of  $C_{11}$  by 3.01 %,  $C_{22}$  by 8.98 % and slightly underestimate the bulk ( $B$ ) and young ( $E$ ) modulus by 10.36 % and 6.21 % respectively when compared to experimental observation [39]. From the elastic parameter calculation of  $\alpha$ -Al<sub>2</sub>O<sub>3</sub>, the calculated values given by r++SCAN are better compared to the results obtained by PBE functional [40], where the PBE functional significantly underestimates all elastic parameters (9.23 % for  $C_{11}$ , 9.58 % for  $C_{66}$ , 17.14 % for  $B$ , and 19.29 % for  $E$ ). Furthermore, the experimental values of  $C_{11}$  and  $C_{66}$  are obtained at room temperature ( $\sim$ 297 K) and tends to be reduced with an increasing temperature. Thus, by fitting the reported data with the 2<sup>nd</sup> order polynomial function, the fitted value at 0 K is 510 GPa and 171 GPa for  $C_{11}$  and  $C_{66}$  respectively, aligning more with our calculated r++SCAN results. To the best of author’s knowledge, there is no experimental report on  $\alpha$ -Al<sub>2</sub>S<sub>3</sub> elastic parameter, however similar trend is observed where r++SCAN functional gives larger elastic parameters compared to the PBE functional.

**Table 2.** Calculated elastic parameters of  $\alpha$ -Al<sub>2</sub>O<sub>3</sub> and  $\alpha$ -Al<sub>2</sub>S<sub>3</sub>

	$C_{11}$ (GPa)	$C_{66}$ (GPa)	$B$ (GPa)	$E$ (GPa)
$\alpha$ -Al <sub>2</sub> O <sub>3</sub>				
r++SCAN	513	182	251	423
GGA-PBE <sup>a</sup>	452	151	232	364
Experiment <sup>b</sup>	498	167	280	451
$\alpha$ -Al <sub>2</sub> S <sub>3</sub>				
r++SCAN	162	59	77	127
GGA-PBE <sup>a</sup>	150	55	71	116

<sup>a</sup>This work <sup>b</sup>Ref. 39

## CONCLUSION

Structural, electronic, and elastic properties of  $\alpha$ -Al<sub>2</sub>O<sub>3</sub> and  $\alpha$ -Al<sub>2</sub>S<sub>3</sub> were studied using DFT technique by utilizing r++SCAN functional. Calculated lattice parameters show improvement over LDA and GGA-PBE functionals. Insulating gap of  $\alpha$ -Al<sub>2</sub>O<sub>3</sub> and  $\alpha$ -Al<sub>2</sub>S<sub>3</sub> are determined to be 10.3 eV and 4.1 eV. Compared to the known experimental values,

calculated values of  $\alpha\text{-Al}_2\text{O}_3$  is larger in contrast to the underestimated gap trend of semilocal functional. For  $\alpha\text{-Al}_2\text{S}_3$  system, the values are slightly underestimated and shows better accuracy compared to the past studies based on LDA, GGA, and hybrid functionals. Detailed description of  $\alpha\text{-Al}_2\text{O}_3$  electronic orbital in the conduction states shows hybridized s-p-d orbital confirming the interpretation of known XANES data. Calculated bulk and young modulus for  $\alpha\text{-Al}_2\text{O}_3$  are 251 and 423 GPa respectively, and relatively consistent with the known experimental data.

#### Acknowledgments

This study is supported by ITS grant No.941/PKS/ITS/2022 and No. 1724/PKS/ITS/2023. The computation in this work has been done using the facilities of MAHAMERU BRIN HPC, National Research and Innovation Agency of Indonesia (BRIN).

#### ORCID

©Fahmia Astuti, <https://orcid.org/0000-0003-1767-6202>; ©Muhammad Redo Ramadhan, <https://orcid.org/0000-0002-5115-5307>

#### REFERENCES

- [1] Y. He, B. Matthews, J. Wang, S. Li, X. Wang, and G. Wu, *Journal of Materials Chemistry. A, Materials for Energy and Sustainability* **6**, 735 (2018). <https://doi.org/10.1039/C7TA09301B>
- [2] X. Zhang, L. Li, E. Fan, Q. Xue, Y. Bian, F. Wu, and R. Chen, *Chemical Society Reviews*, **47**, 7239 (2018). <https://doi.org/10.1039/C8CS00297E>
- [3] D.-W. Han, S.-J. Lim, Y.-I. Kim, S.-H. Kang, Y.C. Lee, and Y.-M. Kang, *Chemistry of Materials*, **26**, 3644 (2014). <https://doi.org/10.1021/cm500509q>
- [4] T.K. Mueller, G. Hautier, A. Jain, and G. Ceder, *Chemistry of Materials* **23**, 3854 (2011). <https://doi.org/10.1021/cm200753g>
- [5] W. Chu, X. Zhang, J. Wang, S. Zhao, S. Liu, and H. Yu, *Energy Storage Materials*, **22**, 418 (2019). <https://doi.org/10.1016/j.ensm.2019.01.025>
- [6] B. Krebs, A. Schiemann, and M. Läge, *Zeitschrift Für Anorganische Und Allgemeine Chemie*, **619**, 983 (1993). <https://doi.org/10.1002/zaac.19936190604>
- [7] A. Eftekhari, *Solid State Ionics*, **167**, 237 (2004). <https://doi.org/10.1016/j.ssi.2004.01.016>
- [8] W.-K. Kim, D. Han, W. Ryu, S. Lim, and H. Kwon, *Electrochimica Acta*, **71**, 17 (2012). <https://doi.org/10.1016/j.electacta.2012.03.090>
- [9] M. Lucht, M. Lerche, H.-C. Wille, Yu.V. Shvyd'ko, H.D. Rüter, E. Gerdau, and P. Becker, *Journal of Applied Crystallography*, **36**, 1075 (2003). <https://doi.org/10.1107/S0021889803011051>
- [10] R.H. French, *Journal of the American Ceramic Society*, **73**, 477 (1990). <https://doi.org/10.1111/j.1151-2916.1990.tb06541.x>
- [11] R.H. Bube, *Photoconductivity of Solids*, (Wiley, 1960). pp. 172
- [12] Y. Xu and W. Y. Ching, *Physical Review B*, **43**, 4461 (1991). <https://doi.org/10.1103/physrevb.43.4461>
- [13] T.V. Perevalov, V.A. Gritsenko, and V.V. Kaichev, *European Physical Journal-Applied Physics*, **52**, 30501 (2010). <https://doi.org/10.1051/epjap/2010159>
- [14] M. Bortz, and R.H. French, *Applied Physics Letters*, **55**, 1955 (1989). <https://doi.org/10.1063/1.102335>
- [15] M.E. Innocenzi, R.T. Swimm, M. Bass, R.H. French, A. Villaverde, and M.R. Kokta, *Journal of Applied Physics*, **67**, 7542 (1990). <https://doi.org/10.1063/1.345817>
- [16] M. Choi, A. Janotti, and C.G. Van De Walle, *Journal of Applied Physics*, **113**, 044501 (2013). <https://doi.org/10.1063/1.4784114>
- [17] J. Muscat, A. Wander, and N.M. Harrison, *Chemical Physics Letters*, **342**, 397 (2001)., [https://doi.org/10.1016/S0009-2614\(01\)00616-9](https://doi.org/10.1016/S0009-2614(01)00616-9)
- [18] D. Zhang, X. Zhang, B. Wang, S. He, S. Liu, M. Tang, and H. Yu, *Journal of Materials Chemistry, A, Materials for Energy and Sustainability*, **9**, 8966 (2021). <https://doi.org/10.1039/D1TA01422F>
- [19] S. Lysgaard, and J.M.G. Lastra, *Journal of Physical Chemistry C*, **125**, 16444 (2021). <https://doi.org/10.1021/acs.jpcc.1c04484>
- [20] B. Ramogayana, D. Santos-Carballal, K.P. Maeneta, N.H. De Leeuw, and P.E. Ngoepe, *ACS Omega*, **6**, 29577 (2021) <https://doi.org/10.1021/acsomega.1c03771>
- [21] J. Sun, A. Ruzsinszky, and J.P. Perdew, *Physical Review Letters*, **115**, 036402 (2015). <https://doi.org/10.1103/physrevlett.115.036402>
- [22] C. Lane, J.W. Furness, I. Buda, Y. Zhang, R.S. Markiewicz, B. Barbiellini, J. Sun, and A. Bansil, *Physical Review B*, **98**, 125140 (2018). <https://doi.org/10.1103/physrevb.98.125140>
- [23] M.R. Ramadhan, F. Astuti, J. Anavisha, I.M. Al-Hafiz, W.R. Tiana, A. Oktaviana, M. Meireni, and D. Parwatiningsy, *Computational Condensed Matter*, **32**, e00709 (2022). <https://doi.org/10.1016/j.cocom.2022.e00709>
- [24] Y. Yao, and Y. Kanai, *Journal of Chemical Physics*, **146**, (2017). <https://doi.org/10.1063/1.4984939>
- [25] J. Anavisha, A.F. Gunawan, D. Alfanny, W.R. Tiana, L. Yuliantini, J. Angel, D. Parwatiningsy, and M.R. Ramadhan, *AIP Conference Proceedings*, **2708**, 020006 (2022). <https://doi.org/10.1063/5.0122539>
- [26] H.-D. Saßnick, and C. Cocchi, *Electronic Structure*, **3**, 027001 (2021). <https://doi.org/10.1088/2516-1075/abfb08>
- [27] A.P. Bartók, and J.R. Yates, *Journal of Chemical Physics*, **150**, 161101 (2019). <https://doi.org/10.1063/1.5094646>
- [28] D. Mejía-Rodríguez, and S.B. Trickey, *Physical Review B*, **102**, 121109 (2020). <https://doi.org/10.1103/PhysRevB.102.121109>
- [29] J.W. Furness, A.D. Kaplan, J. Ning, J.P. Perdew, and J. Sun, *Journal of Chemical Physics*, **156**, 034109 (2022). <https://doi.org/10.1063/5.0073623>
- [30] R. Kingsbury, A. Gupta, C.J. Bartel, J.M. Munro, S. Dwaraknath, M. Horton, and K.A. Persson, *Physical Review Materials*, **6**, 013801 (2022). <https://doi.org/10.1103/PhysRevMaterials.6.013801>
- [31] P. Giannozzi, S. Baroni, N. Bonini, M. Calandra, R. Car, C. Cavazzoni, D. Ceresoli, et al., *Journal of Physics: Condensed Matter*, **21**, 395502 (2009). <https://doi.org/10.1088/0953-8984/21/39/395502>
- [32] P. Giannozzi, O. Andreussi, T. Brummel, O. Bunä, M. B. Nardelli, M. Calandra, R. Car, et al., *Journal of Physics: Condensed Matter*, **29**, 465901 (2017). <https://doi.org/10.1088/1361-648x/aa8f79>
- [33] S. Lehtola, C. Steigemann, M.J.T. Oliveira, and M.A.L. Marques, *SoftwareX*, **7**, 1 (2018). <https://doi.org/10.1016/j.softx.2017.11.002>

- [34] K. Momma, and F. Izumi, Journal of Applied Crystallography, **44**, 1272 (2011). <https://doi.org/10.1107/S0021889811038970>
- [35] R.C.R. Santos, E. Longhinotti, V.N. Freire, R.B. Reimberg, and E.W.S. Caetano, Chemical Physics Letters, **637**, 172 (2015). <https://doi.org/10.1016/j.cplett.2015.08.004>
- [36] A. Jain, G. Hautier, C. Moore, S.P. Ong, C.R. Fischer, T. Mueller, K.A. Persson, and G. Ceder, Computational Materials Science, **50**, 2295 (2011). <https://doi.org/10.1016/j.commatsci.2011.02.023>
- [37] S. Swathilakshmi, R.K.V. Devi, and G.S. Gautam, (2023). <https://arxiv.org/abs/2301.00535>
- [38] J.A. Van Bokhoven, T. Nabi, H. Sambé, D.E. Ramaker, and D.C. Koningsberger, Journal of Physics: Condensed Matter, **13**, 10247 (2001). <https://doi.org/10.1088/0953-8984/13/45/311>
- [39] S.V. Sinogeikin, D.L. Lakshtanov, J.D. Nicholas, J.M. Jackson, and J.D. Bass, Journal of the European Ceramic Society, **25**, 1313 (2005). <https://doi.org/10.1016/j.jeurceramsoc.2005.01.001>
- [40] M. De Jong, W. Chen, T. Angsten, A. Jain, R. Notestine, A. Gamst, M.H.F. Sluiter, et al., Scientific Data **2**, (2015), <https://doi.org/10.1038/sdata.2015.9>

#### РОЗРАХУНОК ЕЛЕКТРОННОЇ СТРУКТУРИ СИСТЕМИ $\alpha$ -Al<sub>2</sub>X<sub>3</sub> (X=O,S) НА ОСНОВІ ФУНКЦІОНАЛУ R++SCAN

Мухаммад Р. Рамадхан<sup>a</sup>, Салва А. Ханса<sup>a</sup>, Коріана Зуліндра<sup>a</sup>, Діан П. Хандаяні<sup>a</sup>, Ніна А. Вардані<sup>a</sup>, Фахмія Астуті<sup>b</sup>

<sup>a</sup> Кафедра хімічної інженерії, факультет промислової інженерії, 55283 Слеман, Індонезія

<sup>b</sup> Кафедра фізики, Факультет науки та аналізу даних, Інститут технологій Сепулук Нопембер, 60111 Сурабая, Індонезія

Через необхідність зменшення залежності від викопного палива кілька систем вважаються альтернативою та/або додатковою підтримкою для існуючого матеріалу батарей. У цьому звіті структурні та електронні властивості оксиду алюмінію (Al<sub>2</sub>O<sub>3</sub>) і сульфїду алюмінію (Al<sub>2</sub>S<sub>3</sub>) з гексагональною симетрією ( $\alpha$ -фаза) досліджуються за допомогою техніки теорії функціоналу густини на основі функціоналу r++SCAN. Розрахований параметр решітки та ізоляційний зазор для обох систем добре узгоджуються з попередніми експериментальними дослідженнями та демонструють вищу точність порівняно з результатами досліджень апроксимації локальної щільності (LDA) та узагальненої градієнтної апроксимації (GGA). Розраховані значення ізоляційного зазору становлять 10,3 еВ і 4,1 еВ для  $\alpha$ - Al<sub>2</sub>O<sub>3</sub> і  $\alpha$ - Al<sub>2</sub>S<sub>3</sub> відповідно. Для системи  $\alpha$ - Al<sub>2</sub>O<sub>3</sub> ми спостерігали гібридизовану s-p-d-орбіталь Al-O у станах провідності, що узгоджується з інтерпретацією минулих даних поглинання рентгенівського випромінювання біля краю структури (XANES). Нарешті, об'ємний і молодий модуль для  $\alpha$ - Al<sub>2</sub>O<sub>3</sub> визначено як 251 ГПа і 423 ГПа, що дуже близько до відомих експериментальних значень 280 ГПа і 451 ГПа.

**Ключові слова:** DFT; мета-GGA; r++SCAN;  $\alpha$ -Al<sub>2</sub>O<sub>3</sub>,  $\alpha$ -Al<sub>2</sub>S<sub>3</sub>



## NUMERICAL STUDY OF T-GATE AlGaN/AlInGaN/GaN MOSHEMT WITH SINGLE AND DOUBLE BARRIER FOR THZ FREQUENCY APPLICATIONS

Amina Noual<sup>a#</sup>,  Messai Zitouni<sup>b</sup>, Zine-eddine Touati<sup>b</sup>,  Okba Saidani<sup>b</sup>,  Abderrahim Yousfi<sup>b\*</sup>

<sup>a</sup> LIST Laboratory, University of M'Hamed Bougara, Boumerdes, Algeria

<sup>b</sup> ETA Laboratory, Department of electronics, Faculty of technology, University Mohamed El Bachir El Ibrahimi of Bordj Bou Arréridj-34030, Algeria

\*Corresponding Author e-mail: [Abderrahim.yousfi@univ-bba.dz](mailto:Abderrahim.yousfi@univ-bba.dz); [a.noual@univ-boumerdes.dz](mailto:a.noual@univ-boumerdes.dz)

Received October 1, 2023; revised October 16, 2023; accepted November 5, 2023

This paper presents a comprehensive investigation into the DC analog and AC microwave performance of a state-of-the-art T-gate double barrier AlGaN/AlInGaN/GaN MOSHEMT (Metal Oxide Semiconductor High Electron Mobility Transistor) implemented on a 4H-SiC substrate. The study involves meticulous numerical simulations and an extensive comparison with a single barrier design, utilizing the TCAD-Silvaco software. The observed disparity in performance can be attributed to the utilization of double barrier technology, which enhances electron confinement and current density by augmenting the polarization-induced charge during high-frequency operations. Remarkably, when compared to the single barrier design, the double barrier MOSHEMT exhibits a notable 15% increase in drain current, a 5% increase in transconductance, and an elevated breakdown voltage (VBR) of 140 V in E-mode operation. Furthermore, the radio frequency analysis of the double barrier device showcases exceptional performance, setting new records with a maximum oscillation frequency ( $f_{max}$ ) of 1.148 THz and a gain cutoff frequency ( $f_t$ ) of 891 GHz. These impressive results obtained through deck-simulation affirm the immense potential of the proposed double barrier AlGaN/AlInGaN/GaN MOSHEMT for future applications in high-power and terahertz frequency domains.

**Key words:**  $TiO_2$ -MOSHEMT; T-gate; Double barrier; AlInGaN Quaternary material; Maximum THz frequency; TCAD-Silvaco

**PACS:** 73.40.-c, 85.30.Pq

### 1. INTRODUCTION

The emerging generation of power switching circuits has garnered significant attention due to the impressive capabilities of AlGaN/GaN HEMTs (High Electron Mobility Transistors) in facilitating high power and high-frequency operations. These HEMTs are poised to find applications in diverse fields such as 5G technology, sensors, automotive systems, defense, and space communications [1, 2]. The exceptional performance of AlGaN/GaN HEMTs can be attributed to the presence of a high-mobility two-dimensional electron gas (2DEG) formed and accumulated at the AlGaN/GaN interface, resulting from a strong sheet polarization charge effect [3]. To reduce gate leakage current and enhance performance, a MOS (Metal Oxide Semiconductor) HEMT heterostructure is employed by introducing an oxide layer at the intersection of the gate electrode and AlGaN barrier. Various gate oxide materials, such as  $TiO_2$ ,  $HfO_2$ ,  $Al_2O_3$ ,  $SiO_2$ , and  $Si_3N_4$ , are commonly used in MOSHEMT transistors [4-7]. Conventionally, GaN-based HEMTs operate in a depletion mode (normally-on operation) since the 2DEG is present at the heterointerface even without gate polarization. However, enhancement mode functionality is preferred to reduce production charge, simplify digital circuits, and enhance safety. Multiple technological approaches have been proposed to achieve normally-off behavior [8-10]. One novel approach, initially suggested by Ketteniss et al. and subsequently confirmed, involves using a thin quaternary AlInGaN barrier layer that introduces polarization engineering between the barrier and the GaN channel, enabling E-mode operation [11, 12]. Quaternary nitride has garnered significant attention as an alternative to AlGaN barrier layers due to its promising DC and RF performance, including the ability to utilize high aluminum content, leading to increased spontaneous polarization induced by high 2DEG carrier density ( $n_s > \sim 1.8 \times 10^{13} \text{ cm}^{-2}$ ) and high mobility ( $\mu > \sim 1800 \text{ cm}^2/\text{V s}$ ) [13-15]. Traditionally, since 1991, HEMT transistors have been designed and fabricated with a single barrier layer [16]. However, in 1999, Gaska et al. first demonstrated a double AlGaN barrier structure [17]. Subsequently, various designs featuring  $Al_{x_1}Ga_{y_1}N/Al_{x_2}Ga_{y_2}N/GaN$  double heterojunctions have been explored theoretically and experimentally, showcasing high current and high-frequency performance due to enhanced carrier confinement properties and higher 2DEG density [18-20]. Moreover, recent investigations have focused on bilayer barrier structures with quaternary alloys, resulting in the development of an  $Al_{x_1}In_{y_1}Ga_{z_1}N/Al_{x_2}In_{y_2}Ga_{z_2}N/GaN$  HEMT with high current density [21, 22]. However, to date, most experimental and theoretical studies have focused on dual AlGaN or double AlInGaN barrier-based HEMTs, with limited optimization efforts targeting the DC and RF properties of an AlGaN/AlInGaN/GaN double heterostructure.

In this study, we propose, for the first time, an E-mode  $Al_{0.30}Ga_{0.70}N / Al_{0.80}In_{0.18}Ga_{0.02}N/GaN$  MOSHEMT with a double barrier structure, incorporating an ultra-thin quaternary spacer layer ( $Al_{0.36}In_{0.08}Ga_{0.56}N$ ). The proposed design aims to enhance electron accumulation in the channel and improve radio frequency performance, extending it into the terahertz regime. To analyze and optimize the structure, we employed the Silvaco-Atlas software, enabling a thorough investigation of the proposed double barrier MOSHEMT and a comparison with a single barrier  $Al_{0.30}Ga_{0.70}N/GaN$  MOSHEMT design.

## 2. DEVICE SETTINGS AND SIMULATION PROCESS

Figure 1 presents a comprehensive 3D view of the proposed GaN-MOSHEMT transistor. The device parameters utilized in this study are listed in Table 1. To enhance the device's characteristics, T-gate technology is employed, allowing for a short gate length of 10nm (corresponding to the base of the T-shape) [23]. Examining the heterostructure design from top to bottom, a Silicon dioxide (SiO<sub>2</sub>) passivation layer is implemented to minimize surface traps. Underneath the source and drain regions, a two-graded, heavily doped n<sup>++</sup> GaN layer with  $2 \times 10^{19} \text{cm}^{-3}$  donors is regrown to minimize access resistance [24]. An oxide layer comprising high-k Titanium dioxide (TiO<sub>2</sub>) with a dielectric constant (k) of 80 is deposited beneath the gate electrode. Research has shown that employing a TiO<sub>2</sub> oxide layer facilitates high off-state breakdown voltage and reduced current losses, thereby enabling E-mode operation [25, 26]. A thin (2nm) GaN cap layer follows the oxide layer. The heterostructure continues with a non-doped AlGaN first barrier layer featuring a 30% aluminum concentration, positioned under the GaN cap. The conventional composition (x) of the ternary alloy leads to material relaxation. To further enhance the device's performance, a thin Al<sub>0.36</sub>In<sub>0.08</sub>Ga<sub>0.56</sub>N spacer layer is inserted between the GaN channel and the AlGaN barrier. Recent research indicates that the 2DEG-charge at the Al<sub>x</sub>In<sub>y</sub>Ga<sub>z</sub>N/GaN interface (associated with the Al<sub>x</sub>In<sub>y</sub>Ga<sub>z</sub>N thin spacer layer) is greater than that at the AlN/GaN interface (related to the AlN spacer layer). This is attributed to the induction of a high polarization charge, resulting in improved mobility and current flow through the region [21, 27]. Therefore, a quaternary material, Al<sub>0.36</sub>In<sub>0.08</sub>GaN, is employed as the spacer layer. To further optimize 2DEG confinement in the channel region, an Al<sub>0.80</sub>In<sub>0.18</sub>GaN second barrier layer with high aluminum/indium content is placed between the AlGaN first barrier and the Al<sub>0.36</sub>In<sub>0.08</sub>GaN spacer (as shown in Figure 1(b)). The calculated Al, In, and Ga composition for the AlInGaN materials ensures lattice-matching with the GaN channel, promoting superior transport performance [28]. These studied structures are grown on a preferred substrate of silicon carbide (4H-SiC). Nanjo et al. have confirmed that the 4H-SiC epitaxial substrate outperforms sapphire substrates, primarily due to its excellent thermal stability [29]. Referring to Figure 1(a) and Figure 1(b), the single barrier device is designated as STR01-SB, while the double barrier device is designated as STR02-DB.

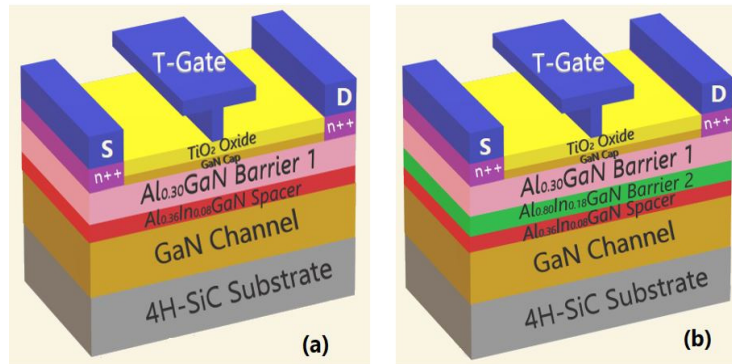


**Figure 1.** 3D view design of a 10nm T-gate (a) Single barrier Al<sub>0.30</sub>Ga<sub>0.70</sub>N / Al<sub>0.36</sub>In<sub>0.08</sub>Ga<sub>0.56</sub>N / GaN MOSHEMT, (b) Double barrier Al<sub>0.30</sub>Ga<sub>0.70</sub>N / Al<sub>0.80</sub>In<sub>0.18</sub>Ga<sub>0.02</sub>N / Al<sub>0.36</sub>In<sub>0.08</sub>Ga<sub>0.56</sub>N / GaN MOSHEMT

**Table 1.** Geometrical specifications of the studied device with single and double barrier.

Gate specifications		Structure specifications		
Parameter	Dimension	Layer	STR01-SB	STR02-DB
Gate structure	T-shape	TiO <sub>2</sub> oxide layer	5 nm	5 nm
Gate foot length	10 nm	GaN cap layer	2 nm	2 nm
Gate head length	400 nm	Al <sub>0.30</sub> GaN 1 <sup>st</sup> barrier	20 nm	20 nm
Gate stem height	50 nm	Al <sub>0.80</sub> In <sub>0.18</sub> GaN 2 <sup>st</sup> barrier	--	4 nm
Gate-drain distance	355 nm	Al <sub>0.36</sub> In <sub>0.08</sub> GaN spacer	2 nm	2 nm
Gate-source distance	355 nm	GaN channel	796 nm	796 nm
Gate work function	5.93	4H-SiC substrate	2165 nm	2161 nm

The electrical parameters of the suggested MOSHEMT transistor are evaluated using a physical model of 2D-TCAD simulation at 300K, the fundamental model used for all semiconductor device is the Drift-Diffusion model; by resolving the Poisson and electron/hole continuity equations. It computes at each moment and any point of the structure the concentration of electrons and the value of the potential. Shockley-Read Hall recombination/generation model, field-dependent mobility model, and polarization model are applied as additional physical models in the deck-simulation. Selberherr's impact ionization model is considered for device breakdown simulation. These physical models are resolved using the numerical Newton's method [30, 31]. The electrical characteristics of the proposed MOSHEMT transistor were assessed through a rigorous evaluation utilizing a 2D-TCAD simulation based on physical models. This evaluation was conducted at a temperature of 300 K. The Drift-Diffusion model, which is widely used for semiconductor devices, was employed as the fundamental model. By solving the Poisson equation and the electron/hole continuity equations, this model determines the concentration of electrons and the potential values at any given point and time within the structure.

In addition to the Drift-Diffusion model, several other physical models were incorporated into the simulation to enhance its accuracy. The Shockley-Read Hall recombination/generation model, which accounts for recombination and generation of charge carriers, was utilized. Furthermore, a field-dependent mobility model and a polarization model were applied to accurately capture the device behavior under different electric fields. To simulate the breakdown behavior of the device, Selberherr's impact ionization model was employed. This model provides insights into the phenomenon of impact ionization, which can lead to device breakdown under certain conditions.

The bandgap energy of  $Al_xGa_zN$  and  $Al_xIn_yGa_zN$  materials is dependent on the composition of mole fraction  $x$ ,  $y$  and  $z$ , using Vegard's Law, it can be expressed as a sum of the bandgap energies of GaN, InN and AlN binary semiconductors with appropriate bowing parameters [21, 25].  $Al_xIn_yGa_zN$  alloy offers an additional degree of freedom in the bandgap mole fraction ratio where  $x + y + z = 1$  compared with  $Al_xGa_zN$ , where  $x + z = 1$ . Equations (1) and (2) describe their expressions:

$$E_g^{Al_xGa_{1-x}N} = xE_g^{AlN} + zE_g^{GaN}, \quad (1)$$

$$E_g^{Al_xIn_yGa_zN} = xE_g^{AlN} + yE_g^{InN} + zE_g^{GaN} - xy(1-z)b_{AlInN} - yz(1-x)b_{InGaN}. \quad (2)$$

The following equations provide the dielectric constant for ternary and quaternary alloys as a function of alloy composition:

$$\epsilon_{Al_xGa_zN} = 8.5x + 8.9z, \quad (3)$$

$$\epsilon_{Al_xIn_yGa_zN} = 8.5x + 15.3y + 8.9z. \quad (4)$$

The creation of a large 2D electron gas density in the heterojunction is the most important operation of the charge polarization property. For sample I (STR01-SB), two negative polarization-induced charges are present at the  $Al_{0.30}Ga_{0.70}N/Al_{0.36}In_{0.08}Ga_{0.56}N$  interface and  $Al_{0.36}In_{0.08}Ga_{0.56}N/GaN$  interface (noted  $\sigma'_1$  and  $\sigma'_2$ , respectively). Thanks to a lattice-matched between the AlInGaN material and the GaN channel, the piezoelectric polarization effect is neglected. Therefore, the total polarization  $\sigma'_{int}$  is a function of spontaneous polarization ( $P_{sp}$ ) as  $\sigma'_{int} = \sigma'_1 + \sigma'_2$  with:

$$\sigma'' = P_{sp}(Al_{0.08}In_{0.18}Ga_{0.02}N) - P_{sp}(Al_{0.30}Ga_{0.70}N), \quad (5)$$

$$\sigma''_2 = P_{sp}(Al_{0.36}In_{0.08}Ga_{0.56}N) - P_{sp}(Al_{0.80}In_{0.18}Ga_{0.02}N), \quad (6)$$

$$\sigma'' = P_{sp}(Al_{0.08}In_{0.18}Ga_{0.02}N) - P_{sp}(Al_{0.30}Ga_{0.70}N). \quad (7)$$

The mathematical equations of the spontaneous polarization of the ternary and quaternary alloys is mentioned in equations (8) and (9), the details is reported in [32, 33].

$$P_{sp}^{AlGaN} = xP_{sp}^{AlN} - zP_{sp}^{GaN} + xzb_{AlGaN}, \quad (8)$$

$$P_{sp}^{AlInGaN} = xP_{sp}^{AlN} + yP_{sp}^{InN} + zP_{sp}^{GaN} + xzb_{AlGaN} + yzb_{InGaN} + xyb_{AlInN}. \quad (9)$$

According to equations (8) and (9), AlInGaN material has a higher spontaneous polarization due to the additional contribution of the spontaneous polarization and the bowing parameter corresponding to indium content, which enhances the 2DEG concentration and the charge carrier density. The calculated polarization of both structures at the active interfaces are displayed in Fig.2.

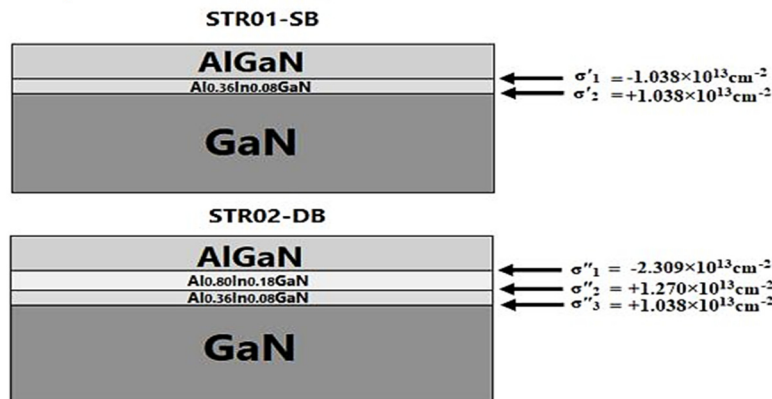


Figure 2. Polarization interface charge of both STR01-SB and STR02-DB.

The sheet charge density  $n_s$  of AlGaN and AlInGaN alloys is a function of interface polarization-induced charge  $Q_b$  and the conduction band offset  $\Delta E_c$  [34], as indicated in equations (10) and (11):

$$n_s^{AlGaN} = \frac{\sigma_{int}(x)}{q} - \frac{\epsilon_0 \epsilon(x) [q\phi_b(x) + E_F + \Delta E_c(x)]}{q^2 d}, \quad (10)$$

$$n_s^{AlInGaN} = \frac{\sigma_{int}(x,y)}{q} - \frac{\epsilon_0 \epsilon(x,y) [q\phi_b(x,y) + E_F + \Delta E_c(x,y)]}{q^2 d}. \quad (11)$$

Where  $d$  is the barrier thickness,  $\epsilon$  is the barrier's dielectric constant,  $\phi_b$  is the Schottky barrier of gate contact and  $E_F$  is the Fermi energy level. The main physical parameters of the several materials extracted during the simulation are shown in Table 2.

**Table 2.** The extracted physical parameters used in this work at 300k

Material	Al0.30GaN	Al0.80In0.18GaN	Al0.36In0.08GaN	GaN
Permittivity $\epsilon$	8.9	9.73	9.27	9.5
Band gap $E_g$ (eV)	3.42	4.55	3.71	3.55
Electron density of state $E_c$ ( $\times 10^{18} \text{cm}^{-3}$ )	2.02	3.01	2.45	1.07
Hole density of state $E_v$ ( $\times 10^{19} \text{cm}^{-3}$ )	9.08	3.30	2.10	1.16
Electron mobility $\mu_e$ ( $\text{cm}^2/\text{V.s}$ )	985.5	1280	1280	1350
Spontaneous polarization $P_{sp}$ ( $\times 10^{13} \text{cm}^{-3}$ )	-1.698	-4.007	-2.736	-1.698
Doping layer ( $\times 10^{18} \text{cm}^{-3}$ )	00	02	03	00

### 3. RESULTS AND DISCUSSION

Figure 3(a) depicts the conduction and valence band discontinuity offset in the proposed heterojunction under unbiased conditions (off-state). The AlInGaN and GaN layers exhibit a difference in their band gaps, leading to an accumulation of electrons in the quantum well and the formation of a two-dimensional electron gas at the interface of the spacer and channel. By incorporating a second barrier layer, a significant conduction band offset and higher sheet polarization density are achieved, resulting in a greater depth of the quantum well below the Fermi level. Numerical simulations indicate that the sheet density of the two-dimensional electron gas is measured at  $4.97 \times 10^{12} \text{ cm}^{-2}$  for STR02-DB, whereas it is  $2.3 \times 10^{12} \text{ cm}^{-2}$  for STR01-SB. Additionally, the extrinsic peak of electron concentration increases, reaching approximately  $1.2 \times 10^{19} \text{ cm}^{-2}$  for sample I and  $2.5 \times 10^{19} \text{ cm}^{-2}$  for sample II, as illustrated in Figure 3(b).

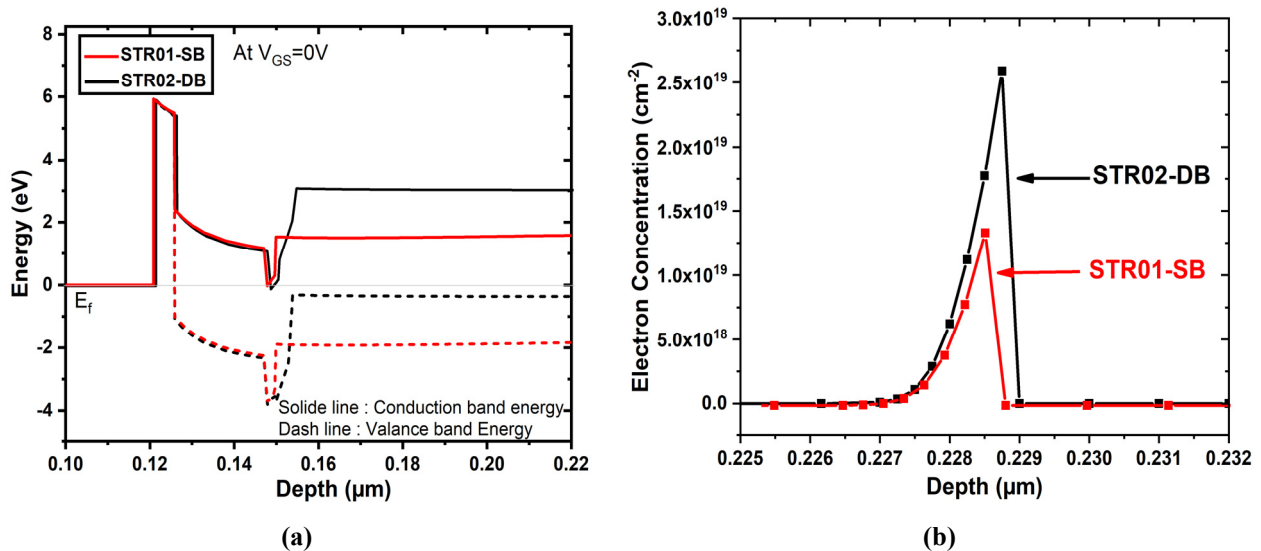


**Figure 3.** (a) Conduction and valence band diagram (b) Electron concentration of the studied device with single and double barrier at zero gate bias

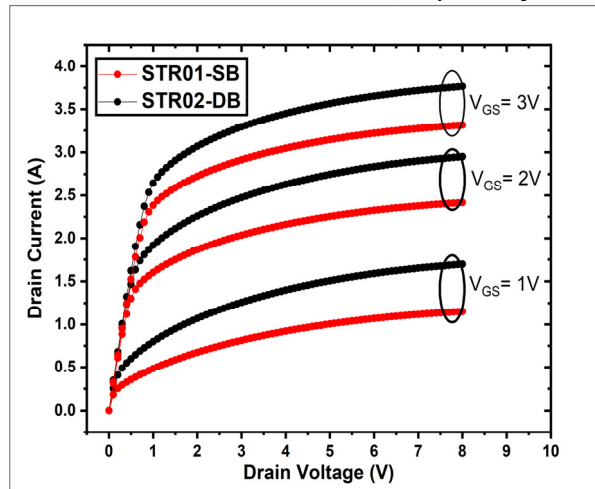
#### 3.1. DC results

This section presents the DC results of the  $\text{TiO}_2$ -based MOSHEMT (Metal-Oxide-Semiconductor High Electron Mobility Transistor) with single and double barriers, including output characteristics, ON-resistance, transfer characteristics, threshold voltage, Ion/Ioff ratio, and transconductance. Table 3 provides an overview of the DC performance metrics of the recommended nano-MOSHEMT.

**Table 3.** Comparison of the DC results of STR01-SB and STR02-DB

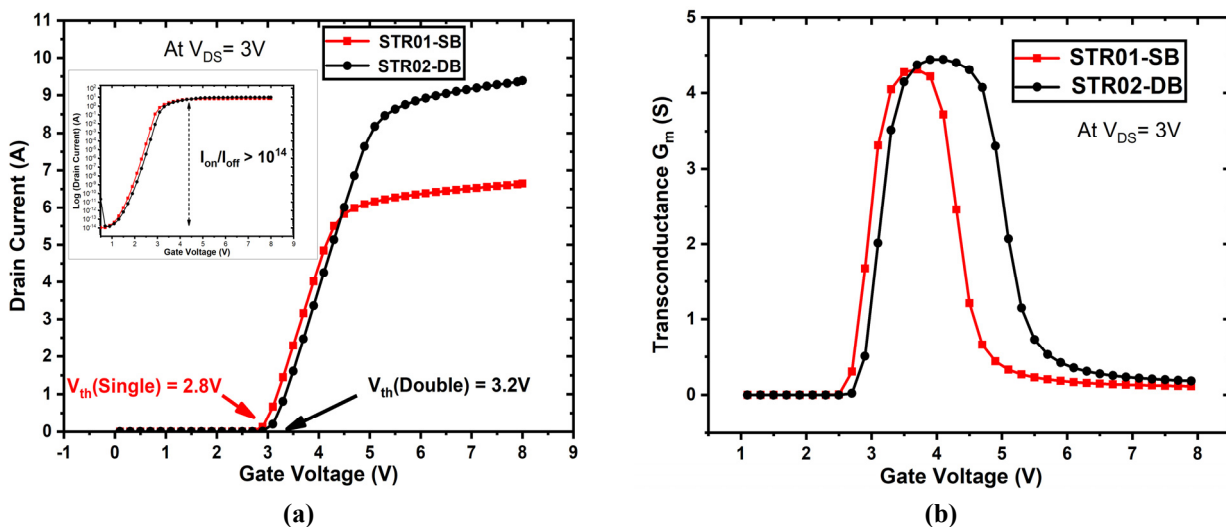
Parameters	Units	Values	
		STR01-SB	STR02-DB
ID,max	mA/mm	3300	3780
Ron	$\Omega$ .mm	5.4	3.9
Vth	V	+ 2.8	+ 3.2
Gm, max	mS/mm	4320	4470

Figure 4 illustrates the drain current as a function of drain voltage at different gate-source voltages ( $V_{GS} = 1, 2, \text{ and } 3 \text{ V}$ ). The maximum drain saturation current ( $I_{D, \text{max}}$ ) for STR01-SB and STR02-DB was observed at 3300 and 3780 mA/mm, respectively, at  $V_{GS} = 3 \text{ V}$  and  $V_{DS} = 8 \text{ V}$ . Notably, the utilization of a high aluminum composition in both the first barrier ( $x = 30\%$ ) and the second AlInGaN barrier ( $x = 80\%$ ) along with an ultrashort gate length ( $L_g = 10 \text{ nm}$ ) significantly enhances the drain current density. STR02-DB exhibits approximately a 15% increase in  $I_{D, \text{max}}$  compared to the STR01-SB device. The ON-resistance ( $R_{on}$ ) is determined from the linear region of the drain current and is found to be 5.4 and 3.9  $\Omega$ .mm for STR01-SB and STR02-DB, respectively.



**Figure 4.** ID-VD characteristics of the simulated GaN MOSHEMT with single and double barrier

In Figure 5(a), the I-V input characteristics at  $V_{DS} = 3 \text{ V}$  are presented. A threshold voltage ( $V_{th}$ ) of +2.8 V and +3.2 V was extracted for sample I and II, respectively, from the linear scale plot. The transistor operates in the enhancement mode (E-mode).



**Figure 5.** Transfer characteristics of the proposed nano-MOSHEMT at  $V_{DS} = 3 \text{ V}$ , (a) ID-VG in a linear scale, inset ID-VG in log scale, showing the  $I_{on}/I_{off}$  ratio, (b) Transconductance  $G_m$

The positive shift in  $V_{th}$  can be attributed to the utilization of the  $\text{TiO}_2$  insulating layer and the activated interface charge of  $1.85 \times 10^{13} \text{ cm}^{-2}$  donors at the oxide/semiconductor interface. This negative charge accumulates at the  $\text{TiO}_2/\text{GaN}$  interface, depleting the 2DEG charge and causing  $V_{th}$  to shift more positively. The inset of Figure 5(a) displays the logarithmic-scale plot of ID-VG, showing an  $I_{on}/I_{off}$  ratio larger than  $10^{14}$ , indicating exceedingly low drain leakage

current in the proposed heterostructure. Figure 5(b) shows the variation of transconductance ( $G_m$ ) as a function of  $V_{GS}$ , calculated from the derivative of the  $I_D$ - $V_{GS}$  curve at a fixed  $V_{DS}$ . Sample II exhibits a high peak extrinsic transconductance of  $\sim 4470$  mS/mm, while sample I demonstrates 4320 mS/mm, both at  $V_{GS} \sim 4$  V and  $V_{DS} = 3$  V. The significant  $G_m$  values can be attributed to the excellent interface charge-induced strong controllability of the very short gate, enabling high-frequency performance. Overall, the suggested 10nm T-gate double barrier  $Al_{0.30}Ga_{0.70}N/Al_{0.80}In_{0.18}Ga_{0.02}N/Al_{0.36}In_{0.08}Ga_{0.56}N/GaN$  MOSHEMT demonstrates superior performance in terms of  $I_D$ ,  $R_{on}$ , and  $G_m$  for achieving normally-off operation.

### 3.2. Breakdown voltage

Figure 6 presents the breakdown voltage characteristics of the proposed nano-MOSHEMT. In high-power millimeter-wave applications, the breakdown voltage ( $V_{BR}$ ) of the transistor plays a critical role and is primarily influenced by the impact ionization phenomenon. To enhance the  $V_{BR}$  profiles in the suggested heterojunctions, a short symmetric T-gate shape is employed. According to the Selberherr's model simulation, the off-state breakdown voltage for STR01-SB and STR02-DB is significantly improved. The breakdown voltage is measured at 126 V for STR01-SB and 140 V for STR02-DB. It is worth noting that employing a single barrier MOSHEMT results in a 10% decrease in breakdown voltage compared to the double barrier device. This reduction in breakdown voltage is clearly illustrated in Figure 6. Overall, the implementation of a short symmetric T-gate shape contributes to the enhancement of breakdown voltage profiles in the suggested heterojunctions, making them well-suited for high-power millimeter-wave applications.

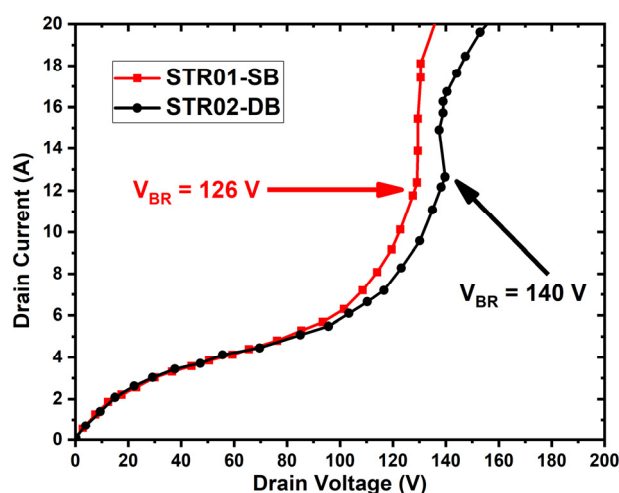


Figure 6. Off-state breakdown voltage simulation results

### 3.3. Microwave results

In this section, an investigation of the AC and RF characteristics has been conducted for the proposed device with single and double barriers. The simulation results are presented in Figures 7, 8, and 9.

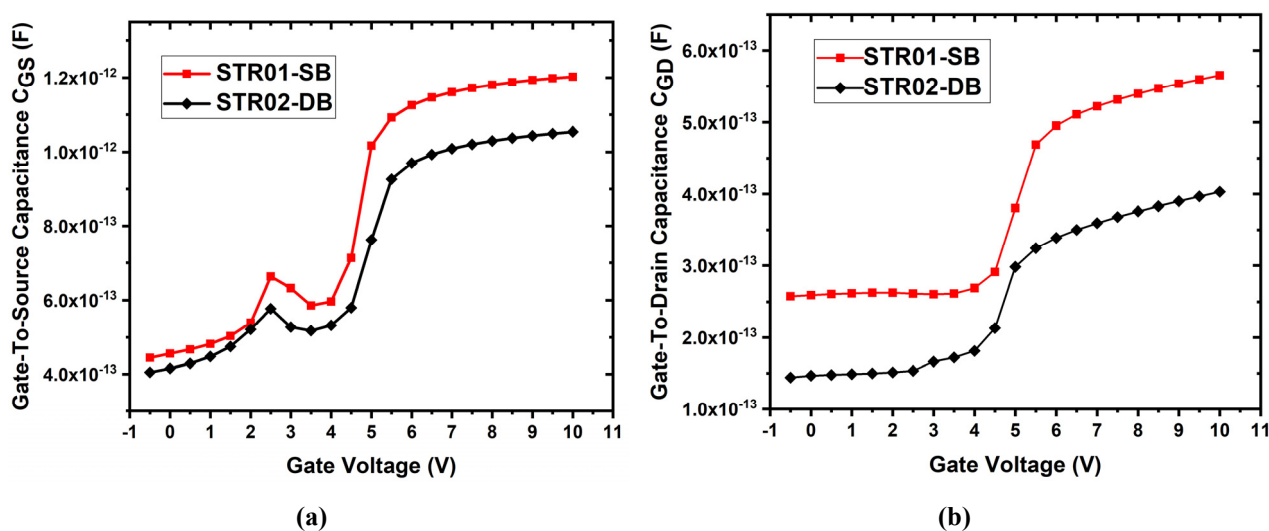


Figure 7. C-V Characteristics of the simulated devices (a) Gate-to-source capacitance ( $C_{GS}$ ), (b) Gate-to-drain capacitance ( $C_{GD}$ )

To analyze the capacitance-voltage characteristics of the simulated devices, measurements were performed at a frequency of 1 MHz. Figure 7(a) and (b) illustrate the variation of the gate-to-source capacitance (CGS) and gate-to-drain capacitance (CGD) as a function of gate-to-source voltage (VGS) at a fixed drain-to-source voltage (VDS) of 5 V. The total gate capacitance, CG, is defined as the sum of CGS and CGD. It is observed that the bilayer device exhibits a lower total gate capacitance, CG, of 1.453 pF compared to 1.767 pF for the single barrier design. This reduction in total gate capacitance indicates improved performance in terms of capacitive effects, which can have a positive impact on high-frequency operation. For future generation of millimeter and terahertz spectrum applications, ft and fmax are figures of merit in radio frequency performances [35-37]. Mathematically, they expressed as follows:

$$f_t = \frac{G_m}{2\pi(C_{GS} + C_{GD})} \quad (12)$$

$$f_{max} = \frac{f_t}{2\sqrt{C_{DS}(R_G + R_S) + 2\pi f_t(R_G C_{GD})}} \quad (13)$$

From equation (12), ft is proportional to Gm and inversely related to CG. Thus, the gate voltage at the maximum Gm should be used as the gate polarization to approximate ft and fmax. Equation (13) demonstrates that fmax is influenced by ft and other factors (where GDS represents drain-to-source conductance and RS, RG stand for source and gate resistance, respectively). The cutoff frequency and the maximum oscillation frequency referred to the frequencies when the curves of the current gain H21 and the power gain Ug are unity [38]. Their expressions in relation to S-parameters is described in equations (14) and (15):

$$H_{21} = \left| \frac{-2S_{21}}{(1 - S_{11})(2 - S_{22}) - (S_{12}S_{21})} \right| \quad (14)$$

$$U_g = \frac{|S_{21}|^2}{(1 - |S_{11}|^2)(1 - |S_{22}|^2)} \quad (15)$$

Based on TCAD simulation, the key RF parameters of the considered device, namely the transit frequency (ft) and the maximum oscillation frequency (fmax), were extracted and are depicted in Figure 8(a) and (b).

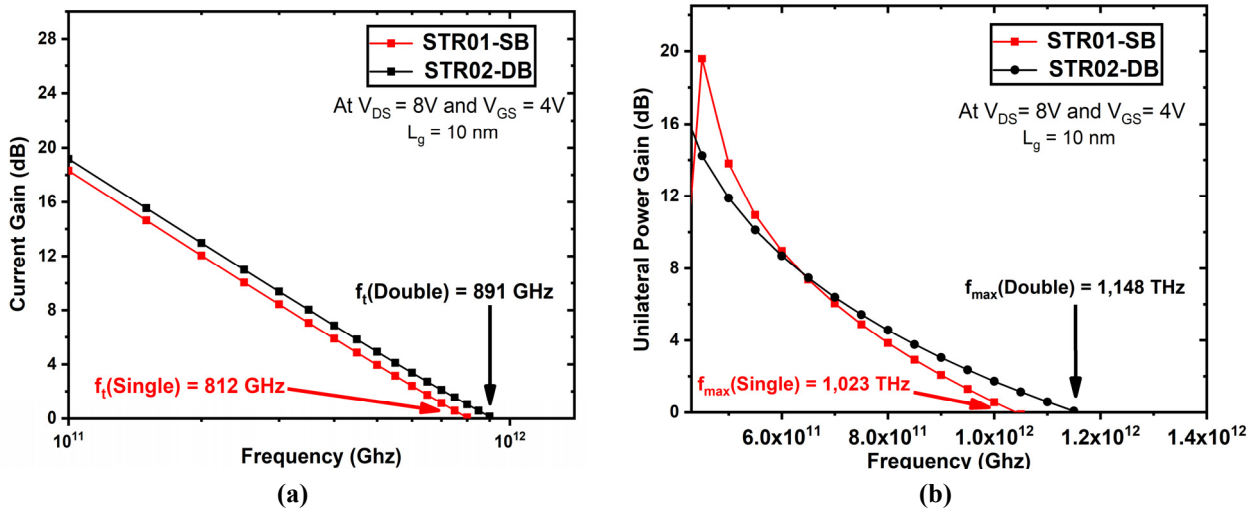
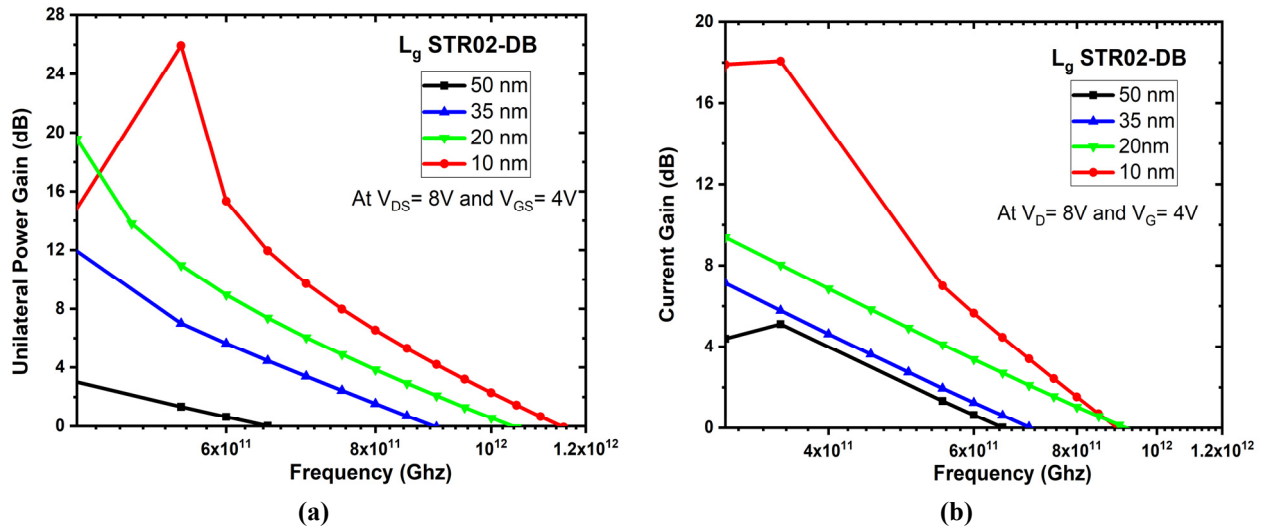


Figure 8. Small signal characteristics with single and double barrier at VGS = 4 V, VDS = 8 V, (a) Current gain, (b) Unilateral power gain

The measurements were conducted at a drain-to-source voltage (VDS) of 8 V and a gate-to-source voltage (VGS) of 4 V, corresponding to the peak transconductance (Gm). Remarkably, the achieved ft/fmax values for STR01-SB and STR02-DB are 812/1023 GHz and 891/1148 GHz, respectively. These represent new records for the highest ft/fmax reported to date in quaternary barrier devices. The superior ft/fmax performance can be attributed to the utilization of a symmetric 10 nm T-gate structure, a TiO2 oxide layer, and a thin quaternary spacer layer.

Figure 9 showcases the optimization of the output current gain and power gain for the proposed AlGaInGaN/GaN MOSHEMT at different gate lengths (Lg = 10, 20, 35, 50 nm). Through simulation analysis, it is evident that the device with an ultrashort gate length exhibits excellent RF efficiency, along with the highest fmax achieved among quaternary barrier devices reported thus far. Notably, as the gate length (Lg) decreases, ft and fmax gradually increase. This behavior can be attributed to the reduction in both CGS and CGD capacitances. According to Equations (14) and (15), ft and fmax exhibit steady growth as the gate capacitance decreases. Therefore, when designing

E-mode GaN MOSHEMTs, it is advisable to reduce the gate length while considering the technological limitations. The proposed design, featuring a 10 nm T-shaped gate in both single and double barrier III-nitride MOSHEMTs grown on a 4H-SiC substrate, demonstrates superior microwave performance compared to recent research works. These  $f_t$  and  $f_{max}$  values set new records for GaN-based MOSHEMTs in terms of high-speed power and terahertz frequency operations. The main electrical characteristics obtained from the proposed MOSHEMT are summarized and compared with previous experimental results in Table 4, highlighting its favorable performance.



**Figure 9.** Small signal characteristics of double barrier GaN-based MOSHEMT with respect of T-gate length ( $L_g = 10, 20, 35,$  and  $50$  nm) (a) Current gain, (b) Unilateral power gain

**Table 4.** Performance comparison of our results with similar experimental reports

Ref	Transistor Device	$ns \times 10^{13} \text{ cm}^{-2}$	ID A	Vth V	Gm mS	VBR V	CG pF	$f_t$ GHz	$f_{max}$ GHz
[18], 2020	Al <sub>0.30</sub> GaN/Al <sub>0.20</sub> GaN/ GaN	--	--	0	68.9	--	220	--	--
[39], 2015	Al <sub>0.85</sub> In <sub>0.10</sub> GaN/ Al <sub>0.15</sub> GaN/AlN/GaN	3.5	0.73	+1.1	--	--	--	--	--
[22], 2019	Al <sub>0.54</sub> In <sub>0.12</sub> GaN/ Al <sub>0.18</sub> In <sub>0.04</sub> GaN /GaN	--	0.76	+0.4	493	--	--	--	--
[21], 2020	Al <sub>0.72</sub> In <sub>0.16</sub> GaN/ Al <sub>0.18</sub> In <sub>0.04</sub> GaN/ Al <sub>0.80</sub> In <sub>0.18</sub> GaN /GaN	1.2	0.11	+0.2	358	--	--	--	--
[40], 2022	Al <sub>0.165</sub> In <sub>0.775</sub> GaN/ Al <sub>0.60</sub> GaN /GaN	1.6	0.2	-1.5	--	--	38	0.95	4.5
[14], 2019	Al <sub>0.74</sub> In <sub>0.16</sub> GaN/AlN/ GaN/Al <sub>0.08</sub> GaN	1.81	2.9	-2.8	900	38	0.275	310	425
This work	STR 01-SB	0.23	3.30	+2.8	4320	126	1.767	812	1023
	STR 02-DB	0.49	3.78	+3.2	4470	140	1.453	891	1148

#### 4. CONCLUSION

In summary, this study presents a comprehensive investigation into the DC analog and AC microwave performance of a state-of-the-art T-gate double barrier AlGaN/AlInGaN/GaN MOSHEMT (Metal Oxide Semiconductor High Electron Mobility Transistor) implemented on a 4H-SiC substrate. The study involves meticulous numerical simulations and an extensive comparison with a single barrier design, utilizing the TCAD-Silvaco software. The observed disparity in performance can be attributed to the utilization of double barrier technology, which enhances electron confinement and current density by augmenting the polarization-induced charge during high-frequency operations. Remarkably, when compared to the single barrier design, the double barrier MOSHEMT exhibits a notable 15% increase in drain current, a 5% increase in transconductance, and an elevated breakdown voltage (VBR) of 140 V in E-mode operation. Furthermore, the radio frequency analysis of the double barrier device showcases exceptional performance, setting new records with a maximum oscillation frequency ( $f_{max}$ ) of 1.148 THz and a gain cutoff frequency ( $f_t$ ) of 891 GHz. These impressive results obtained through deck-simulation affirm the immense potential of the proposed double barrier AlGaN/AlInGaN/GaN MOSHEMT for future applications in high-power and terahertz frequency domains.

#### Acknowledgements

This work was supported by the DGRSDT of the ministry of higher education of Algeria.



## ORCID

Abderrahim Yousfi, <https://orcid.org/0000-0003-2071-728X>; Messai Zitouni, <https://orcid.org/0000-0002-2508-3696>

Okba Saidani, <https://orcid.org/0000-0003-0507-5581>

## REFERENCES

- [1] M. Haziq, S. Falina, A.A. Manaf, H. Kawarada, and M. Syamsul, "Challenges and Opportunities for High-Power and High-Frequency AlGaIn/GaN High-Electron-Mobility Transistor (HEMT) Applications: A Review," *Micromachines*, **13**, 2133 (2022). <https://doi.org/10.3390/mi13122133>
- [2] B. Mounika, J. Ajayan, S. Bhattacharya, and D. Nirmal, "Recent developments in materials, architectures and processing of AlGaIn/GaN HEMTs for future RF and power electronic applications: A critical review," *Micro and Nanostructures*, **168**, 207317 (2022). <https://doi.org/10.1016/j.micrna.2022.207317>
- [3] S. Xiong, W. Huang, A. Hassan, and R. Zhong, "Simulation study on electrical properties of p-GaN gate normally-off HEMT devices affected by Al mole fraction in AlGaIn barrier layer," *Journal of Physics: Conference Series*, **2355**, 012073 (2022). <https://doi.org/10.1088/1742-6596/2355/1/012073>
- [4] A. Mondal, A. Roy, R. Mitra, and A. Kundu, "Comparative study of variations in gate oxide material of a novel underlap DG MOS-HEMT for analog/RF and high-power applications," *Silicon*, **12**, 2251-2257 (2020). <https://doi.org/10.1007/s12633-019-00316-0>
- [5] F. Husna, M. Lachab, M. Sultana, V. Adivarahan, Q. Fareed, and A. Khan, "High-Temperature Performance of AlGaIn/GaN MOSHEMT with SiO<sub>2</sub> Gate Insulator Fabricated on Si (111) Substrate," *IEEE Transactions on Electron Devices*, **59**, 2424-2429 (2012). <https://doi.org/10.1109/TED.2012.2204888>
- [6] M. Copel, M. Gribelyuk, and E. Gusev, "Structure and stability of ultrathin zirconium oxide layers on Si (001)," *Applied Physics Letters*, **76**, 436-438 (2000). <https://doi.org/10.1063/1.125779>
- [7] A. Pérez-Tomás, A. Fontserè, M. Jennings, and P. Gammon, "Modeling the effect of thin gate insulators (SiO<sub>2</sub>, SiN, Al<sub>2</sub>O<sub>3</sub> and HfO<sub>2</sub>) on AlGaIn/GaN HEMT forward characteristics grown on Si, sapphire and SiC," *Materials science in semiconductor processing*, **16**, 1336-1345 (2013). <https://doi.org/10.1016/j.mssp.2012.10.014>
- [8] K. Ahmeda, B. Ubochi, M. Alqaysi, A. Al-Khalidi, E. Wasige, and K.J.M.R. Kalna, "The role of SiN/GaN cap interface charge and GaN cap layer to achieve enhancement mode GaN MIS-HEMT operation," **115**, 113965 (2020). <https://doi.org/10.1016/j.micrel.2020.113965>
- [9] T. Mizutani, M. Ito, S. Kishimoto, and F. Nakamura, "AlGaIn/GaN HEMTs with thin InGaIn cap layer for normally off operation," **28**, 549-551 (2007). <https://doi.org/10.1109/LED.2007.900202>
- [10] J. Kashiwagi, T. Fujiwara, M. Akutsu, N. Ito, K. Chikamatsu, and K. Nakahara, "Recessed-gate enhancement-mode GaN MOSFETs with a double-insulator gate providing 10-MHz switching operation," **34**, 1109-1111 (2013). <https://doi.org/10.1109/LED.2013.2272491>
- [11] H. Hahn, B. Reuters, A. Wille, N. Ketteniss, F. Benkhalifa, O. Ambacher, H. Kalisch, et al., "First polarization-engineered compressively strained AlInGaIn barrier enhancement-mode MISHFET," **27**, 055004 (2012). <https://doi.org/10.1088/0268-1242/27/5/055004>
- [12] N. Ketteniss, L.R. Khoshroo, M. Eickelkamp, M. Heuken, H. Kalisch, R. Jansen, and A. Vescan, "Study on quaternary AlInGaIn/GaN HFETs grown on sapphire substrates," **25**, 075013 (2010). <https://doi.org/10.1088/0268-1242/25/7/075013>
- [13] F. Sonmez, E. Arslan, S. Ardali, E. Tiras, E. Ozbay, "Determination of scattering mechanisms in AlInGaIn/GaN heterostructures grown on sapphire substrate," *Journal of Alloys and Compounds*, **864**, 158895 (2021). <https://doi.org/10.1016/j.jallcom.2021.158895>
- [14] P. Murugapandiyam, A. Mohanbabu, V.R. Lakshmi, M. Wasim, and K.M. Sundaram, "Investigation of Quaternary Barrier InAlGaIn/GaN/AlGaIn Double-Heterojunction High-Electron-Mobility Transistors (HEMTs) for High-Speed and High-Power Applications," *J. Electron. Mater.* **49**, 524-529 (2020). <https://doi.org/10.1007/s11664-019-07731-4>
- [15] R. Brown, D. Macfarlane, A. Al-Khalidi, X. Li, G. Ternent, H. Zhou, I. Thayne, et al., "A sub-critical barrier thickness normally-off AlGaIn/GaN MOS-HEMT," **35**, 906-908 (2014). <https://doi.org/10.1109/LED.2014.2334394>
- [16] M. Khan, J. Kuznia, D. Olson, W. Schaff, J. Burm, and M. Shur, "Deep submicron AlGaIn/GaN heterostructure field effect transistors for nfcrowave and high temperature applications," in: *52nd Annual Device Research Conference*, Boulder, (CO, USA, 1994), pp. 149-150. <https://doi.org/10.1109/DRC.1994.1009451>
- [17] R. Gaska, M. Shur, T. Fjeldly, and A. Bykhovski, "Two-channel AlGaIn/GaN heterostructure field effect transistor for high power applications," *Journal of applied physics*, **85**, 3009-3011 (1999). <https://doi.org/10.1063/1.369621>
- [18] T.-L. Wu, S.-W. Tang, and H.-J. Jiang, "Investigation of recessed gate AlGaIn/GaN MIS-HEMTs with double AlGaIn barrier designs toward an enhancement-mode characteristic," *Micromachines*, **11**, 163 (2020). <https://doi.org/10.3390/mi11020163>
- [19] A.B. Khan, M.J. Siddiqui, and S.G. Anjum, "Comparative study of single and double quantum well AlGaIn/GaN HEMT structures for high power GHz frequency application," *Materials Today: Proceedings*, **4**, 10341-10345 (2017). <https://doi.org/10.1016/j.matpr.2017.06.377>
- [20] D.R. Androse, S. Deb, S.K. Radhakrishnan, and E. Sekar, "T-gate AlGaIn/GaN HEMT with effective recess engineering for enhancement mode operation," *Materials Today: Proceedings*, **45**, 3556-3559 (2021). <https://doi.org/10.1016/j.matpr.2020.12.1076>
- [21] N.M. Shrestha, Y. Li, C.-H. Chen, I. Sanyal, J.-H. Tarng, J.-I. Chyi, and S. Samukawa, et al., "Design and simulation of high-performance lattice matched double barrier normally off AlInGaIn/GaN HEMTs," **8**, 873-878 (2020). <https://doi.org/10.1109/JEDS.2020.3014252>
- [22] N.M. Shrestha, C.-H. Chen, Z.-M. Tsai, Y. Li, J.-H. Tarng, and S. Samukawa, "Barrier engineering of lattice matched alingan/gan heterostructure toward high performance e-mode operation," in: *2019 International Conference on Simulation of Semiconductor Processes and Devices (SISPAD)*, (Udine, Italy, 2019), pp. 1-4. <https://doi.org/10.1109/SISPAD.2019.8870407>
- [23] R. Singh, T. Lenka, and H. Nguyen, "T-gate shaped AlN/ $\beta$ -Ga<sub>2</sub>O<sub>3</sub> HEMT for RF and high power nanoelectronics," 2021. <https://doi.org/10.36227/techrxiv.15023094.v1>
- [24] S. Dasgupta, D. F. Brown, F. Wu, S. Keller, J.S. Speck, and U.K. Mishra, "Ultralow nonalloyed ohmic contact resistance to self-aligned N-polar GaN high electron mobility transistors by In (Ga) N regrowth," *Applied Physics Letters*, **96**, 143504 (2010). <https://doi.org/10.1063/1.3374331>

- [25] T. Zine-eddine, H. Zahra, and M. Zitouni, *Journal of Science: Advanced Materials and Devices*, “Design and analysis of 10 nm T-gate enhancement-mode MOS-HEMT for high power microwave applications,” **4**, 180-187 (2019). <https://doi.org/10.1016/j.jsamd.2019.01.001>
- [26] H. Liu, C. Lee, W. Hsu, T. Wu, H. Huang, S. Chen, Y.C. Yang, et al., “AlGaN/GaN MOS-HEMTs with TiO<sub>2</sub> gate dielectric by using non-vacuum ultrasonic spray pyrolysis deposition,” in: *2015 IEEE 11th International Conference on Power Electronics and Drive Systems*, 2015, pp. 578-580. <https://doi.org/10.1109/PEDS.2015.7203398>
- [27] H.R. Mojaver, J.-L. Gosselin, and P. Valizadeh, “Use of a bilayer lattice-matched AlInGaN barrier for improving the channel carrier confinement of enhancement-mode AlInGaN/GaN hetero-structure field-effect transistors,” *Journal of Applied Physics*, **121**, 244502 (2017). <https://doi.org/10.1063/1.4989836>
- [28] D. Biswas, H. Fujita, N. Torii, and T. Egawa, “Effect of in composition on electrical performance of AlInGaN/GaN-based metal-insulator-semiconductor high electron mobility transistors (MIS-HEMTs) on Si,” **125**, 225707 (2019). <https://doi.org/10.1063/1.5098365>
- [29] T. Nanjo, M. Suita, T. Oishi, Y. Abe, E. Yagyu, K. Yoshiara, and Y. Tokuda, “Comparison of characteristics of AlGaN channel HEMTs formed on SiC and sapphire substrates,” **45**, 424-426 (2009). <https://doi.org/10.1049/el.2009.0129>
- [30] M. Gassoumi, A. Helali, H. Maaref, and M. Gassoumi, “DC and RF characteristics optimization of AlGaN/GaN/BGaN/GaN/Si HEMT for microwave-power and high temperature application,” *Results in Physics*, **12**, 302-306 (2019). <https://doi.org/10.1016/j.rinp.2018.11.063>
- [31] A. Yousfi, H. Bencherif, L. Saidi, et al (2018, December). “Role of High-K and gate engineering in improving Rf/analog performances of In<sub>0.2</sub>Ga<sub>0.8</sub>As/Al<sub>0.3</sub>Ga<sub>0.7</sub>As HEMT,” in: *International Conference on Communications and Electrical Engineering (ICCEE)*, (IEEE, 2018), pp. 1-4.
- [32] I. Gorczyca, T. Suski, N.E. Christensen, and A. Svane, “Band gap bowing in quaternary nitride semiconducting alloys,” *Appl. Phys. Lett.* **98**, 241905 (2011). <https://doi.org/10.1063/1.3597795>
- [33] O. Ambacher, J. Majewski, C. Miskys, A. Link, M. Hermann, M. Eickhoff, et al., “Pyroelectric properties of Al (In) GaN/GaN hetero- and quantum well structures,” *Journal of physics: condensed matter*, **14**, 3399 (2002). <https://doi.org/10.1088/0953-8984/14/13/302>
- [34] P.K. Kaushik, S.K. Singh, A. Gupta, A. Basu, and E.Y. Chang, “Impact of Surface States and Aluminum Mole Fraction on Surface Potential and 2DEG in AlGaN/GaN HEMTs,” *Nanoscale Research Letters*, **16**, 159 (2021). <https://doi.org/10.1186/s11671-021-03615-x>
- [35] P.-T. Tu, I. Sanyal, P.-C. Yeh, H.-Y. Lee, L.-H. Lee, C.-I. Wu, et al., “Quaternary Barrier AlInGaN/GaN-on-Si High Electron Mobility Transistor with Record F T-L g Product of 13.9 GHz- $\mu\text{m}$ ,” in: *2020 International Symposium on VLSI Technology, Systems and Applications (VLSI-TSA)*, (IEEE, Piscataway, NJ, USA, 2020), pp. 130-131.
- [36] Z.-e. Touati, Z. Hamaizia, and Z. Messai, “DC and RF characteristics of AlGaN/GaN HEMT and MOS-HEMT,” in: *Electrical Engineering (ICEE), 2015 4th International Conference on*, (Boumerdes, Algeria, 2015), pp. 1-4. <https://doi.org/10.1109/INTEE.2015.7416850>
- [37] R. Wang, G. Li, J. Verma, B. Sensale-Rodriguez, T. Fang, J. Guo, Z. Hu, et al., “220-GHz quaternary barrier InAlGaN/AlN/GaN HEMTs,” **32**, 1215-1217 (2011). <https://doi.org/10.1109/LED.2011.2158288>
- [38] M. Sharma, R. Chaujar, and M. C. A. Engineering, J. I. J. o. R. “Ultrascaled 10 nm T-gate E-mode InAlN/AlN HEMT with polarized doped buffer for high power microwave applications,” *International Journal of RF and Microwave computer aided engineering*, **32**, e23057 (2022). <https://doi.org/10.1002/mmce.23057>
- [39] R. Kajitani, K. Tanaka, M. Ogawa, H. Ishida, M. Ishida, and T. Ueda, “Novel high-current density GaN-based normally off transistor with tensile-strained quaternary InAlGaN barrier,” *Japanese Journal of Applied Physics*, **54**, 04DF09 (2015). <https://doi.org/10.7567/JJAP.54.04DF09>
- [40] J. Jorudas, P. Prystawko, A. Šimukovič, R. Aleksiejūnas, J. Mickevičius, M. Kryško, P.P Michałowski, et al., “Development of quaternary InAlGaN barrier layer for high electron mobility transistor structures,” *Materials*, **15**, 1118 (2022). <https://doi.org/10.3390/ma15031118>

#### ЧИСЛОВЕ ДОСЛІДЖЕННЯ T-GATE AlGaN/AlInGaN/GaN MOSHEMT З ОДИНАРНИМ ТА ПОДВІЙНИМ БАР'ЄРОМ ДЛЯ ЗАСТОСУВАНЬ НА ЧАСТОТІ ТГц

Аміна Нуал<sup>a</sup>, Мессай Зігуні<sup>b</sup>, Зін-Еддін Туаті<sup>b</sup>, Окба Сайдані<sup>b</sup>, Абдеррахім Юсфі<sup>b</sup>

<sup>a</sup> Лабораторія LIST, Університет М'Хамед Бугара, Бумердес, Алжир

<sup>b</sup> Лабораторія ЕТА, кафедра електроніки, технологічний факультет, Університет Мохамеда Ель Бачіра Ель Ібрагімі Бордж Бу Аррерідж -34030, Алжир

У цій статті представлено всебічне дослідження аналогових та змінних мікрохвильових характеристик сучасного Т-образного подвійного бар'єру AlGaN/AlInGaN/GaN MOSHEMT (метал-оксид-напівпровідниковий транзистор з високою мобільністю електронів), реалізованого на підкладці 4H-SiC. Дослідження передбачало ретельне числове моделювання та широке порівняння з проектом одного бар'єру з використанням програмного забезпечення TCAD-Silvaco. Спостережувану різницю в продуктивності можна пояснити використанням технології подвійного бар'єру, яка покращує утримання електронів і щільність струму шляхом збільшення заряду, викликаного поляризацією під час високочастотних операцій. Примітно, що в порівнянні з конструкцією з одним бар'єром подвійний бар'єр MOSHEMT демонструє помітне збільшення струму стоку на 15%, збільшення коефіцієнта провідності на 5% і підвищену напругу пробою (VBR) 140 В у режимі E-mode. Крім того, радіочастотний аналіз подвійного бар'єрного пристрою демонструє виняткову продуктивність, встановлюючи нові рекорди з максимальною частотою коливань (f<sub>max</sub>) 1,148 ТГц і граничною частотою підсилення (ft) 891 ГГц. Ці результати, отримані за допомогою дек-симуляції, підтверджують величезний потенціал запропонованого подвійного бар'єру AlGaN/AlInGaN/GaN MOSHEMT для майбутніх застосувань у високопотужних і терагерцевих частотних областях.

**Ключові слова:** TiO<sub>2</sub>-MOSHEMT; T-образний затвор; подвійний бар'єр; AlInGaN четвиртинний матеріал; максимальна частота ТГц; TCAD-Silvaco

SIMULATION OF INTERACTION PROCESSES OF C<sub>20</sub> FULLERENE WITH GRAPHENE

✉ I. Ishmumin D. Yadgarov<sup>a\*</sup>, Farid F. Umarov<sup>b</sup>, Asroriddin S. Kosimov<sup>c</sup>, ✉ Khayitmurod I. Jabborov<sup>d</sup>, Shodibek Y. Aminov<sup>c</sup>

<sup>a</sup> Institute of Ion-Plasma and Laser Technologies named after U.A. Arifov, Uzbekistan Academy Sciences, Tashkent, 100125 Uzbekistan

<sup>b</sup> Kazakh-British Technical University, Almaty, 050000, Kazakhstan;

<sup>c</sup> Termez State University, Termez, 190111 Uzbekistan

<sup>d</sup> Tashkent University of Information Technologies named after Muhammad al-Khwarizmi, Tashkent, 100084 Uzbekistan

\*Corresponding Author e-mail: [ishmuminyadgarov@gmail.com](mailto:ishmuminyadgarov@gmail.com)

Received September 4, 2023; revised October 23, 2023; accepted October 31, 2023

Graphene, a carbon sheet one atom thick, with carbon atoms arranged in a two-dimensional honeycomb configuration, has a number of intriguing properties. Fullerenes are a promising material for creating electro-active elements in solar cells and active layers in thin-film organic transistors. A computer model of the C<sub>20</sub> fullerene molecule was constructed using the energy minimization method with the second-generation Brenner potential (REBO). A computer model of "infinite" defect-free graphene was built, designed to consider the process of adsorption of a C<sub>20</sub> fullerene molecule on its surface. To study adsorption process computer models of fullerene and "infinite" graphene were approached to the required distance with a different set of geometric arrangement of fullerene with respect to the graphene surface. It has been established that the adsorption of fullerene C<sub>20</sub> on the surface of graphene can be carried out in three different ways, differing in the number of interacting fullerene and graphene atoms. The binding energies and adsorption lengths for C<sub>20</sub> fullerene molecules adsorbed on the graphene surface in different ways are calculated. The way of adsorption corresponding to the highest binding energy and the shortest adsorption length was revealed.

**Keywords:** Fullerene molecule; Graphene; Adsorption; Simulation; Brenner potential

**PACS:** 61.46.-w, 02.70.Ns

## INTRODUCTION

Graphene, a carbon sheet one atom thick, with carbon atoms arranged in a two-dimensional (2D) honeycomb configuration, has a number of intriguing properties. Graphene has been extensively studied and is expected to find applications in many areas, especially in nanoelectronic devices [1-4]. Fullerenes are a promising material for creating electro-active elements in solar cells and active layers in a thin-film organic transistor [5, 6]. Many researchers have focused their attention on the interaction of fullerene molecules with solid surfaces. From the seminal article by Li et al. in [7] and later, the study of the interaction of fullerenes with a surface turned out to be an exciting area of research. In particular, while some researchers in this field have obtained results showing that the fullerene molecule experiences physical adsorption [8-10], others, on the contrary, have shown that the fullerene molecule is chemisorbed [11-16].

The study of C<sub>20</sub> molecules and solids from C<sub>20</sub> molecules can help expand the possibilities of using C<sub>20</sub> molecules and solids from these molecules. In addition to the above applications, a known application of the C<sub>20</sub> fullerene molecule is in the high temperature superconductivity (T<sub>c</sub>) region due to its stronger electron-phonon coupling than C<sub>60</sub> fullerene [17,18]. This is due to the fact that the vibronic coupling increases as the cluster size decreases [19]. As a result, it was suggested that the condensed form of the smallest fullerene C<sub>20</sub> [20–22] may be the best potential candidate for high-temperature superconductors [23]. However, the use of this promising molecule, for example, in fullerene-based heterostructures, requires understanding the nature of C<sub>20</sub> adsorption on various two-dimensional materials, since their interface interaction and binding properties play an important role in the molecular functionality of heterostructural nanomaterials.

The purpose of this research is to determine the energy and bond length for various methods of adsorption of a C<sub>20</sub> fullerene molecule on a graphene surface, as well as changes in the geometry of molecular fullerene after adsorption. The geometry of adsorbed fullerenes can significantly influence their chemical properties, so analysis of the molecular system C<sub>20</sub> + graphene may be of some interest.

At present, objects based on fullerenes C<sub>60</sub>, C<sub>70</sub> and others, the synthesis methods of which are quite developed, are mainly being studied. Low-atomic fullerenes (C<sub>20</sub>, etc.) are studied to a less extent. The goals of the proposed work are aimed at some clarification of the mechanisms of interaction of C<sub>20</sub> fullerene with graphene, which may be of interest for optimizing methods for their synthesis.

In connection with the above, in this work, research results related to the interaction of the C<sub>20</sub> molecule with graphene were highlighted, and the interaction process was considered using molecular dynamics (MD) simulation.

### METHODS AND INVESTIGATED MATERIALS

Using the energy minimization method with the second-generation Brenner potential (REBO), which describes carbon structures well [24], a computer model of the  $C_{20}$  fullerene molecule was constructed, the atomic coordinates of which were taken from [25]. As a result, it was found that the cohesive energy  $E_f$  of each carbon atom in fullerene is 6.123 eV. Then a computer model of "infinite" defect-free graphene was built, designed to consider the issues of interaction and adsorption of the  $C_{20}$  fullerene molecule on its surface. For this, a rectangular section of graphene was chosen, consisting of 112 carbon atoms (Figure 1). The construction and substantiation of the model is described in more detail in [26].

Defect-free graphene is a flat carbon structure consisting only of hexagons, similar to  $C_{60}$  fullerene hexagons, with each carbon atom in the fullerene molecule surrounded by three neighbors, with each of which it is connected by a simple covalent bond. In the smallest fullerene  $C_{20}$ , C-C bonds form only regular pentagons, in other fullerenes, in addition to pentagons, there are hexagons, and, for example, in the most common fullerene  $C_{60}$ , C-C bonds form 20 hexagons and 12 pentagons (Figure 2). Each carbon atom in a fullerene molecule is surrounded by three neighbors, with two of which it is connected by a single covalent bond and with the third by a double bond.

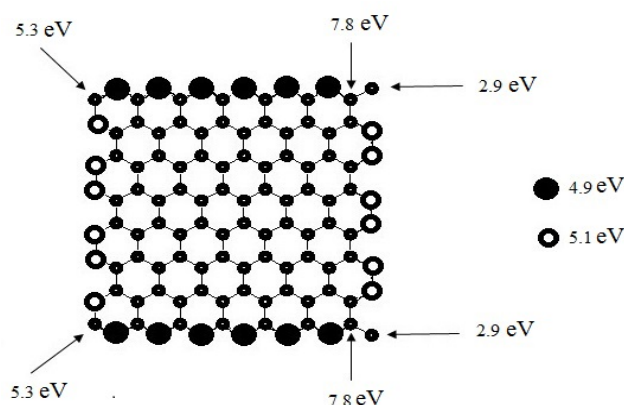


Figure 1. Atomic structure of a defect-free 112-atom rectangular section of graphene

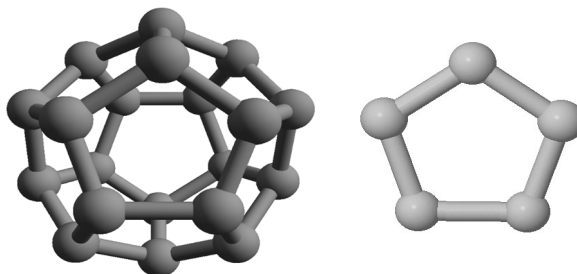
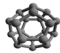


Figure 2. Spatial configuration of atoms and the  $C_{20}$  fullerene face

After computer models of single defect-free objects were obtained: fullerene  $C_{20}$ , "infinite" graphene, the process of adsorption of fullerene on the surface of graphene was studied. To study the process of fullerene adsorption on graphene, computer models of fullerene and "infinite" graphene were approached to the required distance with a different set of geometric arrangement of fullerene with respect to the graphene surface, followed by the application of the energy minimization method within the framework of the Brenner potential and periodic boundary conditions on the edge atoms of graphene.

The  $C_{20}$  fullerene molecule with a graphene layer is studied by the energy minimization method, where we use the conjugate gradient algorithm. Since the energy is a function of different degrees of freedom, i.e. bond lengths, bond angles, and dihedrals, this method finds the energetically preferred conformation of the system, which is equivalent to locating all minima of its energy function. This article explores the lowest energy state and the other most important local minimum states. On the other hand, empirical or parametric methods give the interaction potential in an analytical form and are based on the corresponding parameters determined by comparison with experimental data. Due to the analytical form of the potential, it is convenient for further calculations of other properties of the material. Here we use a version of the Brenner potential specifically parameterized for carbon and hydrocarbon systems. The expression of this potential and its parameters used in our calculation can be found in [27]. This potential describes the carbon-carbon interaction very well. Here we further demonstrate its suitability for characterizing hydrocarbon systems. In Table 1, the binding energy and bond length calculated using the modified Brenner potential are in very good agreement with available other theoretical data. This confirms our model for the interaction of graphene with the  $C_{20}$  fullerene molecule.

**Table 1.** Values of bond energy and bond length for carbon-carbons obtained in the current approach (bold), DFT B3LYP [28] and TD-DFT [29] methods

carbon	Binding energy (eV/atom)	Bond length (Å)
<b>C<sub>20</sub></b> 	<b>6.123</b> 6.086 [28] -	<b>1.46</b> 1.445 [28] 1.44-1.51 [29]

## RESULTS AND DISCUSSION

It was found that the adsorption of fullerene C<sub>20</sub> on the surface of graphene can be carried out in different ways. The paper lists only 3 selected methods of such adsorption. Horizontal edges of nanographene are zigzag edges, vertical edges are armchair edges. Atoms whose cohesion energy differs from 7.4 eV are marked with large sizes or arrows indicating their cohesion energies.

The following are the ways of C<sub>20</sub> fullerene adsorption on the graphene surface:

I) through the interaction of one atom of fullerene and one atom of graphene (C-ATP),

II) through the interaction of two neighboring fullerene atoms and two neighboring graphene atoms (BRI),

III) through the interaction of two nearest non-neighboring fullerene atoms and two nearest non-neighboring graphene atoms.

Table 2 shows the geometric characteristics of adsorbed fullerene obtained by analyzing the results of computer simulation of three selected adsorption methods. Since the radius of the free C<sub>20</sub> fullerene is 1.99 Å, and its spherical symmetry leads to the fact that the values of its maximum and minimum radii are equal to each other and their ratio is equal to 1, then, according to Table 2, as a result of adsorption, the spherical symmetry of the C<sub>20</sub> fullerene is violated and this is a violation of the symmetry depends on the way the molecule is adsorbed on the graphene surface.

**Table 2.** Geometric characteristics of fullerene C<sub>20</sub>, adsorbed on the surface of graphene

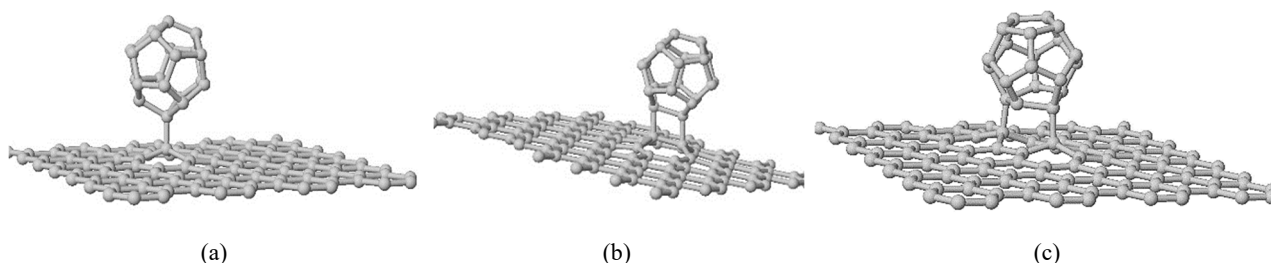
	Adsorption ways		
	I C-ATP	II BRI	III
radius averaged, Å	1.99	1.99	1.99
maximum radius, Å	2.19	2.19	2.21
minimum radius, Å	2.07	2.06	2.05
ratio of maximum radius to minimum	1.05	1.06	1.07

Three variants of fullerene adsorption on the graphene surface are considered: a) through the interaction of one fullerene atom and one graphene atom, b) through the interaction of two neighboring fullerene atoms and two neighboring graphene atoms, c) through the interaction of two nearest non-neighboring fullerene atoms and two nearest non-neighboring graphene atoms (Figure 3).

The binding energy  $E_{ads}$  for C<sub>20</sub> molecule adsorbed on the surface of the graphene substrate is the difference between the total potential energy of the substrate and the adsorbed molecule  $E_{ads/sub}^{tot}$  from the potential energy of the substrate in the state where they do not interact  $E_{ads}^{tot}$  and the potential energy of the adsorbed molecule  $E_{sub}^{tot}$  equals to [30]:

$$E_{ads} = E_{ads/sub}^{tot} - (E_{sub}^{tot} + E_{ads}^{tot}).$$

The following binding energies and adsorption lengths for C<sub>20</sub> fullerenes adsorbed on graphene were obtained: a) 1.63 eV; 1.52Å, b) 1.07 eV; 1.58Å and c) 0.83 eV; 1.57Å. Thus, the first of the three adsorption variants a) corresponds to the highest binding energy of fullerene molecules with graphene and the shortest adsorption length.

**Figure 3.** Adsorption processes of the C<sub>20</sub> fullerene molecule on the surface of graphene. (a) interaction of one atom of fullerene and one atom of graphene (C-ATP), (b) interaction of two neighboring fullerene atoms and two neighboring graphene atoms (BRI), (c) interaction of two nearest non-neighboring fullerene atoms and two nearest non-neighboring graphene atoms

## CONCLUSIONS

A model experiment of the interaction of C<sub>20</sub> fullerene molecules with the surface of graphene has been carried out. The geometric characteristics of fullerene molecules adsorbed on the surface of graphene are determined. It is shown that as a result of adsorption, the spherical symmetry of fullerene molecules is violated. It has been established that the degree

of symmetry breaking depends on the method of fullerene molecule adsorption on the graphene surface. Binding energies and adsorption lengths are calculated for C<sub>20</sub> fullerene molecules adsorbed on the graphene surface in three different ways. The variant of adsorption with the highest binding energy and the shortest adsorption distance was determined.

#### Acknowledgements

The authors are grateful for fruitful collaborations with Dr. Farid Umarov. This work was assisted by the fundamental research program of the Academy Sciences of Uzbekistan.

#### ORCID

✉ **Ishmumin D. Yadgarov**, <https://orcid.org/0000-0002-4808-2258>; ✉ **Khayitmurod I. Jabborov**, <https://orcid.org/0000-0002-8262-7055>

#### REFERENCES

- [1] S.K. Tiwari, S. Sahoo, N. Wang, and A. Huczko, "Graphene research and their outputs: Status and prospect," *Journal of science: Advanced materials and devices* **5**, 10-29 (2020). <https://doi.org/10.1016/j.jsamd.2020.01.006>
- [2] M. Hoseini-Ghahfarokhi, S. Mirkiani, N. Mozaffari, M.A.A. Sadatlu, A. Ghasemi, S. Abbaspour, M. Akbarian, et al., "Applications of Graphene and Graphene Oxide in Smart Drug/Gene Delivery: Is the World Still Flat." *International journal of Nanomedicine* **15**, 9469-9496 (2020). <https://doi.org/10.2147/IJN.S265876>
- [3] S. Singh, M.R. Hasan, P. Sharma, and J. Narang, "Graphene nanomaterials: The wondering material from synthesis to applications," *Sensors International*, **3**, 100190 (2022). <https://doi.org/10.1016/j.sintl.2022.100190>
- [4] S. Korkmaz, and I.A. Kariper, "Graphene and graphene oxide based aerogels: synthesis, characteristics and supercapacitor applications," *Journal of Energy Storage*, **27**, 101038 (2020). <https://doi.org/10.1016/j.est.2019.101038>
- [5] F. Zabihi, Q. Chen, Y. Xie, and M. Eslamian, "Fabrication of efficient graphene-doped polymer/fullerene bilayer organic solar cells in air using spin coating followed by ultrasonic vibration post treatment," *Superlattices and Microstructures*, **100**, 1177-1192 (2016). <https://doi.org/10.1016/j.spmi.2016.10.087>
- [6] M. Paukov, C. Kramberger, I. Begichev, M. Kharlamova, and M. Burdanova, "Functionalized Fullerenes and Their Applications in Electrochemistry," *Solar Cells, and Nanoelectronics, Materials*, **16**(3), 1276 (2023). <https://doi.org/10.3390/ma16031276>
- [7] Y.Z. Li, J.C. Patrin, M. Chander, J.H. Weaver, L.P.F. Chibante, and R.E. Smalley, "Ordered Overlayers of C<sub>60</sub> on GaAs(110) Studied with Scanning Tunneling Microscopy," *Science*, **252**(5005), 547-548 (1991). <https://doi.org/10.1126/science.252.5005.547>
- [8] S. Laref, A.M. Asaduzzaman, W. Beck, P.A. Deymier, K. Runge, L. Adamowicz, and K. Muralidharan, "Characterization of graphene-fullerene interactions: Insights from density functional theory," *Chemical Physics Letters*, **582**, 115-118 (2013). <https://doi.org/10.1016/j.cplett.2013.07.033>
- [9] D. Chen, and D. Sarid, "An STM study of C<sub>60</sub> adsorption on Si(100)-(2×1) surfaces: from physisorption to chemisorption," *Surface Science*, **329**, 206-218 (1995). [https://doi.org/10.1016/0039-6028\(95\)00051-8](https://doi.org/10.1016/0039-6028(95)00051-8)
- [10] D. Klyachko, and D.M. Chen, "Ordering of C<sub>60</sub> on Anisotropic Surfaces," *Physics Review Letters*, **75**, 3693-3696 (1995). <https://doi.org/10.1103/physrevlett.75.3693>
- [11] S. Haghgoo, and A.R. Nekoei, "Metal oxide adsorption on fullerene C<sub>60</sub> and its potential for adsorption of pollutant gases; density functional theory studies," *RSC Advances*, **11**(28), 17377-17390 (2021). <https://doi.org/10.1039/d1ra02251b>
- [12] M.R. Cerón, C. Zhan, P.G. Campbell, M.C. Freyman, C. Santoyo, L. Echegoyen, B.C. Wood, et al., "Integration of Fullerenes as Electron Acceptors in 3D Graphene Networks: Enhanced Charge Transfer and Stability through Molecular Design," *ACS Applied Materials and Interfaces*, **11**(32), 28818-28822 (2019). <https://doi.org/10.1021/acsami.9b06681>
- [13] X. Du, F. Chen, X. Chen, X. Wu, Y. Cai, X. Liu, and L. Wang, "Adsorption geometry of individual fullerene on Si surface at room-temperature," *Applied Physics Letters*, **97**, 253106 (2010). <https://doi.org/10.1063/1.3529446>
- [14] P.J. Moriarty, "Fullerene adsorption on semiconductor surfaces," *Surface Science Reports*, **65**, 175-227 (2010). <http://dx.doi.org/10.1016/j.surfrep.2010.08.001>
- [15] J. Li, Y. Cui, L. Zhang, "C<sub>60</sub> adsorption on defective Si (1 0 0) surface having one missed dimer from atomic simulations at electrical level," *Arabian Journal of Chemistry*, **16**, 104816 (2023). <https://doi.org/10.1016/j.arabjc.2023.104816>
- [16] J. Li, D. Zhao, and L. Zhang, "Strain acting on adsorption of C<sub>60</sub> onto graphene from DFTB algorithm," *Carbon Trends*, **5**, 100138.1-100138.9. (2021). <https://doi.org/10.1016/j.cartre.2021.100138>
- [17] S.K. Shrivastava, "Superconductivity in organic materials," *Journal of Emerging Technologies and Innovative Research*, **6**, 45-52 (2019). <https://www.jetir.org/papers/JETIR1907B71.pdf>
- [18] Y. Yu, X.-W. Yan, F. Ma, M. Gao, and Z.-Y. Lu, "Candidates of intrinsic superconducting carbon allotrope," *Condensed Materials*, **3**, 12324 (2023). <https://doi.org/10.48550/arXiv.2301.12324>
- [19] I. Spagnolatti, M. Bernasconi, and G. Benedek, *European Physics Letters*, **59**, 572 (2002). <https://doi.org/10.1209/epl/i2002-00384-1>
- [20] V.A. Helden, M.T. Hsu, N.G. Gotts, P.K. Kemper, and M.T. Bowers, "Do small fullerenes exist only on the computer? Experimental results on C<sub>20</sub> and C<sub>24</sub>," *Chemical Physics Letters*, **204**, 15-22 (1993). [https://doi.org/10.1016/0009-2614\(93\)85599-J](https://doi.org/10.1016/0009-2614(93)85599-J)
- [21] H. Handschuh, G. Gantefor, B. Kessler, P.S. Bechthold, and W. Eberhardt, "Stable Configurations of Carbon Clusters: Chains, Rings, and Fullerenes," *Physics Review Letters*, **74**, 1095 (1995). <https://doi.org/10.1103/PhysRevLett.74.1095>
- [22] D.J. Klein, W.A. Seitz, and T.G. Schmalz, "Scanning tunnelling microscopy of solid C<sub>60</sub>/C<sub>70</sub>," *Nature*, **323**, 703-706 (1986). <https://doi.org/10.1038/323703a0>
- [23] G.B. Adams, O.F. Sankey, J.B. Page, and M. O'Keeffe, "Jahn-Teller distortions in solid C<sub>20</sub> and other fullerene structures," *Chemical Physics*, **176**, 61-66 (1993). [https://doi.org/10.1016/0301-0104\(93\)85007-u](https://doi.org/10.1016/0301-0104(93)85007-u)
- [24] D.W. Brenner, O.A. Shenderova, J.A. Harrison, S.J. Stuart, B. Ni, and S.B. Sinnott, "A second-generation reactive empirical bond order (REBO) potential energy expression for hydrocarbons," *J. Phys: Condens. Matter*, **14**, 783-802 (2002). <https://doi.org/10.1088/0953-8984/14/4/312>
- [25] A.S. Baltenkov, "Spherical Coordinates of Carbon Atoms in C<sub>20</sub> Fullerene Cage, <https://arxiv.org/pdf/1812.07878.pdf>

- [26] V.G. Stelmakh, I.D. Yadgarov, and A.N. Ulukmuradov, "Adsorption of C<sub>60</sub> fullerene on defect-free graphene," *Uzbek Journal of Physics*, **5**, 305-308 (2018). <https://doi.org/10.52304/v20i5.122> (in Russian)
- [27] D.W. Brenner, O.A. Shenderova, J.A. Harrison, S.J. Stuart, B. Ni, and S.B. Sinnott, "A second-generation reactive empirical bond order (REBO) potential energy expression for hydrocarbons," *J. Phys. Condens. Matter*, **14**, 783-802 (2002). <https://doi.org/10.1088/0953-8984/14/4/312>
- [28] H.Y. Ammar, and H.M. Badran, "Ti deposited C<sub>20</sub> and Si<sub>20</sub> fullerenes for hydrogen storage application, DFT study," *International journal of hydrogen energy*, **46**, 14565-14580 (2021). <https://doi.org/10.1016/j.ijhydene.2021.01.231>
- [29] R. Rahimi, S. Kamalinahad, and M. Solimannejad, "Adsorption of rare gases on the C<sub>20</sub> nanocage: A theoretical investigation," *Mater. Res. Express*, **5**(3), 035006 (2018). <https://doi.org/10.1088/2053-1591/aab0e3>
- [30] Y.S. Al-Hamdani, D. Alfe, O.A. von Lilienfeld, and A. Michaelides, "Tuning dissociation using isoelectronically doped graphene and hexagonal boron nitride: Water and other small molecules," *J. Chem. Phys.* **144**, 154706 (2016). <https://doi.org/10.1063/1.4945783>

#### МОДЕЛЮВАННЯ ПРОЦЕСІВ ВЗАЄМОДІЇ ФУЛЕРЕНУ C<sub>20</sub> З ГРАФЕНОМ

Ішмумін Д. Ядгаров<sup>а</sup>, Фарід Ф. Умаров<sup>б</sup>, Асрорідін С. Косимов<sup>с</sup>, Хаїтмурод І. Джабборов<sup>д</sup>, Шодібек Ю. Амінов<sup>с</sup>

<sup>а</sup> Інститут іонно-плазмових і лазерних технологій імені У.А. Аріфова, Академія наук Узбекистану,  
Ташкент, 100125 Узбекистан

<sup>б</sup> Казахсько-Британський технічний університет, Алмати, 050000, Казахстан

<sup>с</sup> Термезький державний університет, Термез, 190111 Узбекистан

<sup>д</sup> Ташкентський університет інформаційних технологій імені Мухаммеда аль-Хорезмі,  
Ташкент, 100084 Узбекистан

Графен, вуглецевий лист товщиною в один атом, з атомами вуглецю, розташованими у двовимірній стільниковій конфігурації, має ряд цікавих властивостей. Фулерени є перспективним матеріалом для створення електроактивних елементів в сонячних елементах і активних шарів в тонкоплівкових органічних транзисторах. Методом мінімізації енергії з потенціалом Бреннера другого покоління (REBO) побудовано комп'ютерну модель молекули фулерену C<sub>20</sub>. Побудовано комп'ютерну модель «нескінченного» бездефектного графену, призначену для розгляду процесу адсорбції молекули фулерену C<sub>20</sub> на його поверхні. Для дослідження процесу адсорбції комп'ютерні моделі фулерену та «нескінченного» графену були наближені до необхідної відстані з іншим набором геометричного розташування фулерену відносно поверхні графену. Встановлено, що адсорбція фулерену C<sub>20</sub> на поверхні графену може здійснюватися трьома різними способами, які відрізняються кількістю взаємодіючих атомів фулерену і графену. Розраховано енергію зв'язку та довжину адсорбції для молекул фулерену C<sub>20</sub>, адсорбованих на поверхні графену різними способами. Виявлено шлях адсорбції, що відповідає найбільшій енергії зв'язку і найменшій довжині адсорбції.

**Ключові слова:** молекула фулерену; графен; адсорбція; моделювання; потенціал Бреннера

## AB-INITIO INVESTIGATION INTO THE PHYSICAL CHARACTERISTICS OF CuInSe<sub>2</sub> AND CuInTe<sub>2</sub> COMPOUNDS

✉ **Yousra Megdoud**<sup>b,c</sup>, ✉ **Yamina Benkrima**<sup>a\*</sup>, ✉ **Redha Meneceur**<sup>f</sup>, **Latifa Tairi**<sup>c,d</sup>, ✉ **Abdelghani Lakel**<sup>e</sup>, **Sebti Ghemid**<sup>e</sup>, ✉ **Hocine Meradji**<sup>e</sup>

<sup>a</sup> Ecole Normal Supérieur de Ouargla, 30000 Ouargla, Algeria

<sup>b</sup> Institute of Sciences, University Center of Tipaza, Morsli Abdallah, Algeria

<sup>c</sup> LPR Laboratory, Département of Physics, Faculty of Science, Badji Mokhtar –Annaba-Address, Algeria

<sup>d</sup> Research Center in Industrial Technologies, CRTI, P.O. Box 64, Cheraga16014 Algiers Algeria

<sup>e</sup> Laboratory of Metallic and Semiconducting, Materials, University of Biskra, BP 145 RP, 07000, Biskra, Algeria

<sup>f</sup> Unit for the Development of Renewable Energies in Arid Zones (UDERZA), El Oued University, Algeria

\*Corresponding Author e-mail: [b-amina1@hotmail.fr](mailto:b-amina1@hotmail.fr)

Received: September 3, 2023; revised November 05, 2023; accepted November 10, 2023

In this study, an analysis of chalcopyrite compounds CuInTe<sub>2</sub> and CuInSe<sub>2</sub> is presented, with a focus on their electronic, structural, optical, and thermal properties. The full-potential linearized augmented plane wave (FP-LAPW) method is employed for the investigation of these properties, based on a first-principles approach rooted in density functional theory (DFT). Two distinct approximations for the exchange and correlation potential, namely the WC-GGA and mBJ-GGA approximations, are considered in our calculations to ensure a robust and accurate examination of the materials under scrutiny. The findings obtained closely align with previously established theoretical and experimental data, thereby validating the reliability of our computational methodology. It is noteworthy that a novel dimension is introduced by this study, as the influence of both pressure and temperature on the thermal parameters of CuInTe<sub>2</sub> and CuInSe<sub>2</sub> compounds is explored. This facet of the research is distinguished by its innovative nature, as there is no prior record, to the best of our knowledge, of a similar analysis in the existing literature. The thermal properties are deemed of paramount significance, particularly in the context of crystal growth process optimization and the prediction of performance under extreme thermodynamic conditions.

**Keywords:** Photovoltaic; Chalcopyrite; FP-LAPW; Bandgap; Thermal properties

**PACS:** 73.20.At, 78.20.Ci

### 1. INTRODUCTION

In the domain of optoelectronics, two principal facets of material interest reside in the domains of light emission and the manifestation of the photovoltaic or photoelectric effect [1]. For applications encompassing luminous sources such as light-emitting diodes or laser diodes, an inherent prerequisite dictate that the material in question assume the role of a direct gap semiconductor. The wavelength of emitted light, and by extension, its color, intimately hinges upon the energy gap characterizing the constituents forming the p-n junction. Amidst the pantheon of energy sources, the sun emerges as the preeminent fount, characterized by its unparalleled abundance and unwavering reliability [2]. Consequently, the focal point has gravitated toward the development of solar energy converters through photovoltaic mechanisms. For materials earmarked for integration into solar cells, a pivotal criterion necessitates the possession of a high absorption coefficient, thereby favoring a substantial direct gap, ideally in proximity to 1.4 eV, to adeptly capture light across the visible spectrum [3]. Historically, the pervasive impediments of high costs and diminished efficiency have relegated solar cells to the fringes of ubiquitous everyday utility. Nevertheless, the evolving landscape has witnessed a proliferation of inquiry into novel materials primed for photovoltaic technology, coupled with advancements in solar cell fabrication techniques. Conventional stalwarts such as amorphous or crystalline silicon and cadmium telluride (CdTe) have shared the limelight alongside chalcogenides I-III-VI<sub>2</sub> in the realm of photovoltaic applications. Notably, a distinct focus has been channeled towards the intensive investigation of CuInSe<sub>2</sub> and CuInTe<sub>2</sub>, endowed with high capacitance, and thus, proficient in light absorption [4]. Facilitated by electrochemical depositions, these compounds are predominantly harnessed in solid solution synergy with CuInSe<sub>2</sub> and CuInTe<sub>2</sub>, fostering the creation of thin film solar cells with commendable efficiencies scaling up to 20% [5]. Engendering further intrigue is the quest for alternative materials that not only mirror these properties but concurrently feature an optimal energy gap to optimize device efficiency. One promising avenue lies in the realm of II-IV-V<sub>2</sub> compounds, which serve as ternary analogs to binary III-V configurations, wherein the group III element undergoes substitution with constituents from groups II and IV. In the majority of III-V semiconductors, such substitutions invariably impart distortions upon the 1×1×2 super cell of the sphalerite structure, concomitantly recognized as the chalcopyrite structure, akin to CuInSe<sub>2</sub>. In such configurations, the lattice parameter ratio c/a typically deviates slightly from 2, and the distortion parameter u diverges from the idealized value of 1/4. These deviations bestow fresh fundamental attributes upon materials, encompassing but not confined to facets of electronics, transport, and optics [6].

**Cite as:** Y. Megdoud, Y. Benkrima, R. Meneceur, L. Tairi, A. Lakel, S. Ghemid, H. Meradji, East Eur. J. Phys. 4, 231 (2023), <https://doi.org/10.26565/2312-4334-2023-4-29>

© Y. Megdoud, Y. Benkrima, R. Meneceur, L. Tairi, A. Lakel, S. Ghemid, H. Meradji, 2023; CC BY 4.0 license



Within the expanse of II-IV-V2 semiconductors, a profusion of possibilities awaits exploration, predicated upon the judicious selection of elements from groups II, IV, and V. Regrettably, scant literature dedication is afforded to chalcopyrites encompassing copper, with CuInSe<sub>2</sub> and CuInTe<sub>2</sub> comprising the sole subjects of inquiry. Moreover, an observable lacuna exists, bereft of both experimental and theoretical insights pertaining to Cu-In-V2 compounds, notwithstanding the promise they hold for structural, electronic, or optical investigations [7-9].

From the array of materials under consideration, our focus has been directed toward the CuInX<sub>2</sub> compounds, where X represents selenium (Se) or tellurium (Te). Notably, these compounds manifest themselves in the crystalline chalcopyrite phase [10, 11]. It is imperative to underscore that the compounds under investigation in this study have commanded attention in prior research endeavors. R.C. Gupta et al. [12] delved into the mechanical stability parameters characterizing chalcopyrites and pnictides, with a particular emphasis on their relevance to optoelectronic materials. In a separate endeavor, Hao Yu et al. [13] embarked on an integrated exploration, combining experimental methodologies with first-principles investigations, thereby unraveling the intricacies of lattice dynamics within thermoelectric CuInTe<sub>2</sub>. Further contributions from the scientific community include the work of Guanwei Jia et al. [14], who scrutinized the synthesis of CdS/CuInSe<sub>2</sub> and CuInTe<sub>2</sub>/CuInSe<sub>2</sub> nanorod heterostructures through catalyst-assisted solution-liquid-solid techniques.

Temperature-dependent phonon anharmonicity and thermal transport properties in CuInTe<sub>2</sub> were scrutinized by Hao Yu, et al. [15], providing invaluable empirical insights. Notably, theoretical examinations conducted by E. Mazalan, et al. [16] enriched our understanding, focusing on the crystal structures and bulk modulus of CuInX<sub>2</sub> compounds, where X encompasses sulfur (S), selenium (Se), and their binary combination (S-Se), vital in the context of solar cell absorbers.

The structure of this paper is delineated as follows: "Section 2" expounds upon the CuInSe<sub>2</sub> and CuInTe<sub>2</sub> ternary compounds, elucidated via the utilization of the Wien2K code, rooted in the density functional theory (DFT). The ensuing "Section 3" derives implications for the utilization of these materials within the realm of photovoltaic applications, predicated upon the results gleaned. Finally, "Section 4" culminates in a comprehensive summary of the paper's conclusions, accompanied by the listing of the corresponding author.

## 2. DETAILS OF CALCULATIONS

In the scope of this investigation, we conducted initial-principle computations, employing the theoretical foundation of density functional theory (DFT) and adopting the Full-Potential Linearized Augmented Plane Wave (FP-LAPW) methodology. These calculations were executed utilizing the computational code WIEN2k. [17,20].

In order to determine the overall energy properties of the crystalline materials under investigation, a deliberate selection was made to evaluate the exchange-correlation energy [21] and potential functional elements using WC-GGA (Wu-Cohen Generalized Gradient Approximation) approach [21]. This method guarantees a thorough comprehension of the electronic attributes of the materials. Furthermore, in pursuit of greater precision regarding the structure of the electronic band and the values of band gap energy, an innovative strategy was adopted. Specifically, the TB-mBJ exchange potential was harnessed, in conjunction with GGA for the correlation contribution [22,23]. This amalgamation of methodologies is instrumental in elucidating the electronic behavior of the compounds under investigation with heightened accuracy. The computational methodology encompassed the partitioning of the crystal unit cell into distinct regions, namely the (IR) and the atomic spheres mimicking muffin-tin (MT) geometries, precisely centered around atomic positions. Within the interstitial region, the basis set was systematically expanded using plane waves to furnish an elaborate depiction of electronic characteristics in this domain. Conversely, within the MT spheres, the basis set was formulated as a linear amalgamation of atomic-like wave functions intricately associated with spherical harmonics. In addressing the issue of charge density and potential treatment within the unit cell's distinct regions, it is essential to highlight our methodology. A key aspect involves setting specific parameters for truncating spherical harmonics. In this regard, we opted for values of  $R_{MT}K_{max} = 8$ , with  $K_{max}$  representing the maximum value of the reciprocal lattice vector found within the first Brillouin zone of reciprocal space. Simultaneously,  $R_{MT}$  signifies the average radii encompassing the atomic-like spheres situated at atomic nuclei. The consideration of spherical harmonics expansion encompassed the maximum angular momentum value, signified as  $l_{max} = 10$ . It is pivotal to underscore that no shape approximations were invoked throughout this computational regimen. Consequently, a comprehensive consideration of all electrons, inclusive of core electrons, was accommodated, warranting the nomenclature "all electrons/full potential methods." In addition, the treatment of core electrons was administered in a fully relativistic manner. To capture the relativistic effects, the computational protocol entailed considering the spherically symmetric potential and numerically solving the radial Dirac equation. In stark contrast, valence and semi-core states were treated in a scalar relativistic fashion. To ensure not only reasonable convergence but also the prevention of charge leakage from the core, prudent choices were made regarding the muffin tin (MT) radii for distinct atomic species. Specifically, the selected values for Cu, In, Se, and Te atoms were set at 2.0 atomic units (u.a), exemplifying an approach to encompassing core electron interactions. Furthermore, within the framework of Brillouin zone integration for total energy calculations, a selection of 99-k-points within the irreducible part of the Brillouin zone was made to substantiate the integrity of the computations.

In pursuit of achieving convergence within the self-consistent iteration process, the maximum value of  $G_{max}$  was systematically set at  $12 (Ry)^{1/2}$  for the Fourier expansion of the charge density. This parameterization collectively yielded total energy calculations with convergence levels comfortably below  $10^{-4}$  Ry.

### 3. RESULTS AND DISCUSSION

#### 3.1. Structural properties

This section directs its attention to investigating the structural properties of the compounds under study, specifically  $\text{CuInSe}_2$  and  $\text{CuInTe}_2$ . These compounds are categorized within the I-III-VI<sub>2</sub> family, representing a superlattice structure that originates from the ZnS phase. In this arrangement, the group II elements found in ZnS, such as Zn ions, are systematically and interchangeably substituted with group I transformation metal ions like Cu, along with group III ions, which are common semiconductors. Consequently, each anion, whether Te or Se, is intricately coordinated by two Cu ions and two In cations, as illustrated in Figure 1.

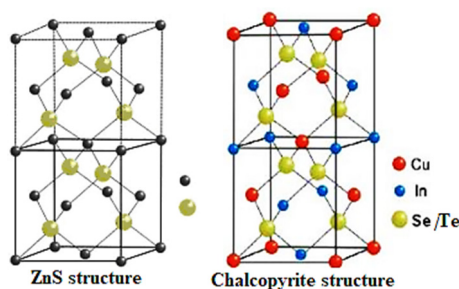


Figure 1. Crystalline structure of  $\text{CuInSe}_2$  and  $\text{CuInTe}_2$

Significantly, a four anions tetrahedral arrangement surrounds each Cu and In cation, mirroring the structural motif of ZnS. However, the systematic interchange of In and Cu cations within the square lattice introduces two notable structural deviations compared to the zinc-blende phase.

The first of these alterations manifests as a tetragonal distortion along the (001) direction, marked by a distortion parameter  $\eta = c/2a$  [58], where  $\eta$  deviates from unity. This distortion arises due to dissimilar ionic radii between Cu and In cations.

The second structural modification arises from the presence of two distinct chemical bonds with unequal bond lengths within the tetrahedral framework, as depicted in Figure 1 (additional details provided in the supplementary materials). This complexity introduces a secondary form of distortion known as tetrahedral distortion.

In this distortion, Te and Se atoms are displaced from their idealized tetrahedral positions, defined as (1/4, 1/4, 1/4), thereby introducing an additional free parameter denoted as "u" within the chalcopyrite phase. It is noteworthy that in the zinc-blende phase, this parameter u remains fixed at 0.25. Here, u becomes intricately tied to the internal coordinates governing the positions of Te and Se anions.

These structural modifications result in a shift in the space group from  $F4\bar{3}m$  (Space group of Zinc Blende structure) [58] to  $I4\bar{2}d$  (Space group of Chalcopyrite structure) [58]. Within the chalcopyrite structure of these compounds, the Cu, In, Te, and Se atoms assume specific positions: (0, 0, 0), (0, 0, 0.5), and (u, 0.25, 0.125), respectively. To determine the equilibrium structural parameters of  $\text{CuInSe}_2$  and  $\text{CuInTe}_2$  using the WIEN2K package [17,20], our methodology encompassed several key steps. Initially, we computed the energy as a function of volume while maintaining the c/a ratio constant to ascertain the equilibrium volume. Subsequently, the c/a ratio was optimized by assessing its relationship with energy while maintaining the equilibrium volume established in the first phase. In the final phase, we minimized the parameter "u" using the Mini procedure, an integral component of WIEN2k [17,20]. Upon achieving minimized values for volume, c/a ratio, and "u," we obtained the optimal curve illustrating the total energy versus volume (See Fig 2).

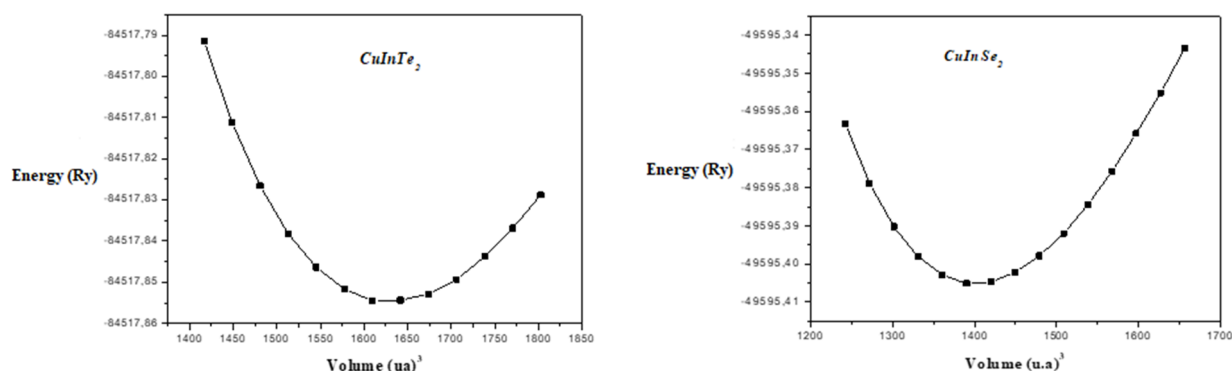


Figure 2. Total energy versus volume calculated for compounds  $\text{CuInSe}_2$  and  $\text{CuInTe}_2$

Using the Murnaghan equation of state (EOS) [24], we performed a curve fitting on this data. This allowed us to derive bulk modulus (B) and the equilibrium lattice constants (a and c). The calculated for the investigated compounds are presented in Table 1, alongside theoretical and other experimental results [12-16].

**Table 1.** Elastic Lattice parameters (a,c) (Å), compressibility modulus B (GPa), and its derivative B' of CuInSe<sub>2</sub> and CuInTe<sub>2</sub> compounds

Compounds		a (Å)	c (Å)	c/a	B(GPa)	B'
CuInSe <sub>2</sub>	<b>Our calcs</b>	<b>5.84</b>	<b>11.671</b>	<b>1.99</b>	<b>53.8357</b>	<b>5.1027</b>
	<b>Exp</b>	5.782 <sup>a</sup>	11.620 <sup>a</sup>	2.009	-	-
		5.78 <sup>b</sup>	11.62 <sup>b</sup>	2.010	-	-
		5.782 <sup>c</sup>	11.619 <sup>c</sup>	2.009	-	-
	<b>Other calcul</b>	5.836 <sup>d</sup>	11.657 <sup>d</sup>	1.997	54.236 <sup>d</sup>	5.364 <sup>d</sup>
		5.833 <sup>e</sup>	11.735 <sup>e</sup>	1.998	53.987 <sup>e</sup>	4.9875 <sup>e</sup>
CuInTe <sub>2</sub>	<b>Our calcs</b>	<b>6.221</b>	<b>12.463</b>	<b>2.003</b>	<b>50.3970</b>	<b>4.8513</b>
	<b>Exp</b>	6.197 <sup>f</sup>	12.453 <sup>f</sup>	2.009	-	-
		6.256 <sup>g</sup>	12.531 <sup>g</sup>	2.003	-	-
	<b>Other calcul</b>					

<sup>a</sup>Ref [8], <sup>b</sup>Ref [9], <sup>c</sup>Ref [10], <sup>d</sup>Ref [11], <sup>e</sup>Ref [12] <sup>f</sup>Ref [13] <sup>g</sup>Ref [14]

Notably, our findings obtained with the WC-GGA approximation closely align with experimental data and exhibit a higher degree of agreement compared to previous theoretical calculations. This concordance underscores the reliability of our theoretical results and instills confidence in the subsequent property calculations, given that these structural parameters serve as a foundational component of each subsequent computation. It is worth noting that the lattice parameters (a and c) exhibit a rise from CuInTe<sub>2</sub> to CuInSe<sub>2</sub>. This increase in bond lengths corresponds to a weakening of bond forces, evident in the decreased bulk modulus ( $B_{\text{CuInTe}_2} < B_{\text{CuInSe}_2}$ ). Importantly, the increase in lattice constants for these compounds from CuInTe<sub>2</sub> to CuInSe<sub>2</sub> is concomitant with a reduction in bulk modulus. The observed trend corresponds to the established relationship between bulk modulus (B) and lattice constant, as expressed by  $B \propto V^{-1}$ , with V representing the volume of the primitive cell [25].

### 3.2. Electronic properties

This section delves into an exploration of the electronic characteristics of CuInSe<sub>2</sub> and CuInTe<sub>2</sub>, with a primary focus on the computation of energy band structures. Our calculations encompass the band structures of these compounds along high-symmetry lines within the first Brillouin zone, employing both the WC-GGA and mBJ approximations. As a representative illustration, Figure 3 showcases the computed band structures for CuInSe<sub>2</sub> and CuInTe<sub>2</sub>.

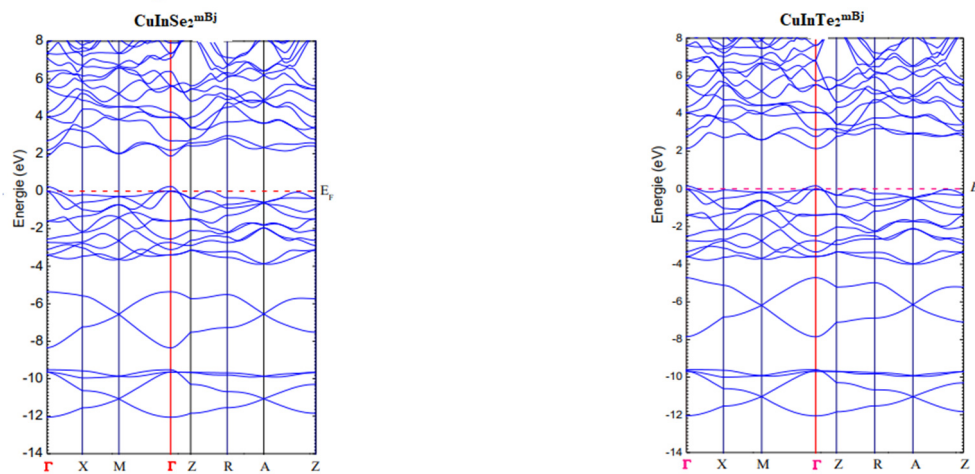


**Figure 3.** Calculated band structures of CuInSe<sub>2</sub> and CuInTe<sub>2</sub> compounds using the mBJ approximation

Across all compounds under investigation, a noteworthy consistency emerges: both the valence band maximum and the conduction band minimum are consistently situated at the  $\Gamma$  point. This arrangement engenders a direct energy gap for both CuInSe<sub>2</sub> and CuInTe<sub>2</sub>. The specific values of the obtained band gaps are meticulously documented in Table 2, enabling a comprehensive comparison with preceding theoretical and experimental outcomes [12-16]. Crucially, the electronic band structures derived from the mBJ scheme bear qualitative resemblance to those obtained via the WC-GGA approximation. However, it is the quantitative aspect that truly sets them apart. The band gap values yielded by the mBJ approach significantly outperform those derived from the WC-GGA, drawing them closer to experimental data. It is widely recognized that mBJ represents a substantial enhancement over GGA concerning the accurate prediction of band gaps.

**Table 2.** Band gap value  $E_g$  for CuInSe<sub>2</sub> and CuInTe<sub>2</sub> with WC-GGA approximation and mBj

	$E_g$ (eV) ( $\Gamma - \Gamma$ )			
	Our calculus		Experimental	Other calculus
	WC-GGA	mBj		
CuInSe <sub>2</sub>	0.75	1.03	1.01 <sup>a</sup>	0.99 <sup>a</sup>
CuInTe <sub>2</sub>	0.66	0.98	0.96 <sup>b</sup>	1.05 <sup>b</sup>

<sup>a</sup>Ref [15], <sup>b</sup>Ref [16]

The mBJ approximation constitutes an enhancement in the treatment of potential exchange through the incorporation of a semi-local orbital [26]. Furthermore, hybrid functionals like B3PW91 [27] partially rectify the self-interaction error by introducing nonlocal Hartree-Fock (HF) exchange. It is worth noting that a consistent reduction in the bandgap is observed as the transition is made from CuInSe<sub>2</sub> to CuInTe<sub>2</sub>, a trend that aligns with experimental observations [12-16]. This trend in bandgap reduction can be comprehended in light of our earlier analysis of structural characteristics. The expansion of lattice parameters (a, c) upon the substitution of Te for Se leads to a concomitant decrease in the bulk modulus (B) from CuInSe<sub>2</sub> to CuInTe<sub>2</sub>, as visually depicted in Figure 3. These structural variations manifest as a reduction in the bandgap from CuInSe<sub>2</sub> to CuInTe<sub>2</sub>. Additionally, the disparity in electronegativity between Te and Se further contributes to a subtle reduction in the bandgap.

### 3.3. Optical properties

The optical properties of solids provide valuable insights into the intricate interactions between electromagnetic waves and the electrons and ions within solid materials. At a microscopic level, these interactions can be precisely elucidated. However, to offer a macroscopic and quantitative description of these phenomena, the dielectric function  $\epsilon(\omega)$  becomes indispensable. Mathematically,  $\epsilon(\omega)$  is defined as  $\epsilon(\omega) = \epsilon_1(\omega) + i\epsilon_2(\omega)$  [28-31]. Here,  $\epsilon_2(\omega)$  is intricately linked to the electronic transitions responsible for absorption processes and can be meticulously computed by examining the momentum matrix elements that connect occupied and unoccupied electronic states [32]. On the other hand,  $\epsilon_1(\omega)$  is intimately tied to polarization and can be derived from the imaginary part  $\epsilon_2(\omega)$  through the well-established Kramers-Kronig relationships [33,34]. Using established mathematical relations, it's important to emphasize that one can directly derive all other optical constants, such as the absorption coefficient  $\alpha(\omega)$  and the refractive index  $n(\omega)$ , from the components of the dielectric function.

Within the context of this research, the primary objective is to conduct an investigation into the optical properties of CuInSe<sub>2</sub> and CuInTe<sub>2</sub> utilizing the mBJ approach, with the aim of providing a comprehensive understanding of their significance in photovoltaic and other optoelectronic applications [21]. Notably, these materials exhibit anisotropy, originating from the electric field orientation perpendicular to the Oz axis ( $\epsilon_{xy}$ ), which signifies the average of spectra along the x and y directions, as well as the electric field aligned parallel to the Oz axis ( $\epsilon_z$ ). To characterize this anisotropy, the following relation is employed to determine the average value between the dielectric components ( $\epsilon_{\perp c}$ ) and ( $\epsilon_{\parallel c}$ ):  $\epsilon = (2\epsilon_{\perp c} + \epsilon_{\parallel c})/3$ . Importantly, it should be noted that this relation is equally applicable to other optical parameters.

#### 3.3.1. The Dielectric Function's Real Part

Figure 4 showcases the real part of the dielectric function,  $\epsilon_1(\omega)$ , for CuInSe<sub>2</sub> and CuInTe<sub>2</sub> compounds, covering photon energies up to 40 eV.

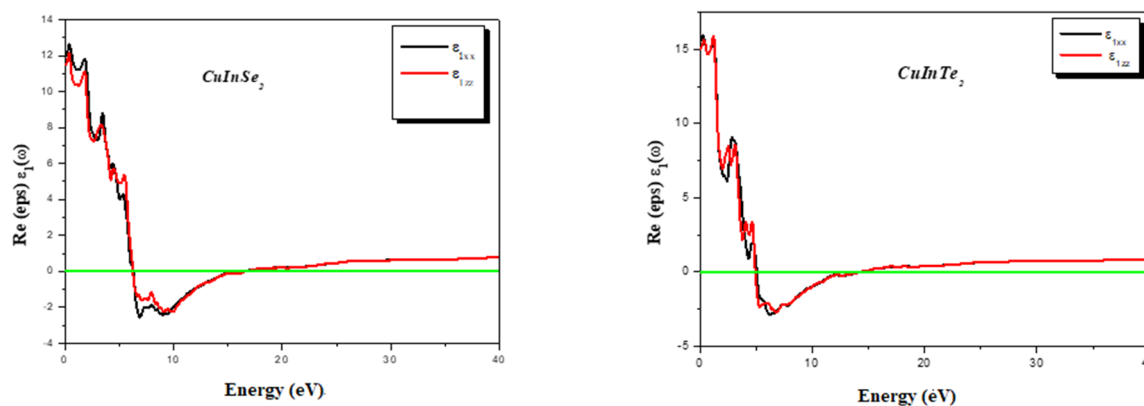


**Figure 4.** Calculated real parts of the complex dielectric constant for CuInSe<sub>2</sub> and CuInTe<sub>2</sub> compounds

These two compounds exhibit similar spectra, with an important observation that they both display isotropic behavior at lower energies. Notably, as depicted in Figure 4, the energy of the primary peak decreasing from 1.80 eV for CuInSe<sub>2</sub> to 1.55 eV for CuInTe<sub>2</sub>. This shift in energy can be attributed to the electronic band structures of these compounds. Specifically,  $\epsilon_1(\omega)$  reaches zero energy in the ultraviolet region, signifying the absence of dispersion [35]. Beyond this point, the spectrum progressively falls below unity in the ultraviolet (UV) range, ultimately surpassing unity at approximately 11.87 eV (CuInSe<sub>2</sub>) and 15.08 eV (CuInTe<sub>2</sub>). These frequencies correspond to the plasma frequency  $\omega_p$  and are in alignment with the energy of the primary peak of energy loss [36]. Within the energy range where  $\epsilon_1(\omega) < 0$ , electromagnetic waves do not propagate, leading to a significant increase in the reflectivity of these compounds and inciting a metallic behavior [37]. This observation suggests that the investigated compounds (CuInSe<sub>2</sub> and CuInTe<sub>2</sub>) could be employed for shielding against high-frequency electromagnetic waves [38]. In Table 3, we present a comprehensive summary of the static dielectric characteristics for the compounds under investigation, complemented by pertinent theoretical and experimental findings.

**Table 3.** Static Dielectric Function ( $\epsilon_1(0)$ ) and Static Refractive Index ( $n(0)$ ) Calculations for CuInSe<sub>2</sub> and CuInTe<sub>2</sub> Compounds

	n (0)		$\epsilon_1(0)$	
	Nos calcul WC-GGA	Autre calculs	Nos calcul WC-GGA	Autre calculs
CuInSe <sub>2</sub>	3.43	3.65	11.38	11.23
CuInTe <sub>2</sub>	3.87	3.95	15.01	15.23

<sup>a</sup>Ref [21]

It's important to highlight that  $\epsilon_1(0)$  serves as an insightful metric, representing the electronic contribution to the static dielectric constant. These metric sheds light on the strength of interactions among electronic states within the valence and conduction bands when subjected to an external electric field. As a result,  $\epsilon_1(0)$  is intricately linked to the energy gap value inherent to these compounds. Examining Table 3, it becomes evident that  $\epsilon_1(0)$  increases from CuInSe<sub>2</sub> to CuInTe<sub>2</sub>, a trend arising from the decreasing energy gap as one progresses from Se to Te. This relationship between the energy gap and  $\epsilon_1(0)$  is governed by Penn's relation, which states that  $\epsilon_1(0) \approx 1 + (\hbar\omega_P / E_g)$  [39], with  $\hbar\omega_P$  representing the valence electron plasmon frequency. It's worth highlighting that the obtained values for  $\epsilon_1(0)$  are consistent with prior theoretical findings. Although there is limited experimental data available for comparison, except for CuInTe<sub>2</sub> [40-41], our results closely align with the experimental work conducted by Wassim et al. [42] and Riede et al. [43].

### 3.3.2. The Dielectric Function's Imaginary Part

The dielectric function encompassing absorption phenomena, is displayed up to 40 eV in Figure 5. Importantly, it should be noted that consideration of indirect band transitions was intentionally omitted in our optical calculations. This exclusion is rooted in the fact that the influence of phonon scattering on dielectric screening, associated with indirect band transitions, is not significantly affected [44]. The critical energy point in  $\epsilon_2(\omega)$ , denoting the fundamental absorption edge, is observed at approximately 0.202 for CuInSe<sub>2</sub> and 0.485 for CuInTe<sub>2</sub>. Within the context of this investigation, a noteworthy correlation emerges between the determined mBJ bandgap values for the compounds under scrutiny and the absorption edge. This absorption edge, in perfect accordance with the band structure, serves as the starting point for direct interband transitions at the  $\Gamma$  point. These transitions involve the highest occupied states of the valence band (BV) transitioning to the lowest unoccupied states of the conduction band (BC). Beyond the edge of absorption, as depicted in Figure 5,  $\epsilon_2(\omega)$  undergoes a rapid increase. This increase is a consequence of the multitude of interband transitions that are present in the system. The principal peaks originate from direct interband transitions occurring between distinct levels within the conduction and valence bands. Notably, the energies associated with the maxima of these peaks are displaced towards lower values, specifically 5.89 eV for CuInSe<sub>2</sub> and 1.423 eV for CuInTe<sub>2</sub>. This shift can be attributed to the differences in the underlying band structures of these two compounds.

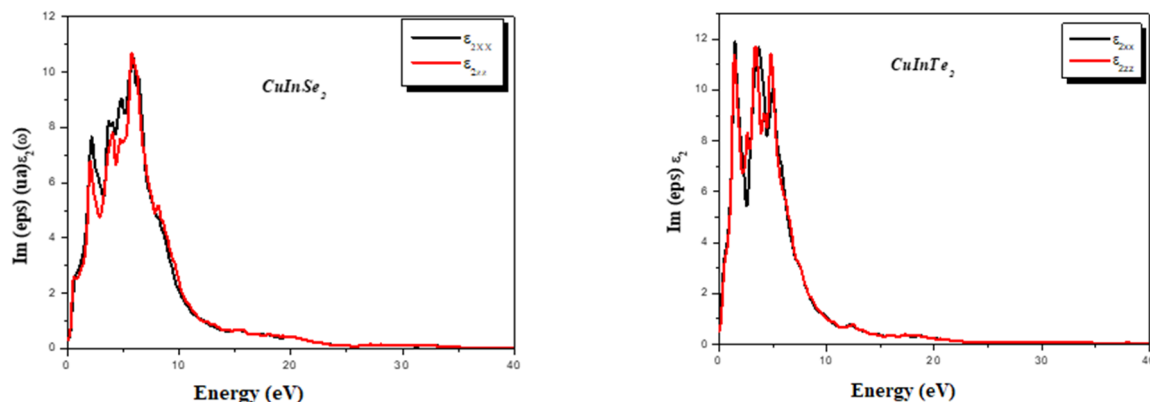


**Figure 5.** Computed Imaginary Parts of the Complex Dielectric Constant for CuInSe<sub>2</sub> and CuInTe<sub>2</sub> Compounds

### 3.3.3. The Refractive index

The refractive index [45], denoted as  $n(\omega)$ , represents a dimensionless number that provides a macroscopic depiction of the material's polarization response to incident electromagnetic waves, despite its microscopic origins. This refractive index is derived from the values of  $\epsilon_1(\omega)$  and  $\epsilon_2(\omega)$  [45]. Figure 6 illustrates the refractive indices for the compounds under investigation. It is noteworthy that  $n(\omega)$  exhibits the same isotropic behavior as  $\epsilon_1(\omega)$ . The static refractive index values [46], determined using the equation  $n(0) = \sqrt{\epsilon_1(0)}$  [46], closely align with those directly obtained from the refractive index plots for the compounds. Specifically, the values are 3.51 for CuInSe<sub>2</sub> and 4.03 for CuInTe<sub>2</sub>, as detailed in Table 3. Furthermore, Table 3 highlights that the static values of  $n(0)$  increase as we transition from CuInSe<sub>2</sub> to CuInTe<sub>2</sub>. This behavior mirrors the increase observed in  $\epsilon_1(0)$ , attributable to the diminishing band-gap ( $E_g$ ). According to Penn's relation, the band-gap ( $E_g$ ) and, subsequently,  $n(0)$  are inversely proportional [47-49].

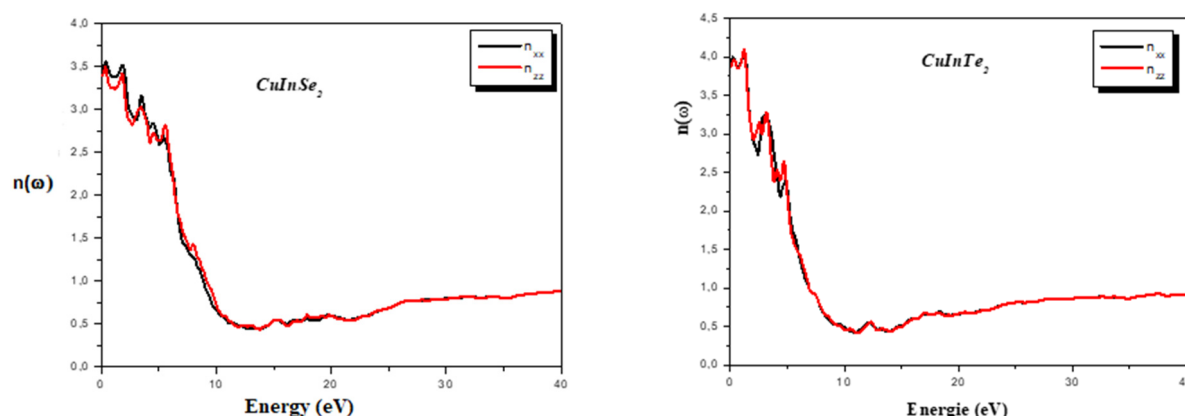


Figure 6. Variation of Refractive Index  $n(\omega)$  for CuInTe<sub>2</sub> and CuInSe<sub>2</sub> Compounds

Our determined refractive indices closely align with prior theoretical investigations, underlining the consistency of our findings. An intriguing characteristic of chalcopyrite compounds is their inherent anisotropy, which results in birefringence. This birefringence imparts exceptional nonlinear optical properties to our studied compounds, enabling phase matching through a simple adjustment of the crystal's orientation concerning the incident beam [49]. This unique attribute positions our compounds ideally for applications in second harmonic generation (SHG) and optical parametric oscillation (OPO) [48, 49]. These favorable attributes lay a strong foundation for the potential development of high-performance laser systems utilizing our researched compounds.

### 3.3.4. Absorption coefficient

In the realm of photovoltaic conversion, photoconductivity, which involves the generation of charge resulting from incident radiation absorption, plays a pivotal role. The material's ability to allow light of a specific wavelength to penetrate before absorption hinges on the absorption coefficient—a crucial parameter for evaluating the potential of our compounds in visible spectrum photovoltaic conversion [58].

To investigate the suitability of our compounds for photovoltaic applications in the visible spectrum, the absorption coefficient  $\alpha(\omega)$  up to 40 eV have been depicted in Figure 7. These optical features can be deduced from the real and imaginary components of the dielectric function [49].

In Figure 7, the absorption  $\alpha(\omega)$  threshold, indicating the direct band gap ( $E_g$ ), is found to be approximately 0.30 eV for CuInSe<sub>2</sub> and 0.09 eV for CuInTe<sub>2</sub>. Based on these findings, it can be inferred that CuInTe<sub>2</sub> and CuInSe<sub>2</sub> compounds are better suited for harnessing the visible spectrum for photovoltaic conversion. Our compounds exhibit transparency and low reflectivity below the absorption threshold.

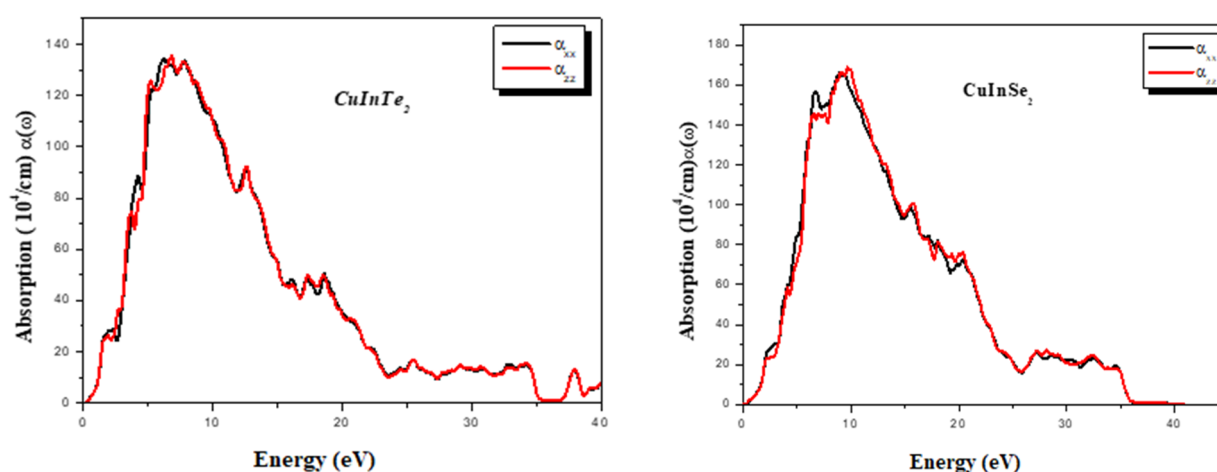


Figure 7. Calculated absorption coefficient  $\alpha(\omega)$  versus energy (eV) for CuInSe<sub>2</sub> and CuInTe<sub>2</sub> compounds.

### 3.3.5. The Reflectivity spectrum

Figure 8 portrays the reflectivity behavior of our investigated compounds across an energy spectrum spanning 0-40 eV. Notably, the curves exhibit prominent peaks at 48% around 9.84 eV for CuInSe<sub>2</sub> and 49% at 8.02 eV for CuInTe<sub>2</sub>. These findings strongly indicate the potential suitability of our ternary compounds for applications in the visible light range.

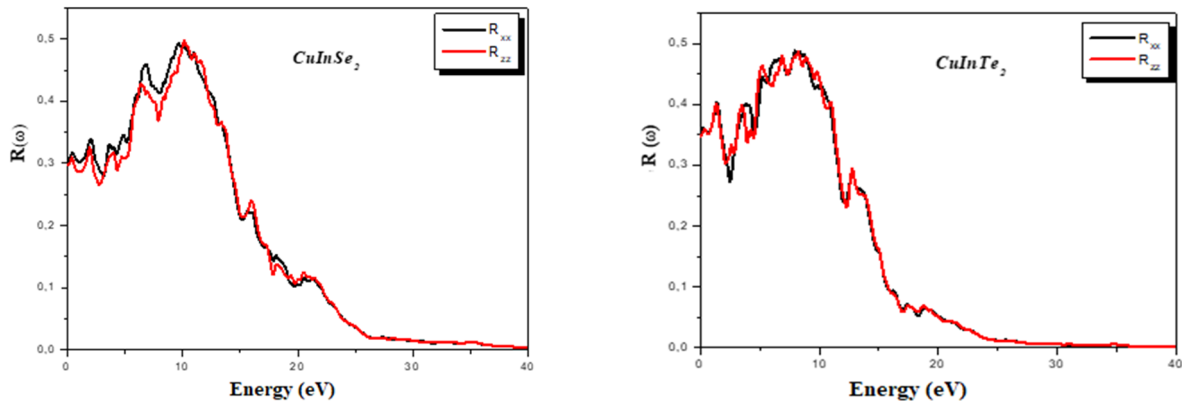


Figure 8. Reflectivity  $R(\omega)$  Variation for  $\text{CuInSe}_2$  and  $\text{CuInTe}_2$  Compounds

### 3.4. Thermal properties

The investigation of thermal properties is fundamental in the realm of solid-state physics and various technological applications. Investigating how materials respond to high-pressure or high-temperature conditions allows us to gain insights into their unique behavior. In our research, we delve into the impact of temperature on the thermal properties of semiconductor materials, specifically  $\text{CuInSe}_2$  and  $\text{CuInTe}_2$ . In pursuit of this objective, we utilize a Gibbs program [50] built upon the quasi-harmonic Debye model. This approach empowers us to delve into the thermal characteristics of these compounds. The non-equilibrium Gibbs function, denoted as  $G^*(V, P, T)$ , is formulated as the sum of various components. These components encompass the total energy  $E(V)$ , the imposition of hydrostatic pressure  $PV$ , and the vibrational Helmholtz free energy  $A_{\text{vib}}$ .

$$G^*(V, P, T) = E(V) + PV + A_{\text{vib}}(T, \theta(V)) \quad (1)$$

Utilizing Debye's model for the phonon density of states, we can represent the vibrational term ( $A_{\text{vib}}$ ) as follows: [51, 52]:

$$A_{\text{vib}}(\theta, T) = nk_{\beta} \left[ \frac{9\theta}{8T} \right] + 3 \ln(1 - e^{-\theta/T}) D(\theta/T) \quad (2)$$

Here,  $D(\theta/T)$  and  $n$  denote the Debye integral and the number of atoms per formula unit, respectively. In the case of an isotropic solid, the expression for  $\theta_D$  is given as follows [53]:

$$\theta_D = \frac{h}{k_{\beta}} [6\pi^2 V^{1/3} n]^{1/3} f(\sigma) \sqrt{\frac{B_S}{M}} \quad (3)$$

Here,  $M$  represents the molecular mass per unit cell, while  $B_S$  stands for the adiabatic compressibility modulus. We can estimate  $B_S$  by approximating it as the static compressibility [50]:

$$B_S \cong B_T V \left( \frac{d^2 E}{dV^2} \right) \quad (4)$$

The Poisson's ratio, denoted as  $f(\sigma)$ , is assigned a value of 0.25 [54, 55]. Consequently, we can proceed to minimize the unbalanced Gibbs function  $G^*(V, P, T)$  with respect to the volume  $V$  in the following manner:

$$\left[ \frac{\partial G^*(V, P, T)}{\partial V} \right] = 0. \quad (5)$$

The equilibrium curve  $V(P, T)$  can be derived, allowing us to obtain the isothermal compressibility modulus ( $B_T$ ), heat capacity ( $C_V$ ), and thermal expansion ( $\alpha$ ) using the following method [50]:

$$C_V = 3nk \left[ 4D \left( \frac{\theta}{T} \right) - \frac{3\theta/T}{e^{\theta/T} - 1} \right], \quad (6)$$

$$S = nk \left[ 4D \left( \frac{\theta}{T} \right) - 3 \ln(1 - e^{-\theta/T}) \right], \quad (7)$$

$$\alpha = \gamma C_V / V B_T \quad (8)$$

By employing Debye's quasi-harmonic model, we conducted comprehensive calculations of the thermal properties across various pressure conditions for our materials. These calculations were based on the equilibrium data for the E-V

relationship, which we initially derived at  $T = 0$  and  $P = 0$  as part of the WC approximation - GGA. Our exploration of thermal properties encompassed a temperature range spanning from 0 to 1000 K, while we also examined the impact of pressure across a range of 0 to 6 GPa.

### 3.4.1. Heat capacity et constant volume $C_V$

The investigation of crystal heat capacity is a well-established domain within condensed matter physics [50-51]. Understanding the heat capacity of a substance not only furnishes crucial insights into its vibrational characteristics but also holds significance in various practical applications.

Figure 9 illustrates the change in heat capacity at constant volume, ( $C_V$ ) as a function of temperature ( $T$ ) under different applied pressures for CuInSe<sub>2</sub> and CuInTe<sub>2</sub> compounds. The  $C_V$  of the studied systems exhibits distinct behaviors contingent upon the temperature range considered. At elevated temperatures, it tends to approach the Dulong-Petit limit [56] ( $C_V \approx 3R$  for monatomic solids). This behavior is a common trait shared by all solids at high temperatures. Conversely, at sufficiently low temperatures, it follows a proportionality to  $T^3$  [57].

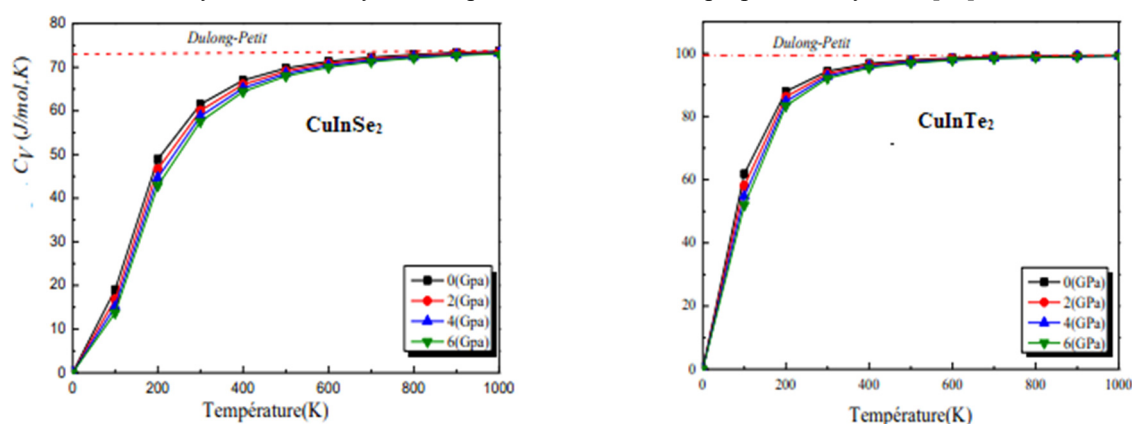


**Figure 9.** Variation of Specific Heat Capacity ( $C_V$ ) with Temperature at Different Pressures for CuInSe<sub>2</sub> and CuInTe<sub>2</sub> Compounds

As shown in Figure 9, the heat capacity  $C_V$  significantly increases at low temperatures with rising temperature, after which the rate of increase becomes gradual at higher temperatures, eventually reaching the Dulong-Petit limit in accordance with theoretical expectations. The  $C_V$  values determined at  $T=300$  K and  $P=0$  GPa for CuInSe<sub>2</sub> and CuInTe<sub>2</sub> are 61.49 and 94.38 J/mol·K, respectively.

### 3.4.2. Thermal expansion $\alpha$

The phenomenon of thermal expansion in solids is a ubiquitous yet often inconspicuous effect, concealing significant consequences. In a solid, atoms possess thermal energy and undergo vibrations around their equilibrium positions. These vibrations are temperature-dependent and are also influenced by the neighboring atoms, specifically, the interatomic potential generated by the surrounding atoms. At lower temperatures, these interatomic potentials can be approximated as harmonic, signifying that at temperatures close to  $T = 0$  K, atoms remain centered around their mean position  $r_0$ . However, as temperatures rise, the anharmonicity of interatomic potentials introduces a temperature-dependent shift in the average position of atoms, giving rise to the phenomenon of thermal expansion.

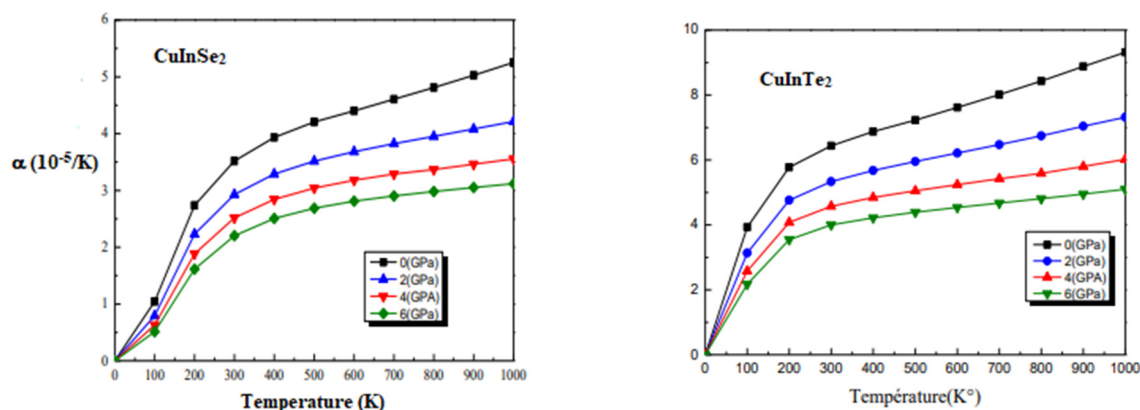


**Figure 10.** Variation of Thermal Expansion Coefficient ( $\alpha$ ) with Temperature at Different Pressures for CuInSe<sub>2</sub> and CuInTe<sub>2</sub> Compounds

The coefficient of thermal expansion characterizes the relationship between temperature and volume. As depicted in Figure 10, the variation in the coefficient of thermal expansion with temperature is illustrated at different pressures for the two ternary compounds, CuInSe<sub>2</sub> and CuInTe<sub>2</sub>.



In the figure, it is observed that, at a given pressure, thermal expansion experiences a significant increase as temperature rises, up to approximately 200 K. Beyond  $T > 200$  K, the thermal expansion rate gradually becomes more linear, suggesting that at high temperatures, thermal expansion is less influenced. Additionally, it's notable that thermal expansion is notably sensitive to temperature changes. At a given temperature, thermal expansion diminishes with increasing pressure. The calculated values of the coefficient of thermal expansion for  $\text{CuInSe}_2$  and  $\text{CuInTe}_2$  are  $3.519 \times 10^{-5} \text{ K}^{-1}$  and  $6.436 \times 10^{-5} \text{ K}^{-1}$  respectively.

### 3.4.3. The Debye temperature $\theta_D$

The Debye temperature, a vital parameter tightly interconnected with a range of solid-state properties like specific heat and melting temperature, holds a key role in comprehending the behavior of solids. In Figure 11, we present the Debye temperature ( $\theta_D$ ) variation in response to temperature at different pressures for the two ternary compounds,  $\text{CuInSe}_2$  and  $\text{CuInTe}_2$ .

Upon closer examination of the figure, it becomes apparent that, while pressure remains constant, the Debye temperature gradually decreases in a nearly linear fashion as the temperature rises. Conversely, at a fixed temperature, the Debye temperature ( $\theta_D$ ) rises with applied pressure. This pattern aligns with the behavior observed in the evolution of the compressibility modulus concerning temperature and pressure. Significantly, it underscores the principle that harder materials typically exhibit higher Debye temperatures. Furthermore, under substantial applied pressure, the Debye temperature displays reduced sensitivity to changes in temperature.

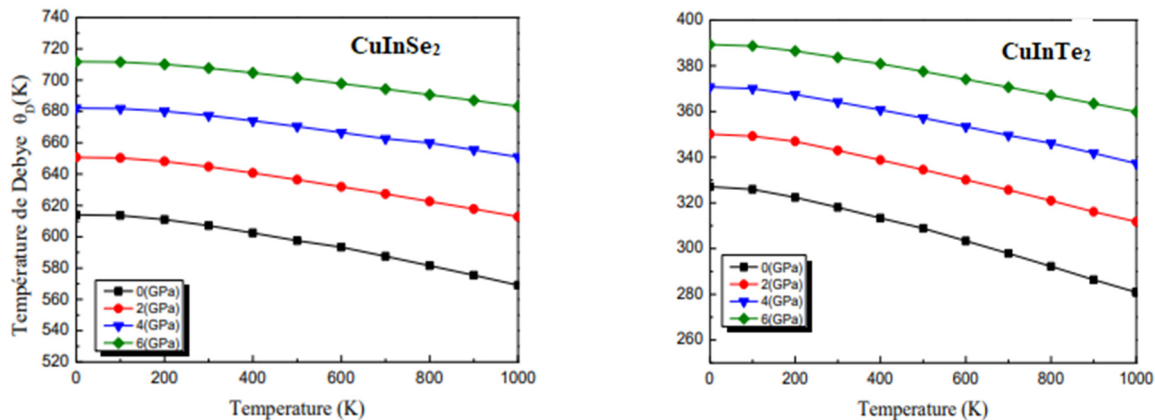


Figure 11. Variation of Debye Temperature ( $\theta_D$ ) with Pressure at Different Temperatures for  $\text{CuInSe}_2$  and  $\text{CuInTe}_2$  Compounds

### 3.4.4. The entropy of the system S

Entropy (denoted by the symbol S) is highly significant in describing the dispersion of energy and matter in systems. At the microscopic level, entropy functions as an indicator of the level of disorder within a system. Figure 12 illustrates the relationship between entropy (S), temperature, and pressure.

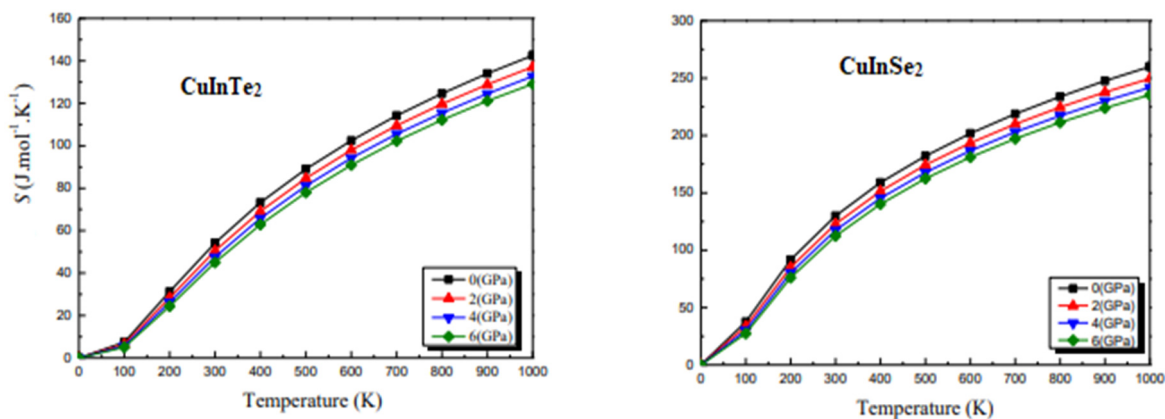


Figure 12. Entropy S versus pressure at various temperatures for  $\text{CuInSe}_2$  and  $\text{CuInTe}_2$  compounds

From the figure, it is evident that entropy exhibits a significant increase with rising temperature at a constant pressure, illustrating the system's tendency towards greater disorder as temperature climbs. Conversely, at a fixed temperature, entropy diminishes with increasing pressure, indicating a reduction in disorder under elevated pressure conditions. Notably, the calculated entropy values for  $\text{CuInSe}_2$  and  $\text{CuInTe}_2$  are 54.17 and 129.95  $\text{J/mol}\cdot\text{K}$ , respectively.

#### 4. CONCLUSION

In conclusion, our investigation employed the FP-LAPW approach within the WIEN2K code [17,20] to comprehensively explore the structural, optoelectronic, and thermal properties of CuInSe<sub>2</sub> and CuInTe<sub>2</sub> compounds. Our findings exhibited notable agreements with experimental data, surpassing previous theoretical research, particularly in terms of bandgaps, lattice parameters (a and c) and static optical parameters. Notably, we introduced a novel application potential for our compounds by analyzing their birefringence, showcasing their suitability for high-performance laser applications, a first within the domain of DFT-based research. Furthermore, our analysis of the absorption spectrum underscored the exceptional promise of CuInSe<sub>2</sub> and CuInTe<sub>2</sub> compounds for photovoltaic conversion within the visible range. Remarkably, we ventured into uncharted territory by investigating the thermal properties of these compounds using the Gibbs code, unveiling their suitability for extreme thermodynamic conditions, marking a significant contribution to the understanding of these materials.

#### ORCID

- **Hocine Meradji**, <https://orcid.org/0000-0002-3359-3725>; ● **Yamina Benkrima**, <https://orcid.org/0000-0001-8005-4065>  
 ● **Abdelghani Lakel**, <https://orcid.org/0000-0001-5098-849X>; ● **Redha Meneceur**, <https://orcid.org/0000-0002-1801-0835>  
 ● **Yousra Megdoud**, <https://orcid.org/0000-0001-8999-8134>

#### REFERENCES

- [1] E. Rosencher, and B. Vinter, Structural Study, *Vibrational, Optical, Thermal Properties and Hirshfeld Surface Analysis of a New Iron (III) Complex Optoelectronics*, (Cambridge University Press, Cambridge, UK, (2002). <https://doi.org/10.1017/CBO9780511754647>
- [2] A. Luque, Will we exceed 50% efficiency in photovoltaics, *J. Appl. Phys.* **110**, 031301 (2011). <https://doi.org/10.1063/1.3600702>
- [3] R.H. Bube, *Photovoltaic Materials*, (Imperial College Press, London, 1998). [https://doi.org/10.1016/S1369-7021\(07\)70275-4](https://doi.org/10.1016/S1369-7021(07)70275-4)
- [4] W.N. Shafarman, and L. Stolt, in: *Handbook of Photovoltaic Science and Engineering*, edited by A. Luque, and S. Hegedus (Wiley, Chichester, UK, 2003) pp. 567–616. <http://dx.doi.org/10.1002/9780470974704.ch1>
- [5] M.A. Green, K. Emery, Y. Hishikawa, and W. Warta, “Solar cell efficiency tables,” *Prog. Photovolt: Res. Appl.* **18**, 346-352 (2010). <https://doi.org/10.1002/pip.1021>
- [6] S. Siebentritt, and U. Rau, editors, *Wide-Gap Chalcopyrites*, (Springer, Berlin, Heidelberg, Germany, 2006). [https://link.springer.com/chapter/10.1007/3-540-31293-5\\_9](https://link.springer.com/chapter/10.1007/3-540-31293-5_9)
- [7] F. Chiker, B. Abbar, A. Tadjer, S. Bresson, B. Khelifa, and C. Mathieu, “Electronic structure and optical properties of ternary CdXP<sub>2</sub> semiconductors (X = Si, Ge and Sn) under pressure,” *Physica B*, **349**, 181-191 (2004). <https://doi.org/10.1016/j.physb.2004.03.087>
- [8] F. Chiker, B. Abbar, A. Tadjer, S. Bresson, B. Khelifa, and C. Mathieu, “The reflectivity spectra of ZnXP<sub>2</sub> (X=Si, Ge, and Sn) compounds,” *J. Solid State. Chem.* **177**(11), 3859-3867 (2004). <http://dx.doi.org/10.1016/j.jssc.2004.07.020>
- [9] B. Kocak and Y.O. Ciftci, “Ab-initio calculations of semiconductor,” *Mater. Res. Bull.* **77**, 300-306 (2016). <https://doi.org/10.1016/j.materresbull.2016.02.008>
- [10] Y. Marfaing, “Énergie photovoltaïque,” *J. Phys. IV France*, **12**, Pr 2 – 145 (2002). <https://doi.org/10.1051/jp420020021>
- [11] J. Müller, J. Nowoczin, and H. Schmitt, “Composition, structure and optical properties of sputtered thin films of CuInSe<sub>2</sub>,” *Thin Solid Films*, **496**, 364-370 (2006). <https://doi.org/10.1016/j.tsf.2005.09.077>
- [12] R.C. Gupta, P. Varshney, Pravesh, M. Lal, D. Kumar, K. Singh, and A.S. Verma, “Mechanical stability parameters of chalcogenides and pnictides based optoelectronic materials,” *Chalcogenide Letters*, **20**(2), 101–112 (2023). <https://doi.org/10.15251/CL.2023.202.101>
- [13] H. Yu, G. Huang, Q. Peng, L.-C. Chen, H.-J. Pang, X.-Y. Qin, P.-F. Qiu, et al., “A combined experiment and first-principles study on lattice dynamics of thermoelectric CuInTe<sub>2</sub>,” *Journal of Alloys and Compounds*, **822**, 153610 (2020). <https://doi.org/10.1016/j.jallcom.2019.153610>
- [14] G. Jia, and J. Du, “Catalyst-Assisted Solution–Liquid–Solid Synthesis of CdS/CuInSe<sub>2</sub> and CuInTe<sub>2</sub>/CuInSe<sub>2</sub> Nanorod Heterostructures,” *Inorg. Chem.* **58**(1), 695-702 (2018). <https://doi.org/10.1021/acs.inorgchem.8b02870>
- [15] H. Yu, L.-C. Chen, H.-J. Pang, P.-F. Qiu, Q. Peng, and X.-J. Chen, “Temperature-dependent phonon anharmonicity and thermal transport in CuInTe<sub>2</sub>,” *Physical Review B*, **105**, 245204 (2022). <https://doi.org/10.1103/PhysRevB.105.245204>
- [16] E. Mazalan, M.S.A. Aziz, N.A.S. Amin, F.D. Ismail, M.S. Roslan, and K. Chaudhary, “First-principles study on crystal structures and bulk modulus of CuInX<sub>2</sub> (X = S, Se, S-Se) solar cell absorber,” *Journal of Physics: Conference Series*, **2432**, 012009 (2023). <http://dx.doi.org/10.1088/1742-6596/2432/1/012009>
- [17] O.K. Anderson, “Linear methods in band theory,” *Phys. Rev. B*, **42**, 3060 (1975). <https://doi.org/10.1103/PhysRevB.12.3060>
- [18] P. Hohenberg, and W. Kohn, “Inhomogeneous Electron Gas,” *Phys. Rev. B*, **136**, 864 (1964). <https://doi.org/10.1103/PhysRev.136.B864>
- [19] W. Kohn, and L.S. Sham, “Self-Consistent Equations Including Exchange and Correlation Effects,” *Phys. Rev. A*, **140**, 1133 (1965). <https://doi.org/10.1103/PhysRev.140.A1133>
- [20] P. Blaha, K. Schwarz, G.K.H. Madsen, D. Kvasnicka, J. Luitz, *Wien2k. An Augmented Plane Wave Local Orbitals Program for Calculating Crystal Properties*, (Vienna University of Technology, Vienna, 2001).
- [21] Z. Wu, and R.E. Cohen, “More accurate generalized gradient approximation for solids,” *Phys. Rev. B*, **73**, 235116 (2006). <https://doi.org/10.1103/PhysRevB.73.235116>
- [22] F. Tran, and P. Blaha, “Accurate Band Gaps of Semiconductors and Insulators with a Semilocal Exchange-Correlation Potential,” *Phys. Rev. Lett.* **102**, 226401 (2009). <https://doi.org/10.1103/PhysRevLett.102.226401>
- [23] A.D. Becke, and E.R. Johnson, “A simple effective potential for exchange,” *J. Chem. Phys.* **124**, 221101 (2006). <https://doi.org/10.1063/1.2213970>
- [24] F.D. Murnaghan, “The Compressibility of Media under Extreme Pressures,” *P. Natl. Acad. Sci. USA*, **30**, 244-247 (1944). <https://doi.org/10.1073/pnas.30.9.244>

- [25] M.L. Cohen, "Calculation of bulk moduli of diamond and zinc-blende solids," *Phys. Rev. B*, **32**, 7988 (1985). <https://doi.org/10.1103/PhysRevB.32.7988>
- [26] S.N. Rashkeev, and W.R.L. Lambrecht, "Second-harmonic generation of I-III-VI<sub>2</sub> chalcopyrite semiconductors: Effects of chemical substitutions," *Phys. Rev. B*, **63**, 165212 (2001). <https://doi.org/10.1103/PhysRevB.63.165212>
- [27] A.D. Becke, "Density-functional thermochemistry. III. The role of exact exchange," *J. Chem. Phys.* **98**, 5648-5652 (1993). <https://doi.org/10.1063/1.464913>
- [28] J.S. Toll, "Causality and the Dispersion Relation: Logical Foundations," *Phys. Rev.* **104**, 1760 (1956). <https://doi.org/10.1103/PhysRev.104.1760>
- [29] L.D. Landau, and E.M. Lifshitz, *Electrodynamics of Continuous Media*, (Pergamon Press, Oxford, 1960). <https://doi.org/10.4236/ib.2011.33034>
- [30] H. A. Kramers, *Collected Science Papers* (North-Holland Publishing Co, Amsterdam, 1956). <https://doi.org/10.1088/0953-4075/38/13/016>
- [31] R. de L. Kronig, "Mean-Field Formulation of Maxwell Equations to Model Electrically Inhomogeneous and Isotropic Media," *J. Opt. Soc. Am.* **12**, 547 (1926). <https://doi.org/10.4236/ajcm.2018.84023>
- [32] C.M.I. Okoye, "Theoretical study of the electronic structure, chemical bonding and optical properties of in the paraelectric cubic phase," *J. Phys.* **15**, 5945 (2003). <https://doi.org/10.1103/PhysRevB.62.8828>
- [33] P.Y. Yu, and M. Cardona, *Fundamentals of Semiconductors*, (Springer, Berlin, 1996). [http://dx.doi.org/10.1007/3-540-26475-2\\_1](http://dx.doi.org/10.1007/3-540-26475-2_1)
- [34] A.H. Reshak, et al., "First Principle Study of Electronic Structure, Chemical Bonding and Optical Properties of 5-azido-1H-tetrazole," *J. Alloys Compd.* **509**, 6737 (2011). [http://dx.doi.org/10.1016/S1452-3981\(23\)12986-5](http://dx.doi.org/10.1016/S1452-3981(23)12986-5)
- [35] C.S. Schnorr, "Compound semiconductor alloys: From atomic-scale structure to bandgap bowing," *Appl. Phys. Rev.* **2**, 031304 (2015). <https://doi.org/10.1063/1.4930002>
- [36] Z. Lv, C. Cheng, Y. Cheng, X. Chen, G. Ji, "Elastic, thermodynamic and electronic properties of LaF<sub>3</sub> under pressure from first principles," *Computational Materials Science*, **89**(15), 57-64 (2014). <https://doi.org/10.1016/j.commatsci.2014.03.011>
- [37] R. de L. Kronig, "On the theory of dispersion of x-rays," *J. Opt. Soc. Am.* **12**, 547-557 (1926). <http://dx.doi.org/10.1364/JOSA.12.000547>
- [38] A. Shankar, R.K. Thapa, and P.K. Mandal, "Electronic and optical properties of CuInTe<sub>2</sub>," *J. Phys. Conf. Ser.* **765**, 012008 (2016). <http://dx.doi.org/10.1088/1742-6596/765/1/012008>
- [39] D.R. Penn, "Wave-number-dependent dielectric function of semiconductors," *Phys. Rev.* **128**, 2093 (1962). <https://doi.org/10.1103/PhysRev.128.2093>
- [40] S.M. Wasim, and J.G. Albornóz, "Electrical and optical properties of n- and p-type CuInTe<sub>2</sub>," *Phys. Status Solidi A*, **110**, 575-583 (1988). <https://doi.org/10.1002/pssa.2211100231>
- [41] J.G. Davis, P.M. Bridenbaugh, and S. Wagner, "Electrical and optical properties of copper indium ditelluride crystals grown from near-stoichiometric compositions," *J. Electron. Mater.* **7**, 39-45 (1978). <https://doi.org/10.1007/BF02656019>
- [42] V. Riede, H. Neumann, H. Sobotta, R.D. Tomlinson, E. Elliott, and L. Howarth, "Infrared study of lattice and free carrier effects in p-type CuInTe<sub>2</sub> single crystals," *Solid State Commun.* **33**, 557 (1980). [https://doi.org/10.1016/0038-1098\(80\)90859-5](https://doi.org/10.1016/0038-1098(80)90859-5)
- [43] N. Vermeulen, et al., "Post-2000 nonlinear optical materials and measurements: data tables and best practices," *Journal of physics photonics*, **5**(3), 035001 (2023). <https://doi.org/10.1088/2515-7647/ac9e2f>
- [44] N.V. Smith, "Photoelectron energy spectra and the band structures of the noble metals," *Phys. Rev. B*, **3**, 1862 (1971). <https://doi.org/10.1103/PhysRevB.3.1862>
- [45] F. Wooten, *Optical Properties of Solids*, (Academic Press, New York and London, 1972). [https://doi.org/10.1016/0169-4332\(90\)90007-M](https://doi.org/10.1016/0169-4332(90)90007-M)
- [46] A. Ghosh, R. Thangavel, and M. Rajagopalan, "Electronic and optical modeling of solar cell compound CuXY<sub>2</sub> (X = In, Ga, Al; Y = S, Se, Te): first-principles study via Tran-Blaha-modified Becke-Johnson exchange," *J. Mater. Sci.* **50**, 1710-1717 (2015). <http://dx.doi.org/10.1007/s10853-014-8732-z>
- [47] J.T. Goldstein, D.E. Zelmon, A.W. Saxler, S.M. Hegde, J.D. Wolf, P.G. Schunemann, et al., "Infrared properties of a nonlinear optical chalcopyrite semiconductor," *J. Appl. Phys.* **86**, 94 (1999). <http://dx.doi.org/10.1063/1.370704>
- [48] P.A. Franken, A.E. Hill, C.W. Peters, and G. Weinreich, "Generation of optical harmonics," *Phys. Rev. Lett.* **7**, 118 (1961). <https://doi.org/10.1103/PhysRevLett.7.118>
- [49] H. Salehi, and E. Gordanian, "Ab initio study of structural, electronic and optical properties of ternary chalcopyrites emiconductors," *Mat. Sci. Semicon. Proc.* **47**, 51-56 (2016). <https://doi.org/10.1016/j.mssp.2016.02.015>
- [50] R.R. Reddy, Y.N. Ahammed, K.R. Gopal, and D.V. Raghuram, "Optical electronegativity and refractive index of materials," *Opt. Mater.* **10**(2), 95-100 (1998). [https://doi.org/10.1016/S0925-3467\(97\)00171-7](https://doi.org/10.1016/S0925-3467(97)00171-7)
- [51] S. Cui, W. Feng, H. Hu, Z. Feng, and Y. Wang, "First principles studies of phase stability, electronic and elastic properties, computational Materials Science," **47**(4), 968-972 (2010). <https://doi.org/10.1016/j.commatsci.2009.11.030>
- [52] K. Bouamama, P. Djemia, N. Lebga, and K. Kassali, "High Pressure Macromolecular Crystallography," *High Pressure Research*, **27**(2), 269-277 (2007). <https://doi.org/10.1080/08957950701265359>
- [53] M.A. Blanco, A.M. Pendas, E. Francisco, J.M. Recio, and R. Franco, "Thermodynamical properties of solids from microscopic theory: applications to MgF<sub>2</sub> and Al<sub>2</sub>O<sub>3</sub>," *J. Mol. Struct. Theochem.* **368**, 245-255 (1996). [https://doi.org/10.1016/S0166-1280\(96\)90571-0](https://doi.org/10.1016/S0166-1280(96)90571-0)
- [54] E. Francisco, J.M. Recio, M.A. Blanco, A.M. Pendas, and A. Costales, "Quantum-Mechanical Study of Thermodynamic and Bonding," *J. Phys. Chem.* **102**, 1595-1601 (1998). <https://doi.org/10.1021/jp972516j>
- [55] E. Francisco, M.A. Blanco, and G. Sanjurjo, "Nontrivial effect of spin-orbit coupling on the intrinsic resistivity of ferromagnetic gadolinium," *Phys. Rev. B*, **107**, 115101 (2023). <https://doi.org/10.1103/PhysRevB.107.115101>
- [56] V.Kh. Kozlovskiy, "To the Question of Validity Grüneisen Solid State Equation," *World Journal of Condensed Matter Physics*, **2**(4), (2012). <http://dx.doi.org/10.4236/wjcmp.2012.24038>
- [57] A. T. Petit, and P. L. Dulong, "Recherches sur Quelques Points Importants de la Théorie de la Chaleur," *Annales de Chimie et de Physique*, **10**, 395-413 (1819). [http://www.ffn.ub.es/luisnavarro/nuevo\\_maletin/Petit--Dulong\\_1819.pdf](http://www.ffn.ub.es/luisnavarro/nuevo_maletin/Petit--Dulong_1819.pdf)

- [58] R. Mahdjoubi, Y. Megdoud, L. Tairi, H. Meradji, Z. Chouahda, S. Ghemid, and F. El Haj Hassan, "Structural, electronic, optical and thermal properties of CuXTe (X=Al, Ga, In) compounds: an study," International Journal of Modern Physics B, 33(07), 1950045 (2019). <http://dx.doi.org/10.1142/S0217979219500450>

#### AB-INITIO ДОСЛІДЖЕННЯ ФІЗИЧНИХ ХАРАКТЕРИСТИК СПОЛУК CuInSe<sub>2</sub> І CuInTe<sub>2</sub>

Юсра Мегдуд<sup>b,c</sup>, Яміна Бенкріма<sup>a</sup>, Редхе Менесер<sup>f</sup>, Латіфа Таїрі<sup>c,d</sup>, Абдельгані Лекле<sup>e</sup>, Себті Гемід<sup>c</sup>, Хосін Мераджі<sup>c</sup>

<sup>a</sup> Вища нормальна школа Уаргла, 30000 Уаргла, Алжир

<sup>b</sup> Інститут наук Університетського центру Тіпаза, Морслі Абдаллах, Алжир

<sup>c</sup> Лабораторія LPR, департамент фізики, факультет природничих наук, Баджі-Аннаба-Адрес, Алжир

<sup>d</sup> Науково-дослідний центр промислових технологій ЦРТІ, П.О. Вох 64, Черага 16014, Алжир Алжир

<sup>e</sup> Лабораторія металів та напівпровідників, матеріалів, Університет Біскри, ВР 145 РР, 07000, Біскра, Алжир

<sup>f</sup> Відділ розвитку поновлюваних джерел енергії в посушливих зонах (UDERZA), Університет Ель-Уед, Алжир

У цій роботі представлений аналіз сполук халькопіриту CuInTe<sub>2</sub> та CuInSe<sub>2</sub> з акцентом на їх електронні, структурні, оптичні та термічні властивості. Для дослідження цих властивостей використовується повнопотенційний метод лінеаризованої приєднаної плоскої хвилі (FP-LAPW), заснований на підході перших принципів, що ґрунтується на теорії функціоналу щільності (DFT). У наших розрахунках враховуються два різні наближення для обмінного та кореляційного потенціалу, а саме наближення WC-GGA та mBJ-GGA, щоб забезпечити надійне та точне дослідження досліджуваних матеріалів. Отримані результати тісно узгоджуються із раніше встановленими теоретичними та експериментальними даними, тим самим підтверджуючи надійність нашої обчислювальної методології. Примітно, що це дослідження відкриває новий аспект, оскільки досліджується вплив тиску, так і температури на термічні параметри сполук CuInTe<sub>2</sub> і CuInSe<sub>2</sub>. Цей аспект дослідження відрізняється своїм новаторським характером, оскільки, наскільки нам відомо, такого аналізу в існуючій літературі не було. Термічні властивості мають першорядне значення, особливо у контексті оптимізації процесу вирощування кристалів та прогнозування продуктивності в екстремальних термодинамічних умовах.

**Ключові слова:** фотоелектрика; халькопірит; FP-LAPW; заборонена зона; теплові властивості

## DANGEROUS BONDS INDIVIDUAL OF HYDROGENATED AMORPHOUS SILICON AND DEFECT ABSORPTION SPECTRA

✉ Rustamjon G. Ikramov, ✉ Khurshidbek A. Muminov\*, Mashkhura A. Nuritdinova, Bobur Q. Sutonov, Oybek T. Kholmirezayev, A'zamxo'ja A. Mamakhanov

Namangan Engineering and Technology Institute, 7, Kosonsoy Street, Namangan 160115, Uzbekistan

\*Corresponding Author e-mail: [muminov\\_19912406@mail.ru](mailto:muminov_19912406@mail.ru)

Received October 13, 2023; revised October 28, 2023; accepted November 17, 2023

In this work, defect absorption spectra for defects characteristic of hydrogenated amorphous silicon are theoretically studied. It is shown that in order to determine defect absorption spectra using the Kubo-Greenwood formula, the indefinite integral in this formula must be written in a certain form. It was discovered that electronic transitions involving defect states are divided into two parts depending on the energy of absorbed photons. The values of the partial defect absorption spectrum at low energies of absorbed photons have almost no effect on the overall defect absorption spectrum. It has been established that the main role in determining the defect absorption spectrum is played by partial spectra determined by optical transitions of electrons between allowed bands and defects. It is shown that with a power-law distribution of the density of electronic states in allowed bands, the spectra of optical transitions between them and defects do not depend on the value of this power.

**Keywords:** Amorphous semiconductors; Optical transitions of electrons with the participation of defects; Defect absorption spectra; Partial spectra

**PACS:** 61.43Dq, 68.43 Mn

### INTRODUCTION

It is known that hydrogenated amorphous silicon ( $\alpha$ -Si:H), forming dangling bonds in the mobility gap, is divided into three types depending on their charge state.  $D^0$ -neutral defect having one electron and one hole,  $D^-$ -defect with negative charge having two electrons and  $D^+$ -defect with positive charge having two holes. All these defects act as traps for electrons.

It was shown in [1] that, regardless of the charge state, defects are involved in all optical transitions of electrons. Therefore, the experiment gives the total sum of the values of all partial spectra corresponding to optical transitions, including all defect states.

In [2,3], for the energy positions and concentrations of these defects in  $\alpha$ -Si:H obtained in a glow gas discharge, the following are given:  $\varepsilon_{D^0} - \varepsilon_V \approx 0,78$  eV,  $\varepsilon_{D^-} - \varepsilon_V \approx 0,5$  eV,  $\varepsilon_{D^+} - \varepsilon_V \approx 1,28$  eV and  $N_{D^0} = 4.5 \cdot 10^{15}$  cm<sup>-3</sup>,  $N_{D^-} = 3 \cdot 10^{15}$  cm<sup>-3</sup>,  $N_{D^+} = 3 \cdot 10^{15}$  cm<sup>-3</sup>.

It is known that during the absorption of photons, electronic transitions occur with the participation of defect states and the valence band and its tail, as well as with the conduction band and its tail. Depending on the energy of absorbed photons, these optical transitions of electrons are shown in Figure 1.

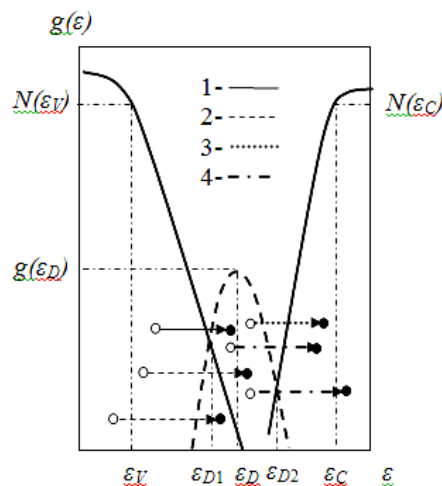


**Figure 1.** Types of optical electronic transitions involving defect states occurring in amorphous semiconductors at the energy of absorbed photons. 1 -  $\varepsilon_{D1} - \varepsilon_V < \hbar\omega$  and 2 -  $\varepsilon_{D1} - \varepsilon_V > \hbar\omega$ , 3 -  $\varepsilon_C - \varepsilon_{D2} > \hbar\omega$  and 4 -  $\varepsilon_C - \varepsilon_{D2} < \hbar\omega$

When the condition  $1 - \varepsilon_{D1} - \varepsilon_V > \hbar\omega$  for the energy of absorbed photons is fulfilled, the electrons participating in the optical transition pass only from the tail of the valence band to the defect, and when the condition  $2 - \varepsilon_{D1} - \varepsilon_V < \hbar\omega$  is fulfilled, the electrons simultaneously pass from the valence band and from tail for a defect. Where  $\varepsilon_{D1}$  is the energy position of the intersection point of the distribution of electronic states, the tail of the valence band and defects (Fig. 1),  $\varepsilon_V$  is the upper boundary of the valence band.

When condition 3 -  $\varepsilon_C - \varepsilon_{D2} > \hbar\omega$  is met, electrons pass only from defects to the tail of the conduction band, and when condition 4 -  $\varepsilon_C - \varepsilon_{D2} < \hbar\omega$  is met, optical transitions of electrons simultaneously occur from defect states to the tail of the conduction band, as well as to the conduction band. Where  $\varepsilon_{D2}$  is the energy position of the intersection point of the distribution, electronic states of the tail of the conduction band and defect states (Fig. 1),  $\varepsilon_C$  is the lower boundary of the conduction band.

It follows from this that eighteen optical transitions involving defect states occur simultaneously in  $\alpha$ -Si:H. Therefore, the theoretical calculation of the defect absorption of  $\alpha$ -Si:H is a very difficult problem in the physics of amorphous semiconductors.

The disorder in the structural lattice of amorphous semiconductors leads to the fact that the wave vector of electrons involved in optical transitions is not a good quantum number. Therefore, the spectra of all types of optical transitions of electrons in noncrystalline semiconductors are calculated using the Kubo-Greenwood formula using the Davis-Mott approximation method

$$\alpha(\hbar\omega) = A \int \frac{g(\varepsilon)g(\varepsilon + \hbar\omega)}{\hbar\omega} d\varepsilon. \quad (1)$$

In this equation A is a proportionality coefficient independent of the energy of absorbed photons,  $g(\varepsilon)$  is the density of initial and  $g(\varepsilon + \hbar\omega)$  final states of electrons participating in optical transitions. It was shown in [4] that the integral in equation (1) should be written in the form of a definite integral to determine the Eigen solutions of the absorption coefficient spectra.

It can be seen from this equation that, in order to determine the analytical solutions of partial defect absorption spectra, it is necessary to know the distribution of electronic states in allowed bands and their tails, as well as in defects; for this, different models are usually used [5, 6]. In all these models, the distribution of electronic states in the allowed bands is parabolic, while the distribution of electronic states in the tails of the allowed bands is exponential. Taking this into account, the following model of the distribution of the density of electronic states in allowed bands and their tails was proposed in [7] in the following forms:

$$g(\varepsilon) = N(\varepsilon_V) \left( \frac{\varepsilon_C - \varepsilon}{E_g} \right)^{n_1}, \quad n_1 = 0, 1/2, 1 \quad \text{and} \quad g(\varepsilon) = N(\varepsilon_V) \exp(-\beta_1(\varepsilon - \varepsilon_V)), \quad (2)$$

$$g(\varepsilon) = N(\varepsilon_C) \left( \frac{\varepsilon - \varepsilon_V}{E_g} \right)^{n_2}, \quad n_2 = 0, 1/2, 1 \quad \text{and} \quad g(\varepsilon) = N(\varepsilon_C) \exp(\beta_2(\varepsilon - \varepsilon_C)), \quad (3)$$

where  $N(\varepsilon_V)$  are the effective values of the density of electronic states in the valence band and  $N(\varepsilon_C)$  in the conduction band,  $E_g$  is the energy width of the mobility gap,  $\beta_1$  and  $\beta_2$  are the parameters that determine the curvature of the exponential tails of the valence band and the conduction band.  $n_1$  - and  $n_2$  - degree of the distribution function of electronic states in the valence band and in the conduction band.

As shown in [8], the distribution of defect states in amorphous semiconductors obeys the distribution of the hyperbolic secant:

$$g(\varepsilon) = \frac{g(\varepsilon_D)}{ch(b(\varepsilon - \varepsilon_D))} = \frac{2g(\varepsilon_D)}{\exp(b(\varepsilon - \varepsilon_D)) + \exp(-b(\varepsilon - \varepsilon_D))}, \quad (4)$$

or Gaussian distribution:

$$g(\varepsilon) = g(\varepsilon_D) \exp(-a(\varepsilon - \varepsilon_D)^2), \quad (5)$$

where  $b$  and  $a$  are the parameters that determine the effective half-width of the distribution of the density of electronic states in defects,  $\varepsilon_D$  is the energy position of the maximum of defect states, and  $g(\varepsilon_D)$  is the maximum value of the distribution of the density of electronic states in defects.

In the same work, it was shown that the defect concentrations determined by equation (4) and (5) will be equal to each other when the condition  $a = b^2/\pi$  is satisfied.

**RESULTS AND DISCUSSION**

We write the integral in the Kubo-Greenwood equation as a definite integral for the condition  $\epsilon_{D1}-\epsilon_V > \hbar\omega$  as follows:

$$\alpha = A \int_{\epsilon_{D1}-\hbar\omega}^{\epsilon_{D1}} g(\epsilon) g(\epsilon + \hbar\omega) \frac{d\epsilon}{\hbar\omega}. \tag{6}$$

Substituting the densities of states (2), (3), and (4) into equation (6), we obtain the following expression:

$$\alpha = A \int_{\epsilon_{D1}-\hbar\omega}^{\epsilon_{D1}} N(\epsilon_V) \exp(-\beta_1(\epsilon - \epsilon_V)) \frac{g(\epsilon_D)}{ch(b(\epsilon - \epsilon_D + \hbar\omega))} \frac{d\epsilon}{\hbar\omega} = \frac{Bg(\epsilon_D)}{bN(\epsilon_C)} \times \exp(b(\epsilon_V - \epsilon_D + \hbar\omega)) (2b\hbar\omega + \ln \frac{(\exp(2b(\epsilon_{D1} - \epsilon_D)) + 1)}{(\exp(2b(\epsilon_{D1} - \epsilon_D + \hbar\omega)) + 1)}), \tag{7}$$

where  $B = AN(\epsilon_V)N(\epsilon_C)$ . To obtain an analytical solution to equation (7), the condition must be satisfied. It will be shown below that the value of b has almost no effect on the defect absorption spectra. Equation (6) is adapted to the optical transitions of electrons, under the condition  $\epsilon_{D1}-\epsilon_V < \hbar\omega$ :

$$\alpha = A \int_{\epsilon_{D1}-\hbar\omega}^{\epsilon_{D1}} g(\epsilon) g(\epsilon + \hbar\omega) \frac{d\epsilon}{\hbar\omega} = A \int_{\epsilon_V}^{\epsilon_{D1}} g(\epsilon) g(\epsilon + \hbar\omega) \frac{d\epsilon}{\hbar\omega} + A \int_{\epsilon_{D1}-\hbar\omega}^{\epsilon_V} g(\epsilon) g(\epsilon + \hbar\omega) \frac{d\epsilon}{\hbar\omega} = \alpha_1 + \alpha_2, \tag{8}$$

where  $\alpha_1$  is the partial spectrum of electronic transitions from the tail of the valence band to the defect, and  $\alpha_2$  is the partial spectrum of optical transitions from the valence band to the defect. For optical transitions of electrons from the tail of the valence band to defects, we obtain the expression:

$$\alpha_1 = A \int_{\epsilon_V}^{\epsilon_{D1}} N(\epsilon_V) \exp(-\beta_1(\epsilon - \epsilon_V)) \frac{g(\epsilon_D)}{ch(b(\epsilon - \epsilon_D + \hbar\omega))} \frac{d\epsilon}{\hbar\omega} = \frac{Bg(\epsilon_D)}{bN(\epsilon_C)\hbar\omega} \exp(b(\epsilon_V - \epsilon_D + \hbar\omega)) (2b(\epsilon_{D1} - \epsilon_V)) + \ln \frac{(\exp(2b(\epsilon_V - \epsilon_D + \hbar\omega)) + 1)}{(\exp(2b(\epsilon_{D1} + \epsilon_D + \hbar\omega)) + 1)}. \tag{9}$$

To obtain equation (9), the condition  $\beta_1 = b$  was also required. The partial spectra of optical transitions of electrons from the valence band to defects are calculated. For the case when  $n_l = 0$  we get the expression:

$$\alpha_2 = A \int_{\epsilon_{D1}-\hbar\omega}^{\epsilon_V} N(\epsilon_V) \frac{g(\epsilon_D)}{ch(b(\epsilon - \epsilon_D + \hbar\omega))} \frac{d\epsilon}{\hbar\omega} = \frac{2Bg(\epsilon_D)}{bN(\epsilon_C)\hbar\omega} \times (\arctg \exp(b(\epsilon_V - \epsilon_D + \hbar\omega)) - \arctg \exp(b(\epsilon_{D1} - \epsilon_D))). \tag{10}$$

And for the case when  $n_l = 1$ :

$$\alpha_2 = A \int_{\epsilon_{D1}-\hbar\omega}^{\epsilon_V} N(\epsilon_V) \left( \frac{\epsilon_C - \epsilon}{E_g} \right) \frac{g(\epsilon_D)}{ch(b(\epsilon - \epsilon_D + \hbar\omega))} \frac{d\epsilon}{\hbar\omega} = \frac{2Bg(\epsilon_D)}{bN(\epsilon_C)E_g\hbar\omega} (\epsilon_C - \epsilon_D + \hbar\omega) \times (\arctg \exp(b(\epsilon_V - \epsilon_D + \hbar\omega)) - \arctg \exp(b(\epsilon_{D1} - \epsilon_D))) - \frac{Bg(\epsilon_D)}{2aN(\epsilon_C)E_g\hbar\omega} (\exp(-a(\epsilon_V - \epsilon_D + \hbar\omega)^2) - \exp(-a(\epsilon_{D1} - \epsilon_D)^2)). \tag{11}$$

In expressions (10) and (11), the quantity b can take arbitrary values. An analytical solution for the case when  $n_l = 1/2$  could not be obtained, so it was calculated using approximate calculation methods. When  $\epsilon_C - \epsilon_{D2} > \hbar\omega$  to calculate the spectra of optical transitions of electrons from the defect to the tail of the conduction band, we write the Kubo-Greenwood formula as follows:

$$\alpha = A \int_{\epsilon_{D2}-\hbar\omega}^{\epsilon_{D2}} g(\epsilon)g(\epsilon+\hbar\omega)\frac{d\epsilon}{\hbar\omega}. \tag{12}$$

Let's carry out calculations by substituting the distribution functions given by equations (2)-(4) into equation (12):

$$\begin{aligned} \alpha &= A \int_{\epsilon_{D2}-\hbar\omega}^{\epsilon_{D2}} \frac{g(\epsilon_D)}{ch(b(\epsilon-\epsilon_D))} N(\epsilon_C) \exp(\beta_2(\epsilon-\epsilon_C+\hbar\omega)) \frac{d\epsilon}{\hbar\omega} = \\ &= \frac{Bg(\epsilon_D)}{N(\epsilon_V)b\hbar\omega} \exp(b(\epsilon_D-\epsilon_C+\hbar\omega)) \ln \frac{(1+\exp(2b(\epsilon_{D2}-\epsilon_D)))}{(1+\exp(2b(\epsilon_{D2}-\epsilon_D-\hbar\omega)))} \end{aligned} \tag{13}$$

Equation (13) was calculated for  $\beta_2 = b$ .

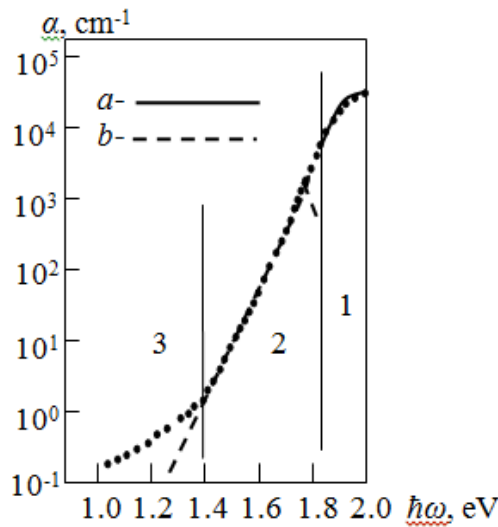


**Figure 2.** Experimentally determined optical absorption spectrum of amorphous hydrogenated silicon  
1 – region of interband absorption, 2 – region of exponential absorption, 3 – region of defective absorption.

Now we agree on equation (12) for the condition  $\epsilon_C-\epsilon_{D2}<\hbar\omega$  to optical transitions of electrons:

$$\alpha = A \int_{\epsilon_{D2}-\hbar\omega}^{\epsilon_{D2}} g(\epsilon)g(\epsilon+\hbar\omega)\frac{d\epsilon}{\hbar\omega} = A \int_{\epsilon_C-\hbar\omega}^{\epsilon_{D2}} g(\epsilon)g(\epsilon+\hbar\omega)\frac{d\epsilon}{\hbar\omega} + A \int_{\epsilon_{D2}-\hbar\omega}^{\epsilon_C-\hbar\omega} g(\epsilon)g(\epsilon+\hbar\omega)\frac{d\epsilon}{\hbar\omega} = \alpha_1 + \alpha_2. \tag{14}$$

where  $\alpha_1$  are the partial spectra of optical transitions of electrons from defect states to the conduction band, and  $\alpha_2$  are from the defect to the tail of the conduction band. Let us calculate partial spectra for electron transitions from a defect to conduction bands by substituting distribution functions (2)–(5) into equation (14). For the case  $n_2=0$ :

$$\alpha_1 = A \int_{\epsilon_C-\hbar\omega}^{\epsilon_{D2}} \frac{g(\epsilon_D)}{ch(b(\epsilon-\epsilon_D))} N(\epsilon_C) \frac{d\epsilon}{\hbar\omega} = \frac{2Bg(\epsilon_D)}{b\hbar\omega N(\epsilon_V)} (\text{arctg}(\exp(b(\epsilon_{D2}-\epsilon_D))) - \text{arctg}(\exp(b(\epsilon_C-\epsilon_D-\hbar\omega)))). \tag{15}$$

in the case of  $n_2=1$ , we obtain the expressions:

$$\begin{aligned} \alpha_1 &= A \int_{\epsilon_C-\hbar\omega}^{\epsilon_{D2}} \frac{g(\epsilon_D)}{ch(b(\epsilon-\epsilon_D))} N(\epsilon_C) \left( \frac{\epsilon-\epsilon_V+\hbar\omega}{E_g} \right) \frac{d\epsilon}{\hbar\omega} = \\ &= \frac{2Bg(\epsilon_D)}{b\hbar\omega E_g N(\epsilon_V)} (\text{arctg}(\exp(b(\epsilon_{D2}-\epsilon_D))) - \text{arctg}(\exp(b(\epsilon_C-\epsilon_D-\hbar\omega)))) - \\ &- \frac{Bg(\epsilon_D)}{2a\hbar\omega E_g N(\epsilon_V)} (\exp(-a(\epsilon_{D2}-\epsilon_D)^2) - \exp(-a(\epsilon_C-\epsilon_D-\hbar\omega)^2)) \end{aligned} \tag{16}$$

For  $n_2=1/2$ , it was not possible to obtain an analytical solution, so it was calculated using approximate calculation methods. In equations (15) and (16),  $b$  can take arbitrary values.



Let us now calculate the partial spectrum of optical transitions of electrons from the defect to the tail of the conduction bands:

$$\alpha_2 = A \int_{\varepsilon_{D2}-\hbar\omega}^{\varepsilon_C-\hbar\omega} \frac{g(\varepsilon_D)}{ch(b(\varepsilon-\varepsilon_D))} N(\varepsilon_C) \exp(\beta_2(\varepsilon-\varepsilon_C+\hbar\omega)) \frac{d\varepsilon}{\hbar\omega} = \frac{Bg(\varepsilon_D)}{b\hbar\omega N(\varepsilon_C)} \times \exp(b(\varepsilon_D-\varepsilon_C+\hbar\omega)) Ln \frac{(1+\exp(2b(\varepsilon_C-\varepsilon_D-\hbar\omega)))}{(1+\exp(2b(\varepsilon_{D2}-\varepsilon_D-\hbar\omega)))} \quad (17)$$

In equation (17), calculations were made for  $\beta_2 = b$ . In equations (15) and (16), the quantity  $b$  can take arbitrary values. To calculate the values of the above partial spectra, it is necessary to determine the parameters  $B, E_g, \beta_1, \beta_2$ , for which we will use the experimentally determined values of the optical absorption spectrum of the absorption coefficient. The work [9] presents the absorption coefficient spectrum determined from the experiment of amorphous hydrogenated silicon grown in a high-frequency glow gas discharge (Fig. 2).

Let us divide this spectrum into the regions of interband, exponential, and defect absorption. Considering  $B$  and  $E_g$  in the analytically calculated equation as fitting parameters, we determine by comparing the values of the interband absorption spectra obtained from the experiment. Precisely, in the same way we determine  $\beta_1$ , and  $\beta_2$  from the region of exponential absorption. In [10], an analytical expression was obtained for the interband absorption spectrum when:

$$n_1 = n_2 = 1/2: \quad \alpha(\hbar\omega) = \frac{B}{4\hbar\omega E_g} \left[ 2(\hbar\omega - E_g) \sqrt{E_g \hbar\omega} - (E_g - \hbar\omega)^2 \operatorname{arctg} \left( \frac{E_g - \hbar\omega}{2\sqrt{E_g \hbar\omega}} \right) \right]. \quad (18)$$

It was determined that when,  $B = 1.71 \cdot 10^5 \text{ sm}^{-1}$  and  $E_g = 1.78 \text{ eV}$  corresponds to the experimentally determined and calculated results obtained from formula (18) for the interband absorption spectrum (Fig. 2 - curve a).

In [11] studied the spectra of exponential absorption and for the analytical solution of exponential absorption, the following expressions were obtained:

$$\alpha(\hbar\omega) = \frac{B}{(\beta_2 - \beta_1)\hbar\omega} \exp(\beta_1(\hbar\omega - E_g)) \exp((\beta_1 - \beta_2)(\varepsilon_C - \varepsilon_0)) [\exp((\beta_2 - \beta_1)\hbar\omega) - 1]. \quad (19)$$

It is also shown there that  $B$  and  $E_g$  have equal values for the entire region of the optical absorption coefficient.

It was found that the results calculated by the equation (19) of the exponential absorption determined from the experiment are consistent with each other, then  $\beta_1 = 24.2 \text{ eV}^{-1}$  and  $\beta_2 = 31.7 \text{ eV}^{-1}$  (Fig. 2, curve b). Since  $\varepsilon_{D1}$  and  $\varepsilon_{D2}$  are the intersection points of the exponential tails of allowed bands and the distribution of electronic states in defects, we calculate them using the following equations:

$$N(\varepsilon_C) \exp(\beta_2(\varepsilon_{D2} - \varepsilon_C)) = 2g(\varepsilon_D) \exp(b(\varepsilon_{D2} - \varepsilon_D)), \quad (20)$$

$$N(\varepsilon_V) \exp(-\beta_1(\varepsilon_{D1} - \varepsilon_V)) = 2g(\varepsilon_D) \exp(-b(\varepsilon_{D1} - \varepsilon_D)). \quad (21)$$

From this we obtain the following expressions:

$$\varepsilon_{D1} = \left( \ln \left( \frac{N(\varepsilon_V)}{2g(\varepsilon_D)} \right) + b\varepsilon_D + \beta_1\varepsilon_V \right) / (b + \beta_1), \quad (22)$$

$$\varepsilon_{D2} = \left( \ln \left( \frac{2g(\varepsilon_D)}{N(\varepsilon_C)} \right) + b\varepsilon_D + \beta_2\varepsilon_C \right) / (b + \beta_2). \quad (23)$$

Calculations using equations (22) and (23) showed that when the value of  $\beta_1 = b$  and  $\beta_2 = b$  changes in the range (12–35)  $\text{eV}^{-1}$ , the values of  $\varepsilon_{D1}$  and  $\varepsilon_{D2}$  change within  $\Delta\varepsilon \approx 0.1 \text{ eV}$ . Calculations of the partial spectra of the absorption coefficient in defects showed that these changes in  $\varepsilon_{D1}$  and  $\varepsilon_{D2}$  do not significantly affect the shape of the defect absorption spectra.

Calculated equations (7), (13) for the conditions  $\varepsilon_{D1}-\varepsilon_V < \hbar\omega$  and  $\varepsilon_C-\varepsilon_{D2} < \hbar\omega$ . Calculated equations (9), (17), (15) and (10), (11) and (16) and for the conditions  $\varepsilon_{D1}-\varepsilon_V < \hbar\omega$  and  $\varepsilon_C-\varepsilon_{D2} > \hbar\omega$ .

The forms of these equations are close to each other; it can be considered that the partial spectra of defect absorption calculated by these equations almost do not differ from each other. Therefore, we calculate the partial spectra of defective absorption only for the defect  $\varepsilon_D-\varepsilon_V=0.5 \text{ eV}$  and  $g(\varepsilon_D^+) = 3 \times 10^{15} \text{ eV}^{-1} \text{ cm}^{-3}$  for optical transitions of electrons from the defect to the tail of the conduction band.

It can be seen from the above equations that as the value of  $g(\varepsilon_D)$  increases or decreases, these spectra move in parallel up or down, respectively. Calculations were obtained using equations (10) and (11) for  $n_l=1, n_l=0$ , and

numerical calculations obtained for  $n_1=1/2$  showed that these spectra do not differ from each other at all (Fig. 3). To establish the value of  $g(\epsilon_D)$ , we use the equation for determining the concentration of defective states and obtain:

$$N_D = \int_{-\infty}^{\infty} \frac{g(\epsilon_D)}{ch(b(\epsilon - \epsilon_D))} d(\epsilon) = \frac{2}{b} g(\epsilon_D) \arctg \exp(b(\epsilon - \epsilon_D)) \Big|_{-\infty}^{\infty} = \frac{2\pi}{b} g(\epsilon_D), \quad g(\epsilon_D) = \frac{bN_D}{2\pi} \quad (24)$$

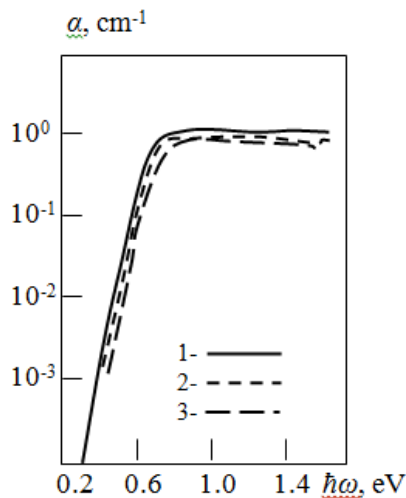


Figure 3. Partial spectra of optical transitions of electrons between allowed zones and defects  $1-n_1=1, 2-n_1=1/2, 3-n_1=0$ . Calculations are made for defect  $D_0$ .

The calculation results obtained by equation (24) are shown in Table 1.

Table 1. Calculated data for  $g(\epsilon_D)$  obtained using equation (24).

	$b, eV^{-1}$	$g(\epsilon_D), eV^{-1} sm^{-3}$	$b, eV^{-1}$	$g(\epsilon_D), eV^{-1} sm^{-3}$	$b, eV^{-1}$	$g(\epsilon_D), eV^{-1} sm^{-3}$
$D^0$	12	$8.6 \times 10^{15}$	24	$1.72 \times 10^{16}$	32	$2.29 \times 10^{16}$
$D^-$	12	$5.73 \times 10^{15}$	24	$1.15 \times 10^{16}$	32	$1.53 \times 10^{16}$
$D^+$	12	$5.73 \times 10^{15}$	24	$1.15 \times 10^{16}$	32	$1.53 \times 10^{16}$

The results of calculations obtained by equations (7) and (9) for various values of  $b$  at  $\epsilon_D - \epsilon_V = 0.5 eV$  and  $g(\epsilon_D^-)$  are shown in Figure 4. This figure also shows the spectrum for comparison optical transitions of electrons from a defect to the conduction band, calculated by equation (11). It can be seen from this figure that the partial spectra determined by the optical transitions of electrons between defects, the tails of allowed bands, at different values of  $b$  have practically no effect on the value of the defect absorption spectrum.

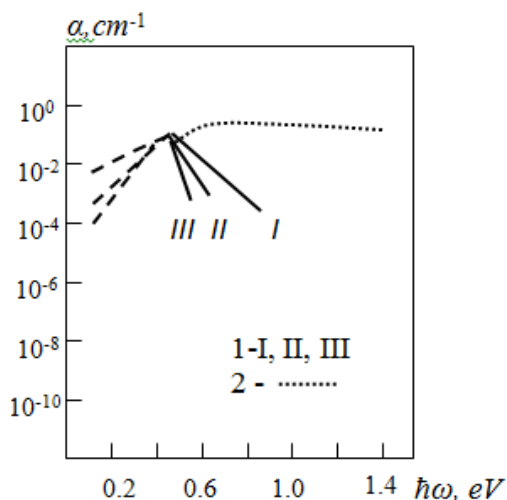


Figure 4. Partial spectra of optical transitions of an electron 1-from a  $D^-$  defect to the tail of the conduction band I -  $b=12 eV^{-1}$ , II -  $b=24 eV^{-1}$ , III -  $b=32 eV^{-1}$ , -when  $\epsilon_{D^-} - \epsilon_V > \hbar\omega$ , - when  $\epsilon_{D^-} - \epsilon_V < \hbar\omega$ . 2-partial spectrum of optical transitions of an electron from a  $D^-$  defect to the conduction band

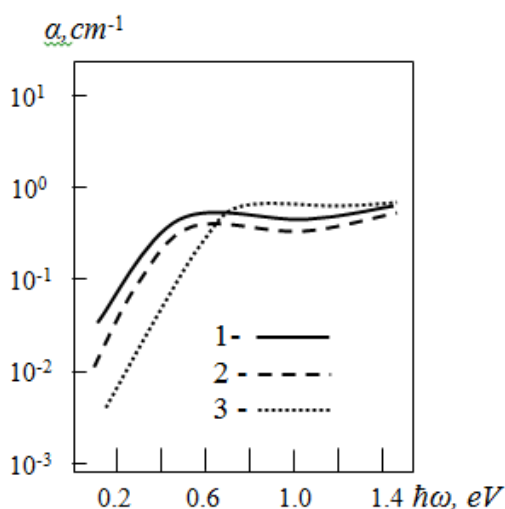


Figure 5. Total values of partial spectra of the defect absorption coefficient obtained using equations (7), (9), (11), (13), (16), (17). For 1- $D^+$ , 2- $D^-$  and 3- $D^0$ , forming optical transitions between defect states and allowed bands and their tails. Calculations were carried out for  $b=12 eV^{-1}$

It is known that the total sum of partial absorption spectra corresponding to all optical transitions of electrons with the participation of defect states is determined in the experimental spectra of defective absorption. Therefore, for each defect  $\varepsilon_{D0-\varepsilon_V}=0.78$  eV,  $\varepsilon_{D-\varepsilon_V}=0.5$  eV,  $\varepsilon_{D+\varepsilon_V}=1.28$  eV calculated by equations (7), (9), (10) (11) and (13), (15), (16), (17) sums of partial absorption spectra are shown in Fig. 5. It should be noted that the experiment gives the total value of these spectra. It can be seen that when the energy of absorbed photons is greater than 0.6 eV, these spectra have almost the same form. But, none of them can explain the defective absorption spectrum of the representations in Fig. 2. Probably, this sample has the values of the energy position, or the concentration of these defects does not correspond to the above values.

## CONCLUSIONS

Thus, in the present work, we carried out a theoretical study of the defect absorption spectra of hydrogenated amorphous silicon. It was found that partial spectra determined by optical transitions of electrons between allowed bands and defects play a key role in determining the defect absorption spectrum. It was found that the spectrum of defective absorption in the case of a power-law distribution of the density of electronic states in allowed bands does not depend on the value of the exponent.

## ORCID

✉ Rustamjon G. Ikramov, <https://orcid.org/0000-0003-1629-1300>; ✉ Khurshidbek A. Muminov, <https://orcid.org/0000-0001-6547-2592>

## REFERENCES

- [1] V.I. Fistul, *Introduction to semiconductor physics*, (Vysshaya shkola, Moscow, 1984). (in Russian)
- [2] M.S. Ablova, G.S. Kulikov, and S.K. Persheev, "Metastable states of undoped amorphous hydrogenated, created by  $\gamma$  - irradiation," FTP, **36**(8), 1001-1003 (2002). (in Russian)
- [3] M. Gunes, and Ch.R. Wronski, "Differences in densities of charged defect states and kinetics of Staebler-Wronski effect in undoped (nonintrinsic) hydrogenated amorphous silicon thin films," J. Appl. Phys. **81**(8), 3526-3536 (1997). <https://doi.org/10.1063/1.365000>
- [4] R.G. Ikramov, A.A. Mamaxanov, M.A. Nuriddinova, R.M. Jalolov, Kh.A. Muminov, and B.Q. Sultonov, "Calculation of the interband absorption spectrum of amorphous semiconductors using the Kubo-Greenwood formula," Journal of Applied Science and Engineering, **25**(5), 767-772 (2022). <http://jase.tku.edu.tw/articles/jase-202210-25-5-0007>
- [5] G.D. Cody, "Hydrogenated Amorphous Silicon, Part B, Optical Properties," in: *Semiconductors and Semimetals*, vol. 21, edited by J.I. Pankove, (Academic Press Inc., Orlando, 1984).
- [6] S.K. O'Leary, "On the relationship between the distribution of electronic states and the optical absorption spectrum in amorphous semiconductors," Solid State Commun. **109**, 589-594 (1999). [https://doi.org/10.1016/S0038-1098\(98\)00605-X](https://doi.org/10.1016/S0038-1098(98)00605-X)
- [7] S. Zainobidinov, R.G. Ikramov, and R.M. Zhalalov, "Urbach energy and tails of the density of states of amorphous semiconductors," Journal of Applied Spectroscopy, **78**(2), 223-227 (2011). <https://doi.org/10.1007/s10812-011-9450-9>
- [8] R.G. Ikramov. "Distribution function of electron states of dangling bonds in amorphous semiconductors," Estestv. Tekhn. Nauki, **6**, 53 (2007) (in Russian).
- [9] F. Orapunt, and S.K. O'Leary, "A quantitative characterization of the optical absorption spectrum associated with hydrogenated amorphous silicon," Mater Electron. **20**, 1033-1038 (2009). <https://doi.org/10.1007/s10854-008-9825-8>
- [10] S. Zainobidinov, R.G. Ikramov, R.M. Zhalalov, and M.A. Nuriddinova, "Distribution of electron density of states in allowed bands and interband absorption in amorphous semiconductors," Optics and spectroscopy, **110**(5), 762-766 (2011). <https://doi.org/10.1134/S0030400X11030271>
- [11] R.G. Ikramov, M.A. Nuriddinova, and Kh.A. Muminov, "Calculation of the density of electronic states in the valence band from the experimental spectrum of interband absorption of amorphous semiconductors," Journal of Applied Spectroscopy, **88**(3), 378-382 (2021). <https://doi.org/10.1007/s10812-021-01200-9>

## НЕБЕЗПЕЧНІ ЗВ'ЯЗКИ МІЖ ГІДРОГЕНІЗОВАНИМ АМОΡФНИМ КРЕМНІСМ ТА СПЕКТРАМИ ПОГЛИНАННЯ ДЕФЕКТІВ








Рустамжон Г. Ікрамов, Хуршидбек А. Мумінов, Машхура А. Нурітдінова, Бобур Қ. Сутонов,  
Ойбек Т. Холмірзаєв, Азамходжа А. Мамаханов

Наманганський інженерно-технологічний інститут, вул. Косонсой, 7, Наманган 160115, Узбекистан

У даній роботі теоретично досліджено спектри дефектного поглинання дефектів, характерних для гідрогенізованого аморфного кремнію. Показано, що для визначення спектрів поглинання дефектів за формулою Кубо-Грінвуда необхідно записати невизначений інтеграл у цій формулі в певному вигляді. Було виявлено, що електронні переходи за участю дефектних станів поділяються на дві частини в залежності від енергії поглинених фотонів. Значення парціального дефектного спектра поглинання при малих енергіях поглинених фотонів майже не впливають на загальний спектр поглинання дефектів. Встановлено, що основну роль у визначенні спектра поглинання дефектів відіграють парціальні спектри, які визначаються оптичними переходами електронів між дозволеними зонами та дефектами. Показано, що при ступеневому розподілі щільності електронних станів у дозволених зонах спектри оптичних переходів між ними та дефектами не залежать від величини цієї потужності.

**Ключові слова:** аморфні напівпровідники; оптичні переходи електронів за участю дефектів; спектри поглинання дефектів; часткові спектри

## EFFECT OF COMPENSATION DEGREE AND CONCENTRATION OF IMPURITY ELECTROACTIVE SELENIUM ATOMS ON CURRENT AUTO-OSCILLATION PARAMETERS IN SILICON

 Nurulla F. Zikrillaev<sup>#</sup>,  Kutup S. Ayupov,  Manzura M. Shoabdurakhimova\*,  
 Feruza E. Urakova,  Yoldoshali A. Abduganiev,  Abdujalol A. Sattorov,  Latofat S. Karieva

*Tashkent State Technical University, Uzbekistan, 100095, Tashkent, University St., 2*

*\*Corresponding Author e-mail: [shoabduraximova.m@gmail.com](mailto:shoabduraximova.m@gmail.com), #e-mail: [zikrillaev.n@gmail.com](mailto:zikrillaev.n@gmail.com)*

*Received September 25, 2023; revised October 30, 2023; accepted November 1, 2023*

One of the crucial phenomena is auto-oscillations of current in elementary and binary ( $A^{III}B^V$ ,  $A^{II}B^{VI}$ ) semiconductor materials, which allow the creation of solid-state oscillators with a wide frequency range from  $10^{-3}$  to  $10^{-6}$  Hz. In this paper, we show the results of a study on the effect of the degree of compensation ( $K$ ) and the concentration of electroactive impurity selenium atoms on the excitation conditions and parameters (amplitude, frequency) of the auto-oscillation current associated with temperature and electrical instability in silicon. In the research, silicon doped with selenium atoms  $Si\langle Se \rangle$  of identical geometrical dimensions has been used. The compensation degree of the initial boron atoms with impurity selenium atoms in the samples is in the range of  $K = 2N_B/N_{Se} = 0.94-1.1$ . It was found that excitation conditions, the amplitude and frequency of auto-oscillation current significantly vary depending on the degree of compensation of selenium atoms with boron atoms in the initial silicon. Obtained experimental results showed that the auto-oscillation current in silicon doped with impurity selenium atoms is characterized by ease of control with stable parameters (amplitude and frequency), which makes it possible based on this unique physical phenomenon to develop and create oscillatory circuits in information technology.

**Keywords:** *Selenium; Diffusion; Boron; Amplitude; Frequency; Illumination; Concentration; Auto-oscillation; Silicon; Conduction band; Valence band*

**PACS:** 61.82.Bg, 68.55.Ln, 68.60.Dv, 68.47.Fg, 85.30.-z

### INTRODUCTION

The detected auto-oscillations of current in semiconductors, from the scientific and applied point of view, are one of the most striking and promising physical effects enabling the development of a new scientific direction of nonequilibrium thermodynamic effects in solids and their application to electronics [1-4].

A literature review has presented that there has not been sufficiently studied research on the physical mechanisms of current auto-oscillation excitation and the regularities of parameter changes kinetics (such as amplitude and frequency) and the physics of transients for different types of current auto-oscillations within a same semiconductor material [1-4]. Furthermore, there is a lack of reliable theoretical and experimental data regarding the thermodynamic conditions necessary for the existence of an auto-oscillating environment that could serve as a source of regular, stable, reproducible current auto-oscillations with controllable parameters [5-7].

In the applied aspect, the auto-oscillations of current detected in semiconductors have significant potential, particularly in the development of new functional electronic devices (solid-state generators, memory and storage, recording and transmission information, optoelectronic receivers, etc.) and the possibility of a fundamentally new generation of sensors for physical quantities that utilize an amplitude-frequency output [8-10].

The successful resolution of the scientific and practical challenges associated with auto-oscillation processes requires the implementation of these processes within specially created vibrational media based on semiconductor materials that are in a highly non-equilibrium thermodynamic state. An auto-oscillating environment is one in which each physical small element in it should have potential auto-oscillation properties, and these elements are could be connected through transfer processes, such that the excited oscillation propagates through the volume of the material being investigated [12,13]. Therefore, it requires to investigate the physical properties of the thermodynamic conditions for the existence of auto-oscillating environments in semiconductors with highly non-equilibrium thermodynamic states, and to determine the technological feasibility of creating such environments. The analysis of the creation of auto-oscillating environments highlights the importance of studying auto-oscillation processes from both scientific and applied perspectives.

It was found that the existence of deep energy levels of impurity atoms, which are the main requirement for current auto-oscillation excitation in semiconductors and semiconductor structures, is necessary for the observation of current auto-oscillation.

When conducting a literature survey [5-12] on the production of silicon doped with impurity atoms, it was discovered that there are several experimental data points that do not fit into the framework of the current theory of deep levels. These anomalies have been identified and include:

- the presence of sufficiently many energy levels of the same impurities in silicon which cannot be easily explained by the electronic structure or their position in the crystal lattice.
- an unstable state of deep centers where with time or rising temperature new energy levels with different characteristics appear.
- energy level bands with different widths detected for many impurity atoms in silicon cannot be explained using existing theory and no data on energy level distribution inside the bands are available so far.
- for many impurity atoms energy levels with the same values in the band gap of silicon were found.

The above-mentioned data can't be explained by the existing theory of deep-level physics [13,14]. Scientific results which have been obtained by investigation of auto-oscillations of current in silicon diffusively doped with impurity selenium atoms give ground for the creation of a new theory of deep levels.

Researches on the impact of the concentration of electroactive transition group atoms in silicon are important for understanding the nature of deep centers created by these elements in the semiconductor and expanding their use as a new material for semiconductor electronics [11–19]. This study focuses on the effect of the initial concentration of small boron impurity atoms on the concentration of electroactive selenium atoms that create deep energy levels in silicon. The results show that changing the concentration of boron impurity atoms in initial silicon within the range of  $N_B = 1.4 \cdot 10^{14} - 3.1 \cdot 10^{16} \text{ cm}^{-3}$  increases the concentration of electroactive selenium atoms by two orders. However, the concentration of electroactive selenium atoms in silicon was still two orders of magnitude lower than the maximum solubility limit [18-21]. The analysis also described that the concentration of electroactive impurity atoms, which create deep energy levels, depends significantly on the type and concentration of the impurity (boron or phosphorus) in the initial silicon. Furthermore, it was found that these impurity atoms interact not only with the basic atoms of silicon and atoms of the initial impurity but also with other uncontrolled impurities and defects in silicon.

### METHODS

To develop a reproducible technology for producing compensated silicon doped with selenium atoms, we determined the temperature regimes for obtaining samples with the same resistivity and type of conductivity at different concentrations of electroactive impurity atoms based on those described in [22-24]. These results made it possible to clearly define the technological conditions to produce compensated silicon with the maximum concentration of electroactive impurity atoms of selenium. The developed reproducible technology for the production of compensated silicon with given electrophysical parameters allows to control the electrophysical parameters of the material not only by temperature and time of diffusion annealing but also by the choice of concentration of initial impurity boron atoms in silicon (Table 1).

**Table 1.** Possibility to control the electrophysical parameters of the material based on the developed technology

No	The elasticity of selenium atom vapor pressure, atm	Type of conductivity of samples obtained after diffusion	Specific resistance, Ohm·cm	Carrier concentration, $\text{cm}^{-3}$
1	0.1	p	18	$1.2 \cdot 10^{15}$
2	0.3	p	60	$3.5 \cdot 10^{14}$
3	0.5	p	$3.1 \cdot 10^2$	$6.7 \cdot 10^{13}$
4	0.75	p	$4.7 \cdot 10^3$	$4.5 \cdot 10^{12}$
5	1.0	p	$6.8 \cdot 10^4$	$3.1 \cdot 10^{11}$
6	1.5	p	$1.25 \cdot 10^5$	$1.7 \cdot 10^{11}$
7	2.0	n	$1.1 \cdot 10^5$	$6.7 \cdot 10^{10}$
8	2.5	n	$8.3 \cdot 10^4$	$8.2 \cdot 10^{10}$
9	3.0	n	$2.6 \cdot 10^4$	$2.3 \cdot 10^{11}$
10	4.0	n	$5.9 \cdot 10^3$	$8.8 \cdot 10^{11}$
11	Initial sample KDB-10	p	10	$2 \cdot 10^{15}$

The analysis of obtained sample after diffusion showed that impurity selenium atoms strongly destroy the surface of silicon, leading to surface erosion and even complete destruction of the crystal. Therefore, when diffusing selenium atoms into silicon, the main diffusion parameters should be taken into account. One of the main diffusion parameters is the vapor pressure of the diffusant when diffusion occurs at high temperatures. To overcome these difficulties, the task was set to accomplish diffusion at different vapor pressures of diffusant selenium from 0.5 atm to 2 atm.

According to the research that was conducted, it was showed that when the selenium vapor pressure is between 0.5 and 1 atmosphere, there is insignificant erosion observed on the surface of silicon. Further entrainment of diffusant vapor pressure leads to surface erosion and further silicon destruction. Thus, the optimum diffusant vapor pressure for the diffusion of silicon by impurity selenium atoms was established. It was also found that the surface erosion depends on the quality of initial silicon surface treatment - with improvement of silicon surface treatment (in this case, the quality of polishing was changed using White's chemical etchant), the erosion rate was decreased [25]. Thus, it was determined that to reduce surface erosion during diffusion by selenium, it is necessary to treat the surface carefully and to polish the surface of the initial silicon samples.

### EXPERIMENTAL PART

For the investigation, initial monocrystalline silicon of p-type with resistivity values of 1, 2, 10, and 100 Ohm·cm was used. The initial silicon samples had boron impurity concentrations ( $N_B$ ) ranging from  $1.4 \cdot 10^{14}$  to  $3.1 \cdot 10^{16} \text{ cm}^{-3}$ . These

initial silicon materials were obtained using Czochralski's method, and the oxygen concentration in them was practically the same and in the order of  $N_{O_2} = (5-7) \cdot 10^{17} \text{ cm}^{-3}$ . To conduct the research, 50 samples of the same geometric dimensions were produced from each of the initial materials. For the study, 50 pieces of samples with the same geometric dimensions were made from each starting material. Diffusion of selenium was carried out in a "Magnetic" diffusion electric furnace from the gas phase in the same conditions (temperature, diffusion time, diffusant vapor pressure, and cooling rate) in evacuated quartz ampoules to  $P = 10^{-6} \text{ mm Hg}$ . At the same time, two samples from each initial material were placed in each quartz ampoule to ensure the same doping conditions. The experiment was repeated 5 times. Each time, the initial samples were annealed under the same conditions without selenium impurities to assess the influence of selenium impurities in the diffusion process on the electrophysical properties of the initial silicon.

### THEORETICAL CALCULATIONS AND RESEARCH RESULTS

Measurements conducted on electrophysical properties of samples derived from KDB silicon after the diffusion of selenium atoms revealed that the concentration of electroactive selenium atoms varied considerably depending on the initial boron concentration in silicon, despite the identical doping conditions of temperature, diffusion time, and cooling rate. Electrophysical parameters of silicon samples after diffusion were measured based on the Hall effect method using Ecopia HMS-3000 Hall Measurement System. The electroneutrality equation was used to determine the overall concentration of electroactive selenium atoms in the samples obtained after diffusion. During computations, we considered sample parameters that accounted for the extent of filling of both energy levels of selenium ( $E_1 = E_C - 0.24 \text{ eV}$ ;  $E_2 = E_C - 0.5 \text{ eV}$ ) within the silicon band gap [26,27].

Selenium concentration was theoretically determined by the following formula for compensated samples p-Si<B,Se>:

$$N_{Se} = 1/2 \cdot (p_0 - p - N_{TD}), \quad (1)$$

For overcompensated n-Si samples <B, Se> was determined:

$$N_{Se} = (p_0 + n_0 + f(E_1) \cdot N_{Se} + f(E_2) \cdot N_{Se} - N_{TD}), \quad (2)$$

$$f(E_2) = N_{Se} / 2 \cdot (1 + A \cdot \exp(-F - E_2) / k \cdot T), \quad (3)$$

$$F = k \cdot T \ln(N_C / n), \quad (4)$$

$$N_{Se} = 1/2 \cdot (p_0 - p - N_{TD}), \quad (5)$$

where  $p_0$  and  $p$  are concentrations of holes before and after diffusion of selenium atoms, respectively.  $N_{TD}$  is concentration of thermodonors,  $f(E_1)$  and  $f(E_2)$  are degrees of filling of the 1st and 2nd deep energy levels of selenium, respectively.  $n_0$  and  $n$  and electron concentrations before and after diffusion of selenium atoms accordingly, respectively. The values  $p_0$  and  $p$  were determined from Hall measurements of samples before and after diffusion.  $N_{TD}$  is determined by measuring carriers' concentration before and after diffusion in control (undoped) samples, heat-treated under the same diffusion technological conditions in the temperature range  $T = 1100-1250^\circ\text{C}$  in time interval  $t = 5-10$  hours. Also, the solubility values of impurity selenium atoms in silicon at a given diffusion temperature were de-fined.

To determine the value of the ionization energy of impurity selenium atoms in silicon, the infrared (IR) and temperature quenching (TQ) photoconductivity of silicon samples doped with impurity selenium atoms were selected with the same resistivity, conductivity type, and geometric dimensions. The concentration of electrically active selenium atoms in the samples studied differed by about 30 times.

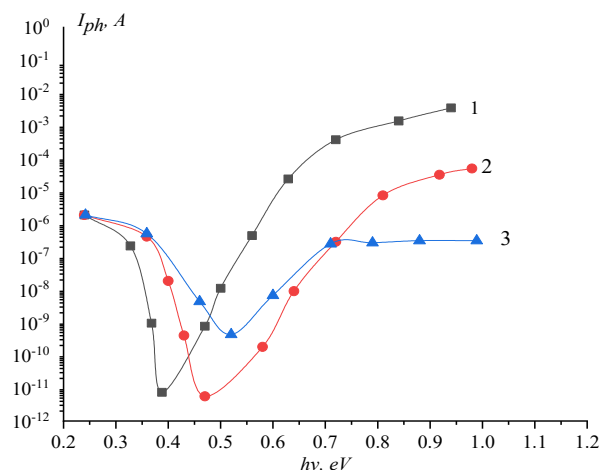


Figure 1. Spectral dependence of photocurrent in Si<Se> samples

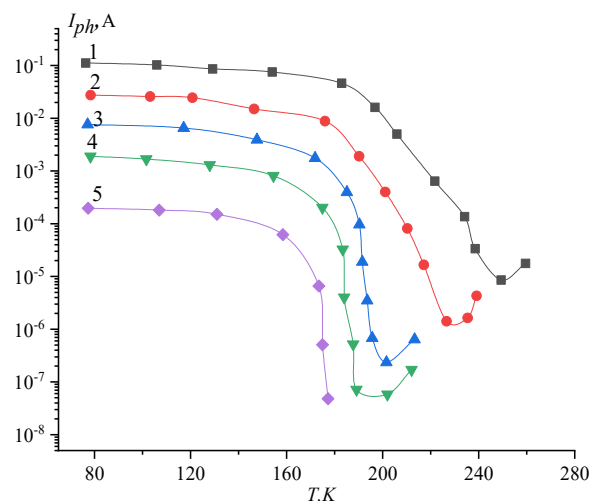
1 –  $\rho = 8.7 \cdot 10^4 \text{ Ohm}\cdot\text{cm}$  (initial KDB-1);  $N_{Se} \approx 3.1 \cdot 10^{16} \text{ cm}^{-3}$ ; 2 –  $\rho = 8 \cdot 10^4 \text{ Ohm}\cdot\text{cm}$  (initial KDB-10)  $N_{Se} \approx 2 \cdot 10^{15} \text{ cm}^{-3}$ ;  
3 –  $\rho = 8 \cdot 10^4 \text{ Ohm}\cdot\text{cm}$  (source KDB-100)  $N_{Se} \approx 1.4 \cdot 10^{14} \text{ cm}^{-3}$  at temperature  $T = 80\text{K}$ ,  $E = 20 \text{ V/cm}$ .

Figure 1 illustrates the spectral dependence of photoconductivity under the same background photocurrent value with different concentrations of selenium atoms as electroactive impurities. In Figure 1, the maximum depth of IR extinction of a photocurrent is observed in the samples where the concentration of electroactive selenium atoms is  $N_{Se} = 3.1 \cdot 10^{16} \text{ cm}^{-3}$  and reaches 5 orders of magnitude. It is established that with decreasing concentration of electroactive impurity atoms, the quenching multiplicity decreases, and the energy of the corresponding quenching maximum shifts to high values.

It is shown that with increasing concentration of electroactive selenium atoms, the quenching interval decreases, i.e., photocurrent decreases more sharply, and the energy interval of incident quanta in which IR quenching of photocurrent is observed narrows.

An anomalous course is observed in silicon doped with impurity selenium atoms when studying the temperature dependence of photocurrent. Figure 2 shows the temperature dependence of photoconductivity quenching (TDPQ) in silicon doped with selenium atoms. As seen from Figure 2, when a temperature rises from  $T = 80 \text{ K}$  to  $T = 140 \text{ K}$ , the photocurrent does not change essentially. In the temperature range  $T = 140\text{--}180 \text{ K}$ , its decrease is observed, i.e., there is a temperature quenching of photoconductivity well-known in the literature [28,29].

The results of TDPQ studies in compensated silicon samples doped with selenium atoms (Se) have shown that the onset and depth of quenching strongly depend on the background illumination intensity, compensation degree, and concentration of electroactive impurity atoms (Figure 2).



**Figure 2.** Temperature quenching of photoconductivity at different background illuminations in Si<Se> with  $\rho = 8 \cdot 10^4 \text{ Ohm}\cdot\text{cm}$ ,  $E = 40 \text{ V/cm}$ , 1 – 25 lux, 2 – 10 lux, 3 – 5 lux, 4 – 1 lux, 5 – 0.1 lux.

It is feasible to observe TDPQ over a broad temperature range by adjusting the degree of compensation, background illumination, and photocurrent value in compensated silicon. The obtained data indicate that the depth, rate, and area of both IR and temperature quenching of photoconductivity in silicon samples containing impurity selenium atoms can be controlled by adjusting the concentration of these electroactive impurity atoms. From the results of the analysis, it was found that the energy levels of impurity selenium atoms with the ionization energy  $\text{Si}\langle\text{Se}\rangle - E_C - 0,5 \text{ eV}$ , which is associated with the double positive ionization of selenium atoms, are responsible for the IR and TQ photoconductivity in silicon.

The results showed that regardless of the compensation degree of boron atoms in the initial silicon doped with impurity selenium atoms, the current auto-oscillation was excited at a certain integral intensity interval ( $I_{\min} - I_{\max}$ ). With the growth of compensation degree value (resistivity), at the same value of threshold field strength  $E_{th}$  at which the auto-oscillation of current is observed, the  $I_{\min}$  intensity value decreased, and the interval between  $I_{\min} - I_{\max}$  widened (Figure 3). Thus, it was found that conditions of auto-oscillation excitation in silicon samples with different compensation degrees (resistivity) have an identical character. It was also found that the amplitude and frequency of current auto-oscillation, in their turn, strongly depend on excitation conditions.

In this work, we focused on determining the parameters of silicon samples doped with impurity selenium atoms with the most optimal characteristics (forms) of current auto-oscillation. Based on the analysis of the findings, we have determined that the silicon p-Si<Se> - samples with a resistivity of  $\rho = 8 \cdot 10^4 \text{ Ohm}\cdot\text{cm}$  is appropriate for studying current auto-oscillations with reproducible and preset parameters from the compensation degree, which was approximately equal to 0.999. When an electric current intensity of  $E = 200 \text{ V/cm}$  was applied to these samples, the maximum and minimum values of current auto-oscillation amplitude varied within the range of  $I_{\min} = 10^{-8} \text{ A}$  to  $I_{\max} = 2.5 \cdot 10^{-1} \text{ A}$ , while the frequency was within the interval of  $f = 10^{-3} - 10 \text{ Hz}$ .

To elucidate the influence of electroactive concentration of impurity selenium atoms on parameters of current auto-oscillations, we received samples with the same size and degree of compensation  $K = 0.999$ . Thus, the concentration of electroactive selenium atoms was in the interval  $N_{Se} = (2\text{--}31) \cdot 10^{15} \text{ cm}^{-3}$  and with increasing of electroactive selenium atoms concentration  $N_{Se}$  value of  $E_{th}$  and amplitude of auto-oscillations was decreasing and the frequency was increased (Table 2).

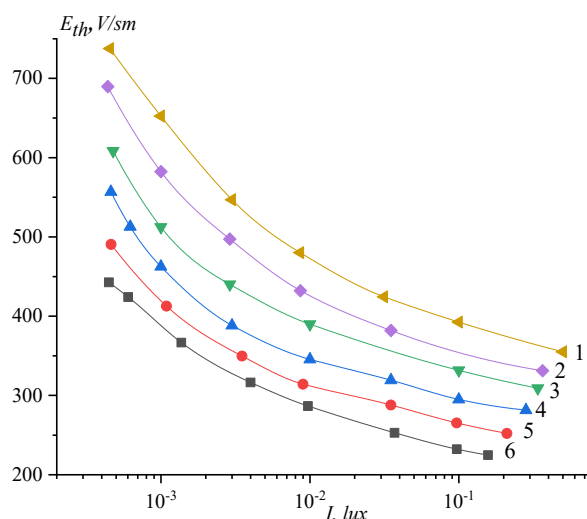


**Figure 3.** The dependence of changing of threshold field  $E_{th}$  on integral light intensity for Si<Se> samples with different resistivities ( $\rho$ ). 1 –  $5.3 \cdot 10^3$ ; 2 –  $8.7 \cdot 10^3$ ; 3 –  $3.2 \cdot 10^4$ ; 4 –  $5.8 \cdot 10^4$ ; 5 –  $9.1 \cdot 10^4$ ; 6 –  $2.1 \cdot 10^5$  Ohm·cm p-type; at  $T = 80$  K,  $E = 200$  V/cm.

**Table 2.** Effects of electroactive concentrations of impurity selenium atoms in silicon on auto-oscillation current parameters

Paragraph number	The concentration of electroactive selenium atoms $N_{Se} = 10^{15} \text{cm}^{-3}$	Threshold field $E_{th}$ , V/cm	Amplitude $J$ , mA	Frequency $f$ , Hz	Note
1	2	250	90	$5 \cdot 10^{-2}$	T = 80 K, I = $2.4 \cdot 10^{-6}$ W/cm <sup>2</sup> ·s at $h\nu = 1.1 \text{eV}$ , with K = 0.999
2	8	276	84	$9.4 \cdot 10^{-2}$	
3	31	315	78	$2.5 \cdot 10^{-1}$	

## DISCUSSION

It has been confirmed that the auto-oscillation of current in silicon samples doped with selenium atoms is observed when the value of compensation degree (K) is in the interval between 0.94 and 1.1, i.e. in crystals, where the Fermi level is within the compensation degree range from  $E_C - 0.45$  to  $E_V + 0.35$  eV. It is clear that in this energy interval in the band gap of silicon, there is only one donor level of double ionized impurity selenium atoms with ionization energy  $E_C - 0.5$  eV which is connected with the presence of clusters consisting of selenium atoms  $Se_4$  and  $Se_6$  [30]. The presence of clusters of selenium atoms consisting of twice positively ionized atoms leads to the appearance of strongly charged centers which allows the obtained silicon samples Si<Se> to be regarded as inhomogeneous material. Inhomogeneous material for which the barrier model of inhomogeneity proposed by authors of books [31,32] is applicable (Figure 3).

According to barrier model, fluctuations of conduction and valence band topography arise in the semiconductor. The appearance of such inhomogeneities in semiconductors is attributed to the presence of impurity atoms, which can reach concentrations of  $N \approx 10^{18} - 10^{19} \text{cm}^{-3}$  under strong doping conditions. Due to their inhomogeneous distribution, these impurities cause fluctuations in the conduction and valence bands, resulting in inhomogeneities. In our situation, the concentration of impurity selenium atoms is two orders of magnitude lower ( $N_{Se} = 3.1 \cdot 10^{16} \text{cm}^{-3}$ ) than under strong doping conditions. It was shown that this impurity in silicon may be in the binary ionized state and form different complexes as  $Se_4$  and  $Se_6$  molecular compounds with charge always greater than  $\pm 2$  ( $n$  – number of selenium atoms in the cluster). The Dabaev screening radius of such complexes overlaps with each other and results in a fluctuating potential relief in compensated silicon. To explain the physical mechanism of the low-frequency current auto-oscillations observed in compensated silicon, a model based on conduction and valence band relief fluctuations is shown in Figure 4. According to the proposed model, at a constant illumination nonequilibrium electron fill the selenium level, while holes are localized in the potential wells of the valence band. In this case, the conductivity is determined by the concentration of holes at the leakage level, the value of which is determined by the value of the drift barrier.

Based on this model, it is possible to imagine that the excitation of current auto-oscillation occurs through the following mechanism. When Si<Se> samples are illuminated with energy greater than the band gap width of silicon at relatively low temperatures ( $T = 80 - 160$  K), non-equilibrium carriers - electrons and holes, which are located on energy barriers of conduction and valence bands are generated. Electrons are captured by clusters of doubly positively ionized selenium atoms, while holes are accumulated in energy minima of the valence band. Some of the holes, upon hitting the leakage level, participate in conduction, leading to an increase in photocurrent. Photocurrents are excited when the photocurrent due to holes at the valence leakage level is sufficient for Joule heating of the crystal. When a hole is heated, it acquires sufficient energy to overcome the recombination barrier and recombine with electrons trapped on clusters consisting of impurity selenium atoms. As a result, the current in the circuit and the temperature of the sample decreases, thus repeating the process periodically.



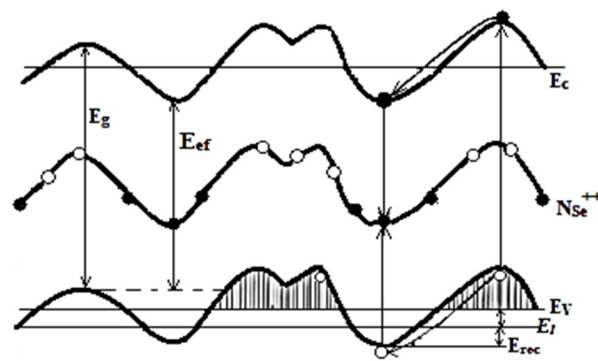


**Figure 4.** Barrier model of compensated silicon doped with impurity selenium atoms.

○-electrons, ●-holes,  $E_g$ -silicon band gap width,  $E_c$ - conduction band,  $E_v$ -valence band,  $E_{ef}$  - effective band gap width of inhomogeneous silicon,  $E_1$  - is the leakage level for the charge carriers (in this case the hole),  $E_{rec}$  - recombination energy.

The excitation conditions and current auto-oscillation parameters change depending on the compensation degree and can be interpreted based on the change of potential relief amplitude. The strongly compensated samples Si<Se> with a compensation degree of  $K \approx 1$  exhibit the highest potential relief values of heterogeneities. Therefore, the most effective separation of photoexcited charge carriers, electrons in conduction band cavities, and accumulation of holes in energy minima of the valence band occurs exactly in these crystals. This explains the maximum amplitude and decrease of the frequency of the current auto-oscillation in Si<Se> samples with resistivity  $\rho = 8 \cdot 10^4$  Ohm·cm. In Si<Se> samples, both at n- ( $K > 1$ ) and p- ( $K < 1$ ), the amplitude of formed potential relief due to material heterogeneity decreases due to the charge state decrease of selenium clusters and Debye screening of heterogeneity by uncompensated holes. Thus, the efficiency of separating carriers decreases, which is accompanied by the decrease of hole concentration participating in conductivity. In n-Si<Se> samples, the potential field of clusters could be compensated by increasing of field or illumination intensity, and in p-Si<Se> samples, the barriers are compensated by equilibrium holes.

The observed features of excitation conditions and current auto-oscillation parameters depending on the concentration of electroactive selenium atoms are related to the concentration of multipolarized clusters of impurity selenium atoms.

## CONCLUSIONS

We conclude that the temperature quenching effect of photoconductivity in silicon diffusively doped with impurity selenium atoms is responsible for the excitation of low-frequency current oscillations. The technology developed for producing silicon doped with impurity selenium atoms with reproducible and predetermined electro-physical parameters enables the creation of sensors for physical quantities such as temperature, illumination, electric and magnetic field, and pressure with amplitude-frequency output and generators of electromagnetic oscillations based on the obtained experimental results.

## Acknowledgments

The authors are grateful to Uzbek-Japanese Innovation Center of Youth, Institute of Ion Plasma and Laser Technology, Academy of Sciences of the Republic of Uzbekistan, and Tashkent State Technical University for providing to obtain scientific data on the elemental composition of silicon samples doped with impurity selenium atoms using the Ecopia HMS-3000 Hall Measurement System. A special thanks to Academician of the Academy of Sciences of the Republic of Uzbekistan R.A. Muminov for discussing the obtained results and valuable advice.

## ORCID

- Nurulla F. Zikrillaev, <https://orcid.org/0000-0002-6696-5265>; ●Kutup S. Ayupov, <https://orcid.org/0000-0002-2521-3921>  
 ●Manzura M. Shoabdurakhimova, <https://orcid.org/0000-0002-1879-6751>; ●Feruza E. Urakova, <https://orcid.org/0000-0001-5831-4019>  
 ●Yoldoshali A. Abduganiev, <https://orcid.org/0009-0008-1861-3805>; ●Abdujalol A. Sattorov, <https://orcid.org/0009-0003-0645-3051>  
 ●Latofat S. Karieva, <https://orcid.org/0009-0009-6147-0317>

## REFERENCES

- [1] L.L. Golik, V.E. Pakseev, Yu.I. Balkareĭ, M.I. Elinson, Yu.A. Rzhanoĭ, and V.K. Yakushin, *Fizika i Tekhnika Poluprovodnikov*, **18**(3), 502 (1984). <https://www.mathnet.ru/eng/phts/v18/i3/p502> (in Russian).
- [2] B.A. Akimov, V.A. Bogoyavlenskii, L.I. Ryabova, V.N. Vasil'kov, and E.I. Slyn'ko, *Semiconductors*, **33**(1), 6 (1999), <https://doi.org/10.1134/1.1187637>
- [3] K. Germanova, *Appl. Phys.* **2**, 321 (1973). <https://doi.org/10.1007/BF00896937>
- [4] A.Sh. Abdinov, Ya.G. Akperov, V.K. Mamedov, and E.P. Yu. Salaev, *Sov. Phys. Semicon.* **14**(4), 440 (1980). (in Russian).
- [5] L.L. Golik, V.E. Pakseev, M.I. Elinson, V.K. Yakushin, and V.S. Loskutov, *Fizika i Tekhnika Poluprovodnikov*, **21**(10), 1832 (1987). <https://www.mathnet.ru/eng/phts/v21/i10/p1832> (in Russian).
- [6] K.A. Ismailov, Kh.M. Iliev, M.O. Tursunov, and B.K. Ismaylov, *Semiconductor Physics, Quantum Electronics and Optoelectronics*. **24**(3), 255 (2021). <https://doi.org/10.15407/spqeo24.03.255>

- [7] G.A. Kartsivadze, Sh.M. Mirianashvili, and D.I. Nanobashvili, *Fizika i Tekhnika Poluprovodnikov*, **17**(7), 1304 (1983), <https://www.mathnet.ru/eng/phts2406>. (in Russian).
- [8] I.M. Vikulin, L.F. Vikulina, and V.E. Gorbachev, *Magnetosensitive semiconductor sensors*, (Odesa, 2016), p. 125. (in Russian).
- [9] Z. Chen, W. Ba, J. Zhang, X. Cong, M.K. Bakhadyrkhanov, and N.F. Zikrillaev, *Chinese Journal of Semiconductors*, **27**(9), 1582 (2006). <http://www.jos.ac.cn/article/id/3e45ea73-b447-4d41-bf01-2b166472d621> (in Chinese)
- [10] M.K. Bakhadyrkhanov, Kh. Azimkhuzhaev, N.F. Zikrillaev, A.B. Sabdullaev, and É. Arzikulov, *Semiconductors*, **34**(2), 171 (2000). <https://doi.org/10.1134/1.1187929>
- [11] I. Balkerei, L.L. Golik, and M.I. Elinson, *Autowave media Radioelectronic Communication*, (Moscow, Znanie, 1985). p. 64. (In Russian)
- [12] L.L. Golik, M.M. Gutman, V.E. Pakseev, M.K. Bakhadyrkhanov, N.F. Zikrillaev, and A.A. Tursunov, *Fizika i Tekhnika Poluprovodnikov*, **21**(8), 1400 (1987). <https://www.mathnet.ru/rus/phts817>. (in Russian)
- [13] K.V. Shalimova, *Physics of Semiconductors*, (Energoatomizdat, Moscow, 1989). (in Russian)
- [14] V.I. Fistulin, *Introduction to Semiconductor Physics*, (Vysshaya Shkola, Moscow, 1984). (in Russian)
- [15] M.K. Bakhadyrkhanov, S.B. Isamov, N.F. Zikrillaev, and M.O. Tursunov, *Semiconductors*, **55**(6), 542 (2021). <https://doi.org/10.1134/S1063782621060038>
- [16] M.K. Bakhadyrkhanov, S.B. Isamov, N.F. Zikrillaev, *Inorganic Materials*. **50**(4), 325 (2014), <https://doi.org/10.1134/S0020168514040025>
- [17] C. Zhaoyang, B. Weizhen, Z. Jian, M.K. Bakhadyrkhanov, and N.F. Zikrillaev, Pan Tao TI Hsueh Pao/Chinese Journal of Semiconductors, **27** (9), 1582 (2006). <http://www.jos.ac.cn/fileBDTXB/oldPDF/20060913.pdf>
- [18] P.G. Kasherininov, A.V. Kichaev, and A.A. Tomasov, *Semiconductors*, **29**(11), 1092 (1995), <https://doi.org/10.48550/arXiv.0704.2703>
- [19] M.K. Bakhadyrkhanov, U.Kh. Kurbanova, and N.F. Zikrillaev, *Semiconductors*, **33**, 20 (1999), <https://doi.org/10.1134/1.1187640>
- [20] T.S. Kamilov, L.L. Aksenova, B.Z. Sharipov, and I.V. Ernst, *Semiconductors*, **49**(10), 1281 (2015), <https://doi.org/10.1134/S1063782615100097>
- [21] M.K. Bakhadyrkhanov, N.F. Zikrillaev, and E.U. Arzikulov, *Pisma v Zhurnal Tekhnicheskoi Fiziki*, **17**(12), 1 (1991). (in Russian).
- [22] N.F. Zikrillaev, M.M. Shoabdurakhimova, K.S. Ayupov, S.B. Isamov, and K.I. Vakhobov, *Pribory*, **8**(266), 45 (2022). (in Russian). ID: 49457547.
- [23] M.K. Bakhadyrkhanov, S.B. Isamov, N.F. Zikrillaev, Kh.M. Iiev, G.Kh. Mavlonov, S.V. Koveshnikov, and Sh.N. Ibodullaev, *Surface Engineering and Appl. Electrochem*. **56**(6), 734 (2020). <https://doi.org/10.3103/S106837520060046>
- [24] A.A. Taskin, E.G. Tishkovskii, *Semiconductors*, **32**(11), 1162 (1998), <https://doi.org/10.1134/1.1187582>
- [25] M.K. Bakhadyrkhanov, Sh. I. Askarov, and N. Norkulov, *Phys. Stat. Solid. (a)*, **142**, 339 (1994), <https://doi.org/10.1002/pssa.2211420206>
- [26] M. Bakhadyrkhanov, B. Boltaks, G. Kulikov, *Sov. Phys. Solid State*, **14**(6), 1671 (1972).
- [27] M.S. Yunusov, A. Akhmadaliev, B.L. Oksengendler, and K.A. Begmatov, *Phys. Stat. Solid. (a)*, **149**, K 29 (1995), <https://doi.org/10.1002/pssa.2211490234>
- [28] Yu.A. Astrov, V.A. Shuman, L. Portsel, and A.N. Lodygin, *Semiconductors*, **48**(3), 428 (2014), <https://doi.org/10.1134/S1063782614030038>
- [29] M.K. Bakhadyrkhanov, S.B. Isamov, and N.F. Zikrillaev, *Russian Microelectronics*, **41**(6), 354(2012), <https://doi.org/10.1134/S1063739712030043>
- [30] A.A. Taskin, and E.G. Tishkovsky, *Phys. and Technic. of Semicon.* **32**(11), 1306 (1998). <https://journals.ioffe.ru/articles/viewPDF/34471> (in Russian)
- [31] V.N. Lozovskiy, G.S. Konstantikova, and S.V. Lozovskiy, *Nanotechnology in electronics* (Moscow, 2008), (in Russian)
- [32] V. Meshkalov, A. Lyubchenko, and M. Sheikman, *Nonequilibrium processes in semiconductors* (Kiev, 1981), (in Russian)

### ВПЛИВ СТУПЕНЯ КОМПЕНСАЦІЇ ТА КОНЦЕНТРАЦІЇ ДОМІШКОВИХ ЕЛЕКТРОАКТИВНИХ АТОМІВ СЕЛЕНУ НА ПАРАМЕТРИ АВТОКОЛИВАНЬ СТРУМУ В КРЕМНІЇ

Нурулла Ф. Зікріллаєв, Кутуп С. Аюпов, Манзура М. Шоабдурахімова, Феруза Е. Уракова, Йолдошлі А. Абдуганієв, Абдуджалол А. Сатторов, Лаофат С. Карієва

Ташкентський державний технічний університет, 100095, вул. Університетська, 2, Ташкент, Узбекистан

Одним із вирішальних явищ є автоколивання струму в елементарних і бінарних ( $A^{III}B^V$ ,  $A^{II}B^VI$ ) напівпровідникових матеріалах, які дозволяють створювати твердотільні осцилятори з широким діапазоном частот від  $10^{-3}$  до  $10^{-6}$  Гц. У даній роботі наведено результати дослідження впливу ступеня компенсації ( $K$ ) і концентрації електроактивних домішкових атомів селену на умови збудження та параметри (амплітуду, частоту) автоколивального струму, пов'язані з температурою і електричною нестабільністю у кремнії. У дослідженнях використовувався кремній, легований атомами селену  $Si<Se>$  однакових геометричних розмірів. Ступінь компенсації вихідних атомів бору домішковими атомами селену в зразках знаходиться в межах  $K = 2N_B/N_{Se} = 0,94-1,1$ . Встановлено, що умови збудження, амплітуда та частота струму автоколивань суттєво змінюються залежно від ступеня компенсації атомів селену атомами бору у вихідному кремнії. Отримані експериментальні результати показали, що автоколивальний струм у кремнії, легovanому домішковими атомами селену, характеризується простотою керування зі стабільними параметрами (амплітуда та частота), що дає змогу на основі цього унікального фізичного явища розробляти та створювати коливальні контури в інформаційних технологіях.

**Ключові слова:** селен; дифузія; бор; амплітуда; частота; освітлення; концентрація; автоколивання; кремній; зона провідності; валентна зона

## STRUCTURE AND PHYSICO-MECHANICAL PROPERTIES OF POLYELECTROLYTE COMPLEXES BASED ON SODIUM CARBOXYMETHYLCELLULOSE POLYSACCHARIDE AND POLYACRYLAMIDE

 **Sabitjan Ya. Inagamov**<sup>a\*</sup>,  **Ummatjon A. Asrorov**<sup>b,c</sup>,  **Erkin B. Xujanov**<sup>c</sup>

<sup>a</sup> Tashkent Pharmaceutical Institute, Mirabad district, Aibekst, 45b, 100015, Tashkent, Uzbekistan

<sup>b</sup> National University of Uzbekistan named after Mirzo Ulugbek, Tashkent, Uzbekistan

<sup>c</sup> Tashkent State Pedagogical University named after Nizami, Tashkent, Uzbekistan

\*Corresponding Author e-mail: [sabitjan1957@mail.ru](mailto:sabitjan1957@mail.ru)

Received August 31, 2023; revised September 22, 2023; accepted September 29, 2023

In this paper, the structure and physico-mechanical properties of films of polyelectrolyte complexes (PEC) based on sodium carboxymethylcellulose (Na-CMC) with linear polyacrylamide (PAA) have been studied. Polyelectrolyte complexes were obtained by mixing aqueous solutions of Na-CMC and PAA components in various ratios of components and pH of the medium. The structure of the obtained products was determined using IR spectroscopy and electron microscopy. IR spectra in the range 400–4000 cm<sup>-1</sup> were recorded on NIKOLET Magna-560 IR and Specord-75IR spectrophotometers (Carl Zeiss, GDR). The mechanical properties of films of polyelectrolyte complexes were determined by stretching at a constant speed of movement of the lower clamp, 50 mm/min, on an Instron-1100 automatic dynamometer (England) at room temperature. IR spectroscopic data showed that polyelectrolyte complexes based on Na-CMC and PAA were stabilized due to the cooperative ionic bond between Na-CMC carboxylate anions (-COO<sup>-</sup>) and amine groups (-NH<sub>2</sub>) of polyacrylamide. It is shown that PEC films with an equimolar ratio of Na-CMC and PAA components have an increased value of mechanical strength ( $\sigma_p = 38$  MPa), elastic modulus ( $E = 73$  MPa) and a minimum relative elongation ( $\epsilon = 0.5\%$ ). And in excess of Na-CMC or PAA leads to a decrease in mechanical strength and elastic modulus, which is associated with a decrease in the frequency of intermolecular bonds. It has been ascertained that water-soluble polyelectrolyte complexes based on Na-CMC and PAA with increased strength properties can be obtained from solutions of components taken at an equimolar ratio of interacting components. By changing the ratio of components, properties such as mechanical strength, modulus of elasticity and elongation can be controlled. This can serve as one of the means of controlling the structure and properties of Na-CMC and PAA polyelectrolyte complexes. The regulation of the physico-mechanical properties of PEC films opens up wide opportunities for their use as a soil structure former in agriculture and water management and as the basis for soft drugs in pharmacy.

**Keywords:** Sodium carboxymethylcellulose; Polyacrylamide; Polycomplex; Interpolymer complex; Films; Structure; Properties; Mechanical strength; Relative elongation; Modulus of elasticity; Electron microscopy

**PACS:** 61.41.+e

### INTRODUCTION

Currently, of great scientific and practical interest is the study of the ability of many water-soluble natural and synthetic polymers to form stable products of cooperative reactions between heterogeneous polymers, called polyelectrolyte complexes (PEC) [1–3]. PEC is a new individual substance formed due to the interaction of a polycation and a polyanion with the formation of an ionic bond. In terms of solving this problem, the interaction products of natural polyelectrolytes that form PECs are of the greatest interest. PECs are promising products in pharmacy and are increasingly used as thickeners and stabilizers for suspensions, prolongers of the drugs action, and film formers for capsules and tablets, as a base for ointments and other soft dosage forms, since they exhibit a number of unique and most valuable properties [4–11].

The possibility of independent variation of formation conditions, the ratio of reagents, and their molecular structure is essentially the basis for controlling the process of formation and production of IPC with a given set of properties [12–16].

Very interesting and promising in this aspect are macromolecular complexes based on sodium carboxymethylcellulose (Na-CMC) (polyanion) and linear polyacrylamide (PAA) (polycation), which form polyelectrolyte complexes (PEC) in aqueous systems. The structure of a natural cellulose polysaccharide derivative, Na-CMC, the presence of polar-functional groups in its macromolecules, which cause intense intermolecular interactions, the high degree of orientation of this rigid-chain polymer, determines its ability to exhibit the properties of a matrix carrier and a complexing agent with linear polyacrylamide.

Of great interest is the unique feature of the PEC systems structure based on Na-CMC and PAA systems, where, as a result of self-organization of macromolecules during the formation of polycomplexes, nanostructures with controlled nanosizes are formed [17]. This feature of polycomplex systems creates the possibility of molecular penetration of their drug compounds at the cellular level, which allows them to be used as drug systems carriers with directed transport properties. The consistency and normality of the structural and mechanical parameters of the bases based on IPC provides optimal bioavailability of medicinal substances, easy, painless application of the ointment to the skin, mucous membranes, etc. [18]. It should be noted that the constituent components of polycomplexes (PC) and PEC are large-tonnage, accessible, and cheap polymers of local origin [19].

In scientific terms, the interest in these objects is explained by the complexity of the complex structure of systems of these polymers, and in practical terms, these studies are relevant due to the possibility of using them in pharmacy as bases for ointments and soft dosage forms [20, 21].

In this regard, this paper is devoted to the study of the structure and physico-mechanical properties of PEC obtained on the basis of Na-CMC with PAA of a linear structure with varying the ratio of the interacting components and depending on the pH of the medium.

Of undoubted interest is the study of the physico-mechanical properties of IPC films, since these properties are directly related to the structure of the polymer body and the possibility of their application [2, 22, 23]. Such a study is of independent scientific value and practical importance, since the structure of the Na-CMC-PAA PEC can be varied by changing the ratio of the interacting components, and the mechanical properties directly depend on both the structure of the initial components and the structure of the PEC, and largely determine the areas of possible their use in the national economy. In the literature, studies in this direction are few, and the interest in the study of the physico-mechanical properties of Na-CMC-PAA PEC films is due to the possibility of obtaining new polymeric materials with desired mechanical properties and their targeted use as bases for soft drugs in pharmacy [24] and as a soil structure former in agriculture and water management [21,25].

## EXPERIMENTAL PART

### Materials

**Sodium carboxymethylcellulose (Na-CMC)** - SSt 5.588-79 and BA 6-05-386-80. Purified sodium carboxymethyl cellulose, a product of the Namangan Chemical Plant, obtained by the method of heterogeneous solid-phase esterification of sulfite wood cellulose with monochloroacetic acid (MCA) of the following structure was used as the main object of the research:

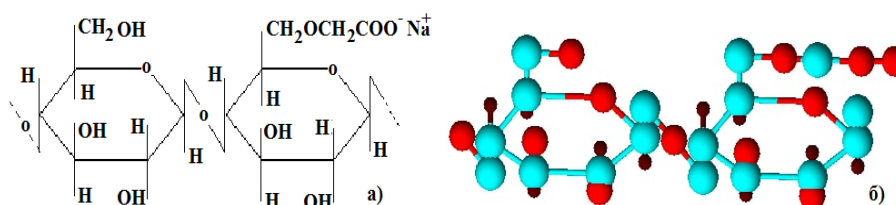


Figure 1. Chemical formula (a) and model structure of Na-CMC (b)

with a degree of substitution (DS) - 70 and a degree of polymerization (DP) - 450. It was repeatedly purified from low molecular weight salts according to the procedure given in [26, 27].

Na-CMC is a weak polyacid, its dissociation constant depends on the C3. When the DS changes from 10 to 80, the dissociation constant changes from  $5.25 \cdot 10^{-7}$  to  $5 \cdot 10^{-5}$ . In practice, CMC is mainly used in the form of the Na salt.

**Polyacrylamide (PAA).** The second component of the polyelectrolyte complex is polyacrylamide, a product of the Navoi Chemical Plant according to TSh 6.1-00203849-64:1997. Polyacrylamide is a polyelectrolyte obtained on the basis of the polymerization of acrylamide containing the element nitrogen, which has a linearly branched structure (Fig. 2) [28-31].

Polyacrylamide is an odorless, amorphous solid with a white-yellowish color, the molecular weight of which is  $10^4$ - $10^7$  (depending on the conditions of preparation). The density of polyacrylamide at room temperature (295-297 K) is about  $1.302 \text{ g/cm}^3$ . The decomposition temperature is about 463 K. Polyacrylamide is a polyelectrolyte with hygroscopic properties, harmless, and forms a soft gel when dissolved in water.

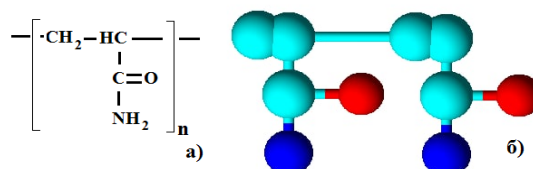


Figure 2. Chemical formula (a) and model structure of PAA (b)

### Synthesis of PEC based on Na-CMC with polyacrylamide

We used solutions of Na-CMC in bidistilled water with a concentration of 0.01 to 0.4 basic mol/l. Reaction mixtures of the required concentrations were prepared by mixing reagent solutions in the appropriate proportion at room temperature and pH 6.0–7.2.

### Obtaining films of polyelectrolyte complexes

Films from polyelectrolyte complexes were obtained by mixing aqueous solutions of Na-CMC and PAA components in equinormal ratios at different contents of components and pH of the medium. The solutions were poured onto an optical glass substrate and evaporated at room temperature. Solid dry films were washed with bidistilled water to neutral pH, then dried at room temperature.

**IR spectroscopic studies**

The structure of the obtained products was determined using IR spectroscopy and electron microscopy. IR spectra in the range 400–4000 cm<sup>-1</sup> were recorded on “NIKOLET Magna-560 IR” and “Specord-75IR” spectrophotometers (Carl Zeiss, GDR). Samples for IR spectroscopy were prepared in the form of pellets with KBr, films on a KRS-5 plate, and films 8–12 μm thick. Films on a KRS-5 plate were obtained by evaporation of the solvent (water) at room temperature (295–297 K).

**Study of mechanical properties**

The mechanical properties of the polyelectrolyte complexes films were determined by stretching at a constant lower clamp speed of 50 mm/min on an Instron-1100 automatic dynamometer (England) and on a Shimadzu AGS-X universal tensile testing machine at room temperature. The maximum measurement error was 1% [25]. Samples of the studied films were prepared in the form of blades with a working area of 5x50 mm and a thickness of 0.07 mm. Samples were measured in an air-dry state, pre-conditioned at a certain air humidity. Tensile stress σ<sub>p</sub> (MPa) in uniaxial tension was calculated by the formula:

$$\sigma_p = \frac{P}{S_0} \tag{1}$$

where, *P*- is the breaking force acting on the sample; *S*<sub>0</sub>- is the initial cross section of the sample.

Relative elongation was calculated by the formula:

$$\varepsilon = \frac{l - l_0}{l_0} \cdot 100\% \tag{2}$$

where, *l*<sub>0</sub> and *l* are the lengths of the original and stretched samples, respectively.

The initial modulus of elasticity was calculated on the initial straight sections of the stretching curves using the formula:

$$E_0 = \frac{\sigma}{\varepsilon} \tag{3}$$

**Viscometric properties**

The viscosity of solutions of polyelectrolyte complexes was determined on an Ubbelohd viscometer (*d* = 2 mm), at various temperatures under thermostatic conditions, and the time of solution outflow from the capillary was determined. The technique for determining the viscosity of solutions is described in detail in the paper [32].

**Electron microscopic studies**

Electron microscopic studies of the surfaces and cleavages (ends) of PEC films were carried out on a “Hitachi-520” scanning electron microscope (Japan) with a resolution of 60 Å. Samples were obtained by the brittle cleavage method at liquid nitrogen temperature [33]. The research results were recorded on electron micrographs.

**RESULTS AND DISCUSSION**

When mixed under certain technological conditions and at a certain temperature, and also, in principle, from different polyelectrolytes with different structures, a new, individual substance was obtained, which differed both in properties and in structure from the original components shown in Fig. 3.

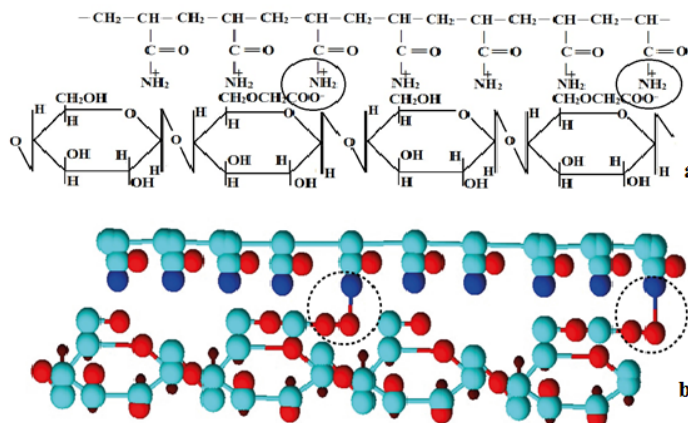


**Figure 3.** Chemical formula (a) and model structure (b) of the polyelectrolyte complex obtained on the basis of Na-CMC and PAA. Shaded area shows the formation of ionic bond between Na-CMC and PAA

Experimental data on the study of the solutions interaction of Na-CMC and polyacrylamide in neutral and slightly acidic media showed that when mixing solutions, a change in the pH of the polyelectrolyte complex compared to the initial components (Fig. 4). It should be noted that the initial components of the polyelectrolyte complex have a pH in the region of neutral values. The initial addition of polyacrylamide to the Na-CMC solution results in a slight change in the

pH reading to an equimolar composition. A further increase in the proportion of the polyacrylamide solution leads to a sharp increase in the pH of the solution of the polyelectrolyte complex. A sharp break in the dependence of the pH of solutions on the ratio of components corresponds to the equimolar composition of the interacting components (Fig. 4).

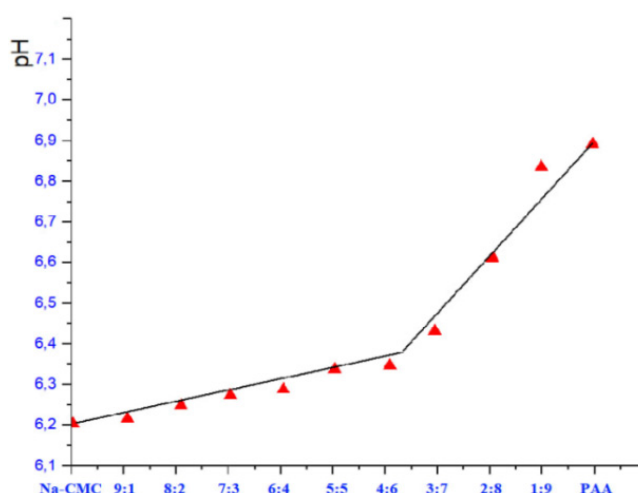


**Figure 4.** The dependence of the pH value of polyelectrolyte complexes on the ratio of Na-CMC and PAA components

The above data are confirmed by data on the study of electrical conductivity and viscosity of solutions of polyelectrolyte complexes from the ratio of Na-CMC:PAA components (table 1). A comparative change in the pH readings, electrical conductivity and viscosity of solutions of polyelectrolyte complexes from additivity indicates the formation of new individual substances compared to the original components.

**Table 1.** Physico-chemical and electrical properties of PEC based on Na-CMC and PAA

PEC Properties	Na-CMC : PAA ratio										
	Na-KMII	9:1	8:2	7:3	6:4	5:5	4:6	3:7	2:8	1:9	ΠAA
Viscosity, $\eta$ , Pa·s	0.71	0.71	0.72	1.03	1.56	2.01	2.32	2.38	2.39	2.20	2.13
Electrical conductivity, $\sigma$ , Cm	186	272	314	390	451	518	575	633	715	770	793

The structure of the resulting PEC based on Na-CMC and polyacrylamide was ascertained by IR spectroscopy and on the basis of literature data [29, 30]. The results of the analysis of the IR spectrum of the initial product Na-KMC showed that the IR spectrum contains such functional groups (Fig. 5) as the carboxylate anion - COO<sup>-</sup> (1603 cm<sup>-1</sup> and 1419 cm<sup>-1</sup>), the carboxyl group - COOH and the hydroxyl group is OH, as well as the presence of absorption bands in the structure at 1650, 1550, 1400, 1250, 1020, 780 cm<sup>-1</sup>, which gives these polymers polyelectrolyte properties (Table 2, Fig. 5). The IR spectrum of the second component contains absorption bands characteristic of a linearly branched structure. Analysis of the IR spectrum of polyacrylamide showed that the structure has absorption bands at 3422, 3180, 1664, 1618, 1401, 1327, 1112, 618 cm<sup>-1</sup>, which exhibits the characteristic properties of a polyelectrolyte (Table 2, Fig. 6).

**Table 2.** Absorption band of functional groups in Na-CMC and PAA macromolecules and in PEC

Na-CMC	Na-CMC: PAA, 80:20	Na-CMC: PAA, 60:40	Na-CMC: PAA, 50:50	Na-CMC: PAA, 40:60	PAA
3443.2	3442.52	3441.83	3429.20	3429.20	3422.96
2923.09	2923.49	-	3205.15	3207.46	3180.47
-	2854.49	-	-	-	-
-	1664.79	1668.27	1667.71	1667.42	1664.71
1603.76	1609.92	1609.46	1609.89	1612.41	1618.95
1419.79	1414.20	1452.46	1451.46	1452.41	1401.76
-	-	1411.60	1407.45	1409.54	-
1270.80	1326.20	1325.32	1324.72	1324.85	1327.14
1114.64	1266.51	1265.71	1117.50	1112.88	1112.51
1060.75	1151.51	1150.79	1066.41	-	-
1022.15	1125.71	1123.39	-	-	-
-	1060.57	1060.30	-	-	-
-	1022.79	-	-	-	-
915.74	915.79	914.13	914.72	915.69	-
701.87	621.73	622.02	619.58	617.32	618.63
599.17	-	-	-	-	-

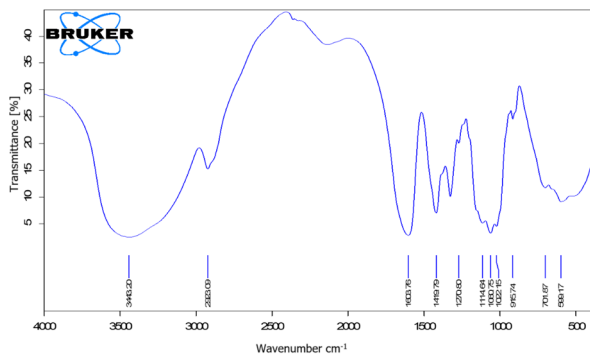


Figure 5. IR spectra of Na-CMC

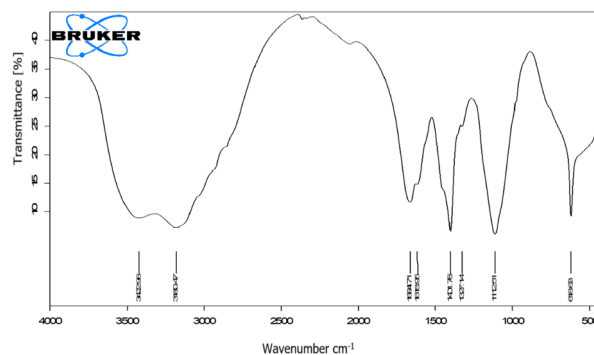


Figure 6. IR spectra of polyacrylamide

The change in intensity and the shift of the absorption band in the area of 1667 cm<sup>-1</sup>, 1609 cm<sup>-1</sup> and in the area of 1407 cm<sup>-1</sup>, 1451 cm<sup>-1</sup> indicates the formation of an ionic bond between the carboxylate anions of Na-CMC and the amine groups of polyacrylamides, which gives this polyelectrolyte complex new properties that differ from the original components (Fig. 7).

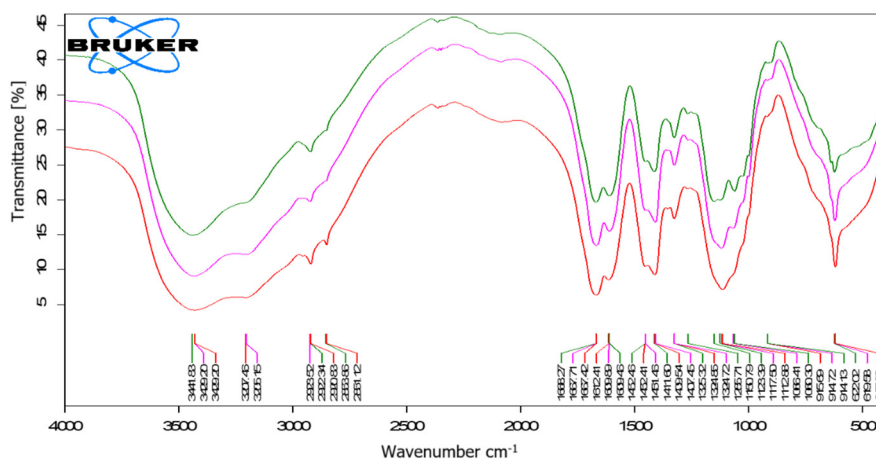


Figure 7. IR spectra of polyelectrolyte complexes from the ratio of components Na-CMC and PAA: 1 - 60:40; 2- 50:50; 3-40:60

Thus, the results of IR spectroscopy of the polyelectrolyte complex obtained on the basis of Na-CMC and polyacrylamide in neutral and slightly acidic media showed that water-soluble polyelectrolyte complexes are formed upon mixing. The resulting product can be used as carriers for soft drugs.

The study of the physico-mechanical properties of polyelectrolyte complex films obtained on the basis of Na-CMC and PAA undoubtedly confirmed the formation of a new individual substance. Since the physico-mechanical properties of such films are related to the structure of the obtained new individual polyelectrolyte complexes, their use in engineering and technology and for the preparation of drugs with prolonged properties, as well as in other substrates, is of great importance. Such studies are of both scientific and practical importance; the physico-mechanical properties and structure of the polyelectrolyte complex films will depend on the structure and properties of its constituent components [34, 35].

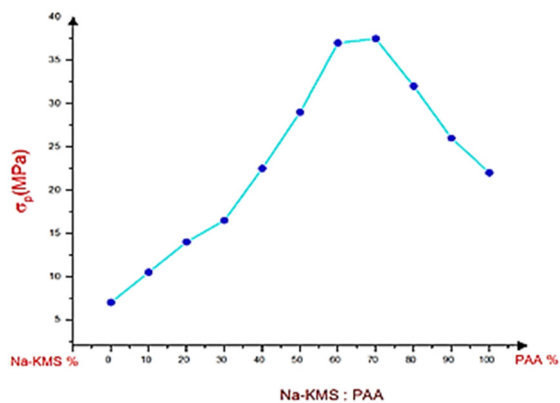


Figure 8. Graph of the dependence of the films strength of polyelectrolyte complexes on the ratio of Na-CMC:PAA components. Temperature T=24°C

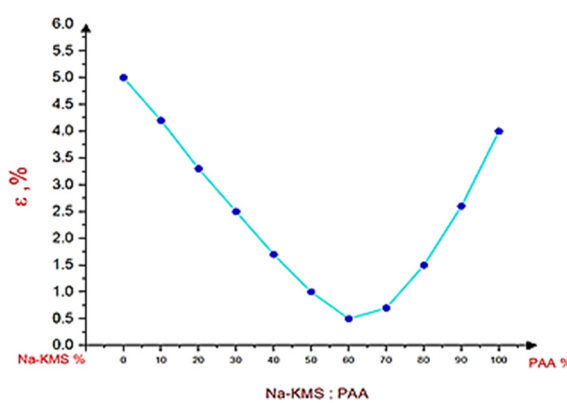
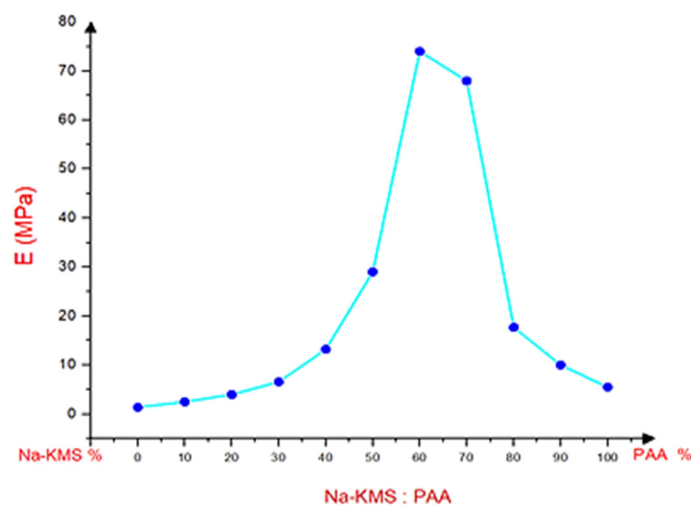


Figure 9. Graph of the dependence of the films elasticity of polyelectrolyte complexes on the ratio of Na-CMC:PAA components. Temperature T=24°C

The physico-mechanical characteristics of the polyelectrolyte complexes films were studied on an Instron-1100 automatic dynamometer (England) and on a Shimadzu AGS-X universal tensile testing machine at room temperature by stretching with a constant lower clamping speed of 50 mm/min. The mechanical strength, relative elongation and modulus of elasticity of the polyelectrolyte complexes films based on Na-CMC and PAA were determined (Fig. 8-10).



**Figure 10.** Graph of the dependence of the films elastic modulus of polyelectrolyte complexes on the ratio of components Na-CMC : PAA. Temperature  $T=24^{\circ}\text{C}$

The results of the experimental data showed that with an increase in the content of PAA in the composition of polyelectrolyte complexes obtained on the basis of Na-CMC and PAA, the interaction between the constituent components of the polyelectrolyte complex increases, which leads to an increase in the mechanical strength of the films to an equimolar composition (Fig. 8). In this case, one can observe a decrease in the relative elongation of films of polyelectrolyte complexes (Fig. 9). By increasing the frequency of crosslinking between the constituent components of the polyelectrolyte complex, the elasticity modulus of the films increases, which can be traced from the graph of the dependence of the elasticity modulus of the polyelectrolyte complexes films on the ratio of Na-CMC: PAA components to the equimolar composition (Fig. 10). A further increase in PAA in the composition of polyelectrolyte complexes leads to a decrease in the mechanical strength of the films (Fig. 8), an increase in relative elongation (Fig. 9) and a decrease in the elastic modulus (Fig. 10).

A further increase in the content of PAA in the composition of the polyelectrolyte complex films and, therefore, one can observe a decrease in the mechanical strength of the films due to an increase in the dispersed phase (Fig. 8), an increase in the relative elongation of the films under tension (Fig. 9) and a decrease in the elastic modulus due to an increase in the heterogeneous structure in films of the polyelectrolyte complex (Fig. 10). This is mainly due to the formation of a heterogeneous structure and, as a result, a decrease in the frequency of intermolecular bonds. In addition, a decrease in the elasticity modulus in films of polyelectrolyte complexes with an excess of Na-KMC or PAA is associated with the formation of a heterogeneous structure, which can be observed from images obtained by scanning electron microscopy (Fig. 11).

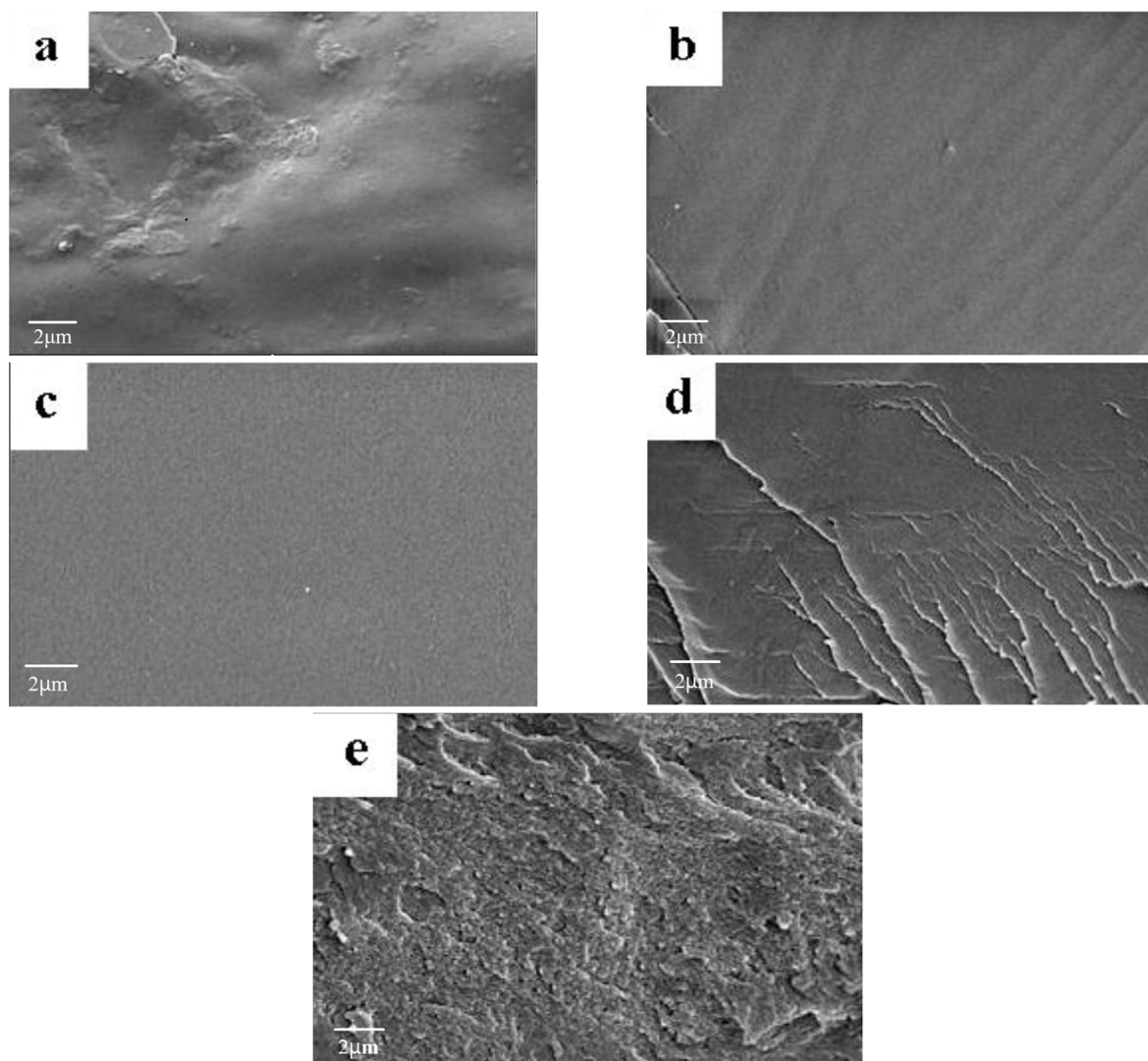
Thus, the resulting polyelectrolyte complex based on Na-CMC and PAA is a new, individual substance, both in structure and in properties differing from the structure and properties of the original products. It should be noted that the pH value for Na-CMC is  $\text{pH} = 6.2$ ; for PAA -  $\text{pH} = 7.0$ , and for PEC with an equimolar composition, it has  $\text{pH} = 6.4$ . Mechanical strength for Na-CMC -  $\sigma_p = 6.1$  MPa; for PAA,  $\sigma_p = 22$  MPa, and for PEC films with an equimolar composition, it has  $\sigma_p = 38$  MPa. Relative elongation for Na-CMC -  $\varepsilon = 5.1\%$ ; for PAA -  $\varepsilon = 4.0\%$ , and for PEC films with equimolar composition it has  $\varepsilon = 0.5\%$ . The modulus of elasticity of films for Na-CMC is  $E = 3.2$  MPa; for PAA -  $E = 8.1$  MPa, and for PEC films with an equimolar composition is  $E = 73$  MPa. All these changes in the properties of films of polyelectrolyte complexes are associated with the formation of a cooperative ionic bond between the carboxylate anions of Na-CMC ( $\text{COO}^-$ ) and the amine groups of polyacrylamide, which was confirmed by IR spectroscopic data. The increase in mechanical strength ( $\sigma_p$ ) and elastic modulus ( $E$ ) and the decrease in the relative elongation of the films of polyelectrolyte complexes is associated with an increase in the density of crosslinking between the constituent components of the polyelectrolyte complex. It should be noted that the obtained films at an equimolar ratio of Na-CMC : PAA components have the maximum mechanical strength ( $\sigma_p$ ), elastic modulus ( $E$ ), and minimum relative elongation ( $\varepsilon$ ).

## CONCLUSIONS

1. Based on the experimental data, it can be concluded that a new individual substance based on Na-CMC and PAA has been obtained. The structure and properties of the obtained polyelectrolyte complex differ from the initial products.
2. From the data of IR spectroscopy, it was revealed that the polyelectrolyte complex based on Na-CMC and PAA is stabilized due to the ionic bond between the carboxylate anions of Na-CMC and the amine groups of polyacrylamides.






3. Ionic bonds largely determine the mechanical strength of the systems under study. Water-soluble polyelectrolyte complexes based on Na-CMC and PAA with increased strength properties can be obtained from solutions of components taken at an equimolar ratio of interacting components. By changing the ratio of components, properties such as mechanical strength, modulus of elasticity and elongation can be controlled. This can serve as one of the means of controlling the structure and properties of Na-CMC and PAA polyelectrolyte complexes.



**Figure 11.** SEM electron microscopy images of Na-CMC (a), PAA (b) and PEC with the ratio of components Na-CMC : PAA=1:1 (c); 2:1(d); 1:2(e).

#### ORCID

-  Sabitjan Ya. Inagamov, <https://orcid.org/0000-0003-0587-7963>; 
  Ummatjon Asrorov, <https://orcid.org/0009-0009-6800-7392>  
 Erkin Xujanov, <https://orcid.org/0000-0003-4725-6903>

#### REFERENCES

- [1] A.K. Bajpai S.K. Shukla, and Smitha Bhanu, “Responsive polymers in controlled drug delivery,” *Progress in Polymer Science*, **33**(11), 1088–1118 (2008). <https://doi.org/10.1016/j.progpolymsci.2008.07.005>
- [2] S.Ya. Inagamov, and G.I. Mukhamedov, “Structure and physical–mechanical properties of interpolymeric complexes based on sodium carboxymethylcellulose,” *Journal of Applied Polymer Science*, **122**(3), 1749-1757 (2011). <https://doi.org/10.1002/app.34222>
- [3] I.I. Alimdjanov, A.A. Abzalov, and G.I. Mukhamedov, “Physical and Chemical properties of polycomplex gels of carboxymethyl cellulose with ureaformaldehyde oligomer,” *International journal of applied and fundamental research*, **6**, 1-2 (2018). <https://www.science-sd.com/478-25493>. (in German)
- [4] A.K. Bajpai, and J. Shrivastava, “Amylase induced enhanced enzymatic degradation of binary grafted polymeric blends of crosslinked starch and gelatin,” *J. Macromol. Sci. Part A: Pure Appl. Chem.* **41**, 949–69 (2004). <https://doi.org/10.1081/MA-120039181>
- [5] A.M. Lowman, B.C. Cowans, and N.A. Peppas “Investigation of interpolymer complexation in swollen polyelectrolyte networks using solid state NMR spectroscopy,” *J. Polym. Sci. Part B: Polym. Sci.* **38**, 2823–2831 (2000). [https://doi.org/10.1002/1099-0488\(20001101\)38:21%3C2823::AID-POLB110%3E3.0.CO;2-5](https://doi.org/10.1002/1099-0488(20001101)38:21%3C2823::AID-POLB110%3E3.0.CO;2-5)

- [6] V.V. Khutoryanskiy, A.V. Dubolazov, Z.S. Nurkeeva, and G.A. Mun, "pH effects in complex formation and blending of poly(acrylic acid) with poly(ethylene oxide)," *Langmuir*, **20**, 3785–3790 (2004). <https://doi.org/10.1021/la0498071>
- [7] G.A. Mun, Z.S. Nurkeeva, V.V. Khutoryanskiy, G.S. Sarybayeva, and A.V. Dubolazov, "pH effects in the complex formation of polymers I. Interaction of poly(acrylic acid) with poly(acrylamide) ," *Eur. Polym. J.* **39**, 1687–1691 (2003). [https://doi.org/10.1016/S0014-3057\(03\)00065-X](https://doi.org/10.1016/S0014-3057(03)00065-X)
- [8] K. Karayanni, and G. Staikos, "Study of lower critical solution temperature behaviour of poly(vinyl methyl ether) aqueous solutions in the presence of poly(acrylic acid). The role of Interpolymer hydrogen bonding interaction," *Eur. Polym. J.* **36**, 2645–2650 (2000). [https://doi.org/10.1016/S0014-3057\(00\)00048-3](https://doi.org/10.1016/S0014-3057(00)00048-3)
- [9] G.A. Mun, Z.S. Nurkeeva, V.V. Khutoryanskiy, and A.D. Sergazyev, "Interpolymer complexes of copolymers of vinyl ether of diethylene glycol with poly(acrylic acid)," *Colloid Polym. Sci.* **280**, 282–289 (2002). <https://doi.org/10.1007/s00396-001-0609-4>
- [10] Z.S. Nurkeeva, V.V. Khutoryanskiy, G.A. Mun, and A.B. Bitekenova, "Complexation of poly(acrylic acid) with poly(vinyl methyl ether) in the presence of inorganic salts and lidocaine hydrochloride," *Polymer science*, **45**, 365–369 (2003), <https://api.semanticscholar.org/CorpusID:53701319>
- [11] F. Bossard, M. Sotiropoulou, and G. Staikos, "Thickening effect in soluble hydrogen-bonding interpolymer complexes influences of pH and molecular parameter," *Journal of Rheology*, **48**, 927–936 (2004). <https://doi.org/10.1122/1.1763941>
- [12] E. Nordmeier, and P.J. Beyer, *Polym. Sci. Pol. Phys.* **37**(4), 335 (1999). [https://doi.org/10.1002/\(SICI\)1099-0488\(19990215\)37:4<335::AID-POLB7>3.0.CO;2-W](https://doi.org/10.1002/(SICI)1099-0488(19990215)37:4<335::AID-POLB7>3.0.CO;2-W)
- [13] V.V. Khutoryanskiy, S. Ryu, and A.V. Yakimansky, "Modern Methods for Studying Polymer Complexes in Aqueous and Organic Solutions," *Polym. Sci. Ser. A*, **60**(5), 553 (2018). <https://doi.org/10.1134/S0965545X18050085>
- [14] V.A. Izumrudov, B.K. Mussabaeva, Z.S. Kassymova, A.N. Klivenko, and L.K. Orazzhanova, "Interpolyelectrolyte complexes: advances and prospects of application," *Russ. Chem. Rev.* **88**(10), 1046 (2019). <https://doi.org/10.1070/RCR4877>
- [15] R.I. Mustafin, "Interpolymer combinations of chemically complementary grades of Eudragit copolymers: a new direction in the design of peroral solid dosage forms of drug delivery systems with controlled release (review)," *Pharm. Chem. J.* **45**(5), 285–295 (2011). <https://doi.org/10.1007/s11094-011-0618-7>
- [16] A.V. Bukhovets, A.Y. Sitenkov, and R.I. Moustafine, "Comparative evaluation study of polycomplex carriers based on Eudragit® EPO/S100 copolymers prepared in different media," *Polym. Adv. Technol.* **32**, 2761 (2021). <https://doi.org/10.1002/pat.5284>
- [17] A.V. Bukhovets, N. Fotaki, V.V. Khutoryanskiy, and R.I. Moustafine, "Interpolymer Complexes of Eudragit® Copolymers as Novel Carriers for Colon-Specific Drug Delivery," *Polymers*, **12**(7), 1459 (2020). <https://doi.org/10.3390/polym12071459>
- [18] J.C. Roy, A. Ferri, S. Giraud, G. Jinping, and F. Salaün, "Chitosan–Carboxymethylcellulose–Based Polyelectrolyte Complexation and Microcapsule Shell Formulation," *Int. J. Mol. Sci.* **19**, 2521 (2018). <https://doi.org/10.3390/ijms19092521>
- [19] M.T. Cook, S.L. Smith, and V.V. Khutoryanskiy, "Novel glycopolymer hydrogels as mucosa-mimetic materials to reduce animal testing," *Chemical Communications*, **51**(77), 14447–14450 (2015). <https://doi.org/10.1039/C5CC02428E>
- [20] E.D.H. Mansfield, K. Sillence, P. Hole, A.C. Williams, and V.V. Khutoryanskiy, "POZylation: a new approach to enhance nanoparticle diffusion through mucosal barriers," *Nanoscale*, **7**(32), 13671–13679 (2015). <https://doi.org/10.1039/C5NR03178H>
- [21] A.V. Bukhovets, N. Fotaki, V.V. Khutoryanskiy, and R.I. Moustafine, "Interpolymer Complexes of Eudragit® Copolymers as Novel Carriers for Colon-Specific Drug Delivery," **12**(7), 1459 (2020). <https://doi.org/10.3390/polym12071459>
- [22] A.I. Chepurnaya, M.P. Karushev, E.V. Alekseeva, D.A. Lukyanov, and O.V. Levin, "Redox-conducting polymers based on metal-salen complexes for energy storage applications," *Pure. Appl. Chem.* **92**(8), 1239–1258 (2020). <https://doi.org/10.1515/pac-2019-1218>
- [23] J. Swarbrick, *Encyclopedia of Pharmaceutical Technology*, vol. 6, 3<sup>rd</sup> ed. (CRC Press, Boca Raton, 2013). <https://doi.org/10.1201/b19309>
- [24] T.M.M. Ways, S.K. Filippov, S. Maji, M. Glassner, M. Ceglowski, R. Hoogenboom, et al., "Mucus-penetrating nanoparticles based on chitosan grafted with various non-ionic polymers: Synthesis, structural characterisation and diffusion studies," *Journal of Colloid and Interface Science*, **626**, 251–264 (2022). <https://dx.doi.org/10.1016%2Fj.jcis.2022.06.126>
- [25] V.V. Khutoryanskiy, Z.S. Nurkeeva, G.A. Mun, A.D. Sergazyev, Z. Ryskaliyeva, and J.M. Rosiak, "Polyelectrolyte complexes of soluble poly-2-[(methacryloyloxy)ethyltrimethylammonium chloride and its hydrogels with poly(acrylic acid)]," *European Polymer Journal*, **39**(4), 761–766 (2003). [https://doi.org/10.1016/S0014-3057\(02\)00293-8](https://doi.org/10.1016/S0014-3057(02)00293-8)
- [26] G.I. Mukhamedov, M.M. Xafizov, and S.Ya. Inagamov, *Interpolymer complexes: structure, properties, application*, (Lambert Academic Publishing Ru, 2018). ISBN 13: 9786138326816
- [27] D. Ren, Y.-H. Li, S.-P. Ren, T.-Y. Liu, and X.-L. Wang, "Microporous polyarylate membrane with nitrogen-containing heterocycles to enhance separation performance for organic solvent nanofiltration," *Journal of Membrane Science*, **610**, 118295 (2020). <https://doi.org/10.1016/j.memsci.2020.118295>
- [28] X. Shan, A.C. Williams, and V.V. Khutoryanskiy, "Polymer structure and property effects on solid dispersions with haloperidol: Poly(N-vinyl pyrrolidone) and poly(2-oxazolines) studies," *International Journal of Pharmaceutics*, **590**, 119884 (2020). <https://dx.doi.org/10.1016%2Fj.ijpharm.2020.119884>
- [29] A. Muterko, "Selective precipitation of RNA with linear polyacrylamide," *Nucleosides, Nucleotides & Nucleic Acids*, **41**(1), 61–76 (2022). <https://doi.org/10.1080%2F15257770.2021.2007397>
- [30] A. Pulyalina, I. Faykov, V. Nesterova, M. Goikhman, I. Podeshvo, N. Loretsyan, A. Novikov, et al., "Novel Polyester Amide Membranes Containing Biquinoline Units and Complex with Cu(I): Synthesis, Characterization, and Approbation for n-Heptane Isolation from Organic Mixtures," *Polymers*, **12**, 645 (2020). <https://doi.org/10.3390/polym12030645>
- [31] E.E. Brotherton, T.J. Neal, D.B. Kaldybekov, M.J. Smalridge, V.V. Khutoryanskiy, and S.P. Armes, "Aldehyde-functional thermoresponsive diblock copolymer worm gels exhibit strong mucoadhesion," *Chemical Science*, **13**(23), 6888–6898 (2022). <https://doi.org/10.1039/D2SC02074B>
- [32] L.E. Agibayeva, D.B. Kaldybekov, N.N. Porfiriyeva, V.R. Garipova, R.A. Mangazbayeva, R.I. Moustafine, I.I. Semina, et al., "Gellan gum and its methacrylated derivatives as in situ gelling mucoadhesive formulations of pilocarpine: In vitro and in vivo studies," *International Journal of Pharmaceutics*, **577**, 119093 (2020). <https://doi.org/10.1016/j.ijpharm.2020.119093>
- [33] C.H.R. Jagadish, A. Ferri, S. Giraud, J. Guan, and S. Fabien, "Chitosan–Carboxymethylcellulose–Based Polyelectrolyte Complexation and Microcapsule Shell Formulation," *Int. J. Mol. Sci.* **19**, 2521 (2018). <https://doi.org/10.3390/ijms19092521>

- [34] P. Tonglairoum, R.P. Brannigan, P. Opanasopit, and V.V. Khutoryanskiy, "Maleimide-bearing nanogels as novel mucoadhesive materials for drug delivery," *Journal of Materials Chemistry B*, **4**(40), 6581–6587 (2016). <https://doi.org/10.1039/C6TB02124G>
- [35] D. Ren, Y.-H. Li, S.-P. Ren, T.-Y. Liu, and X.-L. Wang, "Microporous polyarylate membrane with nitrogen-containing heterocycles to enhance separation performance for organic solvent nanofiltration," *Journal of Membrane Science*, **610**, 118295 (2020). <https://doi.org/10.1016/j.memsci.2020.118295>

#### СТРУКТУРА ТА ФІЗИКО-МЕХАНІЧНІ ВЛАСТИВОСТІ ПОЛІЕЛЕКТРОЛІТНИХ КОМПЛЕКСІВ НА ОСНОВІ ПОЛІСАХАРИДУ КАРБОКСИМЕТИЛЦЕЛЮЛОЗИ НАТРІЮ ТА ПОЛІАКРИЛАМІДУ

Сабітжан Я. Інагамов<sup>a</sup>, Умнатджон А. Асроров<sup>b,c</sup>, Еркін Б. Ксуджанов<sup>c</sup>

<sup>a</sup> Ташкентський фармацевтичний інститут, Мірабадський район, Айбекст, 45 м. 100015, Ташкент, Узбекистан

<sup>b</sup> Національний університет Узбекистану імені Мірзо Улугбека, Ташкент, Узбекистан

<sup>c</sup> Ташкентський державний педагогічний університет імені Нізамі, Ташкент, Узбекистан

У роботі досліджено структуру та фізико-механічні властивості плівок поліелектролітних комплексів (ПЕК) на основі натрійкарбоксиметилцелюлози (Na-КМЦ) з лінійним поліакриламідом (ПАК). Поліелектролітні комплекси отримували змішуванням водних розчинів компонентів Na-КМЦ і ПАА в різних співвідношеннях компонентів і рН середовища. Структуру отриманих продуктів визначали за допомогою ІЧ-спектроскопії та електронної мікроскопії. ІЧ-спектри в діапазоні 400–4000 см<sup>-1</sup> записували на спектрофотометрах NIKOLET Magna-560 IR та Specord-75IR (Carl Zeiss, НДР). Механічні властивості плівок поліелектролітних комплексів визначали розтягуванням при постійній швидкості руху нижнього затискача 50 мм/хв на автоматичному динамометрі Instron-1100 (Англія) при кімнатній температурі. Дані ІЧ-спектроскопії показали, що поліелектролітні комплекси на основі Na-КМЦ і ПАА стабілізувалися за рахунок кооперативного іонного зв'язку між карбоксилат-аніонами Na-КМЦ (-COO-) і амініними групами (-NH<sub>2</sub>) поліакриламід. Показано, що плівки ПЕК з еквімолярним співвідношенням компонентів Na-КМЦ та ПАА мають підвищене значення механічної міцності ( $\sigma_p = 38$  МПа), модуля пружності ( $E=73$  МПа) та мінімальне відносне видовження ( $\epsilon = 0,5\%$ ). А надлишок Na-СМС або ПАА призводить до зниження механічної міцності і модуля пружності, що пов'язано зі зниженням частоти міжмолекулярних зв'язків. Встановлено, що з розчинів компонентів, узятих при еквімолярному співвідношенні взаємодіючих компонентів, можна отримати водорозчинні поліелектролітні комплекси на основі Na-КМЦ і ПАА з підвищеними міцнісними властивостями. Змінюючи співвідношення компонентів, можна контролювати такі властивості, як механічна міцність, модуль пружності та видовження. Це може бути одним із засобів керування структурою та властивостями поліелектролітних комплексів Na-КМЦ та ПАА. Регулювання фізико-механічних властивостей плівок ПЕК відкриває широкі можливості для їх використання як ґрунтоутворювача у сільському та водному господарстві та як основи для м'яких лікарських засобів у фармації.

**Ключові слова:** натрійкарбоксиметилцелюлоза; поліакриламід; полікомплекс; інтерполімерний комплекс; плівки; структура; властивості; механічна міцність; відносне видовження; модуль пружності; електронна мікроскопія